Electron microscopy and multi-scale modelling of radiation damage recovery in tungsten

Francesco Ferroni

A thesis presented for the degree of
Doctor of Philosophy

Department of Materials
University of Oxford
St. Catherine's College
United Kingdom
Sunday 13th March, 2016

Abstract

The thesis is concerned with understanding the recovery mechanisms of radiation damage in tungsten. Tungsten is a key material in next-generation fusion reactors such as ITER, which will be exposed to intense neutron radiation, plasma and high temperatures, and its durability will determine the reactor's competitiveness versus other energy sources.

The thesis makes a comprehensive, quantitative study of recovery and its dependence on temperature, time, and material purity. It employs both experiments (ion-beam irradiation with *ex* and *in situ* analysis via transmission electron microscopy) and multi-scale deterministic and stochastic modelling techniques such as molecular dynamics and dislocation dynamics.

Annealing experiments on ultra-pure tungsten reveal the presence of several recovery stages, and an acceleration of dislocation defect recovery and loop coarsening above $\sim$900°C. They also reveal discrepancies with dislocation climb models in the literature, suggesting the presence of additional recovery pathways leading to coarsening, most notably conservative self-climb.

Presence of helium is found to cause an increase in the equilibrium concentration of defects at a given temperature. Also, very high doses cause morphological changes to the radiation damage structure, from relatively homogeneous defect concentrations of dislocations in a narrow size range, to complex dislocations networks with voids.

Finally, modelling techniques are able to successfully predict dislocation motion phenomena observed in experiments at high temperature (including quantitatively accurate defect densities), but only after extensive modification of publicly available dislocation dynamics codes to include boundary conditions and stochastic behaviour of crystal defects.

Declaration

I herewith certify that all material in this dissertation which is not my own work has been properly acknowledged.

Francesco Ferroni

Acknowledgements

I would like to thank first and foremost my supervisors Prof. Steve Roberts, Dr. Steve Fitzgerald and Dr. Edmund Tarleton for their support and mentoring, whilst juggling a hectic schedule. In particular, Prof Roberts for his multi-decade experience, which proved useful in numerous occasions (experimental planning and analysis, grant and proposal writing, journal publication and thesis corrections etc.), Dr. Fitzgerald for the enthusiastic support and constant, concrete help in developing new computational techniques, and Dr. Tarleton for his almost daily supervision and patience (and coffee).

I would also like to thank Dr. Xiaoou Yi, who has also been my de-facto supervisor in every way except on paper. I am particularly grateful for her training in microscopy techniques, and her help and assistance in experimental campaigns around the globe - in Japan, France and the United States. 非常谢谢！I wish you the very best in your career.

I would also like to thank the materials modelling team at Culham Centre for Fusion Energy (Dr. Thomas Swinburne, Dr. Daniel Mason, Dr. Mark Gilbert, and Prof. Sergei Dudarev) for their advice; collaborators at Oak Ridge National Laboratory and University of Tennessee (Prof. Brian Wirth, Prof. Karl Hammond, and Dr. Marie Backman); and finally Prof. Kazuto Arakawa, Dr. Daniel Caillard, Dr. Mark Kirk, and the CEA Saclay team for use of their facilities.

Francesco Ferroni, Sunday 13th March, 2016, St Catherine's College, Oxford

Publications related to this thesis

- *High temperature annealing of ion irradiated tungsten*, F. Ferroni, X. Yi, K. Arakawa, S.P. Fitzgerald, P.D. Edmondson, and S.G. Roberts, Acta Materialia, 2015 [1].

  The work carried out by myself and reported in [1] is presented primarily in Chapter 3.

- *Dislocation dynamics modelling of radiation damage in thin film*, F. Ferroni, E. Tarleton, and S.P. Fitzgerald, Modelling and Simulation in Materials Science and Engineering, 2014 [2].

  The work carried out by myself and reported in [2] is presented primarily in Chapter 5, Sections 5.3 to 5.4.

- *GPU accelerated dislocation dynamics*, F. Ferroni, E. Tarleton, and S.P. Fitzgerald, Journal of Computational Physics, 2014 [3].

  The techniques developed by myself and reported in [3] are used in the algorithms in Chapter 5, although not presented in the main text but left in Appendix B.

- *Sputtering yields of pure and helium-implanted tungsten under fusion-relevant conditions calculated using molecular dynamics*, F. Ferroni, K.D. Hammond, B.D. Wirth, Journal of Nuclear Materials, 2015 [4].

  The techniques developed out by myself and reported in [4] are presented in parts in Section 4.3.5.

Chapter 4 on dual-beam irradiations, Section 5.5 in Chapter 5 on FEM-DD coupling, and Chapter 6 on stochastic dislocation dynamics and molecular dynamics diffusion simulations of radiation defects are currently unpublished, but are being written into publications for the wider readership.

Contents

Acronyms

APT	Atom Probe Tomography
AWE	Atomic Weapons Establishment
BCC	Body Centred Cubic
BEM	Boundary Element Method
BVP	Boundary Value Problem
CBED	Convergent Beam Electron Diffraction
CCD	Charged-Coupled Device
CCFE	Culham Centre for Fusion Energy
CEA	Commissariat à l'Énergie Atomique (French: Atomic Energy Commission)
CFC	Carbon Fibre Composite
CPU	Central Processing Unit
CTF	Component Test Facility
CUDA	Compute Unified Device Architecture
DD	Dislocation Dynamics
DDD	Discrete Dislocation Dynamics
DEMO	DEMOnstration Power Plant
DFFT	Discrete Fast Fourier Transform
DFT	Density Functional Theory
EDM	Electrical Discharge Machining
EELS	Electron Energy Loss Spectroscopy
EFDA	European Fusion Development Association
ELM	Edge Localized Mode
FCC	Face Centred Cubic
FEM	Finite Element Method

FIM	Field Ion Microscopy
FMM	Fast Multipole Method
GPU	Graphical Processing Unit
IFMIF	International Fusion Materials Irradiation Facility
ITER	International Thermonuclear Experimental Reactor
JEOL	Japan Electron Optics Laboratory
JET	Joint European Torus
MEAM	Modified Embedded-Atom Method
NRT	Norgett-Robinson-Torrens
ODE	Ordinary Differential Equation
PKA	Primary Knock-on Atom
RT	Room Temperature
SIA	Self Interstitial Atom
SRIM	Stopping and Range in Matter
STD	Suzuki-Trotter Decomposition
TDS	Thermal Desorption Spectroscopy
TEM	Transmission Electron Microscope
TOKAMAK	Toroidalnaya Kamera Magnitnaya (Russian: toroidal chamber-magnetic)
UHP	Ultra High Purity
UKAEA	United Kingdom Atomic Energy Agency

Chapter 1

Introduction

1.1 Motivations

In 2012, on the back of an economic downturn, global energy consumption growth slowed significantly to 1.8%, with approximately 90% of net growth taking place in India and China alone [5]. Despite the slowdown, consumption and production reached record levels for all fuels coupled with increasing levels of CO_2 production. Oil remains the world's leading fuel, at 33.1% of global energy consumption, with another 23.9% being covered by natural gas. Despite the ongoing shale-gas revolution, which has opened up the use of unconventional sources of hydrocarbons, it is widely accepted that a continuing growth in consumption of fossil fuels is not sustainable in the long run, with its contribution to climate change and pollution also being a major issue, as shown in Fig. 1.1.

Conventional nuclear energy has been marred by the Fukushima incident in March 2011. Global nuclear output fell by 6.9%, the largest decline on record for a second consecutive year; Japanese output fell by 89%, accounting for 82% of the global decline. Nuclear output accounted for 4.5% of global energy consumption, the smallest share since 1984 [5]. Although it is likely for Japan to be forced to re-instate the use of nuclear power, conventional fission reactors are facing substantial resistance from public opinion and policy makers, with Germany and Switzerland among the countries opting for a total phase-out. Despite the welcomed increase in renewable energy production, many countries, particularly in Europe and Far East, will be un-

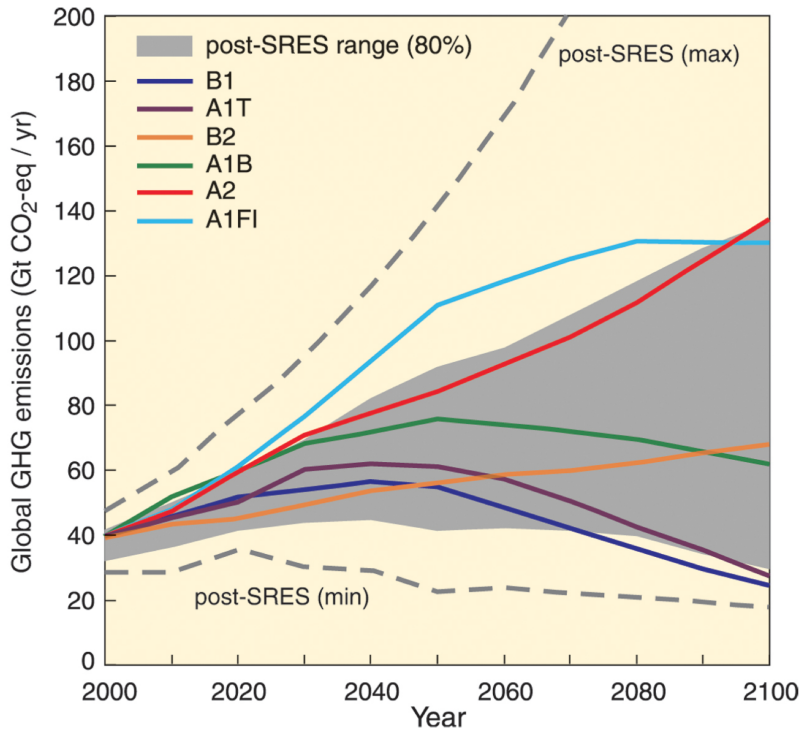

Figure 1.1: Projected global greenhouse gas emissions in absence of additional climate policies with alternative development scenarios. A1 assumes a world of very rapid economic growth, a global population that peaks in mid-century and rapid introduction of new and more efficient technologies. A1 is divided into 3 groups that describe alternative directions of technological change: fossil intensive (A1FI), non-fossil energy resources (A1T) and a balance across all sources (A1B). B1 describes a convergent world, with the same global population as A1, but with more rapid changes in economic structures toward a service and information economy. B2 describes a world with intermediate population and economic growth, emphasising local solutions to sustainability. A2 describes a very heterogenous world with high population growth, slow economic development and no technological change. (SRES stands for *Special Report on Emissions Scenarios*). For more information see the Climate Change Synthesis Report by *Pachuari et al.* [6].

able to meet their energy demands solely on renewables owing to the large associated land footprint, harvesting and energy storage difficulties.

Fusion energy has long been heralded as a revolutionary way of producing electricity. It produces no CO_2 emissions, has a minuscule land-use footprint, uses widely available substances as fuel (or that can be transmuted in-situ into fuel), has no risks of meltdowns like fission energy, and produces significantly smaller quantities of shorter-lived radioactive material. In the past 50 years significant steps have been undertaken to bring this form of energy from an idea to reality, navigating

through phases of more or less support [7]. Currently, ITER, the International Thermonuclear Experimental Reactor, is being built in Cadarache, France, and will be expected to demonstrate sustained net energy output from a fusion reaction.

Despite the progress, there are still enormous hurdles to overcome, particularly in terms of material science and engineering. With plasma temperatures of more than 100 million °C, extreme temperature differentials (hot plasmas to liquid helium coolants) and intense levels of neutron irradiation (30 dpa/year for envisaged commercial reactors), engineering suitable super-materials capable of withstanding such environments reliably still need to be addressed [8, 9]. Advances in this field, particularly with regards to high temperature and irradiation resistance of materials, are key to making fusion energy work, and would also have beneficial effects for conventional nuclear fission and aerospace sectors.

1.2 Fusion materials

1.2.1 Material requirements for a fusion reactor

The ultimate aim of fusion energy research is to harness the power of nuclear fusion reactions for the production of electricity. For a commercial reactor to operate in a commercially viable way, it must produce significantly more power output than input, as defined by Q or the fusion energy gain factor. Although the Joint European Torus (JET) at CCFE in the United Kingdom has demonstrated break even [10], a commercial reactor requires a Q of above ∼10-20 [11] and should be capable of operating for very long pulses reliably. This is not possible for reactor sizes similar to JET. The critical parameter for power generation (L_c) is the triple product:

$$L_c = n_e T \tau_E$$

given by the product of plasma temperature (T), density (n_e) and confinement time (τ_E) [12]. Although density and temperature have been increased in the past

decades using stronger magnetic fields and more powerful ohmic and accelerator-based heating techniques, only confinement time is readily adjustable by increasing the plasma vessel volume, thereby leading to the much larger ITER design and DEMO designs [12]. The trend of increasing vessel volume places increasing demands on the plasma facing materials since fusion power increases with R^3 whereas the heat-dissipating surface area increases with R^2, where R is the vessel radius. In the best plasma operating modes an estimated 90% of the energy may be radiative and thus evenly distributed on vessel tiles [13]. However, the remaining 10% (or more) of thermal energy will preferentially follow magnetic field lines and be extracted by a restricted area at the bottom of the vessel, called the divertor, show in Figure 1.2. The divertor serves as an exhaust system to stabilise the plasma, extract heat and remove helium and other impurities, and is thus by far the most stressed component in the tokamak [14]. Owing to the extreme severity of environmental conditions within a reactor, significant progress is required in materials research to produce a commercial power plant.

The main factors considered when selecting a candidate material for the divertor are:

- Melting temperature and thermal conductivity.
- Radiation tolerance and transmutation effects.
- Tritium retention.
- Plasma sputtering resistance.
- Hydrogen and helium effects.

Current design parameters require the divertor to withstand steady state heat loads of $5MW/m^2$, with peak transient loads of $10MW/m^2$ [15, 16]. An additional $10MW/m^2$ heating from neutron collisions is also expected [17]. Plasma facing components will see operating temperatures of up to 800°C, with neutron damage up to 150dpa over an estimated 5 year operational lifespan, with helium levels (coming

from direct plasma implantation as well as transmutation) reaching 1200appm [18]. One of the selling points of fusion energy compared to conventional nuclear power is the lack of long-lived radioactive isotopes. Although the fuel cycle itself does not produce any radioactive material, the high-energy neutrons created from the reaction will activate the plasma facing materials [19]. This marked peak in high-energy neutrons (14MeV) is shown in Figure 1.3. To limit the amount of radioactive waste produced, only low-activation elements are to be used, severely restricting the material choice to C, Si, Fe, V, Cr, W, and Ta [20].

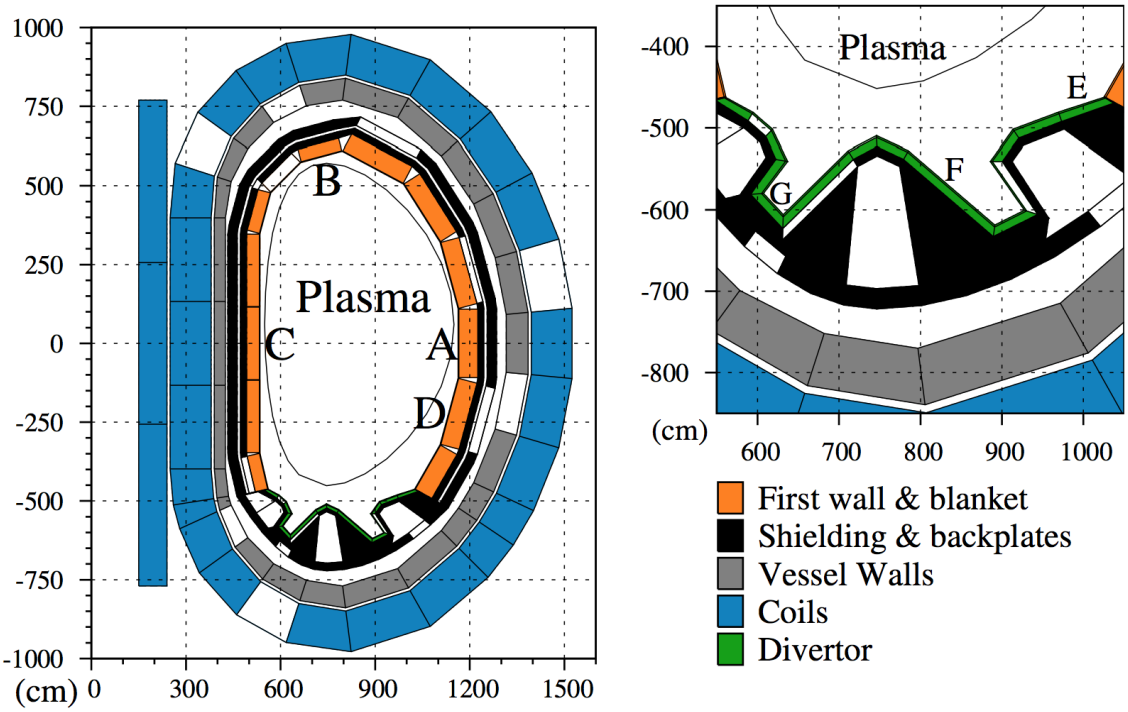

Figure 1.2: Schematic toroidal cross-section of a DEMO reactor [21].

Finally, the material must also have low tritium retention. Tritium is a radioactive isotope of hydrogen used as fuel in the fusion reactor. Thus, for regulatory and safety reasons only small amounts are permitted on-site, meaning that the inventory inside the vessel must be as low as possible.

1.2.2 Candidate materials: why tungsten?

Of the select number of low-activation materials, the only two suitable for the high temperature conditions in the divertor are carbon fibre composites (CFCs),with

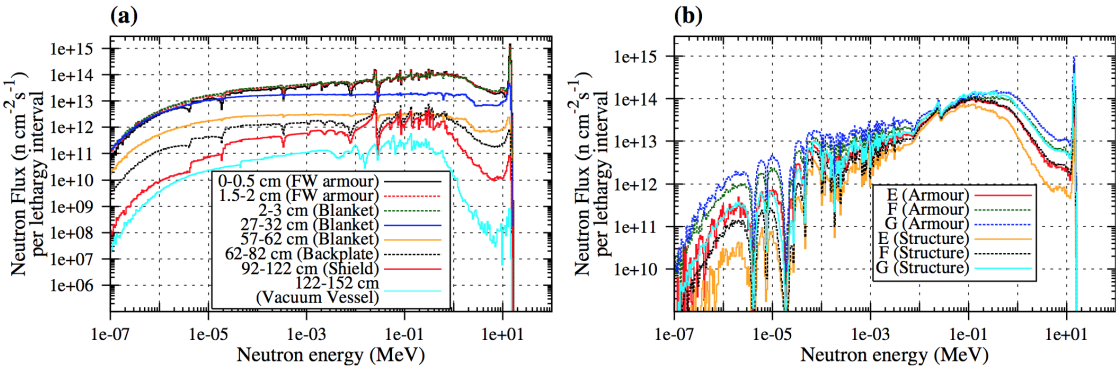

Figure 1.3: Comparison of the neutron-energy spectra in DEMO; (a) as a function of depth into the vessel from the plasma-facing wall at the equatorial position A in Figure 1.2; and (b) in the first two layers of the divertor as a function of position (E-G in Figure 1.2[21].

an operating window of 650-950°C, and tungsten, with an operating window of 1000-1200°C[22]. CFCs have excellent thermal conductivity, do not quench plasma significantly and have good mechanical properties [23]. The reason why ITER and future DEMO power plants exclude CFCs for the divertor is three-fold. Firstly, it is extremely sensitive to radiation damage. At operating conditions, the thermal conductivity of CFCs (200-500W/mK) is reduced by a factor of three after only 1 dpa [24] (See Section 3.1.2 for an explanation of dpa as a measure of radiation dose). Secondly, CFCs have pitiful plasma erosion resistance [25]. The erosion rates in JET have been reported as several microns per pulse, causing re-deposition problems and the creation of organic materials. In DEMO a CFC divertor would be eroded in a matter of days [26]. The required downtime for repair and replacement would be unacceptable for a commercially competitive reactor. To reduce sputtering rates, the material must thus be high-Z [27, 28]. Thirdly, CFC has high tritium retention rates, 10-100 times greater than tungsten [29, 30].

The current preferred candidate material for the divertor is therefore tungsten [31], owing to its high melting point (3422C), good thermal conductivity (174 W/mK), low tritium inventory (2g/1000 plasma discharges), and high sputtering, erosion and neutron displacement damage resistance [18, 32, 33, 34]. The Achilles heel of tungsten is, being a refractory metal, its low fracture toughness, with polycrystalline alloys typically having fracture toughness of less than 10MPa $m^{\frac{1}{2}}$ with intergranular

crack paths [35, 36, 37]. Neutron irradiation further reduces the fracture toughness (radiation embrittlement) [38], with experiments citing up to a factor of ten reduction [39]. Possible physical mechanisms explaining enhanced failure are reviewed in later sections. Unsurprisingly, the overarching goal for tungsten development is increasing the initial ductility of the material, its formability and fracture toughness, without compromising its other beneficial properties. These properties must be sufficient to prevent failures even after neutron radiation-induced degradation.

1.3 Radiation damage

There are many thousands of publications related to the subject of irradiation damage. In this section, the relevant mechanisms and consequences of irradiation damage are presented, specifically for tungsten. The emphasis is on the changes that occur in material microstructure, which can be linked to changes in mechanical behaviour.

1.3.1 Neutrons

To harness electricity from atomic energy, one must release the binding energy of the nuclei involved in the nuclear reaction in the form of kinetic energy, and convert it into heat for generation purposes. Depending on the type of nuclear reaction, fission (splitting) or fusion (combining), the released neutrons have different released energies [12].

$$D^+ + T^+ \rightarrow^4 He^{2+}(3.56\text{MeV}) + n(14.03\text{ MeV}) \tag{1.1}$$

$$^{235}U + n \rightarrow^{236} U \rightarrow^{92} Kr +^{141} Ba + 3n\ (200\text{MeV total}) \tag{1.2}$$

In fission, the resultant neutrons are usually thermalised (slowed down) by interacting with a moderator material. Fusion has a distinct neutron energy peak at 14.03MeV. Figure 1.4 graphically shows the difference in neutron energy spectra

between these two reactions [21].

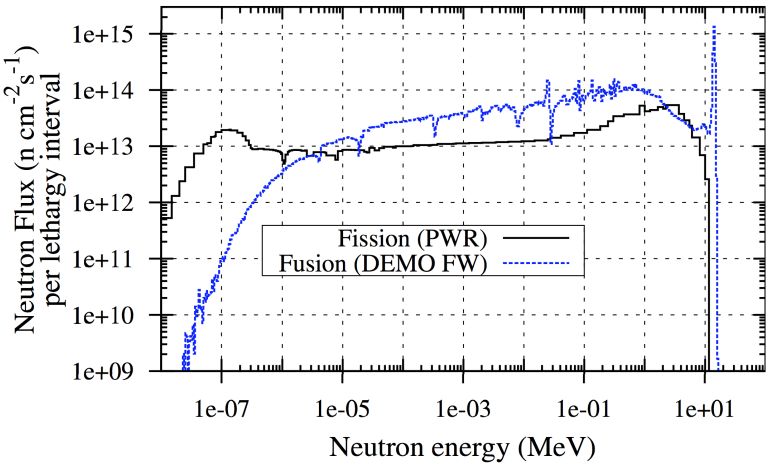

Figure 1.4: Characteristic neutron spectrum in deuterium-tritium fusion reactor and fission pressurised water reactor [21].

A neutron flux incident on a material will cause irradiation damage through *elastic* scattering of the neutrons and neutron absorption leading to *inelastic* scattering and material transmutation. Although by the end of the 19th century the effect of irradiation of various forms had been identified [40], it was the development of fission reactors (and thermonuclear weapons) that accelerated research, increasing the knowledge of the detailed mechanisms involved [41, 42]. Furthermore, the invention of the transmission electron microscope (TEM) meant that irradiation-induced defects could be studied directly [43, 44].

1.3.2 Effects and mechanisms

The macroscopic changes in mechanical properties of an irradiated metal alloy are strongly linked to its microstructural evolution. When irradiated, effects like grain growth, the formation of defect clusters and coalescence into larger dislocation loop structures, radiation enhanced precipitation and solute segregation may all occur [45]. A damage event initiates when an energetic particle (neutron, ion, electron) collides with a nucleus. If the particle can transfer sufficient energy, it will displace the atom from its equilibrium state and produce a primary knock-on atom (PKA), leaving a vacancy site behind. A sufficiently high-energy PKA can displace multiple

atoms, generating a displacement cascade. Once the PKA (and any other displaced atoms) comes to rest, a self-interstitial atom (SIA) defect is produced. The original vacancy and the SIA are referred to as a Frenkel pair. One can approximate the total number of displacements per atom caused by a single PKA using the NRT model (Norgett, Robinson, Torrens [46]), a modified Kinchin-Pease formulation [40].

$$N_d = \frac{\kappa(E - \hat{Q})}{2E_d} = \frac{\kappa\hat{E}}{2E_d}, \quad \hat{E} > \frac{2E_d}{\kappa} \tag{1.3}$$

where E is the total energy transferred in the collision, $\hat{Q}$ is the energy lost to electronic excitation, $\hat{E}$ the energy available for atomic displacements, E_d the threshold energy for displacement and κ is a correction factor (usually $\sim$0.8) to account for non-hard sphere scattering [47, 48]. Once the number of displacements per primary knock-on atom is known, the total number of displacements per atom (dpa), which depends on the incident particle fluence, the collision cross-sections and PKA energy spectrum, can then be calculated. By assuming that the number of displacements caused in the material is proportional to the number of defects generated, the dpa gives a value of the extent of radiation damage independent on material and radiation type, making it a useful way to compare similar materials exposed to different particle fluxes or spectra. Limitations of the NRT model are that it makes no account of the spatial distribution of atoms: hence defect morphologies, clustering and vacancy-interstitial annihilation are not considered [49]. For tungsten, the energy for displacement E_d is 42eV [50] , whereas the formation energy of a Frenkel pair is 90eV [51], with a directional dependence (anisotropic) [52].

Interstitials and vacancies created by irradiation generally have enough mobility at moderate temperatures to mutually annihilate, therefore reducing the surviving defect concentration. The one-dimensional defects can cluster together and form different 2D (perfect and faulted loops of vacancy or interstitial type) and 3D (stacking fault tetrahedra and cavities of vacancy type) damage morphologies. The nucleation and growth of these defect clusters governs the mechanical properties of an irradiated

material, and controls effects such as swelling, hardening and embrittlement.

When estimating the range and extent of damage, simple implementations such as Stopping and Range in Matter (SRIM) [53] are commonly used. SRIM uses displacement energies of atomic species and binary collision approximations to estimate displacement damage, stopping force and projectile range in materials, ignoring crystallography. A damage event with sufficient energy usually evolves as a cascade of collisions in a restricted volume of material, with time scales in the order of picoseconds. Therefore, the NRT model and its assumption of isolated Frenkel pair production is not suitable to describe energetic bombardments [49]. A more comprehensive description is required to understand the generation of the defect population that causes effects on the microstructural level, and how these defects evolve in time. A more extensive literature review on techniques used to model radiation damage production, evolution and annihilation will be provided in Section 1.6. For an in-depth explanation and review of recent modelling of irradiation damage and primary defect production, please refer to the 1st Volume of Comprehensive Nuclear Materials [45].

1.3.3 Mimicking fusion neutron damage

Currently, there are no 14MeV neutrons with high enough fluxes to replicate the conditions found in a fusion reactor. Only small laboratory sources with dose rates in the order of 10^9 neutrons $\cdot\, m^{-2}s^{-1}$ lower than PFC conditions are available, i.e. the ASP accelerator in Atomic Weapons Establishment (AWE) Aldermaston [54], and are used primarily to quantify activation and transmutation of materials. Dedicated material irradiation facilities such as the planned International Fusion Materials Irradiation Facility (IFMIF) [55, 56], or the Component Test Facility [57] are required for accurate conditions, but are unlikely to be built before ITER commences operations (if at all). Until such facilities are available, the closest substitutes are irradiation by thermal or fast neutrons from fission reactors, and high-energy ion damage. This is not ideal since it is well known that different

incident particles produce different recoil-energy spectra [58] and that, to list an example, the irradiating species and energy affects the temperature-dependent dose for material amorphization [59, 60], thus care must be taken to extrapolate data for fusion reactors.

1.3.4 Charged particles

The benefit of using energetic ions to simulate neutron damage is that they allow the different forms of microstructural evolutions without neutron-induced activation, at a fraction of the cost and time. Single-variable experiments examining the effects of dose, dose-rate and irradiation temperature can be done relatively easily. High-energy electrons (1-3MeV) from High Voltage Transmission Electron Microscopes are able to image and damage the specimens in-situ concurrently, using the same beam [61, 62, 63, 64]. Ions (and ions of the same type as the target material, termed self-ions) can be used to simulate PKAs originating from the surface that can simulate the displacement damage of neutrons. However, owing to their charge, these ions experience significant electrostatic interactions with the atoms in the material. Thus, the stopping distance is small and can produce damage structures only within a few microns of the surface for low MeV energies [65]. Compared to neutrons, which have stopping distances in the order of metres rather than microns, ion implantation cannot be used to irradiate bulk specimens for macro-mechanical testing (unless very high energy sources (i.e. GeV protons) are used, which are limited). However, they can be used to produce similar damage microstructures which can be imaged using TEM [66, 67, 68], as well as mechanically tested using micromechanical methods like nano-indentation [69] and micro-cantilever bending [70] and micro pillars [71].

1.4 Radiation damage in tungsten

1.4.1 Neutron Irradiation

There is a limited amount of studies of neutron irradiation damage specific to tungsten, all restricted to fission spectra. The next sections will provide a summary on investigations of damage defects, as well as the property changes experienced by irradiated tungsten. Section 1.5 will be devoted to reviewing literature on the recovery of such defects.

Defect production

As mentioned previously, neutron-irradiation produces point defects that coalesce into dislocation loops and impurities from transmutation events. Pure tungsten exposed to 0.15dpa damage of fast-fission neutrons at 600°C showed nucleation of voids and dislocation loops, reaching sizes and density of $r = 1.3$nm, $\rho = 6.4{\cdot}10^{22}\text{m}^{-3}$ (voids) and $r = 7.9$nm, $\rho = 4.6 \cdot 10^{21}\text{m}^{-3}$ (loops) [72].

Microstructure changes

An added problem with neutron irradiation is transmutation, which over time modifies the composition of a pure or alloyed material [73, 74]. Transmutation of tungsten will produce rhenium and osmium, as well as small amounts of tantalum via β decay and other elements, as shown in Figure 1.5. Modelling work predicts up to $\sim$3.8% Re and $\sim$1.38% Os formed after 5 years, as shown in Figure 1.6 [19]. These elements can lead to the formation of brittle, intermetallic σ and χ phases, to the detriment of the mechanical properties of the PFCs. Because transmutation occurs over the length of years and is dependent on the energy spectra of the impinging particles, Re and Os are usually alloyed to tungsten to attempt to simulate this.

Tanno et al. [76, 77] investigated the effect of transmutation elements in tungsten using TEM. When exposed to 1.54dpa irradiation at 750°C, void lattices were formed for pure tungsten. Irradiations of 0.4dpa caused the formation of randomly

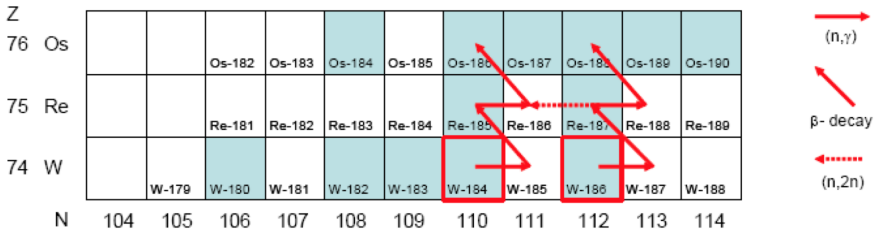

Figure 1.5: Re and Os production pathways through tungsten neutron-induced transmutation. Stable isotopes are shaded blue [75].

distributed smaller voids of approximately 3nm diameter. Similar irradiation conditions were applied to binary alloys W-10%Re, W-26%Re and W-3%Os. These displayed the formation of precipitates, such as mixed needle and spherical-like precipitates of χ phase (Re_3W) in W-26%Re and needle-like precipitates of σ phase (WOs). Limited evidence of voids was found in the W-Re and none in the W-Os, showing that both rhenium and osmium prevent void swelling, possibly by interrupting vacancy cluster formation.

Herschitz and Seidman used atom probe tomography to study radiation-induced segregation in neutron irradiated W-Re alloys [78]. They showed that homogeneous precipitation of intermetallic species in both W-10at%Re and W-25at%Re occurred, with voids also forming in the latter alloy.

Mechanical properties

As of now, methods are still being researched into improving mechanical performance of tungsten-based materials, therefore there are no model PFC materials on which to conduct systematic radiation damage characterisation. Thus, only studies of neutron irradiation on pure tungsten and binary alloys are available. For pure tungsten, the available literature shows an average increase of 200°C in the brittle to ductile transition temperature, to approx. 600°C (E_n >0.1MeV, 10^{21-25}neutrons·m^{-2}, from K_{IC} values) [38, 22]. Separate experiments on the tungsten-rhenium binary alloy also showed rapid embrittlement after irradiation, despite Re having a ductilising effect in the unirradiated state [79]. An investigation on hardening of neutron-irradiated tungsten for doses between 0.17-1.54dpa at 400-750°C has also

Starting composition (at%)	Transmutation products	Concentration of product in appm (in brackets, at%) after irradiating for		
		1 year	3 years	5 years
W (100)	W	9.89×10^5 (98.9)	9.63×10^5 (96.3)	9.40×10^5 (94.0)
	Re	9.06×10^3 (0.91)	2.59×10^4 (2.59)	3.80×10^4 (3.80)
	Os	5.58×10^2 (0.06)	5.28×10^3 (0.53)	1.38×10^4 (1.38)
	He	6.65×10^0 (<0.01)	2.00×10^1 (<0.01)	3.36×10^1 (<0.01)
	H	1.51×10^1 (<0.01)	4.56×10^1 (<0.01)	7.63×10^1 (<0.01)
Ta (100)	Ta	9.32×10^5 (93.2)	7.56×10^5 (75.6)	6.15×10^5 (61.5)
	W	6.37×10^4 (6.37)	2.32×10^5 (23.2)	3.67×10^5 (36.7)
	Hf	4.37×10^3 (0.44)	1.15×10^4 (1.15)	1.67×10^4 (1.67)
	He	2.88×10^0 (<0.01)	1.03×10^1 (<0.01)	2.00×10^1 (<0.01)
	H	1.64×10^1 (<0.01)	5.07×10^1 (<0.01)	8.68×10^1 (<0.01)
Re (100)	Re	8.73×10^5 (87.3)	6.65×10^5 (66.5)	5.08×10^5 (50.8)
	Os	1.22×10^5 (12.2)	3.20×10^5 (32.0)	4.69×10^5 (46.9)
	W	5.67×10^3 (0.57)	1.50×10^4 (1.50)	2.15×10^4 (2.15)
	He	3.58×10^0 (<0.01)	1.14×10^1 (<0.01)	1.98×10^1 (<0.01)
	H	1.89×10^1 (<0.01)	5.81×10^1 (<0.01)	9.82×10^1 (<0.01)
Ti (100)	Ti	9.99×10^5 (99.9)	9.97×10^5 (99.7)	9.95×10^5 (99.5)
	He	1.83×10^2 (0.02)	5.48×10^2 (0.05)	9.13×10^2 (0.09)
	H	5.95×10^2 (0.06)	1.79×10^3 (0.18)	2.98×10^3 (0.30)
V (100)	V	9.98×10^5 (99.8)	9.93×10^5 (99.3)	9.88×10^5 (98.8)
	He	7.26×10^1 (<0.01)	2.18×10^2 (0.02)	3.63×10^2 (0.04)
	H	5.16×10^2 (0.05)	1.55×10^3 (0.16)	2.58×10^3 (0.26)
Fe (100)	Fe	9.98×10^5 (99.8)	9.93×10^5 (99.3)	9.87×10^5 (98.7)
	He	2.19×10^2 (0.02)	6.56×10^2 (0.07)	1.09×10^3 (0.11)
	H	1.01×10^3 (0.10)	3.01×10^3 (0.30)	5.01×10^3 (0.50)
Fe–9% Cr alloy	Fe	9.08×10^5 (90.8)	9.03×10^5 (90.3)	8.98×10^5 (89.8)
Fe (91)	Cr	9.00×10^4 (9.00)	9.00×10^4 (9.00)	9.01×10^4 (9.00)
Cr (9)	He	2.14×10^2 (0.02)	6.40×10^2 (0.06)	1.06×10^3 (0.11)
	H	9.90×10^2 (0.10)	2.96×10^3 (0.30)	4.92×10^3 (0.49)
SiC	Si	4.98×10^5 (49.8)	4.94×10^5 (49.4)	4.90×10^5 (49.0)
Si (50)	C	4.98×10^5 (49.8)	4.94×10^5 (49.4)	4.90×10^5 (49.0)
C (50)	He	2.28×10^3 (0.23)	6.79×10^3 (0.68)	1.13×10^4 (1.13)
	H	8.60×10^2 (0.09)	2.56×10^3 (0.26)	4.25×10^3 (0.43)
C (100)	C	9.96×10^5 (99.6)	9.88×10^5 (98.8)	9.80×10^5 (98.0)
	He	3.50×10^3 (0.35)	1.04×10^4 (1.04)	1.73×10^4 (1.73)
	H	2.96×10^0 (<0.01)	8.98×10^0 (<0.01)	1.53×10^1 (<0.01)
Cu (100)	Cu	9.89×10^5 (98.9)	9.68×10^5 (96.8)	9.48×10^5 (94.8)
	Ni	6.05×10^3 (0.61)	1.80×10^4 (1.80)	2.97×10^4 (2.97)
	Zn	2.71×10^3 (0.27)	8.01×10^3 (0.80)	1.31×10^4 (1.31)
	He	2.14×10^2 (0.02)	6.40×10^2 (0.06)	1.06×10^3 (0.11)
	H	1.49×10^3 (0.15)	4.43×10^3 (0.44)	7.33×10^3 (0.73)
Be (100)	Be	9.93×10^5 (99.3)	9.79×10^5 (97.9)	9.66×10^5 (96.6)
	He	6.57×10^3 (0.66)	1.96×10^4 (1.96)	3.24×10^4 (3.24)
	H	1.02×10^2 (0.01)	3.79×10^2 (0.04)	7.48×10^2 (0.07)

Figure 1.6: Transmutation response for tungsten, its possible alloying elements and other fusion-relevant materials [19].

been conducted, with substantial increases (up to 4×) in hardness both in relation to dose and increase in Re and Os content [80].

Neutron irradiated tungsten has also been thermally shocked with transient heat load treatments [81], in an attempt to simulate edge-localised modes (ELMs) or pulse operation of the tokamak. Electrical resistance (inversely proportionally related to thermal conductivity according to the Wiedemann-Franz Law [82]) saw negligible change for irradiated W-xRe alloys, but great decreases in W-xOs alloys [76]. Crack formations for irradiated and unirradiated materials subject to high thermal fluxes ($<$20MJ$\cdot$m^{-3}) differ if the neutron irradiation is conducted at low temperature and at high dose (200°C, 0.6dpa), and are similar if irradiation is at high temperature and at a low dose (350-700°C, 0.3dpa) [83, 84].

1.4.2 Heavy/self-ion implantation

Older literature on heavy/self-ion implantation of tungsten mainly focused on defect characterisation. Only recently, with the development of micro/nano-mechanical testing methods, has ion implantation been useful for quantification of mechanical property changes by irradiation. The following sections review how tungsten behaves when irradiated by heavy ions and how it compares with the available literature on neutron irradiation.

Defect production

In early work by Haussermann [85, 86], pure tungsten thin-foils were irradiated with Au^+ (20-70keV at room temperature) up to doses of $5 \cdot 10^{17}$ions $\cdot$ m^{-2} in-situ of a TEM. $\frac{1}{2}\langle 111\rangle$ loops were the primary type of defect observed with a small fraction of faulted $\frac{1}{2}\langle 011\rangle$ observed nucleating and transforming into $\frac{1}{2}\langle 111\rangle$ through a shear process within the habit plane.

In other experiments with W^+ irradiation (500°C, 1.0dpa, $10^{18}W^+m^{-2}$) presence of $\frac{1}{2}\langle 111\rangle$ loops was confirmed, along with observation of $\langle 100\rangle$ with a 3:1 ratio [66], although $\langle 100\rangle$ loops are predicted by theoretical models to be less energetically

		UHP-W		W-5wt%Re	
Dose (W^+ ions cm^{-2})	Damage Level (dpa)	Hardness (125nm) (GPa)	Loop Number Density (m^{-3})	Hardness (125nm) (GPa)	Loop Number Density (m^{-3})
0	0	7.62	0	6.45	0
$5.5 \cdot 10^{16}$	0.07	7.97	-	7.24	-
$3.5 \cdot 10^{17}$	0.4	8.45	5.7×10^{22}	7.44	7.92×10^{22}
$1.05 \cdot 10^{18}$	1.2	8.35	2.16×10^{22}	7.30	8.16×10^{22}
$1.0 \cdot 10^{19}$	13	8.35	-	7.8	-
$2.5 \cdot 10^{19}$	33	8.35	1.61×10^{23}	9.33	-

Table 1.1: Dose, damage level, hardness and loop volume density for ion implanted UHP-W and W-5wt%Re alloys [90]

favorable [87]. Addition of 5%Re showed retardation of $\frac{1}{2}\langle 111 \rangle$ motion owing to the pinning effect of Re clusters [66], also observed in separate APT tomography and modeling [88, 89]. Higher damage doses closer to ITER/DEMO requirements have also been investigated for pure tungsten and W-5%Re, showing little change in loop density between 0.4 and 33dpa [69, 90].

Self-ion implantation damage characterisation studies using FIM have also been conducted, for fundamental investigations of atomic mechanisms and for conditions more indicative of damage in thermonuclear reactors [91, 92, 93]. The defect types observed were vacancies, vacancy clusters, and interstitials. The vacancy cluster volume was of the order of $10^3 a_W^3$ for $\mathcal{O}(10^{16})$ $W^+ \cdot m^{-2}$ up to $5 \cdot 10^4 a_W^3$ for $\mathcal{O}(10^{18})$ $W^+ \cdot m^{-2}$, where a_W is the tungsten lattice parameter (15.85Å). Cascade overlap is first observed at doses of $\mathcal{O}(10^{17})$ $W^+ \cdot m^{-2}$ [92].

Microstructure and property changes

Mechanical testing and nanoindentation of W^+ irradiated high-purity W, W-5wt%Ta, and W-5wt%Re [69, 90] has been conducted. Table 1.1 shows summary of the results for pure tungsten.. Generally, hardness was found to increase substantially with irradiation in all experiments, particularly for W-5wt%Ta, with saturation levels depending on composition (∼0.4-33dpa for W, ∼0.07-1.2dpa for W-5wt%Re, and ∼13dpa for W-5wt%Ta), and with no significant changes in Young's modulus. Small rhenium-rich clusters (20-26%Re) for the W-5wt%Re alloy were formed at high damage doses (13-33dpa) and are thought to be precursors of the sigma phases known to harden and embrittle W-xRe alloys.

Comparison to neutron data

Due to the difficulty and expense of neutron irradiation, there are a limited amount of comparison studies of neutron and ion-irradiated tungsten (as well as other materials). With regards to gas retention and bubble formation, there is some doubt as to whether deuterium trapping and desorption mechanisms for neutron irradiated tungsten can be simulated by ion-irradiated specimens. Comparisons of ion- and neutron-irradiated tungsten by Oya [94] and Shimada [95] shows differences in deuterium retention levels. Samples were damaged to 0.025dpa under a fast neutron fluence of $1.1 \cdot 10^{24}\text{neutrons} \cdot \text{m}^{-2}$, as well as with Fe^{2+} and W^{+} ion irradiation up to 3dpa damage, and subsequently exposed to deuterium plasma. The deuterium retention was measured using Thermal Desorption Spectroscopy (TDS) up to 900∘C and it was concluded that no ion could fully reproduce the TDS-spectrum from the neutron irradiated material. Furthermore, levels of deuterium for the 0.025dpa neutron sample were only reached by ion-irradiated specimens at 3dpa damage.

With regards to microstructural effects, no literature comparing ion and neutron irradiation is available for tungsten. However, studies on other BCC metals like Fe/Fe-Cr alloys, show a dependence of dose *rate* of irradiation, not just total damage, on the final mechanical properties [96, 97]. In [96], decreasing the dose rate from $6{\cdot}10^{-4}$dpa/s to $3{\cdot}10^{-5}$dpa/s increased the hardness by up to $\sim 50\%$, with the discrepancy reducing to negligible levels at higher irradiation temperatures (500°C). This is a problem since neutron dose rates are orders of magnitude lower than those tested using ions.

Therefore, it can be assumed from the available body of literature that ion irradiation data *cannot* be used to directly simulate damage and its effects in neutron-irradiated materials. However, until multi-billion dollar systems like IFMIF or CTF are online, ion-irradiation will be useful to delineate general trends and understand underlying mechanisms of radiation damage, allowing materials research to progress.

1.4.3 Hydrogen and helium implantation

Plasma-facing components in a fusion reactor will not only have to withstand high-energy neutron irradiation, but also deuterium and helium ion irradiation from the hot plasma. Small clusters of solute gas atoms can act to pin dislocations, and larger gas voids can disrupt dislocation glide. Most studies use doses and implantation energies that are not particularly relevant to fusion and also ignore the coupling effect of irradiation by neutrons or self-ions [98, 99]. However, some studies have been carried out involving simultaneous dual-irradiation or sequential irradiation, more relevant to the fusion domain [95].

Helium

Hashimoto [100] presented a comparison of helium retention properties of single and poly-crystalline tungsten. For a single implantation of dose $1 \cdot 10^{19}\text{ions} \cdot \text{m}^{-2}$ of 1.3MeV He^+ at 850∘C followed by flash annealing at 2000∘C, 2-3nm gas cavities were observed. Associated TEM analysis suggests that the helium was trapped in cavities that form at grain boundaries in polycrystalline tungsten and in the bulk in single-crystal tungsten [101, 100]

Yoshida [102] and Iwakiri [103] conducted low-energy (<0.5keV) He irradiation on tungsten, finding 2-4x increases in hardness compared to unirradiated samples. Enhanced surface erosion due to He embrittlement and reduction of thermal conductivity in the sub-surface area has also been observed [104].

Bubble formation studies using He^+-ion irradiation show that above the tungsten displacement threshold (0.5keV), interstitials and vacancies are formed beneath the surface; however, owing to the interstitials' low migration energy (0.037-0.085eV) these migrate to form interstitial dislocation loops, whereas less-mobile vacancies trap He atoms. Below ∼900K, high number-density fine He bubbles (∼1nm diameter) were observed [102], with models agreeing with this behaviour [105, 106].

Surface blisters ($\mathcal{O}(10-100)\mu\text{m}$) have also been observed as a result of high-energy and high-dose He implantation, appearing above a critical dose of $10^{21}\text{ions} \cdot \text{m}^{-2}$

for 1.3MeV He^+ at 850∘C, corresponding to a peak He concentration of 4at% (at a depth of $\sim$ 1.7 microns) [107].

Most recently, Armstrong investigated the effect on hardness of tungsten irradiated using sequential tungsten and high-energy helium ion implantation [108]. Substantial hardness increases were seen in the helium implanted regions with smaller hardness increases in regions already self-ion implanted containing pre-existing dislocation loops. This suggested that for the same helium content, helium trapped in distributed vacancies resulted in a greater hardening than helium trapped in vacancies condensed into dislocation loops.

Hydrogen

A number of studies have looked into the retention of deuterium and induced blistering. Thermal desorption experiments show that contrary to helium implanted deuterium is swiftly desorbed at relatively low temperatures, with the majority leaving below 550°C [109]. For typical working conditions of a divertor (800-1200°C), the majority of D would thus diffuse out of the implanted areas. Furthermore, the low activation energy for hydrogen diffusion in tungsten of 0.39eV, and a 1.77-2.08eV energy barrier for uptake of H, means only hydrogen trapped in defects like vacancies is likely to remain within the material. Given a sufficiently high dose, local material decohesion and fracture is predicted [110].

1.5 Radiation damage recovery in tungsten

As discussed previously, several studies have probed the effect of temperature *during* irradiation in tungsten, using both ion irradiation and neutrons. Numerous studies have also been undertaken with regard to the recovery of irradiation-induced defects post-irradiation. However, these have mostly centred around resistivity measurements [111, 112, 113, 114, 115, 116, 117, 118], with some early field ion microscopy work [119, 120] and a single early TEM study on single crystal tungsten [121]. Sim-

ilar TEM work has also been done in molybdenum [122]. Resistivity measurements, although useful in identifying the temperature and activation energies of recovery stages (calculated using the Meechan-Brinkman theory [123]), do not provide a direct method of the observation of defects, their nature and how they change with different annealing conditions. One of the aims of this thesis is to to provide a more complete picture by: 1) quantifying the damage immediately after irradiation, 2) understanding the time and temperature dependence of recovery, 3) directly observing the mechanisms associated with the radiation defect recovery. Such a study has found to be lacking in the literature, with systematic experiments being limited to loops and stacking fault tetrahedra formed during quenching processes of fcc metals [124].

1.5.1 Recovery stages

Studies based on fast neutron-irradiated specimens ($\geq$ 1MeV), have identified five stages of annealing common to BCC metals based on the classifications of Thompson [125]. There seem to be numerous inconsistencies in the literature on the number of recovery stages, their nomenclature, temperature and physical interpretation, particularly at higher temperatures [126].

Stage I occurs below -170°C and is attributed to the movement of free interstitials. Stage II, between -170°C and 350°C, is a steady recovery attributed to the release of interstitals from traps with a wide range of interaction energies from $0.25-1.7$eV [127]. This explains the many sub-stages observed for example in resistivity studies [116]. These two stages occur below fusion reactor operating temperatures, and will not be considered further here. For fusion-relevant temperatures (from 500-1000°C [18]), the recovery of defects created by fast neutrons in tungsten has been observed to occur in three major stages (III-V), at $\sim 0.15T_m/350°C$, $\sim 0.22T_m/640°C$, $\sim 0.31T_m/970°C$ [115].

Stage III, with an onset of $\sim$350°C and activation energy of $\sim$1.7eV, was initially considered to be due to self-interstitial migration, primarily to immobile traps [117].

This explanation was later revised to being due to monovacancy mobility activation [128, 129, 130, 127]; this interpretation is also supported by DFT calculations [131]. The onset temperature has also been shown to shift to lower temperatures with increasing neutron fluence [112].

Higher temperature recovery stages in tungsten have been largely un-researched since the 1970s, with interpretation being limited to resistivity measurements and early FIM experiments [116, 132, 119].

Stage IV recovery, at $0.22T_m$, is still subject to debate [113], being generally attributed to vacancy-impurity complexes [132], or di-vacancies [116]. Recent DFT simulations have shown that di-vacancies are not favoured in tungsten [133]. Other *ab initio* computational studies yield activation energies between 3.00-3.43eV for vacancy-carbon complexes, that may explain this stage as being controlled by the dissolution of vacancy-carbon complexes [134], noting that the experimental activation energy calculated from resistivity measurements is 3.3eV [114]. Similar conclusions for this stage may be drawn by comparing to other materials, such as α-Fe, where the recovery stage above Stage III observed by simulations and positron lifetime measurements was ascribed to VC_n complexes [135, 136, 137].

Stage V recovery, starting at $0.31T_m$ [1], was initially explained as being due to vacancy migration, based on early field-ion microscopy studies [119, 120], but later attributed to the disappearance of "defect clusters" or formation of voids [118]. It is still unclear what is the cause of this recovery stage.

The majority of studies have been carried out on polycrystalline tungsten. In single-crystal tungsten [2], defects were found to be stable up to 1900°C, [116] presumably due to the absence of sinks at grain boundaries. *Bykov et al* [116] identified three stages of annealing: 500°C-800°C (Stage IV), 950°C-1200°C (Stage V), and 1200°C-1900°C (Stage VI).

[1] This stage is referred to as Stage IV in [114].
[2] No crystal orientation is given in this study [116].

1.6 Modelling radiation damage

Radiation damage is inherently multiscale: its formation, recovery, motion and effects on physical/mechanical properties spanning many orders of magnitude in time and size scales, as shown in Figure 1.7. In the context of dislocation modelling, a good review of different approaches to modelling dislocations is given by *Bulatov and Cai* [138]. Due to the explosion in computing power available, coupled with improvements in theoretical descriptions, there have been substantial improvements in the past two decades. Recent developments with respect to radiation damage in fusion reactor materials are summarised in [139]. Methods can be broadly characterised as atomistic, statistical or continuum based.

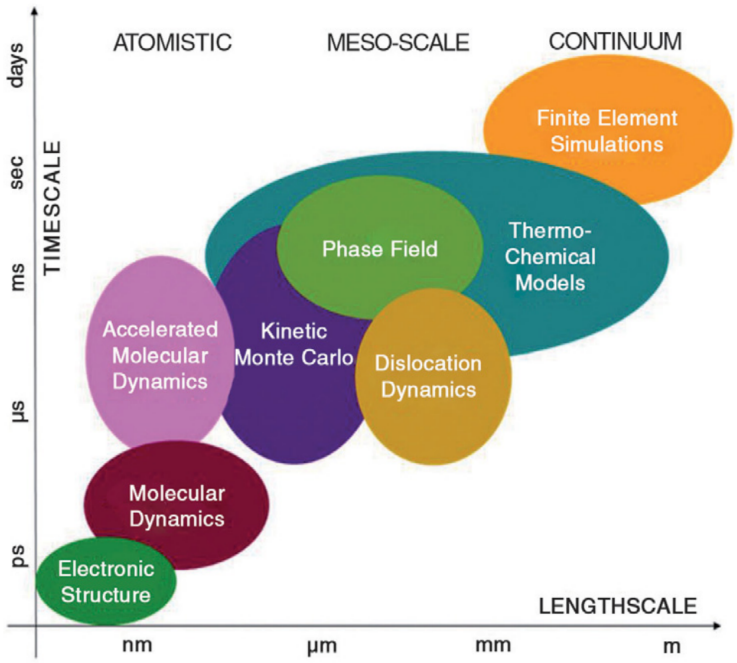

Figure 1.7: Example of multi-scale hierarchy of theoretical and computational methods used for materials model development and computer simulations [140].

1.6.1 Atomistic methods

Atomistic models describe interactions and dynamics of atoms. These include:

- *Ab initio methods*, like density functional theory. These have no experimental input parameters and allow the calculation of interatomic potentials that

attempt to capture the underlying quantum mechanisms such as short-range repulsion and long-range attraction of atoms [141]. They have have been successful in predicting an array of useful material properties and characteristics (free energy, density profiles, phases, potentials etc.), as well as offering insights into the origin of temperature- and dose-dependent response of materials to irradiation. An exhaustive review of DFT specifically for radiation damage is given by *Dudarev* [137]. Because electronic structures of individual atoms are calculated, *ab initio* methods are computationally demanding and thus limited to a small number ($\mathcal{O}(10^{1-2})$) of atoms.

- Molecular dynamics and statics (MD/MS). These methods essentially involve solving Newton's classical laws of motion on groups of atoms[3], using a predefined *potential* which determines the response of atomic interactions. Potentials (Lennard-Jones [142], Finnis-Sinclair [143] etc) are important to the accuracy of molecular dynamics simulations and are generally fitted on material-specific experimental and first principle input parameters. MD modeling has been used to estimate the number and nature of the surviving defects in a cascade event caused by a PKA atom [144, 145]. It has also helped explain fundamental irradiation effects such as macroscopic void swelling in terms of defect production [146], as well as embrittlement [147], and defect motion [148, 19]. Because these methods involve calculations of atom-atom interactions, they are limited in their scope. Large molecular dynamics simulations may involve $\mathcal{O}(10^6)$ atoms, limiting the size domain to the sub-micron range. Furthermore, because of the deterministic solution of the equations of motions, the required numerical time integration limits the maximum time step to generally femto- to picosecond ranges, meaning simulations are generally in the order of nanoseconds.

[3]Excluding quantum molecular dynamics

1.6.2 Continuum methods

Due to computational constraints, if larger length and timescales are desired, modelling individual atoms becomes unwieldy. To overcome this limitation, one approach is to discard the notion of atoms and treat the simulation domain as a continuum, where defects such as dislocations are treated as elastic objects. This is the approach of discrete dislocation dynamics (DDD). As the name suggests, dislocations are treated as elastic interacting objects in a continuum (individual atoms are not resolved). It is a *phenomenological* technique, where dislocation mobilities and interactions with other dislocations or defects (inclusions or particles) are treated using ad-hoc rules rather than stemming from underlying physical mechanisms. However, it allows for larger time and length scales, and (as developed in Chapter 5 of this thesis) can be connected to finite element analysis to simulate mechanical response of mesoscale components [149, 150, 151, 152]. It has been applied to the study of radiation damage in multiple studies [153, 154, 155].

1.6.3 Stochastic methods

Kinetic Monte Carlo (kMC) and other rate theory algorithms offer another way forward to expanding the scope of atomistic simulations, particularly in bridging the gap between the nanosecond timescale accessible to MD and experimental and practical timescales of seconds, weeks and years [139, 127]. These techniques are remarkably flexible in simulating the time evolution of defects, but crucially require that the processes have *known* rates (which are inputs to the simulation). Another statistical method, Langevin Dynamics, which involves the use of stochastic differential equations to model the objects of interest, has recently found applications in radiation damage modelling, in the case of edge and screw mobility [156, 157, 158, 159] and nanoscale defects [160, 161, 162].

1.6.4 Final Remarks

Hierarchical multi-scale modelling using multiple techniques has been successful on some occasions. For example, *Marian et al* carried out simulations of dislocation and stacking-fault tetrahedra interaction in FCC copper using molecular dynamics results to inform faster, larger scale dislocation dynamics simulations, and showed good agreement with irradiation hardening measurements [163]. However, particularly in the case of thermally driven effects such as the ones probed in this thesis, integration of different techniques is a nascent field, ripe for advances. In this thesis, both continuum and atomistic tools will be used (and developed), with the primary development focus being on thermal effects on dislocation dynamics, and how this translates to mechanical performance. As such, a more thorough review of the state of the art DDD will carried out in Chapter 5, directly connecting the technique to mechanical response via finite element analysis, whereas Chapter 6 will delve into atomistic and stochastic methods, and how to integrate them within dislocation dynamics to more exhaustively model thermal effects.

1.7 Aims of this research project

- Gather quantitative information on radiation damage characteristics and morphology for fusion-relevant material (tungsten), emulating thermal and irradiative conditions found in a fusion reactor where feasible.

- Identify damage recovery stages, rates and activation energies for temperatures of interest (RT - 1400°C). Also, identify underlying recovery *mechanisms* via *in situ* experimental observation and/or modelling.

- Use theory and computational tools to attempt simulations of thermal effects on dislocation structures in tungsten, and ultimately relate such dislocations to overall mechanical performance.

Chapter 2

Experimental methods

This chapter will detail the experimental methods and procedures used for the experiments undertaken. The primary experimental analysis tool used was the transmission electron microscope (TEM). Because of its ubiquity, this chapter will not focus on how to operate a TEM, but rather on:

1. Sample preparation
2. Experimental campaigns
3. Analysis procedures

2.1 Sample preparation

Transmission electron microscopy is a technique in which a beam of electrons is transmitted through an ultra-thin specimen. The image is formed on a CCD camera or florescent screen from the interaction of electrons transmitted through the sample, after various magnification and focussing stages in the device. The technique therefore depends on the successful preparation of suitable ultra-thin samples. Preparation steps are the following:

1. Sizing to appropriate dimensions via mechanical punching or EDM.
2. Annealing in vacuum furnace.
3. Mechanical polishing (if required).
4. Bath electro-polishing.
5. Ex-situ bulk irradiation (if required).
6. Ex-situ post-irradiation bulk annealing (if required).
7. TenuPol electro-polishing, either single or double sided.

2.1.1 Sample sizing

TEM holders generally accept 3mm diameter discs. Ultra high purity tungsten was supplied in sheets, of 150 or 25 micron thickness. The discs were obtained by mechanically punching the 100 micron thickness sheets using a Gatan disc punch (Model 659).

2.1.2 Annealing to promote grain growth

After the samples were sized to the correct dimensions, they were annealed in a vacuum furnace for 20 hours at 1400°C to promote grain growth and to ensure a dislocation-free microstructure. The vacuum furnace used a diffusion pump, and

had a pressure below 10^{-6}mbar, to prevent surface contamination. Large grains are desirable, since they simplify the dislocation analysis procedure and ensure a homogeneous experimental area for *in situ* observations. The extent of the change is illustrated in Figure 2.1.

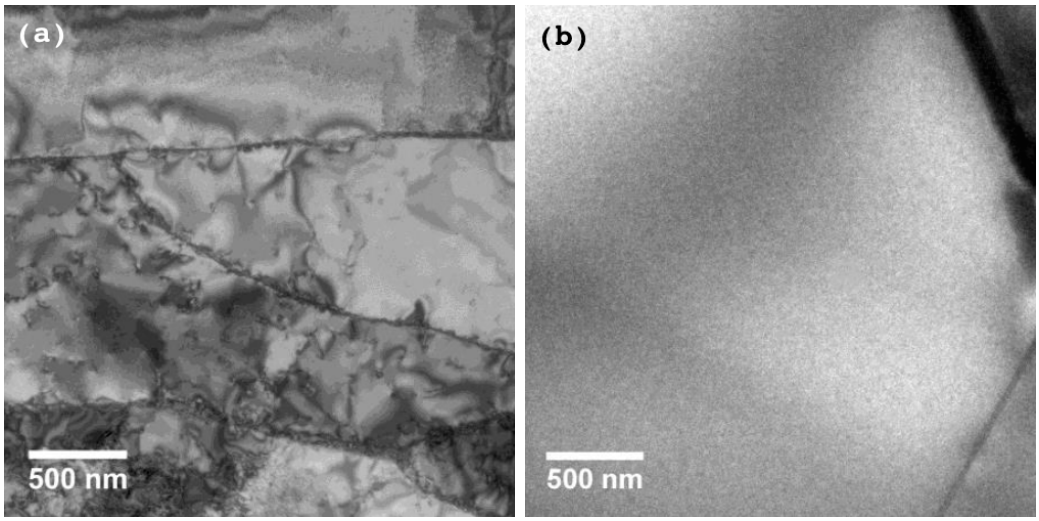

(a) As-rolled **(b)** Annealed

Figure 2.1: Change in microstructure of ultra-high purity tungsten from as-rolled to post-annealed at 1400°C for 20 hours, from [67].

2.1.3 Mechanical polishing

In the case of the 3mm diameter discs, subsequent to annealing, they were mechanically polished to ∼80μm thickness with diamond lapping films (grit sizes 15, 9, 6, 3, and 1 μm), on both sides of the discs, giving a close to mirror finish. For the rectangular *in situ* straining samples, this step was not necessary.

2.1.4 Bath electropolishing

To ensure a close to mirror finish and to remove any oxidation layers from the annealing, the samples were dipped in an electro-polishing bath, consisting of 0.5wt% NaOH aqueous solution at close to 0°C. Figure 2.2 illustrates this set-up. A dedicated pair of tweezers, with its tips coated with platinum (Pt), was used to clamp the peripheral area of the sample, and dipped completely in the electrolyte. The

opposite end of the tweezers was connected to the anode of the (D.C.) power supply, with a voltage of 14V. For all specimens, at least 2μm of material was removed per surface during bath-type electro-polishing, at a rate of $\sim$1μm/min.

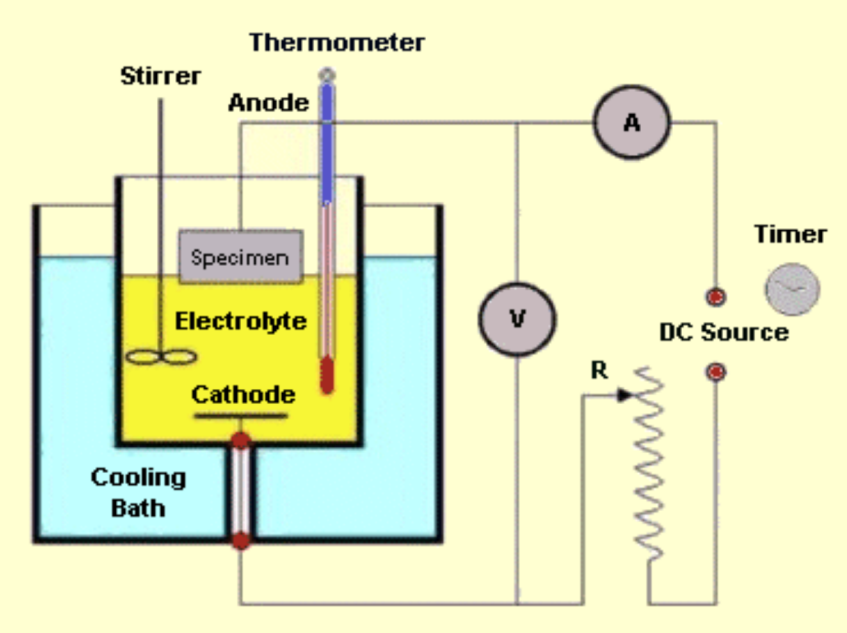

Figure 2.2: A schematic drawing of the bath-type electro-polishing method, from [164].

2.1.5 Ex-situ bulk irradiation

The polished bulk samples were irradiated to 1.5dpa at the National Ion Beam Facility at the University of Surrey, United Kingdom, using 2MeV W^+ ions, at a temperature of 500°C to a fluence of $1 \cdot 10^{14}$ ions/cm^2, producing an estimated dose of 1.5dpa. The dose rate was $\sim 2.73 \cdot 10^{10}$ ions/cm^2/s. Irradiation at the National Ion Beam Facility required construction of an appropriate sample holder, pictured schematically in Figure 2.3.

The 3mm diameter bulk samples were sandwiched between two steel perforated plates and mounted on the target plate of the ion-beam, attached to heating elements. The ion beam was directed perpendicularly to the sample faces and rastered along the samples to achieve the total dose. The irradiation dose was calculated using SRIM 2008, using a displacement threshold energy of 55.3eV [50], yielding the damage profile given in Figure 2.4. The simulation was run using the full-cascade

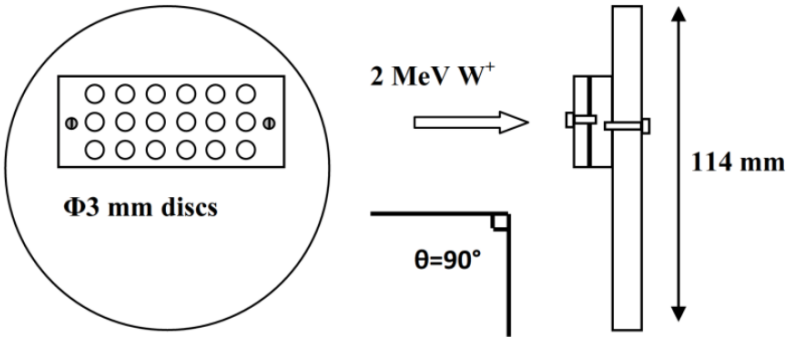

Figure 2.3: Schematic of the sample holder set-up for irradiation at the University of Surrey National Ion Beam Facility (not to scale), from [67].

mode, using 10,000 implantation events, and extracted from the vacancy.txt files produced by the software. The peak damage is approximately at ∼100nm depth, quickly falling to relatively negligible levels doses at <300nm. The displacement energy threshold used was 55.3eV [50]. From this, a nominal dose of 1.5dpa was calculated.

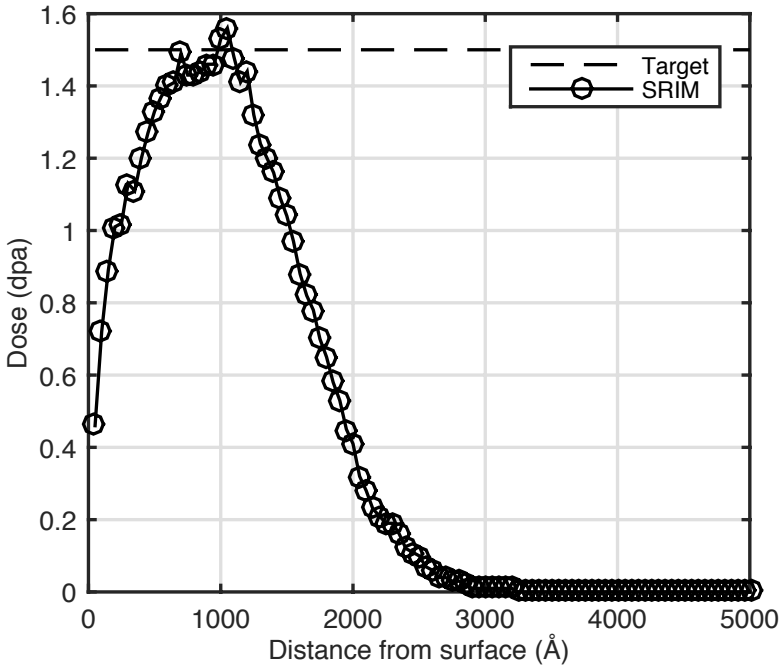

Figure 2.4: SRIM damage profile, as calculated using SRIM 2008, with a displacement threshold energy of 55.3eV [50].

.

2.1.6 Ex-situ post-irradiation bulk annealing

In order to prevent any contamination of the ion-irradiated surface during this annealing stage, the samples were encapsulated in evacuated quartz tubes (washed thoroughly in acetone and subsequently methanol) at a vacuum pressure of $< 10^{-6}$mbar, and annealed in a muffle furnace with argon atmosphere.

2.1.7 Tenupol electropolishing

Following the various treatments, all samples were made into TEM foils via Tenupol electro-polishing, using a twin-jet electropolisher (TenuPol 5), with a 0.5wt%NaOH acqueous solution close to 0°C. To achieve optimal electro-polishing, a balance between the rate of formation of a passivation layer and its removal by aggressive ions in the electrolyte must be achieved [165]. This can be obtained by plotting the variation of current density against voltage during the electro-polishing, as shown in Figure 2.5, where the polishing region is the plateau where current density remains constant with the voltage increase. For ultra-high purity tungsten, these conditions were found at an applied voltage of 14V, with current densities between 1400-2600A/m^2. Specific settings on the TenuPol 5 were the following: voltage applied, 14V; light stop value, 20; jet strength, 30; lower/higher value for pump strength, 75-110. Average single-side polishing for 100μm disc time was ∼10min, at ∼30mA current.

For samples which underwent ex-situ irradiation and/or annealing detailed in Sections 2.1.5 and 2.1.6, electro-polishing was done on a single face, *the non-irradiated face*. These samples were back-thinned with the irradiated side coated with Lacomit varnish (a corrosion resistant coating supplied by Agar Scientific). Once the central part of the samples reached electron-transparency (thickness <200 nm, or ∼18-20 light stop value on the TenuPol), the varnish was removed with a dedicated Lacomit solvent (a mixture of acetone and xylene). This is shown schematically in Figure 2.6.

For samples which did *not* undergo ex-situ irradiation, for example those irradiated

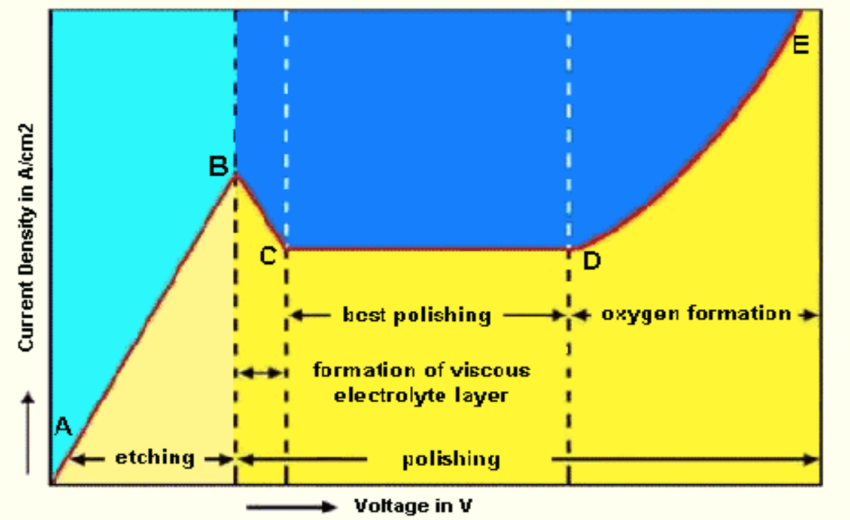

Figure 2.5: Variation of current density with voltage during electro-polishing, from [164]

.

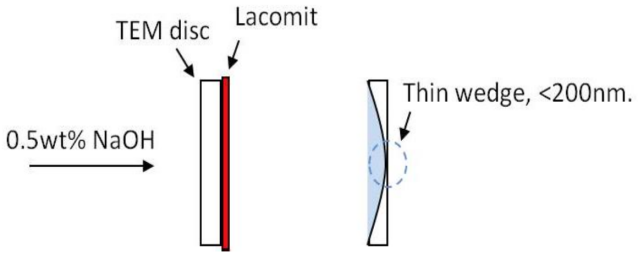

Figure 2.6: A schematic diagram illustrating the back-thinning approach, from [67].

.

in situ, or the rectangular straining samples, the electro-polishing was done on *both* sides of the samples, by not using Lacomit varnish. After this final step, the samples were ready to be analysed in the transmission electron microscope and/or exposed to *in situ* experimental conditions.

2.2 Experimental campaigns

The experiments undertaken in the thesis can be classified into two types:

1. Irradiation

2. Annealing

Irradiation experiments involved using an ion-beam to damage the surface of the samples, replicating fusion reactor conditions as best as possible. Annealing experiments involved heating the irradiated samples using various heat treatments, to quantify and/or observe the recovery of radiation damage in ultra-pure tungsten. Straining experiments involved mechanically straining *non-irradiated* samples at different temperatures, to understand the fundamental behaviour of dislocations in tungsten.
Depending on the type of experiment, they can be further classified as:

1. *Ex situ* experiments.

2. *In situ* experiments.

Ex-situ signifies that the irradiation and/or annealing campaign was undertaken when the sample was in a *bulk* state, and subsequently thinned for TEM analysis. The benefits of ex-situ is the reduced number of free surfaces which may act as artefacts to radiation damage formation. Furthermore, it allows flexibility in the choice of ion-beam source.
In situ signifies the material is altered (by being irradiated, heated, and/or strained) whilst in the TEM. This has obvious benefits of allowing dynamic observation of the events on a nano-scale. However, due to the thickness requirements of the samples, results may not be perfectly representative of macroscale behaviour due to size effects. Furthermore, the requirement of having the sample inside the TEM places serious constraints on the type of conditions the sample can be exposed to, with highly-specialised holders and/or microscope columns necessary.

To clarify the scope of the experiments, an overview of the experimental campaigns is given in Table 2.1.

	Irradiation	Post-irradiation annealing
Ex situ	Section 2.2.1	Section 2.2.1
In situ	Section 2.2.3	Section 2.2.2

Table 2.1: Tabular index of experiments

2.2.1 *Ex situ* irradiation and *ex situ* post-irradiation annealing

The ex-situ irradiation conditions are listed in Table 2.2. These are maintained constant for all samples. The ex-situ post-irradiation annealing conditions are listed in Table 2.3. The choice of temperatures was motivated by the desire to test fusion-relevant temperatures. Couple with variations in time, these allow for both isochronal and isothermal comparisons, which facilitate the estimate of activation energies and identification of recovery stages.

Following the ex-situ irradiation and annealing, the samples were back-thinned using the procedure described in Section 2.1.7, and analysed in the TEM. The samples were fully characterised, looking at defect densities, sizes, Burgers type and nature (void or interstitial). This is a lengthy procedure and is described in Section 2.3. There are also several books dedicated to the subject, such as [44].

Material	Ion energy (keV)	Temperature (°C)	Dose (W^+m^{-2})	dpa	dpa/s
UHP-W	2000 (Surrey)	500	$1{\cdot}10^{18}$	1.5	$3{\cdot}10^{-4}$

Table 2.2: Conditions of *ex situ* irradiation

2.2.2 *Ex situ* irradiation and *in situ* post-irradiation annealing

Ultra-high purity samples of tungsten were irradiated with identical ion-beam conditions to those shown in Table 2.2. These were immediately back-thinned using

Time (hours)	Temperature (°C)	Type
0.5	950	Quartz tube in muffle furnace
1	800 950 1100	
	1400	Vacuum furnace
2	800 950	Quartz tube in muffle furnace
4	800 950 1100	
8	800	

Table 2.3: Summary of *ex situ* annealing treatments of irradiated bulk samples.

the procedure described in Section 2.1.7, loaded in a special TEM holder with a microfurnace, and given the heat treatments summarised in 2.4 whilst being observed in the transmission electron microscope.

Type	Time (hours)	Temperature (°C)
Isothermal	2	800
Isothermal	2	950
Isothermal	1	1100
Dynamic	10 min/stage	100-1200 in steps of 100

Table 2.4: Summary of *in situ* annealing treatments of irradiated bulk samples.

The experiments were carried out using a JEOL 2010 TEM using a Gatan 628.TA single-tilt heating holder, rated to 1300°C.

In the dynamic ramp-up experiments, the temperature was increased in stages: 100°C every 10 minutes, from 100°C to 1200°C. Because the aim is to transition as quickly as possible from one temperature level to another, temperature ramp rates were maximised to ~ 3°C/s. This was found sufficiently high to minimise additional annealing between temperature stages, and low enough to minimise sample drift and deformation. At the end of each 10 minute annealing stage, micrographs were taken. The general procedure consisted in loading the sample in the TEM, pumping down to $\sim 10^{-6}$mbar, calibrating the electron beam, choosing an appropriate sample area and tilting to a $\boldsymbol{g} = \langle 200 \rangle$ condition. This was then followed by the heat treatment, during which the same area was imaged, with slight corrections to the tilt made to

account for thermal expansion. TEM micrographs were taken at room temperature, at regular intervals during annealing process, and at the end of the experiment; the change of the damage microstructure was recorded (on mini-DV tapes) throughout. A more detailed analysis of the dislocation structure (requiring tilts to different g-vectors) and void measurements, was done after the annealing procedure.

2.2.3 *In situ* dual-beam (W^{2+} and He^{+}) irradiation

In situ TEM dual beam irradiation requires custom built TEM/accelerator units. The experiments were conducted at JANNuS Orsay (Joint Accelerators for Nanoscience and Nuclear Simulation) in France, with the support of the EMIR (*Etudes de Materiaux sous Irradiation*) national funding framework. The experimental set-up consisted of two beam-lines, one rated at 2MeV (ARAMIS) and the other at 190keV (IRMA) directed into a Hitachi 200kV transmission electron microscope, shown schematically in Figure 2.7.

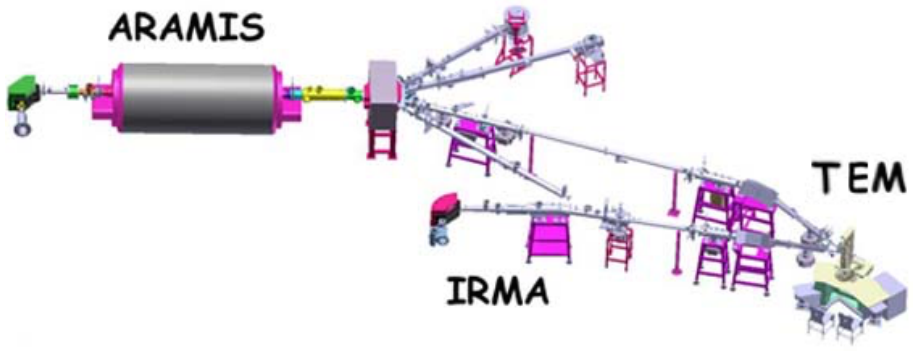

Figure 2.7: Diagram of JANNuS accelerator system, taken from [166].

The precise experimental conditions are summarised in Table 2.5. In all experiments, ultra high purity tungsten was used as raw material, and prepared using double sided electropolishing. A first benchmark irradiation was conducted matching conditions of bulk irradiations (500°C with 2MeV W^2+ ions for a total dose of $1 \cdot 10^{14}$ ions$\cdot$cm^{-2} and estimated damage of 1.5dpa). The dose rate ($2.0 \cdot 10^{10}$ions cm^{-2}s^{-1}) was also

kept as close as possible to bulk irradiation conditions ($2.73 \cdot 10^{10}$ ions cm^{-2} s^{-1}), accounting for the limitations of the source in the ARAMIS accelerator. Because *in situ*, it was possible to image the sample at intervals during the irradiation, allowing to effectively probe the damage saturation threshold of the material at those conditions.

A second experiment was conducted using conditions identical to the benchmark test, with an additional irradiation beam, consisting of 10keV He^+ with a dose rate of $\sim 2.5 \cdot 10^{11}$ ions cm^{-2} s^{-1}. Assuming a ∼100 nm thin film, peak concentration of He was estimated via SRIM to be 1800 appm at a depth of 35 nm, equivalent to 1200appm/dpa. The average concentration of He was estimated to be 800 appm, equivalent to ∼500 appm/dpa.

A third experiment was conducted with an identical dual beam arrangement, but with the sample at 800°C. Finally, in an attempt to see the formation of He bubbles, a fourth experiment was conducted using a higher helium flux of $\sim 2.2 \cdot 10^{12}$ions cm^{-2} s^{-1}. In order to meet this requirement, owing to limitations of the ion sources, a higher accelerating voltage for He was necessary (20keV), and consequently a lower flux rate for tungsten. In this sample, assuming a ∼100 nm thin film, peak concentration of He was estimated via SRIM to be 45'000 appm at a depth of 100 nm, equivalent to ∼25'000 appm/dpa. The average concentration of He was estimated to be 18'000 appm, equivalent to ∼11'000 appm/dpa.

When referring to the experiments, to distinguish between different conditions, the *peak* values will be used.

For all the experiments, micrographs were captured at regular intervals of 0.083, 0.166, 0.25, 0.33, 0.66 and $1 \cdot 10^{14}$ W^{2+} cm^{-2}. At each interval, the beam (or dual beam) was interrupted and the sample tilted back to an optimal imaging condition (diffraction condition was kept constant). Each imaging operation took ∼5 minutes: qualitatively, the damage microstructure did not change during the imaging.

Experiment	Accelerator	Energy (keV)	Ion and charge	Fluence (ions·cm^2)	Swept flux (ions·cm^2·s^{-1})	α	β	Temperature (°C)	Peak appm He
1	ARAMIS	2000	W^{2+}	1e14	2.2e10	-68	22	500	0
2	ARAMIS	2000	W^{2+}	1e14	2.2e10	-68	22	500	1800
	IRMA	10	He^{+}	1.4e15	2.2e11				
3	ARAMIS	2000	W^{2+}	1e14	2.2e10	-68	22	800	1800
	IRMA	10	He^{+}	1.4e15	2.2e11				
4	ARAMIS	2000	W^{2+}	1e14	7.0e9	-68	-22.5	800	45000
	IRMA	20	He^{+}	3.8e16	2.2e12				

Table 2.5: Summary of experiments at JANNuS transmission electron microscope. α and β are the angles of tilt of the sample holder to ensure a perpendicular ion beam to the surface of the sample.

2.3 Analysis procedures

The transmission electron microscopes used for the *ex situ* studies were either a JEOL2000FX, or JEOL2100, operating at 200kV and $\sim 10^{-6}$mbar vacuum.

2.3.1 Ex situ analysis

Grains were chosen close to the $\langle 001 \rangle$ orientation, as samples following pre-irradiation heat treatment had a predomintantly $\{001\}\langle 110 \rangle$ texture [167]. The same sample area ($\sim 0.25 \mu m^2$) was imaged near three poles, exciting a total of eight independent g-vectors in order to determine the Burgers vectors of loops, using the invisibility criterion for a prismatic dislocation loop[1] (see Section 2.3.2).The sign of the Burgers vectors and the nature of the loops were extracted from inside-outside contrast sampling loops >4-5nm in diameter (see Section 2.3.3).

Pole	**g**
001	(200), ($\bar{2}$00), (020), (0$\bar{2}$0), (110), ($\bar{1}\bar{1}$0), (1$\bar{1}$0), ($\bar{1}$10)
1$\bar{1}$3	(2$\bar{1}\bar{1}$), ($\bar{2}$11), (1$\bar{2}\bar{1}$), ($\bar{1}$21)
$\bar{1}\bar{1}$3	($\bar{2}\bar{1}\bar{1}$), (211), ($\bar{1}\bar{2}\bar{1}$), (121)

Table 2.6: Example combination of **g** used for dislocation analysis (or equivalent).

For the sign of the Burgers vector, positive-negative pairs of equivalent **g**-vectors can be compared. For a detailed explanation on how to determine the Burgers vector and nature (interstitial, vacancy) of dislocation loops in TEM, see Refs [44, 168]. In the following sections, the analysis procedures will be briefly reviewed and expanded on.

2.3.2 Burgers vector determination

Based on a wealth of past literature, it is expected for dislocations loops in bcc materials to have Burgers vectors of type $\frac{1}{2}\langle 111 \rangle$, $\langle 100 \rangle$, and perhaps $\frac{1}{2}\langle 110 \rangle$ [169, 86].

[1]The strict version of the invisibility criterion is $\mathbf{g} \cdot \mathbf{R} = 0$, where $\mathbf{R}$ is the lattice displacement. One can expand it to $\mathbf{g} \cdot \mathbf{b} = 0$ and $\mathbf{g} \cdot \mathbf{b} \times \mathbf{u} = 0$, where $\mathbf{u}$ is the dislocation line direction, and $\mathbf{b}$ is the Burgers vector.

Therefore, the diffraction contrast analysis assumed that loops with these Burgers vectors could be present in the irradiated samples. Each dislocation type given by the $\langle\ \rangle$ brackets includes several variants. For example, $\frac{1}{2}\langle 111\rangle$ has 4 possible variants: $\pm\frac{1}{2}[\bar{1}11]$, $\pm\frac{1}{2}[1\bar{1}1]$, $\pm\frac{1}{2}[11\bar{1}]$, $\pm\frac{1}{2}[111]$. To unambiguously determine the specific variant requires a sufficient number of diffraction conditions, such as in Table 2.6.

Let us demonstrate this process by example:

1. Firstly, one must define the set of crystallographic axes, given in Figure 2.10. In this case, $\boldsymbol{z} = [001]$ was defined as the upward normal (pointing out of the paper). Due to the initial high-temperature annealing to promote grain growth, the majority of grains irradiated and characterised were close to $\boldsymbol{z} = [001]$. Reflections near this pole were then assigned appropriate indices, as in Figure 2.11. $\boldsymbol{g_1}$ was assigned a (200) vector, although equally valid vectors could have been $(\bar{2}00)$, (020), $(0\bar{2}0)$, due to four-fold symmetry for this orientation. The important thing is *consistency*: one the choice is made, the remaining diffraction spots must be indexed accordingly using a Thompson tetrahedron.

2. Once indexing of the diffraction pattern is completed, it is useful to refer to Table 2.6 and systematically image an area using the listed $\boldsymbol{g}$, taking both kinematical bright field (*kmbf*), and weak beam dark field (*wbdf*) micrographs. For the *wbdf* condition, excitation errors between $3 - 4\boldsymbol{g}$ were used.

3. Once all the imaging is done, it is convenient to commence the analysis using the $\boldsymbol{g}$ closest to the grain normal $\boldsymbol{z} = [001]$, so $\pm(200)$, $\pm(110)$, $\pm(020)$ and $\pm(1\bar{1}0)$. Examples are given in Figure 2.8. The appearance of individual loops between these micrographs is tracked, assigning a 0 or 1 value to each depending on whether these appear or not in a specific diffraction condition.

4. The procedure is repeated by tilting to two other poles, such as $\boldsymbol{z} = [\bar{1}13]$ and $\boldsymbol{z} = [1\bar{1}3]$ (equally $\boldsymbol{z} = [012]$ could have been used), as shown in Figure 2.9. The exact choice depends mainly on the tilting range of the transmission

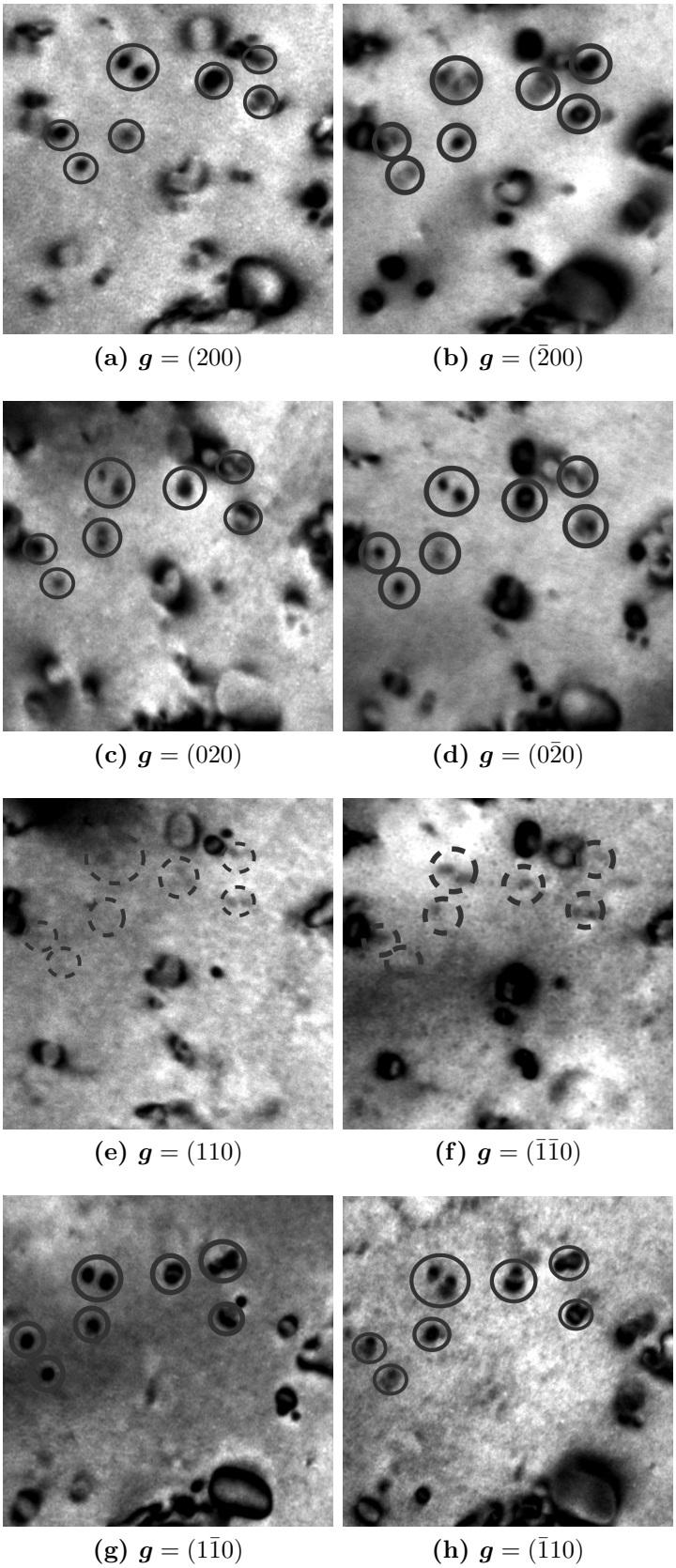

(a) $\boldsymbol{g} = (200)$ **(b)** $\boldsymbol{g} = (\bar{2}00)$

(c) $\boldsymbol{g} = (020)$ **(d)** $\boldsymbol{g} = (0\bar{2}0)$

(e) $\boldsymbol{g} = (110)$ **(f)** $\boldsymbol{g} = (\bar{1}\bar{1}0)$

(g) $\boldsymbol{g} = (1\bar{1}0)$ **(h)** $\boldsymbol{g} = (\bar{1}10)$

Figure 2.8: Kinematic bright field images of dislocations for various excited $\boldsymbol{g}$, taken near the $\boldsymbol{z} = [001]$ pole in ultra-high purity tungsten irradiated to 1.5dpa with 2MeV W^+ ions at 500°C and subsequently annealed to 800°C. Dashed lines signifies invisibility and filled line signifies visibility of loop.

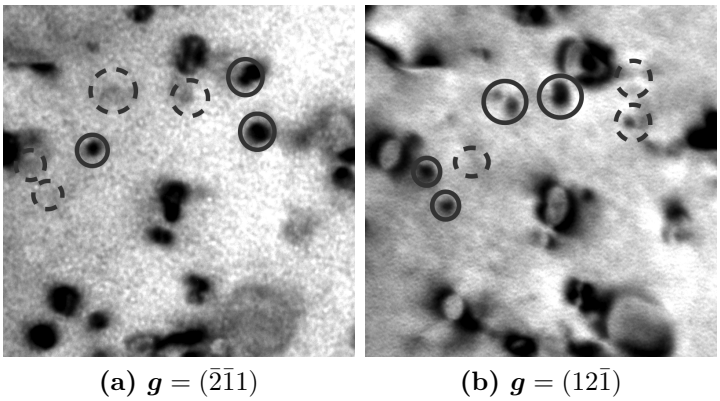

(a) $\boldsymbol{g} = (\bar{2}\bar{1}1)$ **(b)** $\boldsymbol{g} = (12\bar{1})$

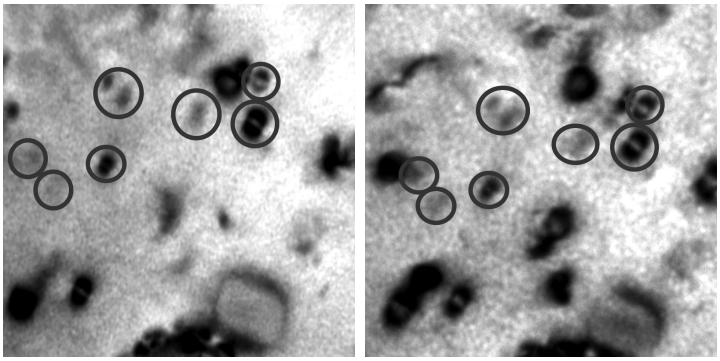

(c) $\boldsymbol{g} = (\bar{1}21)$ **(d)** $\boldsymbol{g} = (\bar{2}11)$

Figure 2.9: Kinematic bright field images of dislocations for various excited $\boldsymbol{g}$, taken near the $\boldsymbol{z} = [113]$ (a-b) and $[1\bar{1}3]$ (c-d) poles in ultra-high purity tungsten irradiated to 1.5dpa with 2MeV W^+ ions at 500°C and subsequently annealed to 800°C. Dashed lines signifies invisibility and filled line signifies visibility of loop.

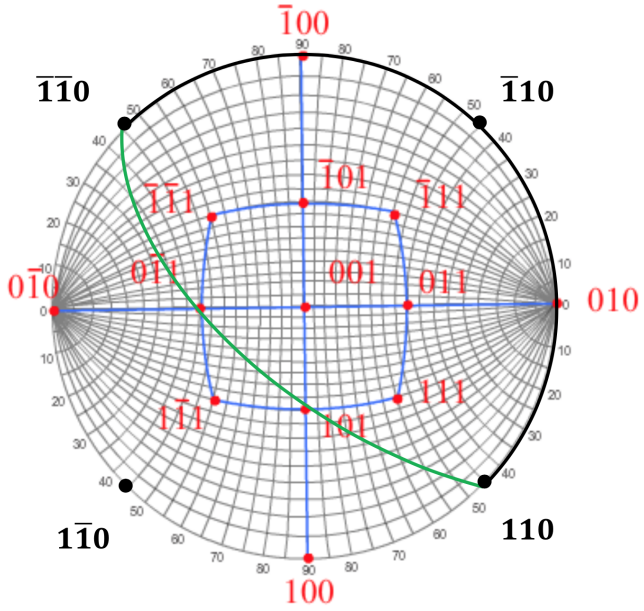

Figure 2.10: The (001) stereographic projection of a BCC lattice, from [170].

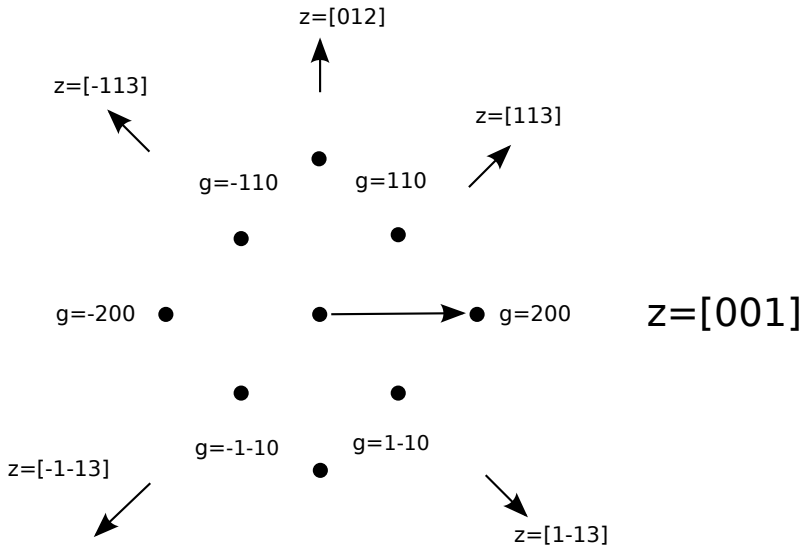

Figure 2.11: Indexing the diffraction spots at $\boldsymbol{z} = [001]$; the relative direction of $[012]$, $[113]$, $[\bar{1}\bar{1}3]$, $[\bar{1}13]$, $[1\bar{1}3]$ with respect to $[001]$.

electron microscope, which can be limited depending on the model, and the condition of the specific grain. The important factor is not to choose symmetric poles.

5. One can then tabulate the instances of individual loops appearing in specific diffraction conditions. Based on Figure 2.8, it can be readily concluded that the tracked loops (circled) in the example have Burgers vector $\boldsymbol{b} = \pm[\frac{1}{2}\bar{1}11]$ or $\boldsymbol{b} = \pm[1\bar{1}1]$. Finally, by looking at Figure 2.9 (a-b) one can see three of the loops are absent for $\boldsymbol{g} = (\bar{2}\bar{1}1)$ meaning they have $\boldsymbol{b} = \pm[1\bar{1}1]$, and the four other loops are absent in $\boldsymbol{g} = (12\bar{1})$ meaning they have $\boldsymbol{b} = \pm[\bar{1}11]$.

It can be appreciated that determining Burgers vector for very small defects (<1-2nm) is difficult, as these are highly sensitive to the diffraction condition, and generally only visible in *wbdf* conditions. As such, the analysis focussed on loops above these dimensions.

2.3.3 Loop nature determination

To deduce whether a particular loop is of vacancy or interstitial nature requires performing an *inside-outside* contrast analysis, originally introduced by *Groves and*

Kelly [171], and later refined by *Maher et al* [172]. This is applicable to $\frac{1}{2}\langle 111\rangle$ loops, which will later be shown to be the predominant Burgers type. *Inside* contrast refers to cases when the loop image size shown is *smaller* than the real size. Vice-versa, *outside* contrast refers to cases when the loop image size shown is *larger* than the real size. To characterise a loop's nature, one needs:

1. Inside-outside contrast for $\pm\boldsymbol{g}$.

2. The Burgers vector $\boldsymbol{b}$.

3. The loop habit plane, defined by plane normal $\boldsymbol{n}$ or sense of inclination.

4. The sign of the deviation parameter $\boldsymbol{s_g}$.

Because it is extremely difficult to determine the habit plane for small defects characteristic of radiation damage, a modified method needing just the contrast behaviour, for *safe* orientations, the Burgers vector $\boldsymbol{b}$ and the sign of the deviation parameter $\boldsymbol{s_g}$ is used. From M.L. Jenkins and M.A. Kirk [44], *safe* orientations refers to the choice of $\pm\boldsymbol{g}$ pairs, where loops of identical Burgers vector with either pure-edge or some shear component all show the same inside-outside contrast behaviour. Such loops would lie in the area of a stereographic projection delimited by $\boldsymbol{n}\cdot\boldsymbol{z}=0$ (edge-on orientation), and $\boldsymbol{n}\cdot\boldsymbol{b}=0$ (pure shear orientation) shown in Figure 2.10. A useful criterion to ensure selection of safe orientations involves assigning an upper limit to the acute angle ϕ between the Burgers vector $\boldsymbol{b}$ and habit plane normal $\boldsymbol{n}$. A crystal orientation $\boldsymbol{z}$ can then be selected, for which $\theta(\boldsymbol{b},\boldsymbol{z})<90^\circ-\phi$. In this scenario, the dislocation loops loops are prismatic with $\boldsymbol{b}=\frac{1}{2}\langle 111\rangle$, with habit plane 110. Therefore $\phi=35^\circ$, and $\theta(\boldsymbol{b},\boldsymbol{z})<55^\circ$. Practically, by choosing $\pm\boldsymbol{g}$ pairs close to the main $\boldsymbol{z}=[001]$ pole, such as $\boldsymbol{g}=\pm[1\bar{1}0]$, ensures this safety limit is fulfilled. Knowing the Burgers vector $\boldsymbol{b}$, the contrast behaviour for a safe $\pm\boldsymbol{g}$ pair and the sign of the deviation parameter $\boldsymbol{s_g}$ allows determination of the nature of the loop, using Figure 2.12 and a Thompson tetrahedron. This is best explained through an example:

1. Consider a loop with Burgers vector $\boldsymbol{b} = \pm\frac{1}{2}[\bar{1}11]$, as determined in the previous section.

2. From the analysis of the $\boldsymbol{g}$ pairs close to $\boldsymbol{z} = [001]$, the loop are observed to have inside contrast (smaller size) for $\boldsymbol{g} = (\bar{2}00)$ and outside contrast (larger size) for $\boldsymbol{g} = (200)$.

3. The sign of the deviation parameter has been kept *positive* for all kinematic bright field micrographs, $\boldsymbol{s_g} > 0$.

4. For inside contrast, the $(\boldsymbol{g} \cdot \boldsymbol{b})\boldsymbol{s_g} < 0$ condition must be fulfilled. For outside contrast, $(\boldsymbol{g} \cdot \boldsymbol{b})\boldsymbol{s_g} > 0$. Therefore, for this particular loop, the inside contrast condition is fulfilled if $\boldsymbol{b} = -\frac{1}{2}[\bar{1}11]$, since $\boldsymbol{s_g}$ is positive and the sign of the dot product of $\boldsymbol{g} = (\bar{2}00)$ and $\boldsymbol{b} = -\frac{1}{2}[\bar{1}11]$ is negative.

5. Since $(\boldsymbol{b} \cdot \boldsymbol{z}) < 0$ the loop are *interstitial*, as shown in Figure 2.12.

6. This sign of the Burgers vector and nature can confirmed by using other $\pm\boldsymbol{g}$ pairs, such as $\pm(020)$ or $\pm(1\bar{1}0)$.

For each sample 30-50 loops were analysed this way to get a nature fraction. Owing to the difficulty and ambiguity in differentiating the inside or outside contrast condition for very small defects, only defects >4nm were chosen.

2.3.4 Foil thickness estimation

Important quantitative information on irradiation damage, such as defect density, depend on the knowledge of foil thickness. Two established techniques (with $\epsilon < 10\%$) for in-situ thickness measurements for TEM samples are to use electron energy loss spectroscopy (EELS) and convergent beam electron diffraction (CBED). However both come with problems: the first requires the use of specific hardware which was not available in all the microscopes used, whereas the second technique works well only for specimens with thicknesses larger than those found in the tungsten TEM foilds (<150nm). Therefore, the local thickness of the samples was es-

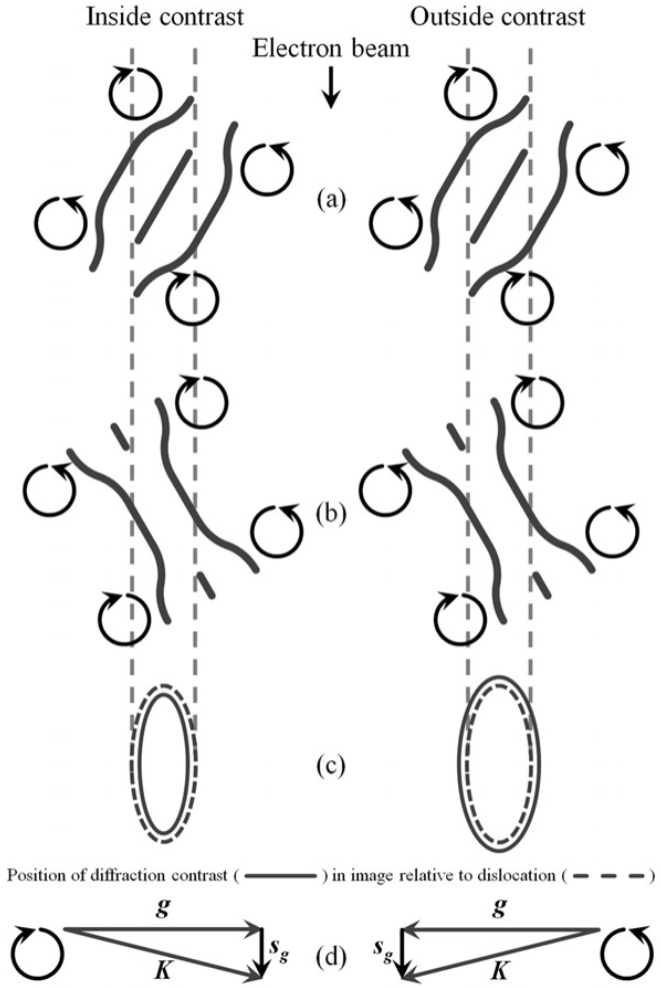

Figure 2.12: Schematic diagram showing the directions in which the planes of a crystal are rotated by the strain fields of (a) interstitial loops and (b) vacancy loops. (d) Illustrates the direction in which the sample must be rotated for the deviation parameter ($\boldsymbol{s_g}$) to be reduced such that these distorted planes approach the Bragg condition (i.e. the diffraction vector, $\boldsymbol{g}$, approaches the scattering wavevector, $\boldsymbol{K}$). For a given combination of diffraction vector direction and sign of deviation parameter, there will be a particular sense of planar rotation required to approach the Bragg condition. Only certain regions of the strain field (pictured as circles) around a dislocation loop will bend the planes of the surrounding crystal towards the Bragg condition and this causes diffraction contrast to be generated either on the inside or the outside of the projection of the dislocation loop. The direction of planar distortion is indicated for four different combinations of loop nature and inclination. Also shown are two combinations of diffraction vector and deviation parameter with the direction of planar rotation required to approach the Bragg condition indicated for each situation. Comparison of the rotation required to approach the Bragg condition with the rotation due to the strain fields around the loops reveals that diffraction contrast will form inside the projection of the dislocation for the examples on the left of the diagram and outside for those on the right. Taken from *Hinks et al* [168].

.

timated by taking the product of the number of thickness fringes observed at the edge of the grain in question, and the extinction distance in tungsten (≈33.2nm for a $\boldsymbol{g}$=(200) condition at 200kV [173]). It has been shown that foil thickness may considerably change the dislocation structure observed, with thinner areas potentially displaying a lower defect density due to the greater impact of free surfaces on absorbing defects [106]. To ensure consistency throughout the numerous analysed samples, the thickness in analysed regions was maintained approximately constant (∼100-120nm), and the TEM foil wedge angle was kept low.

2.3.5 Void imaging

To check for the presence of small voids (<5nm) and gain quantitative measurements, one has to first tilt the sample away from an excited diffraction condition, and subsequently carry out a through-focus study of the sample in bright field. By defocusing, one causes a phase shift between electron waves traversing the material matrix and the void. Fresnel fringes form on to the edge of the void and their intensity depends on the degree of under or over focus of the objective lens. Voids were observed in several experiments and imaged between $\pm 1 \mu m$ focus values. An example is shown in Figure 2.13.

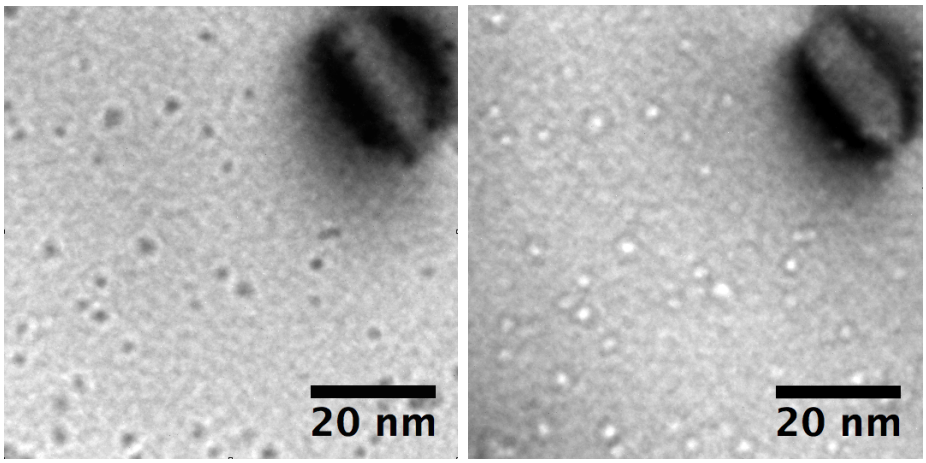

(a) Over-focus (+1000nm) **(b)** Under-focus (-1000nm)

Figure 2.13: Out of focus images of voids in UHP-W irradiated with 2MeV W^+ and subsequently annealed up to 1200°C, from [1]

2.4 Dislocation loop sizing

2.4.1 Diffraction conditions

The visible size of dislocation loops may vary depending on the diffraction condition. For a quantitatively accurate analysis of *small* defects (<10nm), sizing data was averaged when possible from pairs of weak-beam dark-field of the same area of interest using $\boldsymbol{g} = \pm(200)$ and $\pm(020)$, $3 - 4\boldsymbol{g}$. For large grains, multiple areas (2-4) were analysed. For in-situ experiments where it was not possible to analyse multiple diffraction conditions due to time constraints, a single diffraction condition was used but imaging several neighbouring areas. Loops that were smaller than $1nm$ were not taken into account in the overall size distribution analyses, due to difficulties in distinguishing such defects from background noise and due to the resolution limit of diffraction contrast. For particular experimental conditions (such as high-temperature anneals above ∼900°C), dislocation loops were generally too large to be imaged and sized clearly in weak-beam dark field, so kinematic bright field was used instead.

2.4.2 Manual analysis

Manual analysis consisted in measuring individual loop areas (in pixels^2) by delineating loop boundaries, from which a characteristic diameter could be derived. The image processing software used was ImageJ [174]. The boundary was defined as the point at which the intensity of the loop reduced to the local average background value. Understandably, this process was very time consuming, as hundreds of loops were required for a representative size distribution. Therefore, where possible an automated analysis was used, described in Section 2.4.3.

Manual analysis was the only option for high temperature anneals, as loops would frequently be large, elliptical and/or irregularly shaped. Therefore, sizing was done *manually* by calculating the dislocation area for consistency with other data sets, and a characteristic diameter calculated from the area by assuming circularity.

2.4.3 Automated analysis

Automated sizing of defects was employed for suitable micrographs taken in weak-beam dark field, with a relatively homogenous distribution of small loops $< 10nm$ imaged at resolutions where they appeared as single-peak spots, as opposed to double-lobe images. A newly developed modification by Mason [175] of the Ridler and Calvard's isodata algorithm [176] was used, proven against an extensive list of manual measurements. A brief description presented here. The algorithm proceeds in four stages: flattening, identifying, comparing and counting. The flattening stage removes long-wavelength (10-100s nm) variations in image intensity due to foil thickness. Each pixel has an intensity f_i. The parent image is subdivided into smaller images, and the average intensity $\bar{f}_i$ of image subsection is computed, excluding bright pixels over the threshold $f_{thresh} = \frac{1}{2}(\bar{f}_{\text{fore}} + \bar{f}_{\text{back}})$. The intensity of each pixel is then adjusted based on a the target background intensity. All pixels with intensity above $\frac{1}{2}(f_{\text{thresh}} + \bar{f}_{\text{back}})$ are identified, with a spot defined as a contiguous region in this subset with a single maximum with intensity over f_{thresh}. The algorithm then checks whether identified areas are composed of distinct regions (two loops that are close to each other). A maximum diameter is calculated using eigenvalues of an intensity tensor of the spot. By using a reference image of an unirradiated micrograph of the same region (possible for example in *in situ* irradiation experiments in Section 4), the algorithm can identify and eliminate spurious dim spots via statistical analysis.

An example image interpretation using the automated sizing algorithm is shown in Figure 2.14.

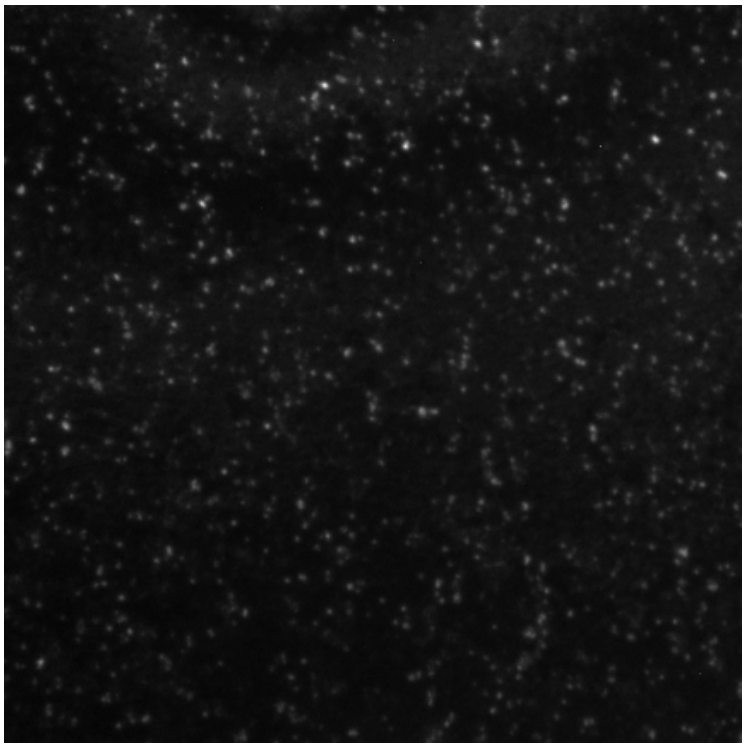

(a)

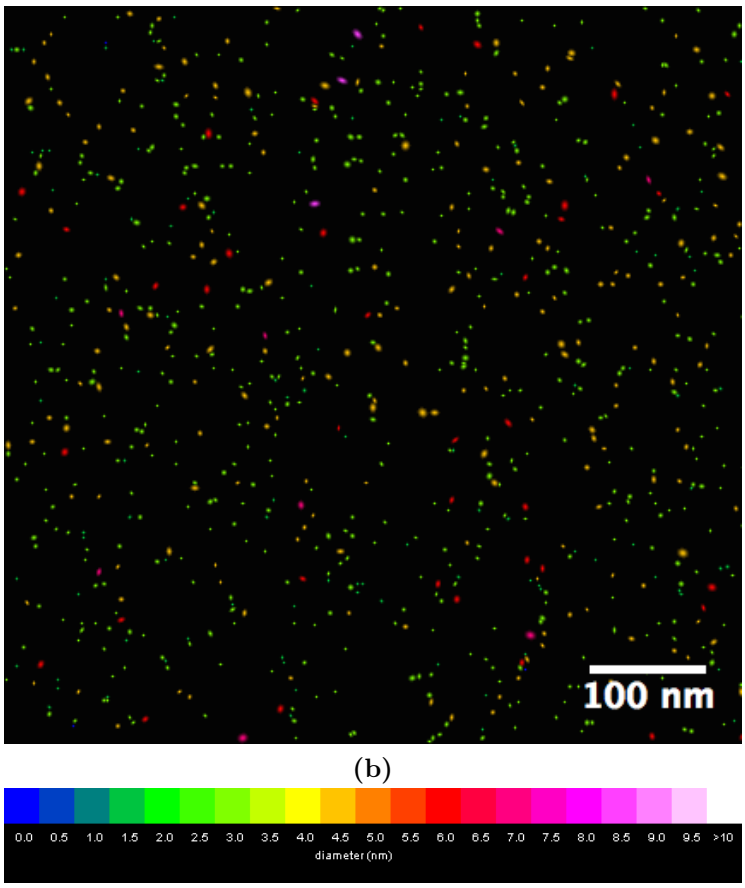

(b)

Figure 2.14: (a) Example *wbdf* micrograph with dislocation loop structure characteristic of radiation damage, (b) Computer generated image of identified loops, with associated sizes.

Chapter 3

Experimental characterisation of tungsten: high temperature recovery of self-ion irradiation damage

3.1 Introduction

The following chapters contains a detailed account of the experimental results for a battery of experiments looking at the defect life-cycle, with a particular focus on *recovery*. The overarching aim is to quantitatively identify the damage response of tungsten to (as closely as possible) fusion-relevant parameters, and the dependence of *temperature* on such damage and recovery processes. I will also seek to provide insights on the role of *helium* on damage formation, and how dislocations in tungsten respond to stress with respect to temperature. This information hopes to achieve two goals: 1) quantify the minimum optimal operating temperature for tungsten to maximise radiation resistance, and 2) inform and act as an experimental benchmark for phenomenological computational models.

The experimental data presented in this chapter will focus on high-temperature recovery. It will present and discuss the results from the following experimental campaigns:

1. *Ex situ* irradiation and *ex situ* post irradiation annealing, as planned in Section 2.2.1.

2. *Ex situ* irradiation and *in situ* post irradiation annealing, as planned in Section 2.2.2.

Here, the damage from self-ion irradiation in bulk tungsten and the effect of various high-temperature heat treatments, relevant for fusion conditions will be characterised. By conducting high temperature annealing experiments *in situ*, the thermal recovery processes of self ion irradiation tungsten at such high temperatures will also be described and identified. The majority of the information has also been published as a journal article in Ref [1].

3.2 Characterisation of thermal recovery in *ex situ* irradiated tungsten for *ex situ* isochronal heat treatments

First of all, to act as a benchmark for high-temperature annealing heat treatments, bulk self-ion irradiation of pure tungsten was carried out as an analogue of fusion neutron damage in a TOKAMAK reactor. The chosen conditions were 1.5 dpa dose, at an irradiation temperature of 500°C. W^+ ions with 2MeV energy were used, at a constant flux of $2 \times 10^{14} W^+ m^{-2} s^{-1}$ (3×10^{-4}dpa/s), building upon previous experimental studies by *Yi* [67]. Similarly to other experimental studies [67], evidence of coexistence of $\frac{1}{2}\langle 111 \rangle$ and $\langle 100 \rangle$ loops was found, in a 5:1 ratio. Quantitative analysis of overall loop size distributions was made from weak-beam dark-field images. Subsequently, as described in the methods chapter, the samples were annealed for 1 hour at temperatures between 800 and 1400°C. Figure 3.1 provides a qualitative overview of the effect of annealing on the dislocation density in ion-irradiated tungsten from this benchmark:

1. A reduction in loop number density with increasing temperature.

2. An increase in average loop size with increasing temperature (particularly transitioning between 800°C and 950°C).

3. The appearance of line dislocations and networks (presumably as glissile loops collide and coalesce) at 950°C and 1100°C.

4. A complete removal of dislocation structures at 1400°C.

By methodically imaging areas of interest using the procedure detailed in Section 2.3, a complete picture of the loop nature can also be achieved, albeit with increasing uncertainty at lower temperatures (unannealed, 800°C) due to a large number of loops being below <2-3nm in size [44].

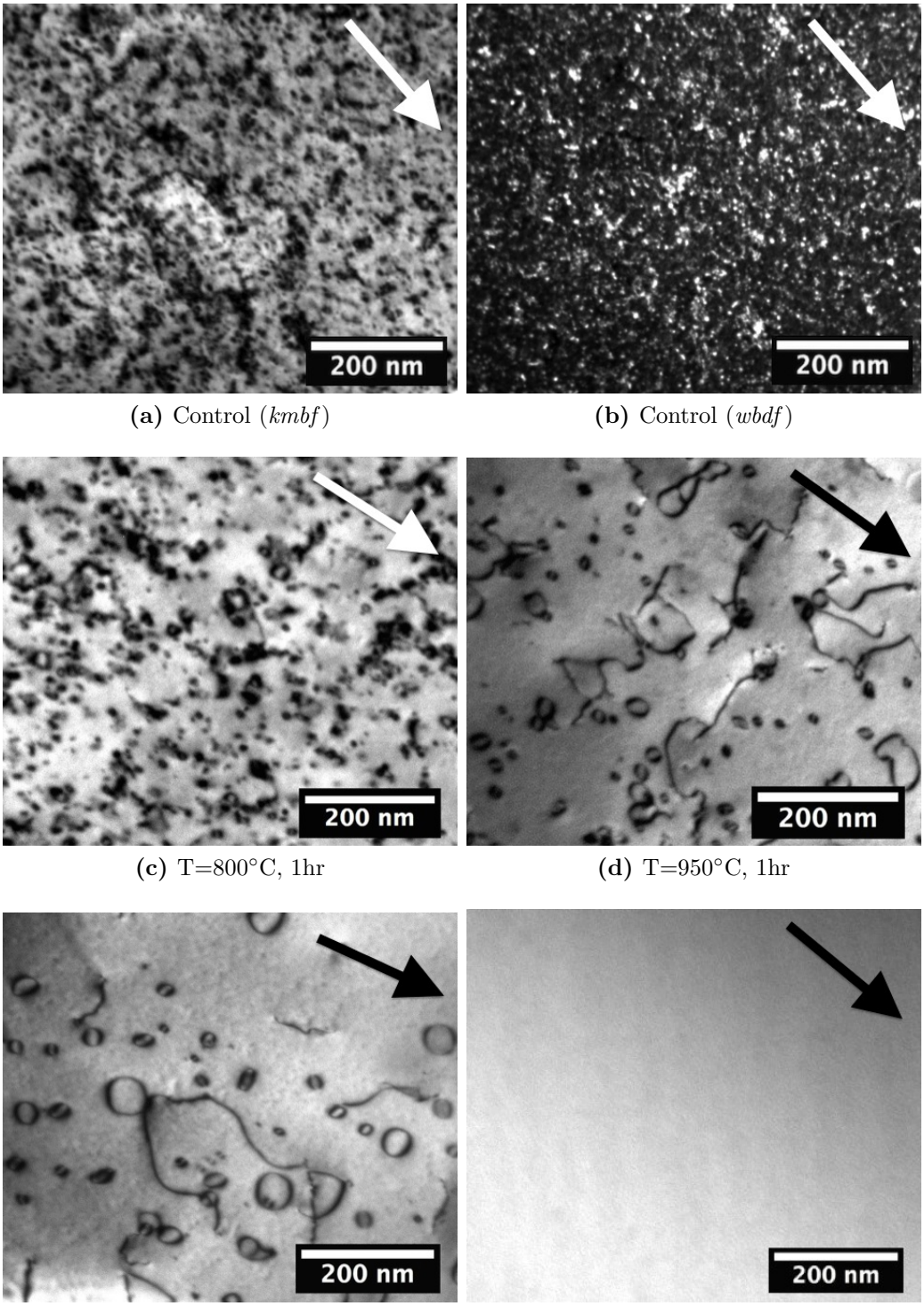

(a) Control (*kmbf*)

(b) Control (*wbdf*)

(c) T=800°C, 1hr

(d) T=950°C, 1hr

(e) T=1100°C, 1hr

(f) T=1400°C, 1hr

Figure 3.1: Damage microstructure in (a,b) as-irradiated tungsten (1.5dpa, 2MeV W^+, 500°C) and post-irradiation annealed tungsten subject to conditions of (c) 800°C for 1hr, (d) 950°C for 1hr, (e) 1100°C for 1hr, (f) 1400°C for 1hr. All micrographs shown were imaged close to [001], with $\boldsymbol{g}$=(200) excited. The arrow in each micrograph shows the direction of the g-vector. (b) is weak-beam dark-field ($\boldsymbol{g}$, 3-4$\boldsymbol{g}$), to pick-up the diffraction contrast of very small loops, 1-2 nm, (a) and (c)-(e) are two-beam kinematical bright-field images.

3.2.1 Total loop population

For total loop population, micrographs were recorded in weak-beam dark field conditions of $\boldsymbol{g}=\pm(200)/(020)$, 3-4$\boldsymbol{g}$. Contrast invisibility correction was not deemed necessary, due to lack of observable $\langle 100 \rangle$-type dislocation defects, as detailed later in Section 3.2.2.

Figure 3.2 suggests that there is a transition between 800°C and 950°C, with a two order-of-magnitude reduction in loop number volume density, from $1.1 \cdot 10^{22}$ to $2.1 \cdot 10^{20}$ loops $\cdot$ m^{-3}. This is in contrast to the transition between unannealed and 800°C, where loop number density decreases ∼30%, or the transition between 950°C and 1100°C where it is decreased by ∼50%. As temperature is increased, there is greater variation in the dislocation loop diameter (see Figure 3.4) as well as fewer loops within an imaged area, despite it being easier to accurately measure the size of single dislocation loops. Nonetheless, it is evident there is an overall increase in size, particularly at 950 and 1100°C.

Dislocation loop size distributions for isochronal anneals are given in Figures 3.3 and 3.4, in the form of cumulative and continuous probability distributions respectively. Experimental data in Figure 3.3 was fitted with a Weibull distribution. This is shown as a continuous probability distribution in Figure 3.4, overlayed to binned experimental data. The following bin sizes were used: for unannealed and 800°C, binning centers at 1,2,4,6,8,10,13.3,16.6,20,30,50,70,90,100 nanometers were used. For 950°C and 1100°C, binning centers at 0,10,20,30,50,70,90,100 were used. A sample size of 3340 for the unannealed sample, 4940 for 800°C, 1116 for 950°C and 231 for 1100°C was used. To the author's knowledge, there is no standard fit for the probability density function (pdf) of loop diameters. A Weibull distribution (which was originally proposed for particle size distribution, and later garnered popularity for fracture statistics in brittle materials [177]), assumes that there exist processes unknown which generate or annihilate loops of different sizes. The probability density function of a Weibull random variable is,

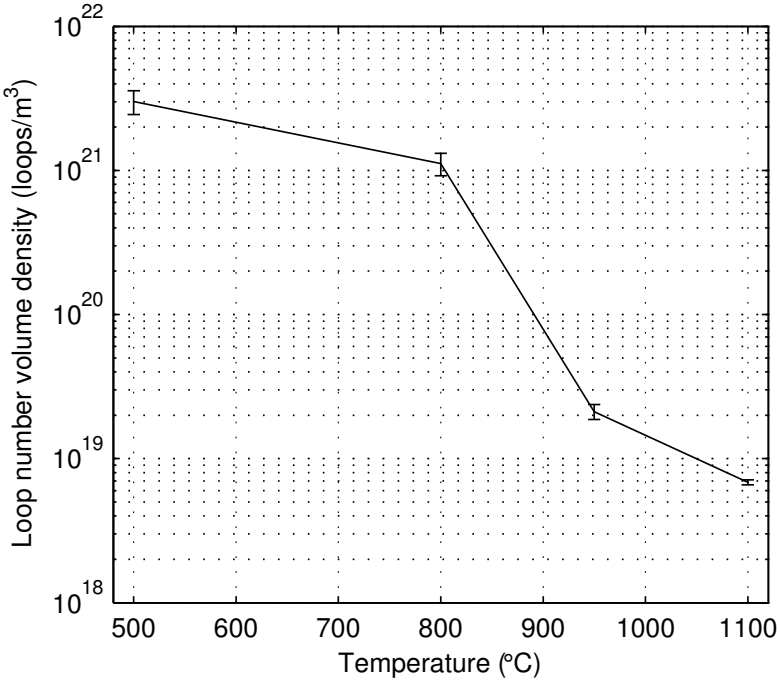

(a)

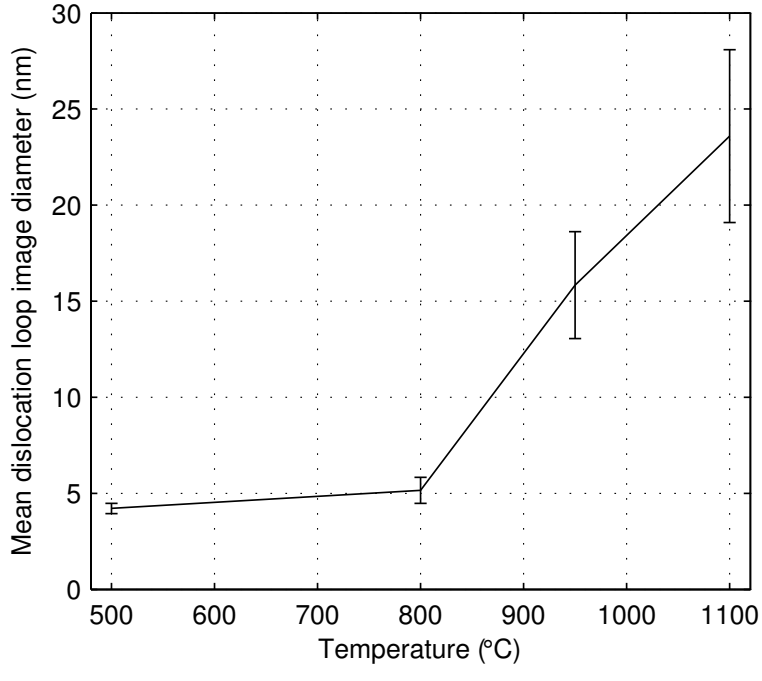

(b)

Figure 3.2: (a) Variation of loop number density (loops/m^3) with annealing temperature (1hr anneal time), (b) Variation of mean dislocation loop image diameter (nm) with annealing temperature (1hr anneal time). Error bars for the mean loop size are calculated using a 95% confidence interval.

$$f(x;\lambda,k) = \begin{cases} \frac{k}{\lambda}\left(\frac{x}{\lambda}\right)^{k-1} e^{-(x/\lambda)^k} & x \geq 0, \\ 0 & x < 0, \end{cases} \tag{3.1}$$

where $k > 0$ is the shape parameter and $\lambda > 0$ is the scale parameter. With a shape parameter of k <1, physical processes are acting to increase the population in the small diameter region, by fragmentation of large loops and/or generation of small ones. Conversely, a shape parameter of k >1 indicates that the physical processes are acting to increase the population in the large diameter region, by coalescence of small loops and/or generation of larger ones. Intuitively, as annealing temperature increases, loops collide and merge. This is confirmed by the shape factor k in each temperature pdf being greater than 1 (specifically, $k_{500°C} = 1.9$, $k_{800°C} = 1.4$, $k_{950°C} = 1.3$, $k_{1100°C} = 1.6$). Data fitting was done using the Matlab Statistics and Machine Learning Toolbox. It can be seen that whereas the as-irradiated sample displays dislocation loops with a pronounced peak at ∼3nm diameter, subsequently annealing the sample produces a broader distribution with larger maximum and average loop sizes, increasing with annealing temperature. The loop size distribution broadening is especially evident between the 800°C and 950°C samples. The mean dislocation loop diameter was calculated by measuring their total effective area (since the majority are elliptical in shape) and calculating a mean diameter using the total number of loops and assuming circularity. Sampling in micrographs was done on distinctly visible loops (>1nm). The same procedure was repeated for later isochronal experiments.

3.2.2 Dislocation loop characteristics

Loops having a diameter of >3nm were exclusively of $\mathbf{b}=\frac{1}{2}\langle 111\rangle$-type. For smaller loops, it becomes increasingly difficult to determine $\mathbf{b}$ reliably. No evidence of $\mathbf{b}=\langle 100\rangle$ vector loops was observed in the annealed samples (50-100 loops analysed per sample, >1nm diameter).

This is consistent with the general trend seen elsewhere [66, 67, 178], of decreasing

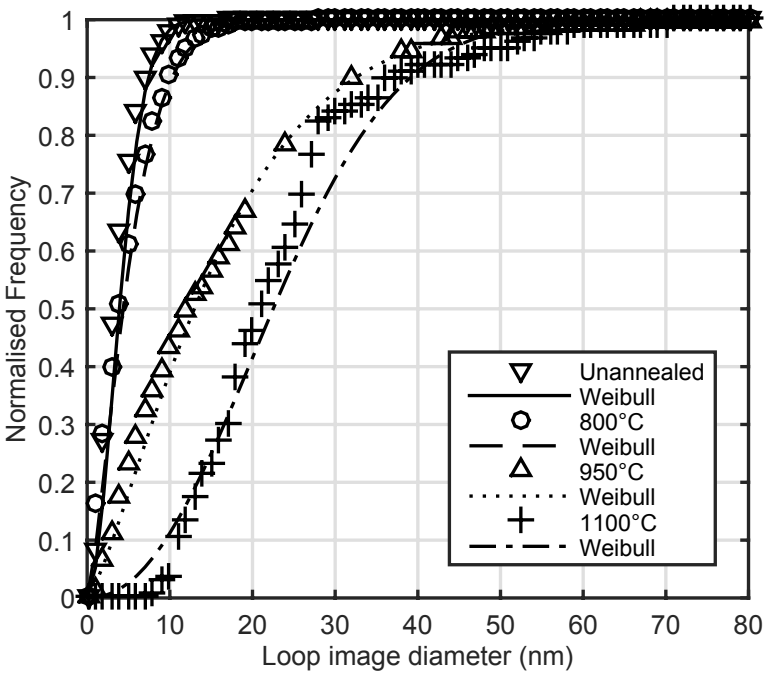

Figure 3.3: Variation of cumulative probability distribution of dislocation loop image diameter following isochronal annealing (1hr anneal time).

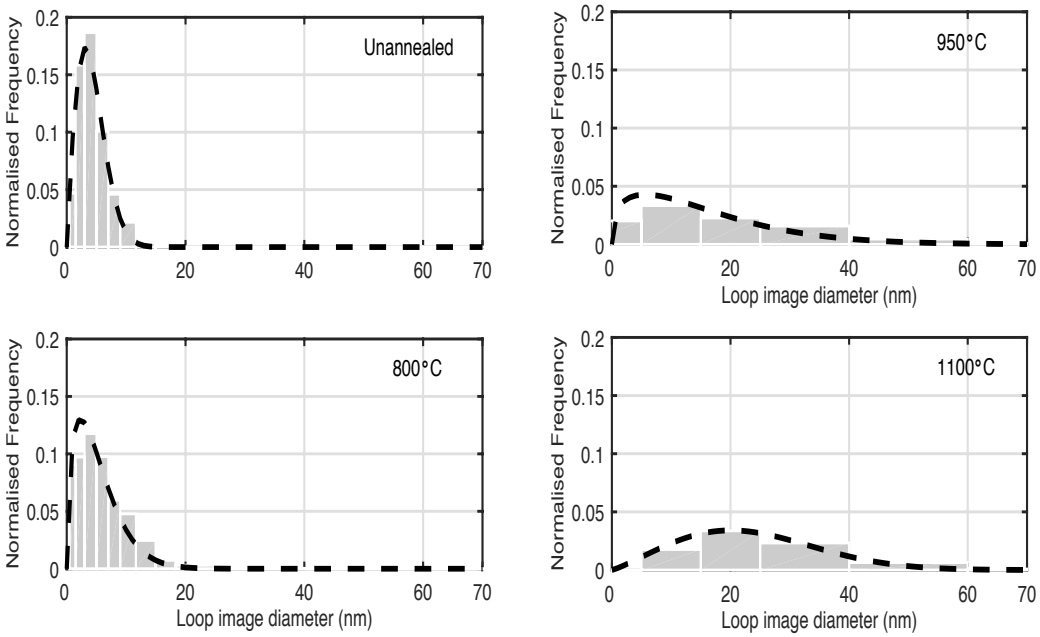

Figure 3.4: Variation of continuous probability distribution of dislocation loop image diameter following annealing for 1hr shown as dashed lines (using fitted Weibull parameters). Histograms show the binned experimental data.

b=⟨100⟩ fractions in UHP-tungsten with increasing ion irradiation temperature. It is also consistent with the hypothesis that ⟨100⟩ loops are metastable defects which form only in high-energy cascades [178], and the observation that such nano-scale defects can be absorbed in a non Burgers vector-conserving fashion by larger $^1/_2$⟨111⟩ loops [179].

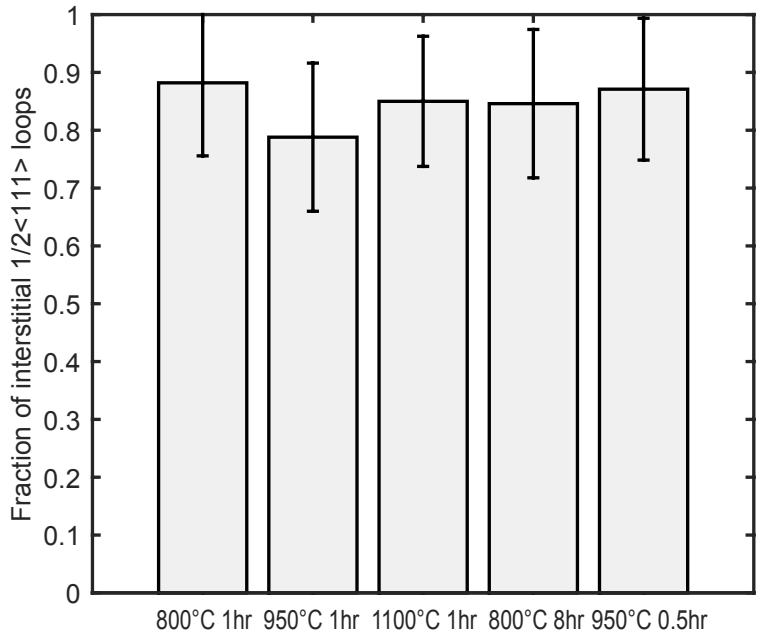

Figure 3.5: Nature type for dislocation loops analysed in 2MeV 500°C 1.5dpa W^+ irradiated UHP-W, followed by bulk isochronal and isothermal anneals.

Nature analysis was carried out for the isochronal bulk experiments, on an average of 30-50 loops (>4nm diameter) for each sample. Dislocation loops were found to be predominantly of interstitial type, as shown in Figure 3.5. The fraction does not appear to vary with annealing treatments, within error (95% confidence interval).

3.2.3 Voids

The dislocation loops, which were primarily of interstitial type, were clearly visible in the as-irradiated conditions. These defects became significantly mobile at temperatures above 800°C, and were annealed away completely at 1400°C. On the other hand, the vacancy population produced by self-ion irradiation was unaccounted for,

and was assumed to be in the form of vacancy clusters which could not be reliably sized using TEM (<1nm diameter, [44]) in the as-irradiated conditions. Once annealed for 1 hour at 800°C and above, voids became visible in the TEM. Example micrographs (under and over-focus pairs) are shown in Figure 3.6 and the results are summarised in Figure 3.7. Until 1100°C the visible voids do not appear to change in size and number density, with an average diameter of ∼1.5±0.1nm, and a density of $\sim 6 \cdot 10^{26}$ voids $\cdot$ m^{-3} . At 1400°C, there is a significant increase in size (∼4.0±0.5nm), and decrease in number density. When performing size measurements for voids, the inside edge of the dark Fresnel fringe in the under-focussed condition was used, as per [44]. The defocus was kept constant at ±800nm.

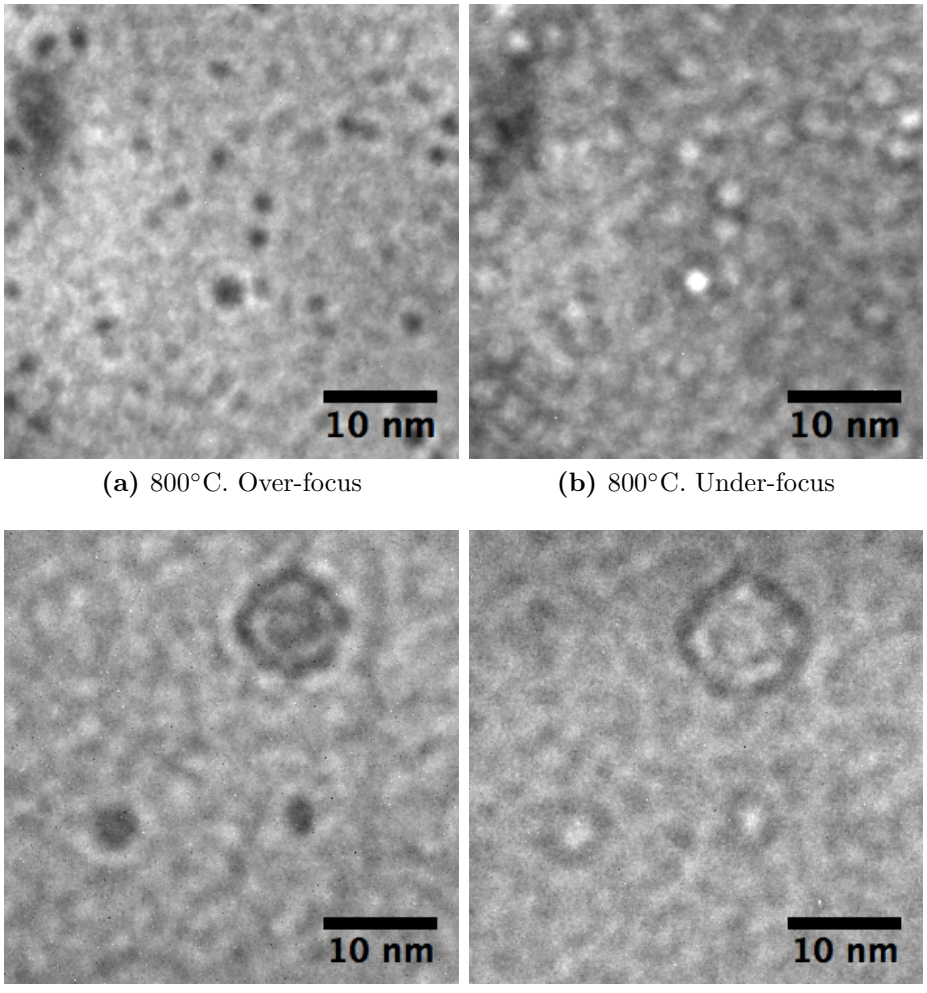

(a) 800°C. Over-focus **(b)** 800°C. Under-focus

(c) 1400°C. Over-focus **(d)** 1400°C. Under-focus

Figure 3.6: Example micrographs of imaged voids at 800°C and 1400°C. The defocus was ±800nm.

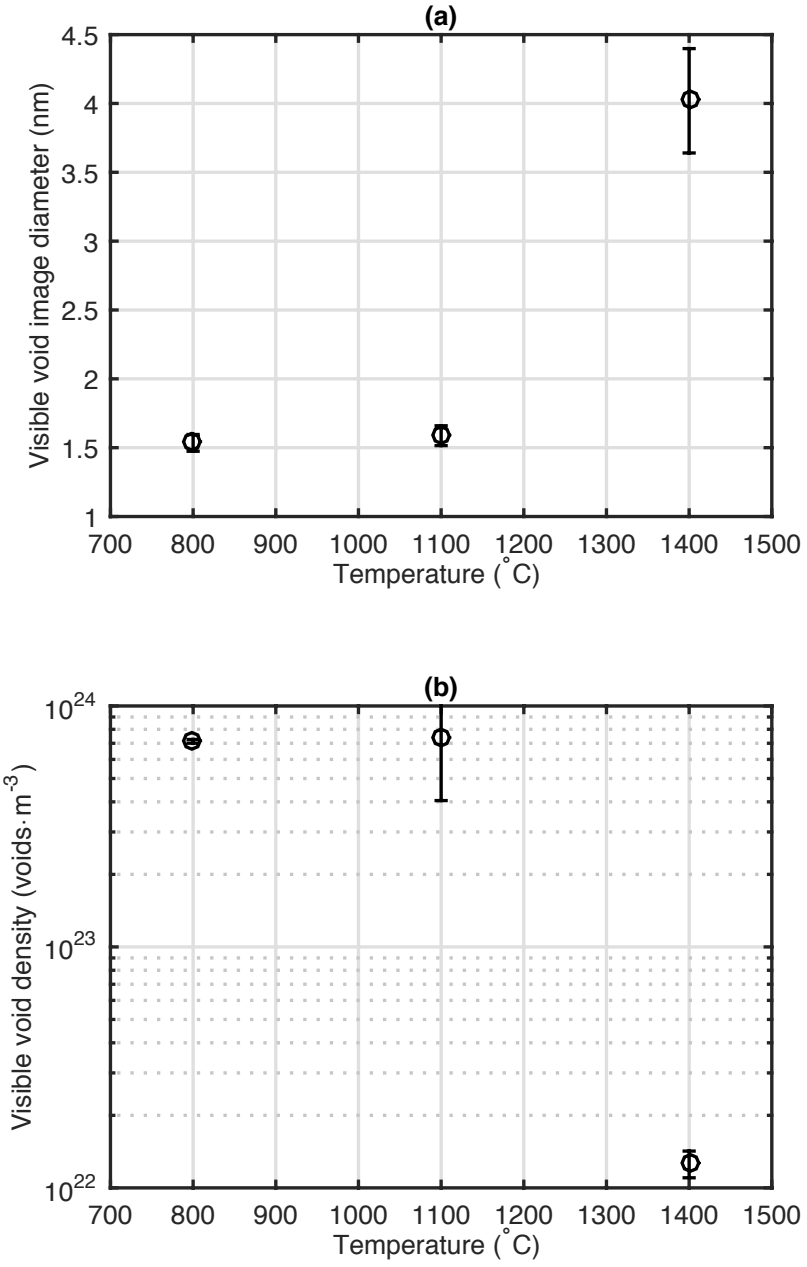

Figure 3.7: (a) Size (diameter, nm) and (b) number density (voids/m^3) of visible voids in under-focussed condition, for varying temperatures (1hr anneals).

3.3 Characterisation of thermal recovery in *ex situ* irradiated tungsten for *ex situ* isothermal heat treatments

This section groups the results of *ex situ* annealing experiments for an isothermal set of heat treatments, to better understand the effect of annealing time on radiation damage recovery. Figure 3.8 summarises the effect of annealing time on mean dislocation diameter for 800°C and 950° conditions. Example damage microstructures can be found in Figure 3.10 for 800°C, and Figure 3.11 for 950°C. Finally, Figures 3.12 and 3.13 give the variation with respect to time of dislocation loop size distributions for 800°C and 950°C respectively.

3.3.1 Total size distribution and loop density

It can be seen quantitatively from Figure 3.8 that for the temperatures tested, loop growth is not just a temperature-dependent but also time-dependent process. Same goes for defect density, as shown in Figure 3.9. For longer anneals, the loops were larger, at lower densities, and significantly more varied in size, requiring the analysis of several micrographs for a statistically valid result. Nonetheless, the rates of loop growth can in principle be compared at different temperatures. For example, a 1hr 950°C anneal yields approximately the same average dislocation loop diameter as a 800°C ∼6.5 hours one. An estimate of activation energies using the bulk isothermal annealing data is made in Section 3.5.2.

Both Figure 3.10 and 3.11 qualitatively show the dislocation coarsening effect of isothermal heat treatments, characterised by an increase in the average size of loops as well as appearance of dislocation lines, probably arising from the coalescence of loop chains. It is evident that an increase of 150°C (small relative to the melting temperature of tungsten) greatly accelerates the process. This is quantitatively displayed in Figure 3.8 and 3.9.

Similarly to Section 3.2, cumulative probability distributions of dislocation loop diameters are provided in Figure 3.12 and 3.13 for the isothermal heat treatments. The experimental measurements appear to follow the Weibull distribution relatively well, considering the inherent measurement uncertainties.

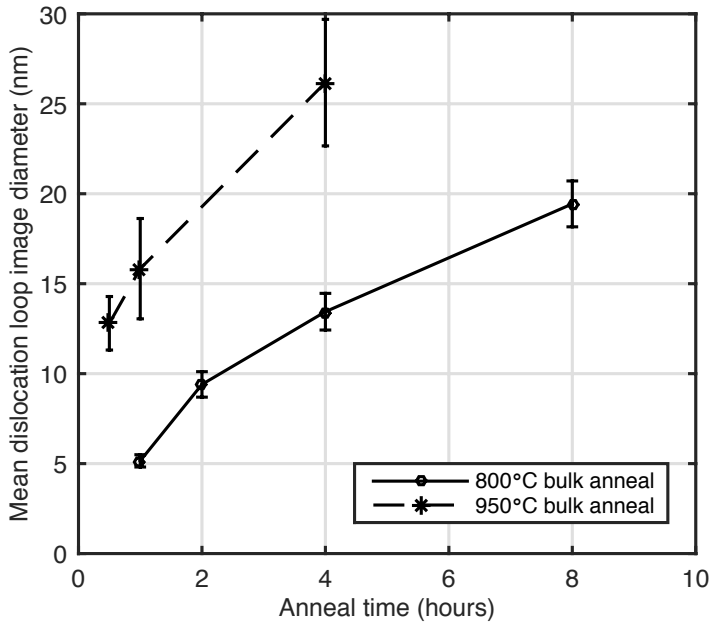

Figure 3.8: Variation of mean dislocation image diameter (nm) with isothermal bulk annealing (800°C and 950°C annealing temperature).

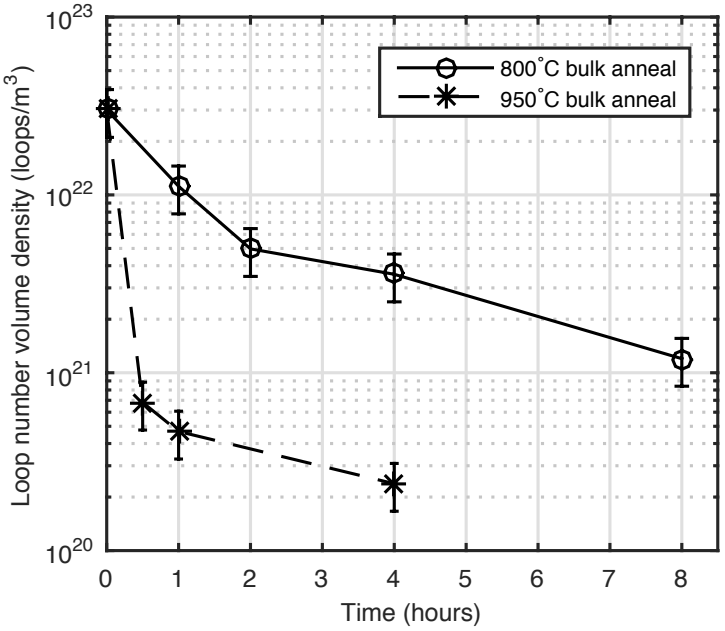

Figure 3.9: Variation of mean loop density with isothermal bulk annealing (800°C and 950°C annealing temperature).

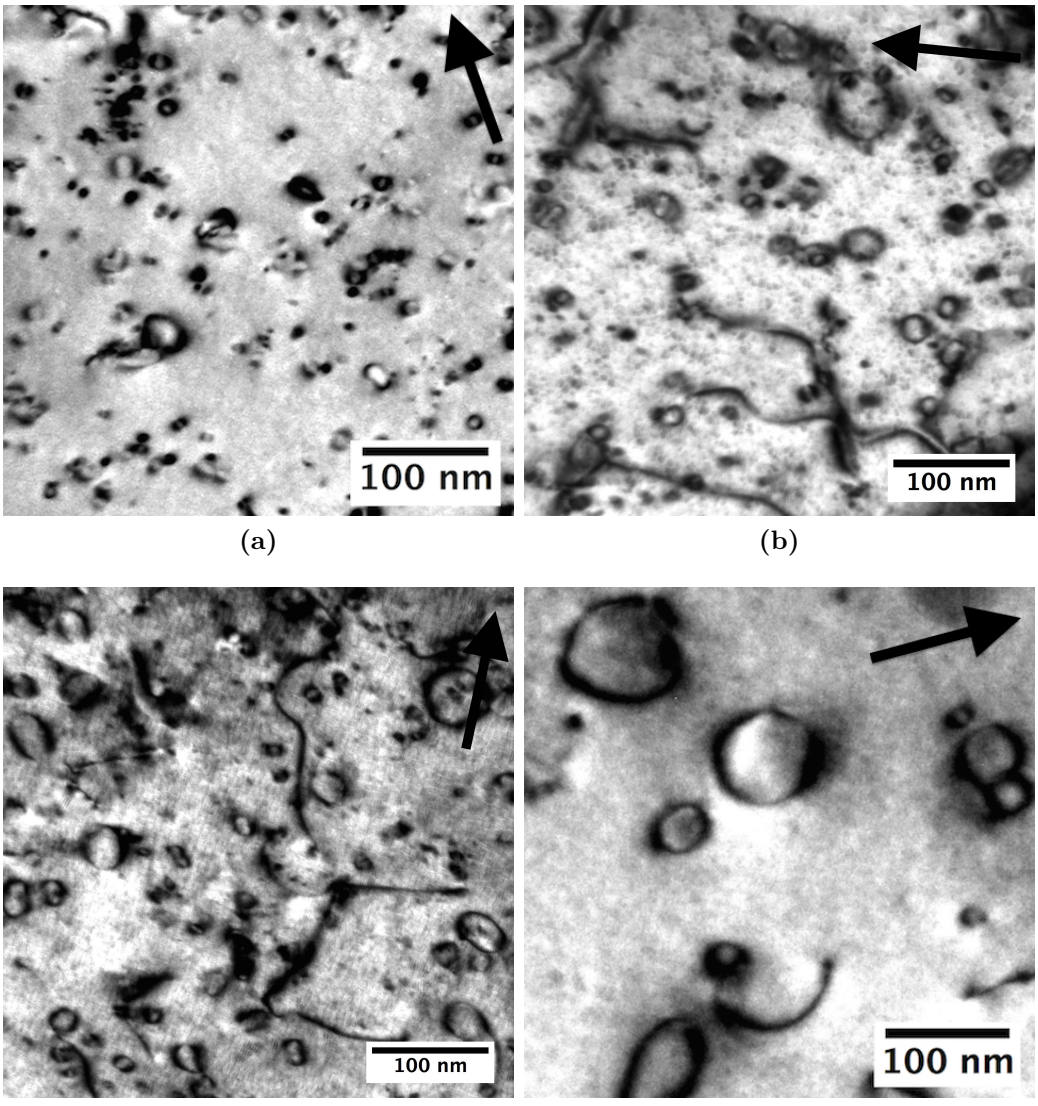

(a) **(b)**

(c) **(d)**

Figure 3.10: Example damage microstructures after (a) 1hr annealing, (b) 2hr annealing, (c) 4hr annealing, (d) 8hr annealing. All annealed at a constant 800°C, with ramp-rate of 1400°C/hr. Kinematic bright-field, at g=(020), with excitation error s>0.

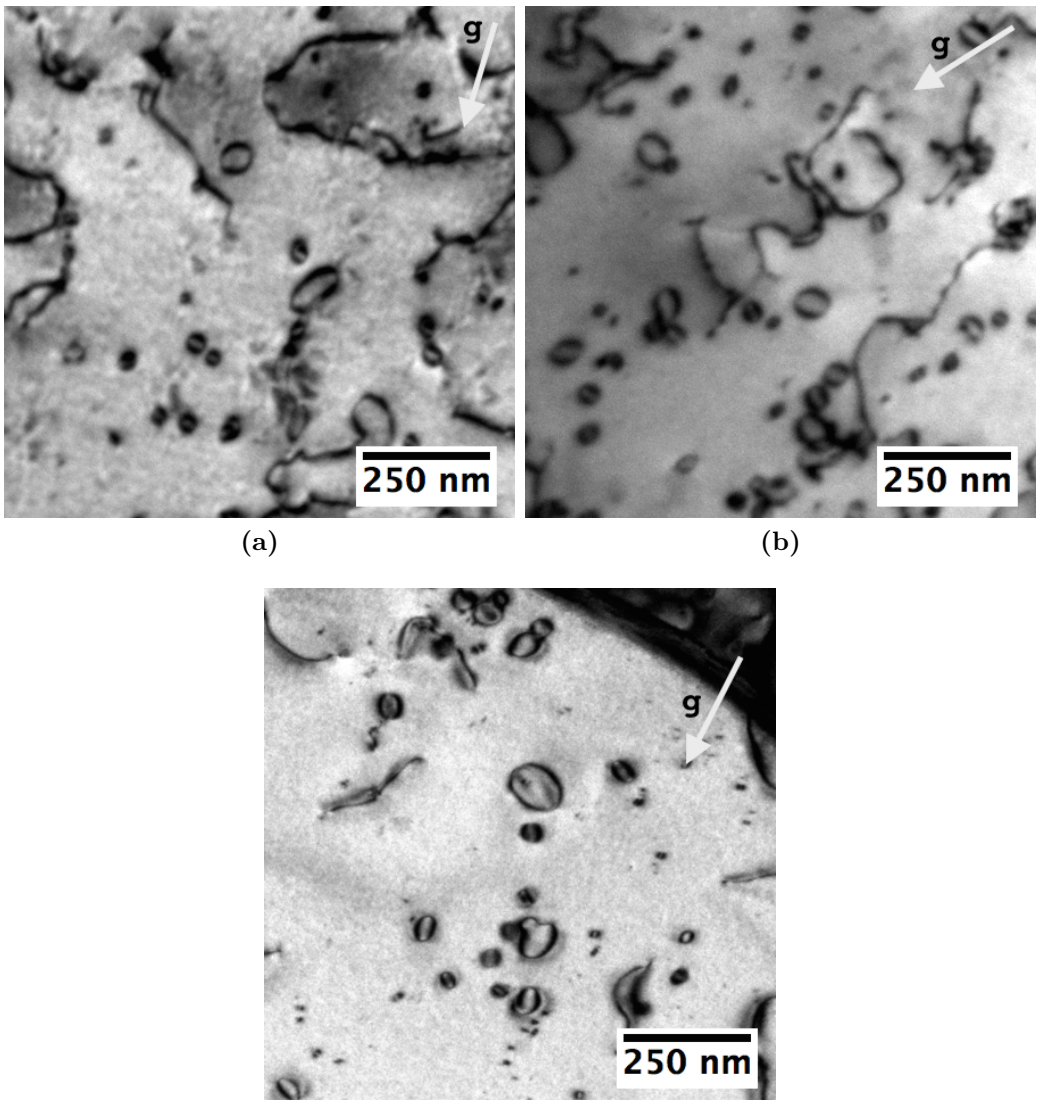

Figure 3.11: Example damage microstructures after (a) 30 minute annealing, (b) 1hr annealing, (c) 4hr annealing. All annealed at a constant 950°C, with ramp-rate of 1400°C/hr. Two-beam kinematical bright-field with $\boldsymbol{g}$=(200) excited.

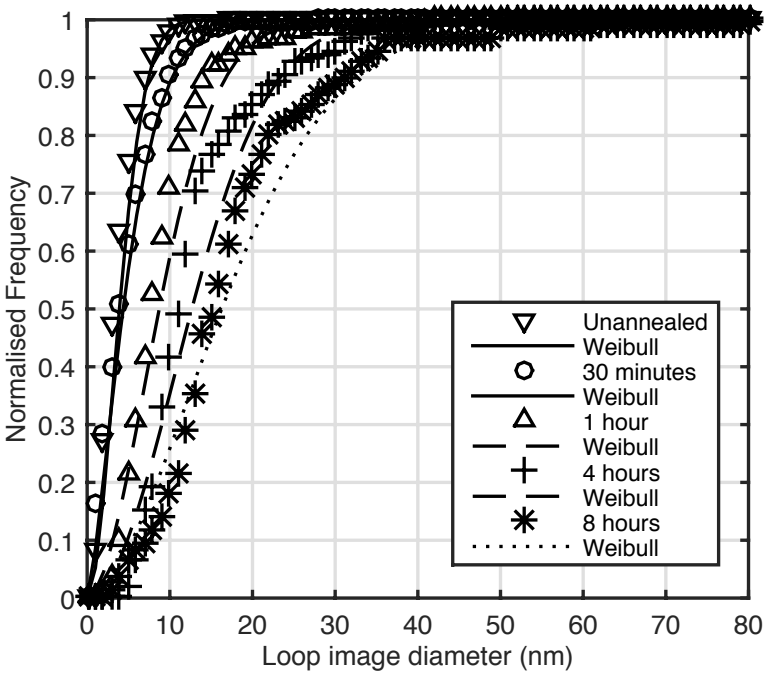

Figure 3.12: Variation of cumulative probability distribution of dislocation loop image diameter following isothermal annealing (800°C annealing temperature).

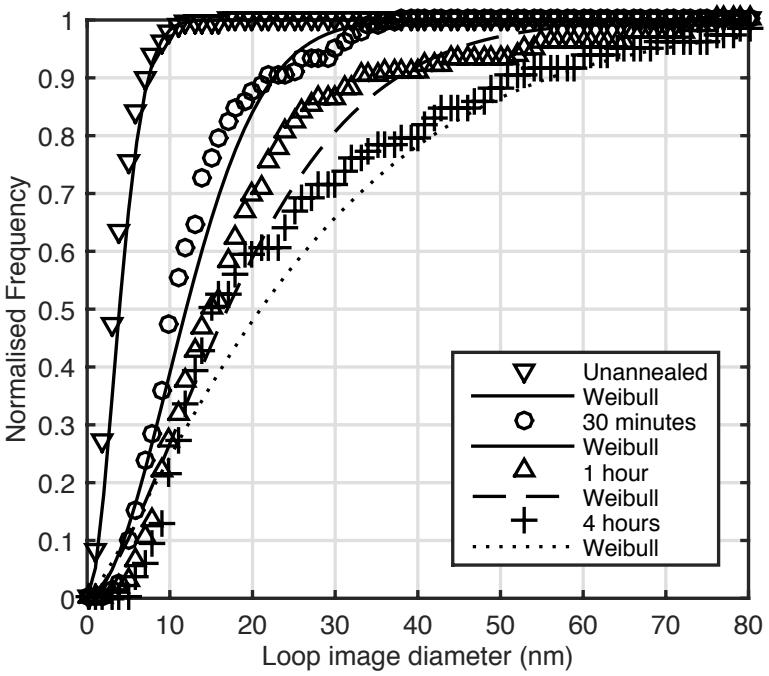

Figure 3.13: Variation of cumulative probability distribution of dislocation loop image diameter following isothermal annealing (950°C annealing temperature).

3.4 Identification of thermal recovery processes using in-situ TEM annealing

In situ annealing experiments allow direct observation of the recovery of radiation-induced dislocation loops. Dynamic temperature ramp-up experiments were conducted and results presented in in Section 3.4.1[1]. The author is grateful of Prof. Kazuto Arakawa from Shimane University in Japan for allowing use of his equipment to conduct such experiments.

3.4.1 Dynamic ramp-up

In the dynamic ramp-up experiments, the temperature was increased in stages: 100°C every 10 minutes, from 100°C to 1200°C, with film micrographs taken at the end of each stage of the same area. In the analysis stage, the micrographs, covering $\sim 2\times2\mu m^2$, were binned into smaller images, magnified and the loops/lines measured manually. The total dislocation line length is the sum of dislocation loop perimeters and lines, for all the bins of a particular micrograph associated to an annealing stage. From Figure 3.14, it can be seen that major dislocation line loss begins at ∼900°C (consistent with bulk experiments). At 1100°C, approximately 90% of the dislocation damage has been annealed out. The morphology of the defects has drastically changed, from very small loops with a well-characterised peak of ∼4nm in diameter at as-irradiated temperatures to very large loops (up to ∼70nm diameter) and dislocation lines at 950°C and 1100°C, similarly to the bulk annealed samples (shown in Figure 3.4).

Figure 3.16 shows a number of dislocation reactions observed during annealing, mainly loop-loop coalescence, loop annihilation from free surfaces (Figure 3.17), and loop-line interactions (Figure 3.18). Intermediate steps for each example are shown with a time label: this signifies the time immediately after the split-second reaction. This is because dislocation motion is generally jerky, whereby a coalescence or interaction event happens within a fraction of a second, followed by periods

[1]Video clips of such processes are provided as supplementary material to this thesis

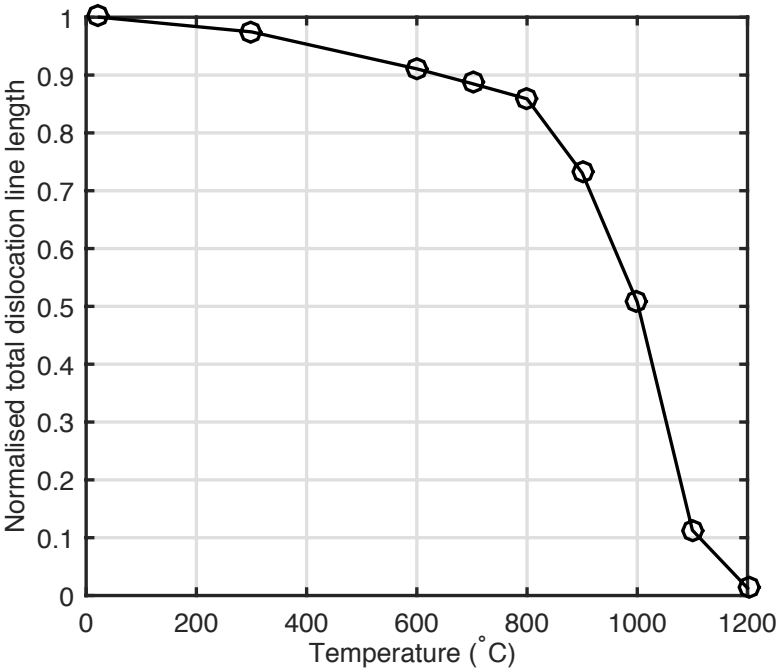

Figure 3.14: Variation of visible total dislocation line length (normalised to that at room temperature) during ramp-up experiment).

of relative stability characterised by small vibrations around a stable or pinned configuration. This suggests the events are stochastic in nature, and also driven by elastic interactions.

The only exception is Figure 3.16 (a)-(c), in which two loops gradually and steadily move towards a third larger loop in the course of ∼1 minute (a-b), in what appears to be a conservative self-climb process, and subsequently (very quickly) merge (c). A similar behaviour has been observed in interstitial loops in molybdenum [122], and uranium oxide [180]. This so called self-climb mechanism is explained in [181] as pipe-diffusion of vacancies, although it remains unclear.

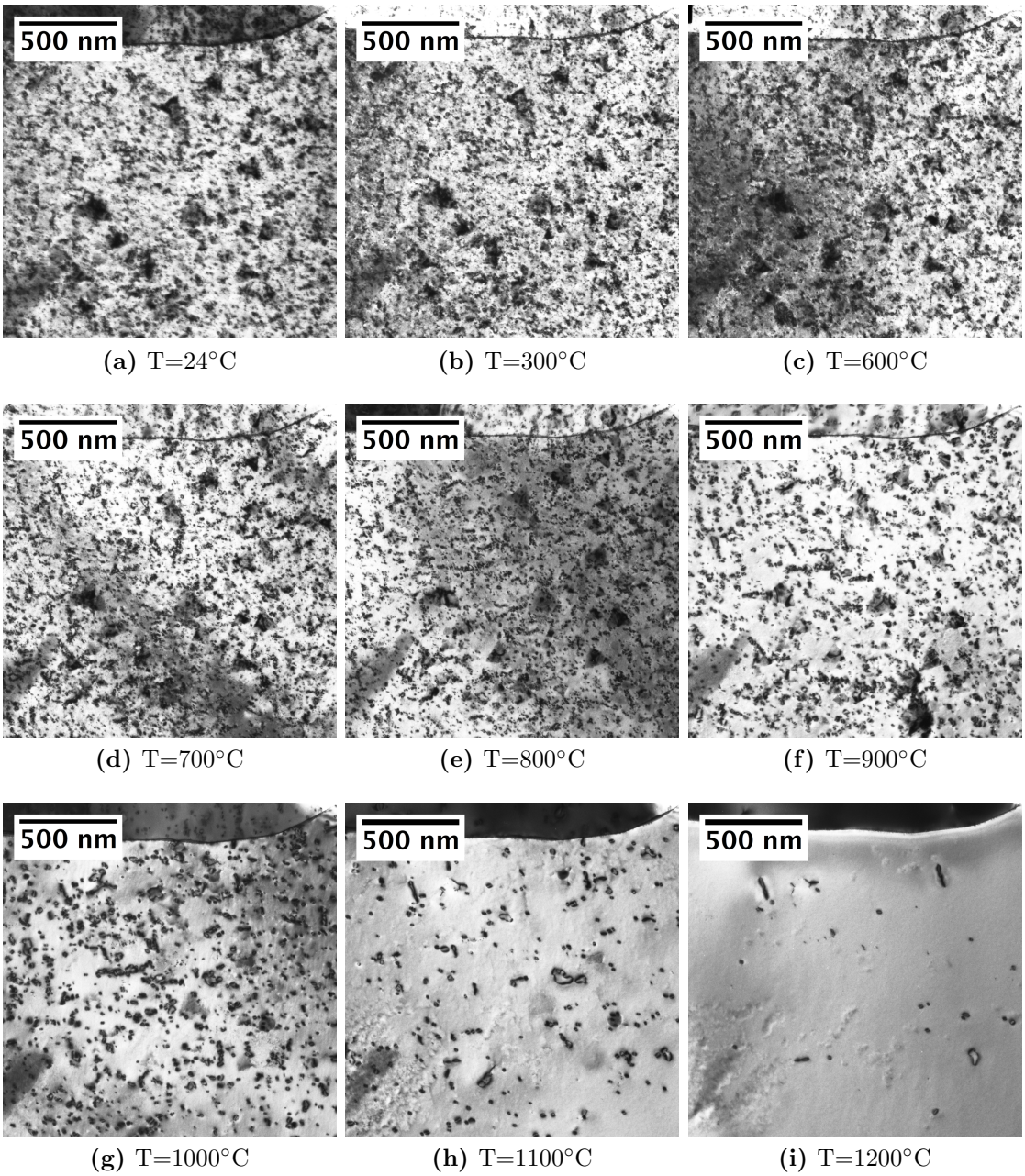

(a) T=24°C **(b)** T=300°C **(c)** T=600°C

(d) T=700°C **(e)** T=800°C **(f)** T=900°C

(g) T=1000°C **(h)** T=1100°C **(i)** T=1200°C

Figure 3.15: Variation of dislocation structure during ramp-up experiment. The same area was analysed at each temperature, at the end of each 10 minute anneal. Magnification and $\boldsymbol{g}=(0\bar{2}0)$ kept constant for all frames.

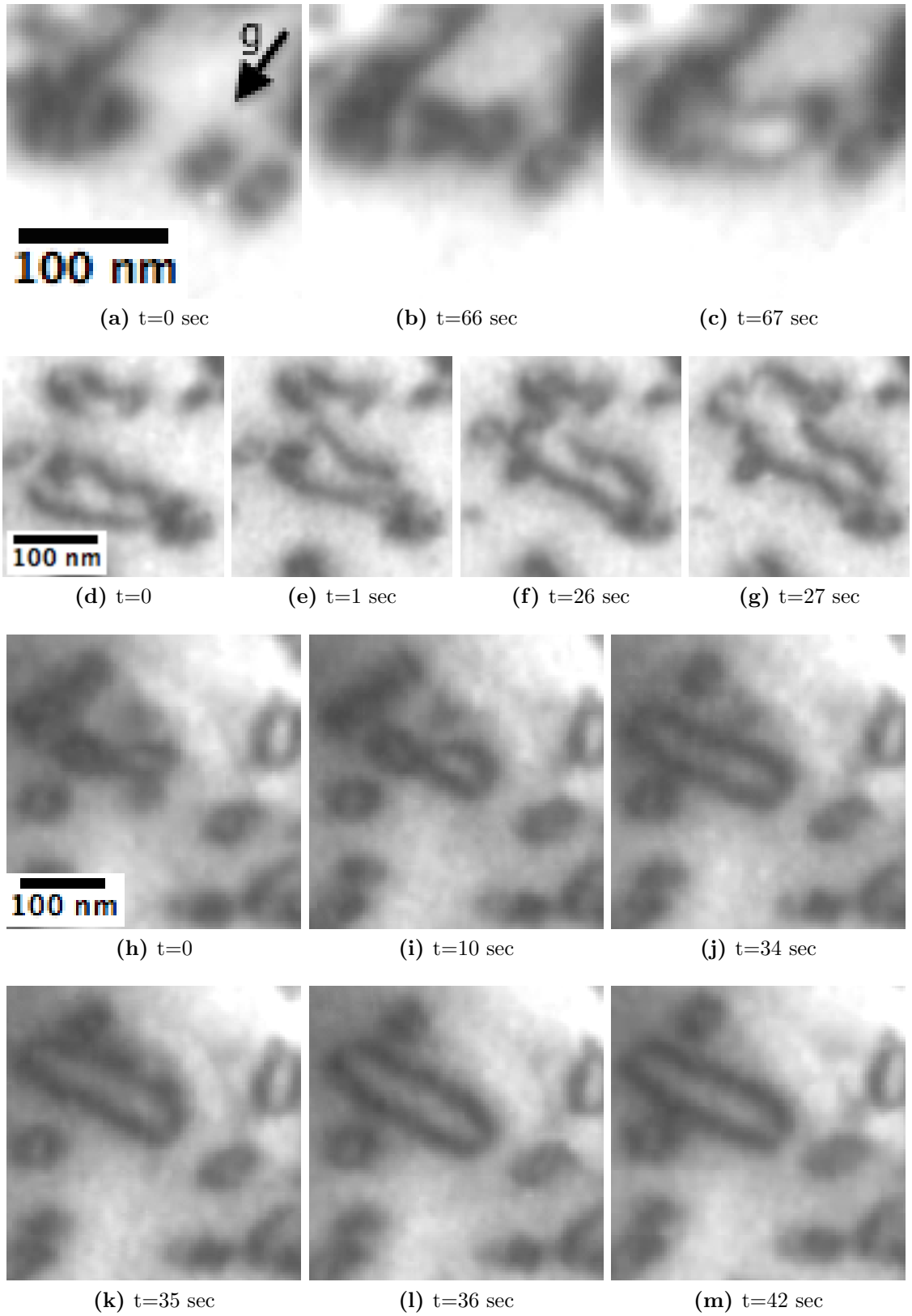

(a) t=0 sec **(b)** t=66 sec **(c)** t=67 sec

(d) t=0 **(e)** t=1 sec **(f)** t=26 sec **(g)** t=27 sec

(h) t=0 **(i)** t=10 sec **(j)** t=34 sec

(k) t=35 sec **(l)** t=36 sec **(m)** t=42 sec

Figure 3.16: Examples of loop coalescence: (a)-(c) at 900°C, a cluster of loops; (d)-(g) at 1000°C, several loops forming a large irregular loop. (h)-(m) at 1000°C, five loops coalescing into an oblong finger loop. $\boldsymbol{g}=(0\bar{2}0)$ held constant through-out the frames.

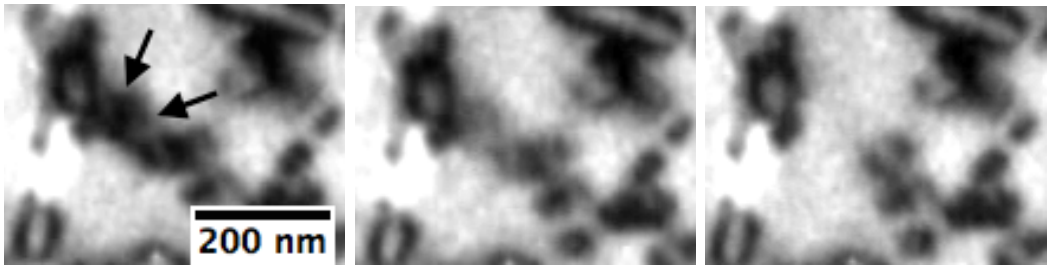

(a) t=0 **(b)** t=0.05 sec **(c)** t=0.1 sec

Figure 3.17: Example of dislocation loops being absorbed by a free surface at 1000°C, as indicated by the pair of arrows in (a). This is a very fast process occurring in a tenth of a second.

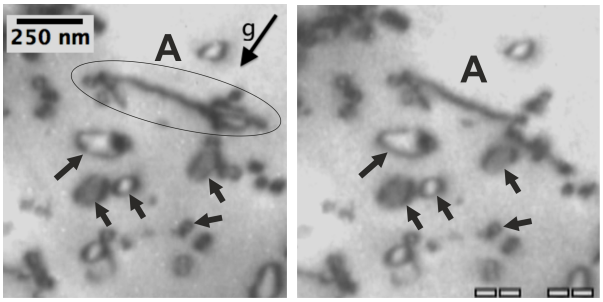

(a) t=0 **(b)** t=10 s

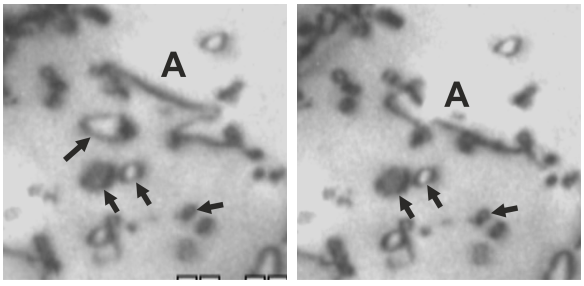

(c) t=12 s **(d)** t=20 s

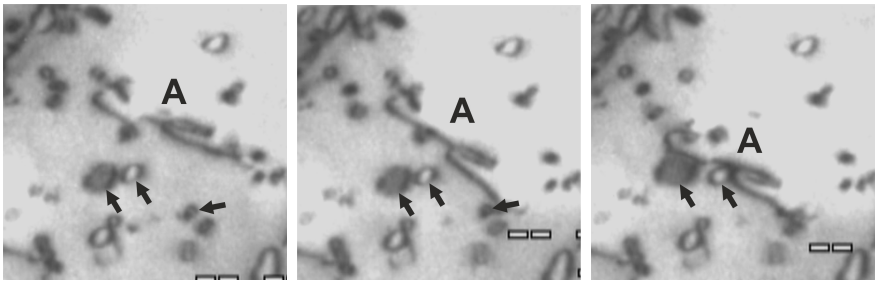

(e) t=23 s **(f)** t=45 s **(g)** t=51 s

Figure 3.18: From *in situ* ramp-up experiment, when held at 1100°C. Example of dislocation line gliding freely, interacting with dislocation loops and either absorbing them or being pinned and released. The dislocation line marked A "sweeps" out other dislocations in its path, marked by arrows. It develops knots which are subsequently straightened out. Magnification and $\boldsymbol{g}=(0\bar{2}0)$ kept constant for all frames.

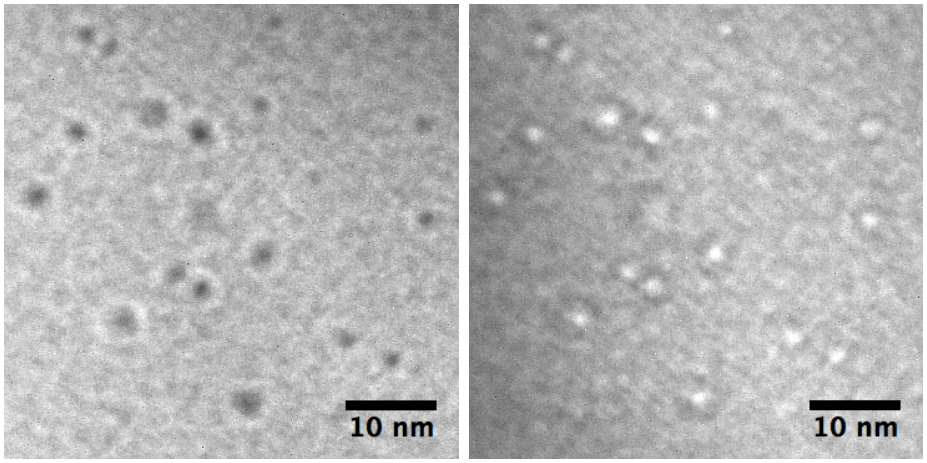

(a) Over-focus (+800nm) **(b)** Under-focus (-800nm)

Figure 3.19: Appearance of small void-like features after in-situ annealing (T=1200°C) in 2MeV W^+ ion irradiated tungsten.

3.4.2 Dislocation recovery stages

From closer inspection of the behaviour of dislocation loops at various temperatures during annealing, one can broadly identify the following sequence of events.

1. RT - 300°C: Stable dislocation structure. No loop hopping or loops being absorbed by the surface were observed.

2. 300°C - 700°C: Smaller $\frac{1}{2}\langle 111 \rangle$ loops were seen hopping in 1D, with sporadic loss of loops to the surface, increasing in frequency at higher temperatures.

3. 700°C - 800°C: Reorganisation of loops from a relatively homogenous distribution into discrete "chains" and clusters.

4. 900°C - 1000°C: Coalescence of loops within chains or clusters, examples of which are shown in Figure 3.16. In the case of chains (where loops rearrange themselves in line, most likely in the same habit plane as this is elastically favourable), coalescence formed oblong finger loops; for clusters (resulting from pinning due to loop-loop interactions), coalescence formed large, sometimes irregularly shaped, dislocation loops. The resulting loops were sometimes observed being subsequently absorbed by the free surfaces (Figure 3.17), or

moving along their glide direction to cluster with another loop. At this temperature, dislocation lines began to be observed.

5. 1000°C - 1200°C: Loss of dislocation loops greatly accelerated, with an additional mechanism: dislocation lines, formed from coalescence and "breaking" of large loops (a surface phenomenon), glided freely in the sample and interacted with dislocation loops in their path. The colliding loops were absorbed into the dislocation line, or occasionally acted as temporary pinning sites for the dislocation line. At higher temperatures, these pinning sites were overcome quickly. Finally, once the dislocation line had finished "sweeping" dislocation lines in its path, it was absorbed by a free surface. This process can be seen in Figure 3.18. Small void-like features were also observed in the post-annealing characterisation.

3.5 Discussion

3.5.1 Defect behaviour

From the bulk isochronal results on number density in Figure 3.2, there is an accelerated decrease between 800°C and 950°C. From the *in situ* results in Figure 3.14, one can confirm that loop loss accelerates from 800°C. Despite contradictory information in the available literature on the underlying mechanisms of the recovery stages, several independent experiments on neutron-irradiated pure tungsten recovery, using resistivity as a measure, observed a recovery stage at $\sim$ 970°C. Whereas early work attributed this to migration of single vacancies [114] (largely due to FIM results by [119, 120]), later studies attribute it to defect clustering: "a complex recovery mechanism and could possibly be related to the disappearance of some defect clusters or formation of voids" [118].

From the TEM studies presented here, dislocation loop coarsening and loss occurs at >950°C, suggesting this contributes to the observed 970°C recovery stage found in resistivity experiments. There are some uncertainties involved in directly comparing the two type of experiments. For example, self-ion irradiation produces a relatively shallow region of damage (<200nm for 2MeV W^+) which can be affected by the presence of foil free-surfaces during the annealing experiments, particularly *in situ* ones. This may distort the actual rate of dislocation loss. Nonetheless, it does not change the underlying physical processes activated: there is a clear dependence on temperature. This may be due to the activation of the motion of large dislocation loops and lines decorated with impurities, such as carbon [182], or to vacancy-activated climb leading to coarsening.

Voids can be seen following the bulk 1-hr anneals at $\geq$800°C. However, the mean size and density of the observed voids does not particularly change up to 1100°C. Only in the 1400°C anneal (Figure 3.7) was there a noticeable increase in average size (and decrease in number density). This is consistent with a recovery well above the onset of Stage V recovery, characterised by an enhanced interaction between

(now mobile) vacancy clusters.

3.5.2 Activation energy estimation

The quantity chosen to measure damage recovery was the total dislocation line length per volume, normalised by that measured in the as-irradiated sample. The motivation behind this choice is two fold. Firstly, particularly at higher temperatures, loops turn into lines, making loop area comparisons within the same sample section erroneous. Secondly, radiation damage recovery in the literature has commonly been measured using resistivity. Above the Debye temperature, the electrical resistivity in the kinetic theory approximation is inversely proportional to the electron scattering time. According to Mattheisen's rule, one can write the scattering rate as the sum over possible contributors, such as impurity scattering, electron-phonon scattering and electron-electron scattering. Dislocations (larger ones more so), would have a constant scattering power per *unit length*, as opposed to enclosed area [183, 184]. This is predicated on the idea that the electron-phonon scattering inside a relatively large loop (above ∼1nm diameter) is virtually zero [185].

Using the data from Figure 3.14, the logarithmic change in normalised dislocation line length between 700°C and 1100°C is calculated against the inverse of temperature to estimate an activation energy from the gradient of the linear fit, as seen in Figure 3.20. This yields $E_a = 1.34 \pm 0.2$eV.

One can also attempt to estimate an activation energy by looking at the isothermal bulk annealing data given in Figure 3.8. Assuming linear behaviour between the 4 and 8 hours data points for 800°C, the mean loop size at ∼6.5hours is equal to a 1-hour anneal. In other words, the loop growth rate at 950°C is ∼6.5 times larger than at 800°C, which yields an activation energy of 1.41 ± 0.1eV. The two approaches yield similar activation energies, within the error bars. The significance of these values are discussed later in Section **??** when compared to loop-impurity interaction energies found using molecular statics calculations.

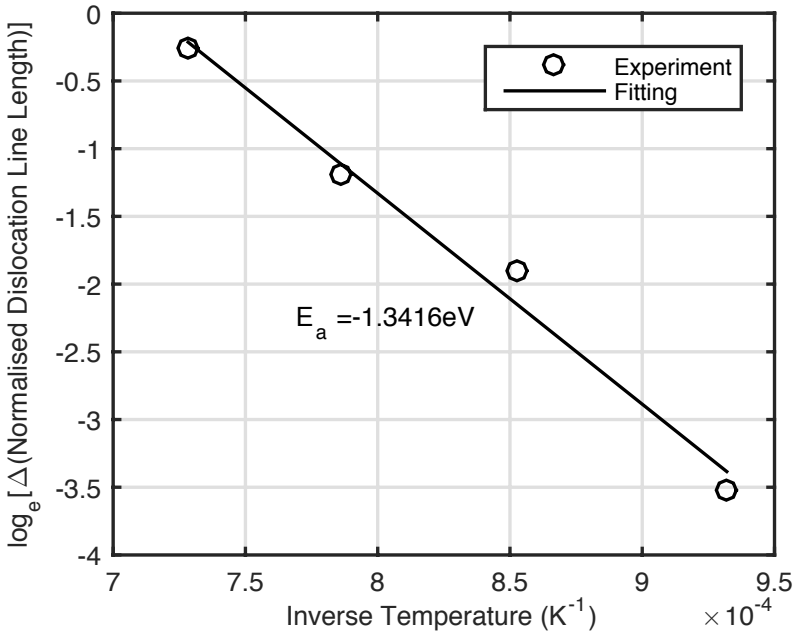

Figure 3.20: log(y) plot of the change in normalised dislocation line length versus inverse temperature, to estimate activation energy.

3.5.3 Estimation of climb mobility

Equilibrium positions of loops can be found using the isotropic elasticity approximation found in Hirth & Lothe [186]. These elastic interactions have been shown to be the driving force of loop re-organisation into chains via glide [187], with some coalescing due to direct collisions. These chains are clearly visible at ∼800°C in Figure 3.1.

One hypothesis for increased recovery above 800°C is the activation of dislocation climb. As shown in Figure 3.16, coalescence seems to occur when two adjacent loops which have reached their elastically-determined equilibrium positions through glide join together via climb, to form oblong loops. For isolated infinite straight dislocations, analytical expressions for climb mobility laws are available [188, 191], which allow estimation of typical timescales expected for climb motion, based solely on vacancies. Assuming a linearly varying dislocation velocity with applied force, climb velocity can be written as (Eq. 3.2).

$$v_{\mathrm{cl}} = M_{\mathrm{cl}} \left[F_{\mathrm{cl}} + F_{\mathrm{os}} \right] \tag{3.2}$$

where M_{cl} is the climb mobility, F_{cl} the climb force, and F_{os} the osmotic force. The osmotic force occurs when there is a vacancy supersaturation [191]. However, in the present analysis, it is considered negligible as large interstitial loops were not observed gradually shrinking through absorption of vacancies. The climb force F_{cl} is the projection of the Peach-Koehler force in the direction perpendicular to the dislocation glide plane and is given by $F_{\mathrm{cl}} = [(\boldsymbol{\sigma b} \times \boldsymbol{l}] \cdot \boldsymbol{n}$, where $\boldsymbol{\sigma}$ is the local stress, $\boldsymbol{b}$ the dislocation Burgers vector, $\boldsymbol{n}$ the climb direction, and $\boldsymbol{l}$ the dislocation line direction. For two infinitely long straight edge dislocations, the climb force reduces to Eq. 3.3, where $|\boldsymbol{r}|$ is the separation distance in the climb direction.

$$F_{\mathrm{cl}} = \pm \frac{|\boldsymbol{b}|^2 \mu}{2\pi(1-\nu)|\boldsymbol{r}|} \tag{3.3}$$

The climb mobility is then given by Eq. 3.4.

$$M_{\mathrm{cl}}(\theta) = \frac{2\pi D_v \Omega c_0^v}{kTb^2 \sin^2(\theta) ln(r_\infty / r_c)} \tag{3.4}$$

where Ω the atomic volume, θ the dislocation character [2], k the Boltzmann constant, T the temperature and r_c the inner core radius of the dislocation line. $D_v = D_v^0 \exp\left(\frac{U_v^m}{kT}\right)$, with U_v^m being the vacancy migration energy, D_v^0 the constant prefactor characterising vacancy diffusion, and $c_0^v = \exp\left[-(U_v^f - P\Delta V_v / kT\right]$, where U_v^f is the vacancy formation energy, and ΔV_v the associated relaxation volume. The vacancy migration and formation energies of tungsten, U_v^m and U_v^f, are 1.78 and 3.56eV respectively [160], and the vacancy diffusion prefactor is $\sim 1.5 \cdot 10^{-5}$ m$^2 \cdot$s^{-1} according to DFT studies [190]. μ is the shear modulus of tungsten, taken as 160GPa.

With this information, one can estimate dislocation climb mobility M_{cl} with varying temperature, and the climb force F_{cl} of two straight infinite edge segments with varying separation distance, and consequently a characteristic timescale, as shown

[2] $\theta = \frac{\pi}{2}$ for pure edge, and 0 for pure screw (capped at a maximum mobility)

in Figure 3.21.

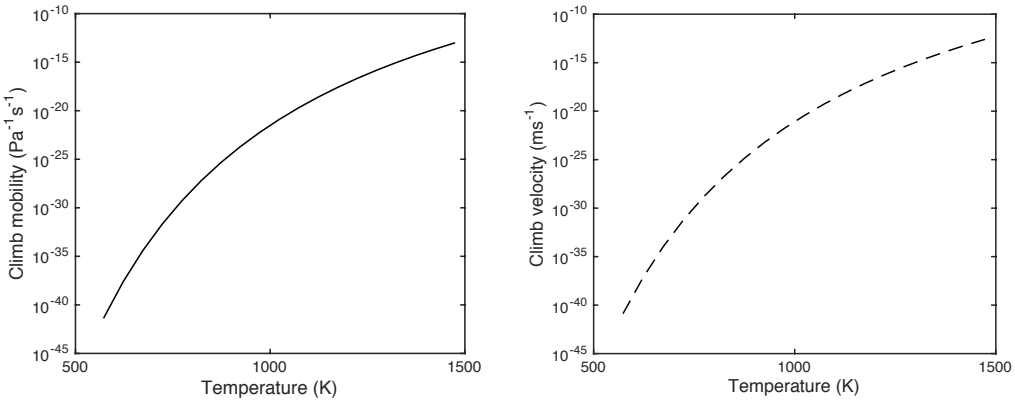

(a) Mobility **(b)** Velocity

Figure 3.21: (a) Bulk vacancy diffusion driven climb mobility in tungsten from Eq 3.4, (b) Climb velocity of straight infinite dislocation edges separated by 1nm distance, with climb force calculated from Eq 3.3.

With the above parameters, the climb mobility is extremely low, even for the highest temperatures and smallest segment separations. For example, at 1200°C two segments with 1nm separation would coalesce solely by bulk vacancy-mediated climb in ∼1hr, making this hypothesis unlikely based on the experimental observations reported here. It is possible the effect is a pipe diffusion mechanism, where point defects along the dislocation lines lead to a transfer of matter around the loops. This generates a conservative translation of the loop in its habit plane, a process known as self-climb or conservative climb [191]. The timescales of this process would be significantly faster, since diffusion of point defects along a dislocation core is higher than in the bulk [192].

3.5.4 Effect of impurities on dislocation loops

?? Impurities, such as carbon, have been shown to play an integral role in defect mobility in other BCC materials such as iron, even for nominally high purity specimens [187]. To relate concentration of impurities c, in atom per site units, near a defect to their concentration c_0 far away, we use equation 3.5, [137]:

$$c = \frac{c_0 \exp\left(-\frac{U}{k_B T}\right)}{1 + c_0 \left[\exp\left(-\frac{U}{k_B T}\right) - 1\right]} \tag{3.5}$$

where U is the energy of interaction between an impurity and an edge dislocation in tungsten. The main impurities found in the ultra-high purity (99.996%) tungsten used in the experiments reported here are carbon (C, 10ppm), phosphorous (P, <10ppm), silicon and oxygen (Si, O, <5ppm) [67]. The major impurity is therefore carbon. To calculate the interaction energy between a carbon atom and a dislocation loop, a molecular statics simulation was carried out using an interatomic potential for W-C systems derived by Chen et al. [193], based on the second-nearest-neighbour modified embedded-atom method (MEAM) scheme. This particular potential was chosen as opposed to others available (e.g. Tersoff potential from Juslin et al. [194]) as it was fitted to experimental values on the formation energy of interstitial carbon atoms, the migration energy of carbon atoms in bcc tungsten, lattice parameters, bulk modulus and cohesive energy of tungsten-carbide systems, based on previously developed MEAM potentials for pure tungsten [195] and carbon [196].

Using the molecular dynamics software LAMMPS [197], two $\langle 111 \rangle$ edge dislocations (of opposite line direction $\pm[11\bar{2}]$) were set-up and relaxed at 0K (grain orientation x=[111], y=$[1\bar{1}0]$, z=$[11\bar{2}]$; size: 12×40×14 lattice units), as shown in Figure 3.22.

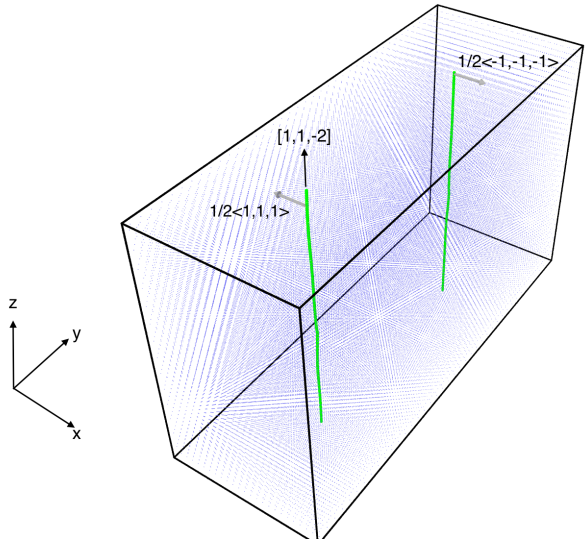

Figure 3.22: Simulation set-up, showing dislocation cores in green.

A carbon atom was introduced in the habit plane of the dislocations in octahedral sites, in a similar procedure as in [198], the system minimised using a steepest-gradient algorithm, and moved along the y-direction {1-10}. The final potential energy of the system and the position of the carbon interstitial was subsequently saved, and the procedure repeated for different initial carbon atom positions, to produce Figure 3.23. This yields a binding energy between the edge and carbon of $\sim$ 1.41eV (given by the potential well in Figure 3.23). This is very similar to the activation energy derived from the loss rate of dislocation line length in Section 6.2 (Figure 3.20).

Taking the trapping energy of the carbon atom to be the minimum in Figure 3.23, $\sim$-1.41eV, for a concentration of $c_0 = 10^{-5}$ (equivalent to 10ppm), the ratio of carbon concentration in thermodynamic equilibrium compared to the bulk near a $\frac{1}{2}\langle 111 \rangle$ edge dislocation can be derived (Figure 3.24). This shows that $c \approx 1$ up to 600-700°C, meaning that in thermodynamic equilibrium at such temperatures, carbon impurities are very likely to decorate defects such as dislocation loops, with the mobility of the loops being impeded by such an impurity atmosphere. At higher temperatures, for example at $\sim$1000°C, where from Figure 3.14 it can be seen that dislocation line density is substantially annealed away, carbon may play a less substantial role. In conclusion, it is possible that this is not the sole explanation for the observed defect recovery stage; however, the role of impurities, even for ultra-high-purity samples, cannot be ignored at lower temperatures, becoming less important only at high temperatures above Stage IV-V.

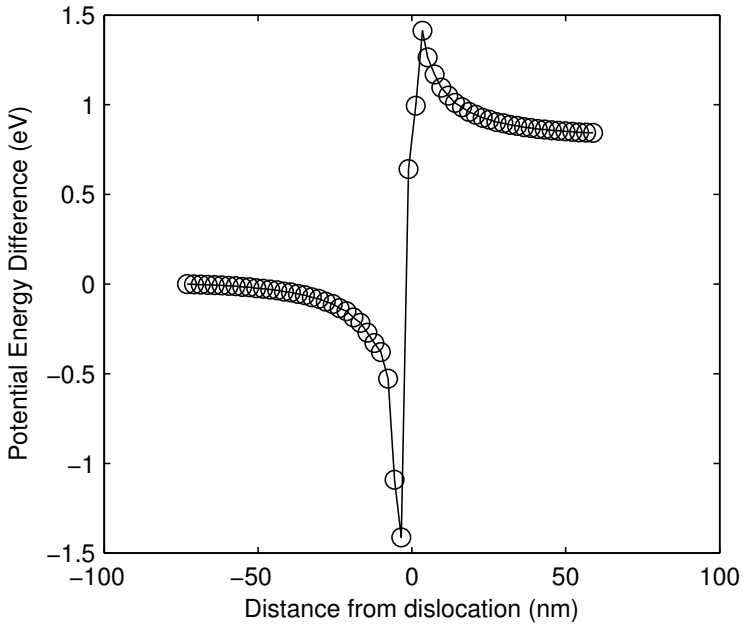

Figure 3.23: Variation of interaction energy between ⟨111⟩ edge dislocation and carbon interstitial with respect to distance of the interstitial to the dislocation, on the habit plane. A minimum can be seen at the edge of the line (where there is a tensile stress), where an interstitial impurity (producing a compressive stress field) will be most stable.

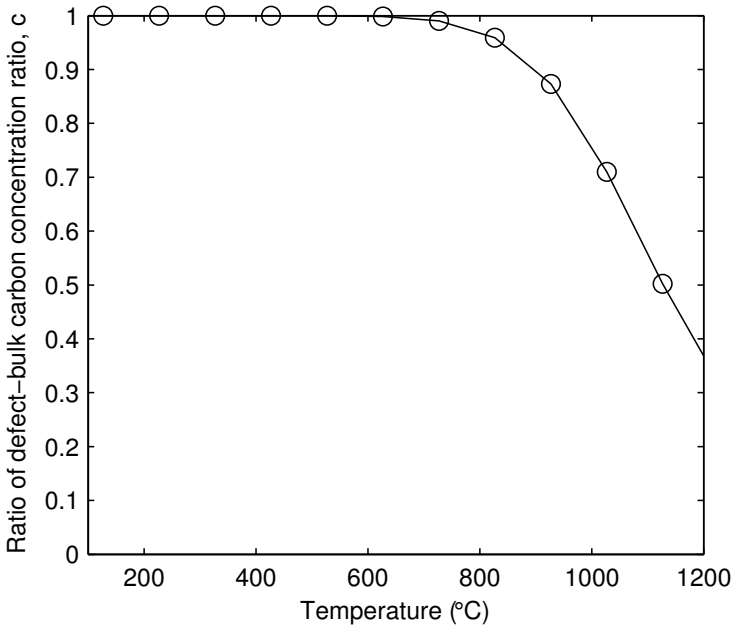

Figure 3.24: Ratio of carbon concentration near a ⟨111⟩ edge dislocation in thermodynamic equilibrium compared to bulk, at different temperatures, with a bulk concentration c_0 of 10ppm.

3.6 Summary

High temperature isochronal (1hour, 800-1400°C) and isothermal (1-8 hours) annealing of pure tungsten was carried out, followed by post-annealing characterisation. No **b**=⟨100⟩-type loops were found for loops above 2-3nm diameter, only ½⟨111⟩-type, of predominantly interstitial nature. Average loop size increased and loop density decreased with increasing temperature, with a particular acceleration above ∼950°C. Average loop diameter after 1 hour annealing was ∼ 5nm at 800°C (1hr) and ∼ 23nm at 1100°C. Virtually no dislocation defects were observed after annealing at 1400°C for 1 hour.

In situ annealing experiments up to 1200°C were also carried out, including dynamic temperature ramp-ups. These confirmed an acceleration of loop loss from 800°C. Small dislocation loops were observed hopping from 300°C, increasing in frequency from 500°C. By 800°C, loops had rearranged into loop "chains" or clusters. Increasing the temperature resulted in formation of larger irregular or oblong finger loops from coalescence of smaller loops in such chains. Above 1000°C, dislocation lines moved relatively freely, interacting with smaller dislocation networks and "sweeping" out damage. Small voids (∼ 2nm) were also observed at such high temperatures. The acceleration of loop loss at ∼ 1000°C may be related to "Stage V" annealing, as observed in previous resistivity recovery experiments on neutron-irradiated tungsten [126]. Voids were observed in all 1-hr anneals at 800°C, but were found to increase substantially in size (up to ∼4nm) and decrease in number density at 1400°C. An activation energy for the annealing of dislocation length was derived from the ramp annealing experiments, finding $E_a = 1.34 \pm 0.2$eV for the 700-1100°C range.

Carbon interaction energy with an edge dislocation of b=½⟨111⟩ was calculated using a semi-empirical MEAM W-C potential, and found to be ∼1.41 ±0.1eV. This similarity in activation energies suggests that the mobility and thermal diffusion of loops and dislocation lines are strongly mediated by impurities and solid solution particles not visible by TEM which decorate such dislocations. This may be related to "Stage IV" annealing, as observed in previous resistivity experiments on neutron-

irradiated tungsten [126].

In some instances, *conservative climb* of dislocation loops was observed in *in situ* annealing at high temperature ($\geq$900°C). However, the rates at which this process occured was found to be inconsistent with current models, suggesting a different kind of pathway. It is hypothesized this process might also be related to the accelerated coarsening of observed dislocation loops at high temperature.

Chapter 4

Experimental characterisation of tungsten: W+He dual beam irradiation damage

4.1 Introduction

This section will explore the effect of introducing He on radiation damage in tungsten. Data from *in situ* irradiations of ultra pure tungsten with conditions similar to the previous ex situ irradiations (500°C, 1.5dpa, 2MeV$^+$) will be presented and compared to experiments conducted with added helium.

The detailed experimental methods and conditions are detailed in Section 2.2.3 and in Table 2.5. For consistency, when referring to helium concentrations, we will use peak appm He quantities predicted by SRIM; if more details are required, such as concentration versus depth and appm/dpa versus depth, please refer to 2.2.3. In summary, four experiments are presented:

1. *In situ* mono beam irradiation of UHP tungsten with 2MeV W$^+$ at 500°C.

2. *In situ* dual beam irradiation of UHP tungsten with 2MeV W$^+$ and 10keV He$^+$ at 500°C. The peak He implanted is estimated at 1800 appm, equivalent to 1200 appm/dpa.

3. *In situ* dual beam irradiation of UHP tungsten with 2MeV W$^+$ and 10keV He$^+$ at 800°C. The peak He implanted is estimated at 1800 appm, equivalent to 1200 appm/dpa.

4. *In situ* dual beam irradiation of UHP tungsten with 2MeV W^+ and 20keV He^+ at 800°C, with a peak concentration of $4.5 \cdot 10^4$ He appm at a 100nm depth, equivalent to $2.5 \cdot 10^4$ appm/dpa.

From characterisation of the radiation damage we can gain insight both on the effect of helium and irradiation temperature.

4.2 Experimental results

4.2.1 Size and density distributions of dislocation defects versus irradiation and temperature conditions

Several micrographs for each stage were analysed, such as those in Figure 4.2 and 4.1. Defects were counted and sized, as explained in the methods section 2.4.3. The processed data is presented in Figures 4.3 to 4.5.

Figure 4.1 shows the effect on the defect microstructure of adding He, whilst keeping temperature and self-ion irradiation conditions constant. One can see, both in the kinematic bright field and weak-beam dark field images, an increase in the loop density when He is added. Furthermore, whereas in the single-beam case loops appear to occasionally form clusters and chains with denuded areas elsewhere, this is not so evident in the dual-beam case, which displays a more homogeneous distribution.

Figure 4.2 shows a characteristic area in weak beam dark field being irradiated by dual beam, at 800°C. Two things are noticeable: the effect of increasing dose over time and the effect of increasing temperature to 800°C on the damage microstructure. Firstly, the loop density increases with increasing dose levels of implanted 2MeV W^+, which is responsible for the overwhelming majority of cascades, starting from an undamaged sample (a). Secondly, when compared to Figure 4.1, one can observe that at an equivalent dose of $0.166 \cdot 10^{14}$ $W^{2+}cm^{-2}$, the damage microstructure at 500°C is characterised by a higher dislocation loop density than at 800°C.

Figure 4.3 gives quantitative values for loop density at increasing dose intervals for the first three experiments: mono-beam irradiation at 500°C, dual-beam irradiation at 500°C, and dual-beam irradiation at 800°C. The intervals are defined by the W^{2+} dose (the self-ion beam conditions are kept constant in all experiments), for consistency between single and dual beam cases. Qualitative observations made in Figure 4.1 and 4.2 are confirmed quantitatively here: increase of loop density when He is added, and a slower increase in loop density with dose in the 800°C irradiation

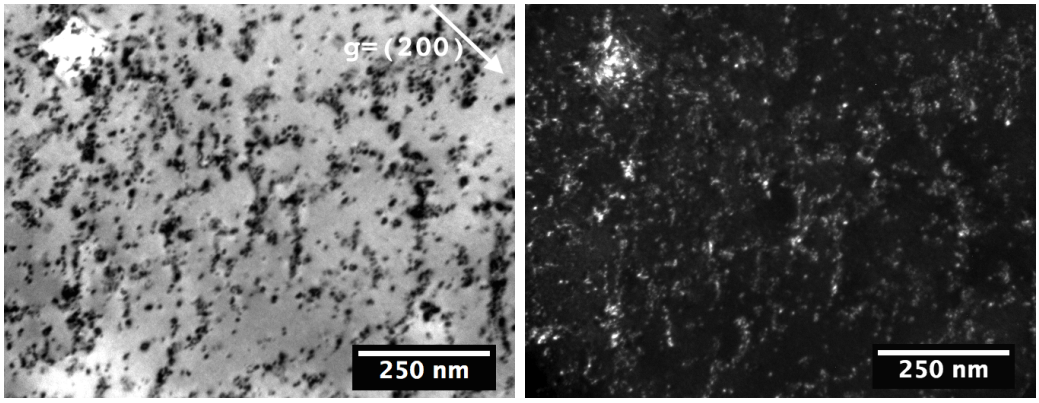

(a) No 10keV He^+ beam, kmbf **(b)** No 10keV He^+ beam, wbdf

(c) With 10keV He^+ beam, kmbf **(d)** With 10keV He^+ beam, wbdf

Figure 4.1: Example kinematic bright field and weak beam dark field micrographs for *in situ* irradiation of UHP tungsten with 2MeV W^+, with (c),(d) and without (a),(b) an additional 10keV He^+ beam. Sample temperature was 500°C in both cases, dose shown is 0.166 $\cdot 10^{14}$ $W^{2+}cm^{-2}$, which is the saturation level for both cases. Diffraction condition used throughout was $\boldsymbol{g}$=(200), 3-4$\boldsymbol{g}$.

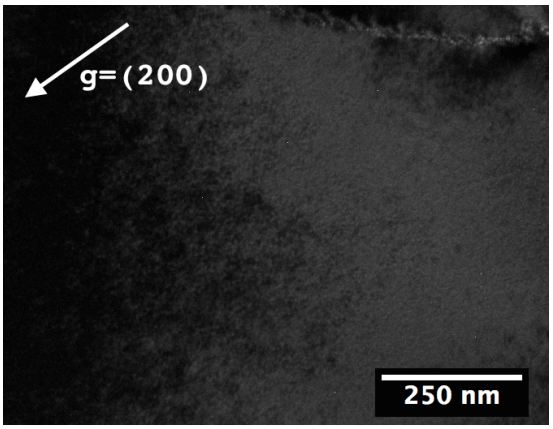

(a) Unirradiated

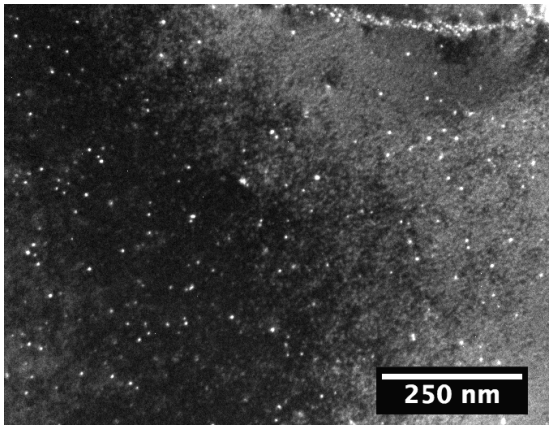

(b) $8.33{\cdot}10^{12}W^{2+}cm^{-2}$; $1.17{\cdot}10^{14}He^{+}cm^{-2}$

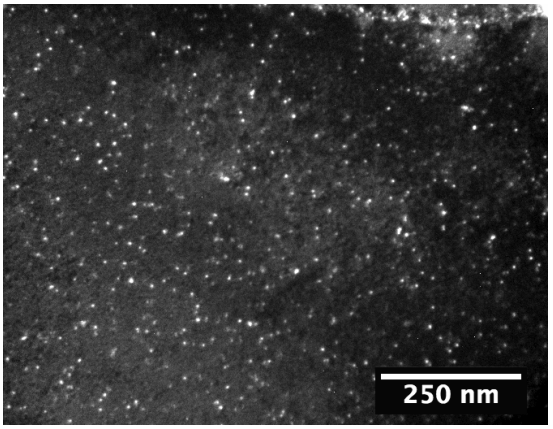

(c) $0.166{\cdot}10^{14}W^{2+}cm^{-2}$; $2.33{\cdot}10^{14}He^{+}cm^{-2}$

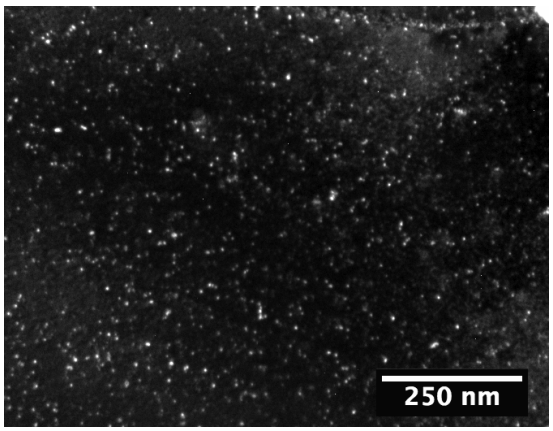

(d) $0.25{\cdot}10^{14}W^{2+}cm^{-2}$; $3.50{\cdot}10^{14}He^{+}cm^{-2}$

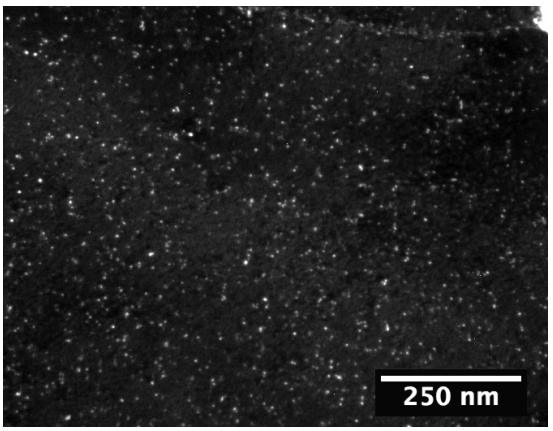

(e) $0.33{\cdot}10^{14}W^{2+}cm^{-2}$; $4.67{\cdot}10^{14}He^{+}cm^{-2}$

Figure 4.2: Example weak beam dark field micrographs at different dose levels for *in situ* irradiation of UHP tungsten with dual beam 2MeV W^{2+} and 10keV He^{+} at 800°C, with peak 1800 appm He. Diffraction condition used throughout was $\boldsymbol{g}$=(200), 3-4$\boldsymbol{g}$.

case up to a saturation at $0.33 \cdot 10^{14}$ $W^{2+}cm^{-2}$, as opposed to 500°C, which saturates at much lower doses of $0.083 \cdot 10^{14}$ $W^{2+}cm^{-2}$.

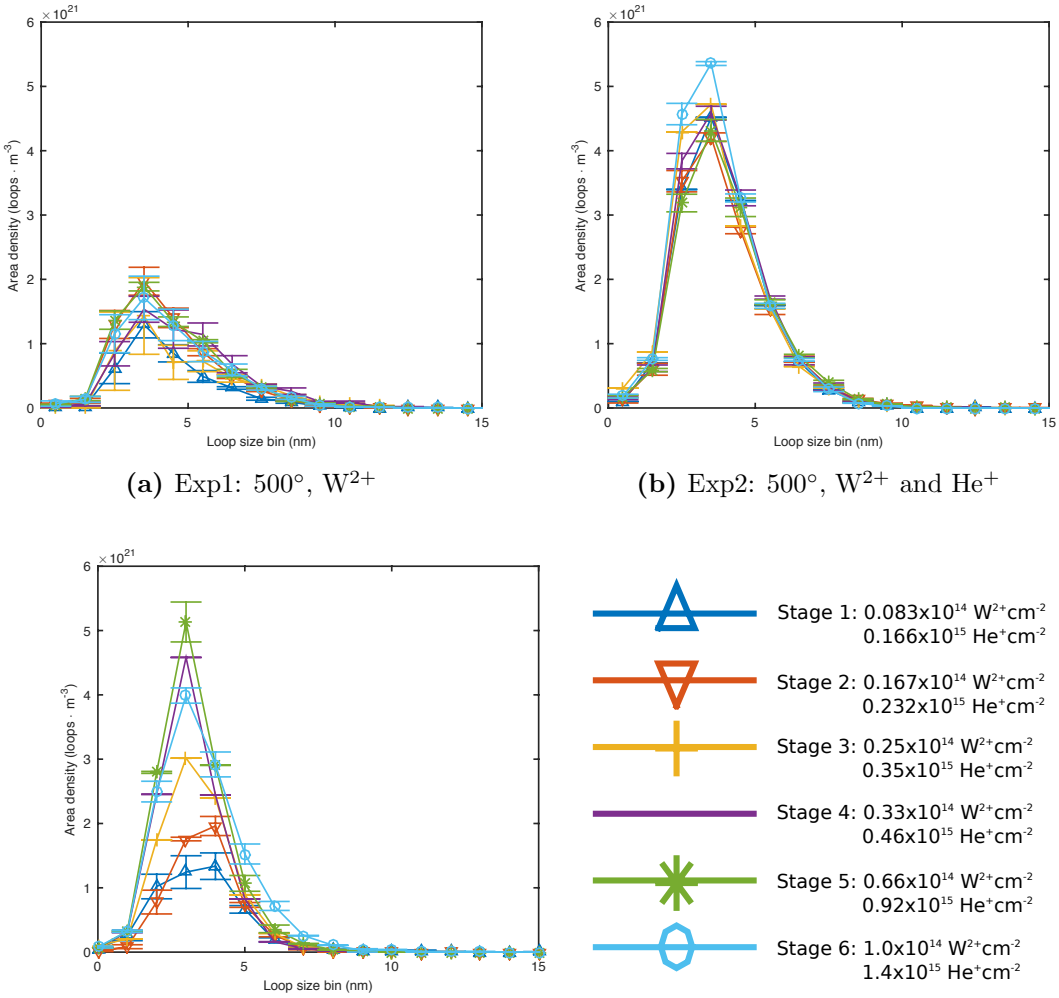

(a) Exp1: 500°, W^{2+}

(b) Exp2: 500°, W^{2+} and He^{+}

(c) Exp3: 800°, W^{2+} and He^{+}

(d) Legend

Figure 4.3: Size-density distribution of radiation damage loops observed at different W^{2+}-ion doses for (a) single W^{2+} beam at 500°C, (b) dual W^{2+} and He^{+} beam at 500°C, and (c) dual W^{2+} and He^{+} beam at 800°C. Diffraction condition used throughout was $\boldsymbol{g}$=(200), 3-4$\boldsymbol{g}$. Error bars are calculated from a 95% confidence interval. For all experiments, W^{2+} had an energy of 2MeV and a flux of $2.0 \cdot 10^{10}$ions $cm^{-2}s^{-1}$, resulting in a peak final 1.5dpa damage. For experiments (b) and (c), He had an energy of 10keV and a flux of $2.2 \cdot 10^{11}$ions $cm^{-2}s^{-1}$, resulting in a final peak 1800 appm He concentration.

4.2.2 Dislocation loop area versus versus irradiation and temperature conditions

Figure 4.4 shows the dislocation loop area versus dose for the first three experiments described in Section 4.1. Comparing (a) single-beam and (b) dual-beam conditions at identical temperatures, one can observe a doubling of the dislocation area when He is present. Furthermore, whereas damage saturation is reached almost immediately at the first dose interval ($0.083 \cdot 10^{14}$ $W^{2+}cm^{-2}$) for dual-beam, this occurs at $0.166 \cdot 10^{14}$ $W^{2+}cm^{-2}$ for single-beam, at a lower plateau.

When comparing (b) dual beam at 500°C and (c) dual beam at 800°C, one can observe that by increasing temperature, the damage saturation slightly decreases, and the irradiation dose necessary to reach such plateau is increased substantially, from $0.083 \cdot 10^{14}$ $W^{2+}cm^{-2}$ at 500°C to $0.66 \cdot 10^{14}$ $W^{2+}cm^{-2}$.

4.2.3 Dislocation loop diameter versus versus irradiation and temperature conditions

Figure 4.5 shows the mean dislocation loop diameter versus dose for the first three experiments described in Section 4.1. Whereas changing experimental conditions had a marked effect on loop number density or dislocation area, mean loop diameter seems relatively stable. When He is present, the average loop diameter appears smaller: 4.5nm for single-beam at 500°C, 3.9nm for dual-beam at 500°C, and 3.8nm for dual beam at 800°C, at the final $1.0 \cdot 10^{14}$ $W^{2+}cm^{-2}$.

4.2.4 Void size and density measurements

The dual-beam irradiated samples were also analysed for voids. While no voids or void-like features could be observed for the samples irradiated at 500°C, voids were visible at 800°C regardless of the amount of helium (1800appm or 45000appm). Void density and size measurements are reported in Table 4.1. At 800°C the average void size did not change appreciably with helium dose; however, from 1800appm to 45000appm the void density increased almost two-fold. Figure 4.6 shows over and

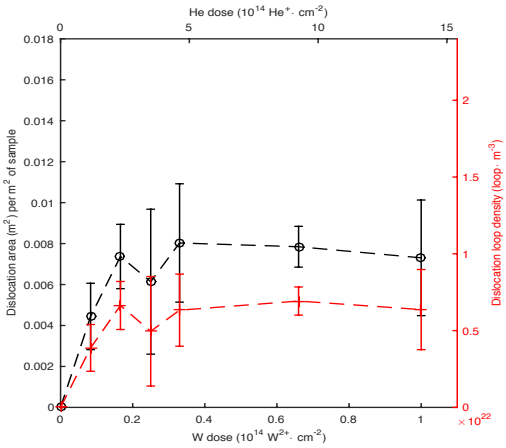

(a) Exp. 1: 500°, W^{2+}

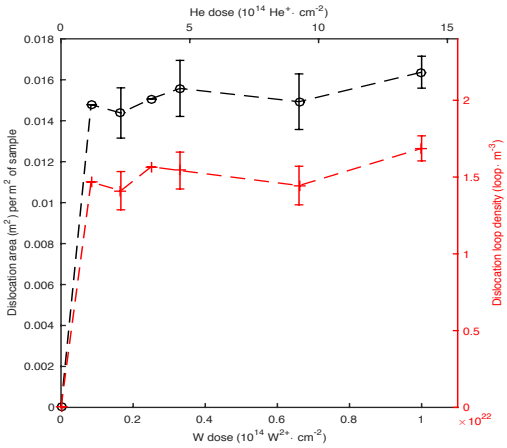

(b) Exp. 2: 500°, W^{2+} and He^{+}

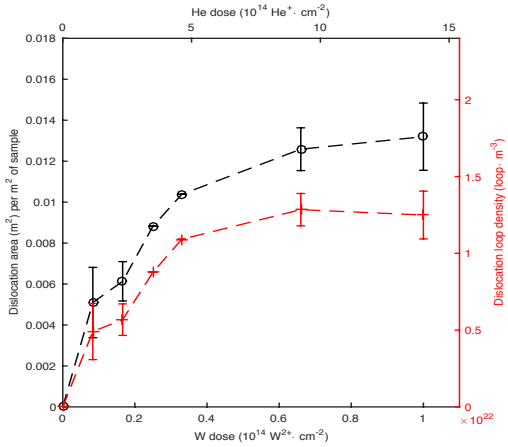

(c) Exp. 3: 800°, W^{2+} and He^{+}

Figure 4.4: Dislocation area and loop density versus W^{2+} or He^{+} dose for (a) single beam at 500°C, (b) dual beam at 500°C, and (c) dual beam at 800°C. Diffraction condition used throughout was $\boldsymbol{g}$=(200), 3-4$\boldsymbol{g}$. Error bars are calculated from a 95% confidence interval. For all experiments, W^{2+} had an energy of 2MeV and a flux of $2.0 \cdot 10^{10} W^{2+}$ $cm^{-2}s^{-1}$, resulting in a peak final 1.5dpa damage. For experiments (b) and (c), He had an energy of 10keV and a flux of $2.2 \cdot 10^{11} He^{+}$ $cm^{-2}s^{-1}$, resulting in a final peak 1800 appm He concentration.

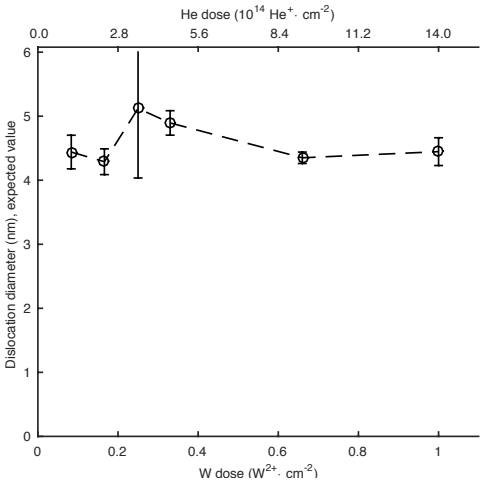

(a) Exp. 1: 500°, W^{2+}

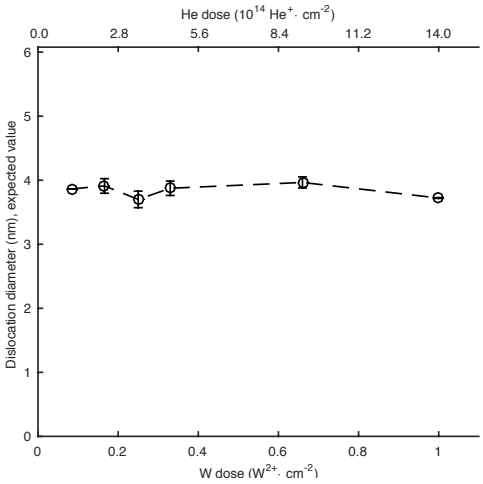

(b) Exp. 2: 500°, W^{2+} and He^{+}

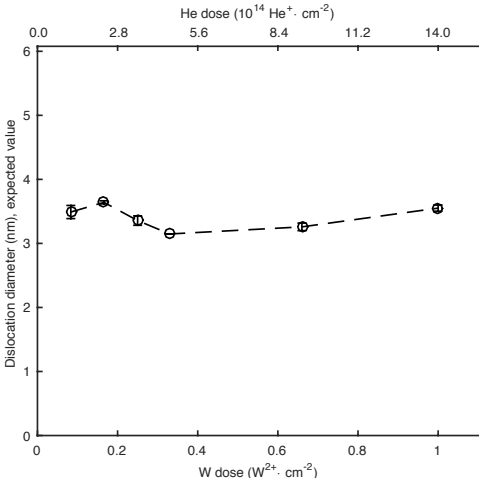

(c) Exp. 3: 800°, W^{2+} and He^{+}

Figure 4.5: Average dislocation loop diameter (nm) versus W^{2+} or He^{+} dose for (a) single beam at 500°C, (b) dual beam at 500°C, and (c) dual beam at 800°C. Diffraction condition used throughout was $\boldsymbol{g}$=(200), 3-4$\boldsymbol{g}$. Error bars are calculated from a 95% confidence interval. For all experiments, W^{2+} had an energy of 2MeV and a flux of $2.0 \cdot 10^{10} W^{2+}$ $cm^{-2}s^{-1}$, resulting in a peak final 1.5dpa damage. For experiments (b) and (c), He had an energy of 10keV and a flux of $2.2 \cdot 10^{11} He^{+}$ $cm^{-2}s^{-1}$, resulting in a final peak 1800 appm He concentration.

underfocus high resolution micrograph pairs of the two irradiation conditions where voids were visible.

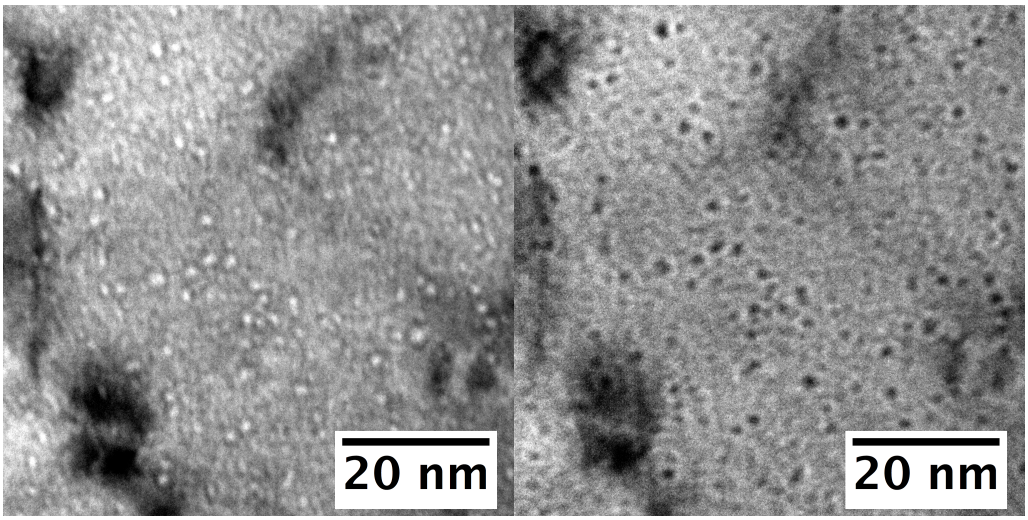

(a) 1800appm, 800°C, underfocus -800nm **(b)** 1800appm, 800°C, overfocus +800nm

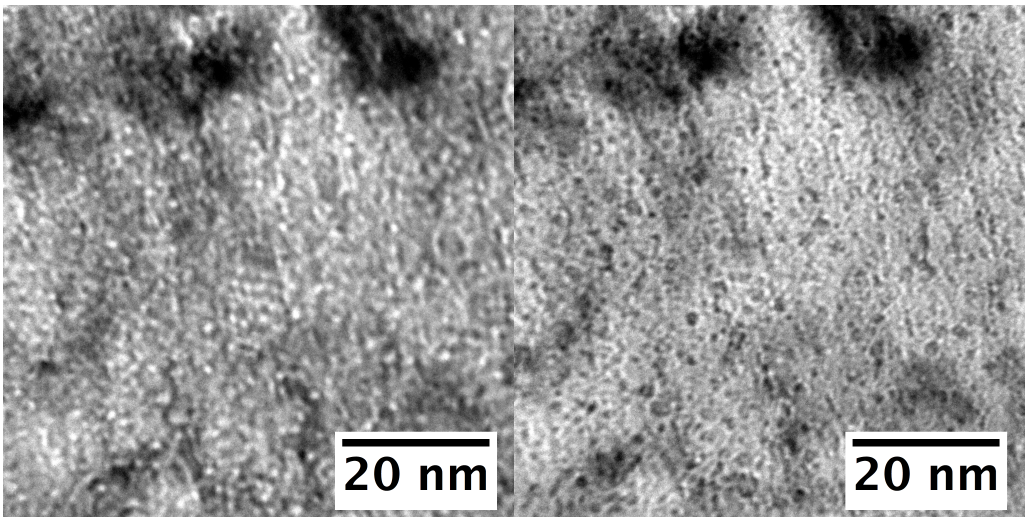

(c) 45000appm, 800°C, underfocus -800nm **(d)** 45000appm, 800°C, overfocus +800nm

Figure 4.6: Over- and underfocus micrographs of tungsten irradiated under dual-beam W^{2+} and He^{+}, up to (a-b) 1800appm and (c-d) 45000appm, at 800°C. One can observe densely packed void-like features in the over- and underfocus micrograph pairs, changing from black to white.

	Density (voids·m^{-3})	Diameter (nm)
1800appm, 800C	8.68e+23	1.07±0.04
45000appm, 800C	1.53e+24	0.84±0.02

Table 4.1: Density and size of void-like features observed in JANNuS dual-beam experiments. (a-b) 1800appm at 800°C, (c-d) 45'000appm at 800°C. No such defects were observed in the samples irradiated at 500°C.

4.3 Discussion

4.3.1 Presence of helium

To explain the experimental observations, it is useful to briefly discuss the effect of He on dislocation formation and mobility. Firstly, from previous studies [199, 200] on α-iron, it appears the presence of helium atoms favours the nucleation of more dislocation loops during irradiation. Secondly, from molecular simulations detailed later in this chapter (Section 4.3.4), helium is also energetically attracted to pre-existing loops and it clusters preferentially around their bounding dislocations (in the case of interstitial-type). Finally, the concept of a Cottrell atmosphere [201], suggests that dislocations in BCC materials are pinned by interstitial impurities such as nitrogen, inhibiting their mobility.

Comparing experiments 1 and 2 in Table 2.5 (irradiation at 500°C with and without the additional He^+ beam), one observes several main things:

1. The damage saturation level, given by the observable loop density, substantially *increases* ($\sim$2.5×) when the material is irradiated with dual W^{2+}+He^+ as opposed to single W^{2+} irradiation, shown in Figure 4.3 (a)-(b). This is unlikely to be due to differences in sample thickness since both imaged areas are $\sim$ 100nm in depth (estimated from thickness fringes). This is also evident qualitatively from the micrographs in Figure 4.1.

For mono-beam W^{2+} irradiation at 500°C the total loop density ($\sim 1.0 \cdot 10^{15}$ loops·m^{-2}) is substantially lower than for the dual-beam scenario at an identical temperature ($\sim 2.8 \cdot 10^{15}$ loops·m^{-2}), as shown in Figure 4.4 (a)-(b). This observation is confirmed by measuring the total dislocation area at end dose: mono-beam irradiation yields an average defect area of $\sim$0.8% in micrographs, as opposed to $\sim$1.6% for the dual-beam case, also shown in Figure 4.4(a)-(b), and also by looking at peak dislocation loop densities in Figure 4.3(a)-(b). The example micrographs in Figure 4.1 also suggest a less homogeneous distribution of dislocation defects when helium is *not* present, with dislocation chains similar to those observed in bulk

irradiation and annealing.

The fact that more dislocation loops exist in the sample when He is present for equivalent dose and temperature conditions (an observation also found in sequential [199] and simultaneous [200, 202] dual-beam irradiation in α-iron) can be explained by several mechanisms: firstly, the presence of He may favour the initial nucleation of a dislocation loop. A possible mechanism may be helium-vacancy complexes trapping self-interstitial atoms and acting as nucleation sites. *Lucas et al* [203] have shown through MD that helium indeed favours the formation of interstitial clusters in displacement cascades, which are the seed for a I-type dislocation loop. A second (complimentary) explanation, is related to the loop-He interactions *after* the creation of dislocation loops. If helium reduces loop mobility, leading to fewer loops gliding and annihilating, the density will be higher. This reduction in loop mobility is supported by the molecular dynamics simulations shown here, but also by dual-beam experimental observations *Brimbal et al* [200] also performed at JANNuS in iron, and MD simulations by *Ventelon et al* [204] also in bcc-iron.

2. The average loop diameter is smaller (3.9nm instead of 4.5nm at 500°C) when He is present, as shown in Figure 4.5 (a)-(b). Also, a sharper peak in the size distribution (around ∼3nm) can be observed when He is present, shown in Figure 4.3 (a)-(b).

Although there is an experimental and modelling agreement (here and in the literature) on the effect of He on 1) increasing the dislocation density, and 2) reducing dislocation loop mobility, there is disagreement on the effect on size: the study by *Brimbal et al* [200] observes an *increase* in average loop size from mono- to dual-beam irradiation. From Figure 4.5(a)-(b) for a peak 1800 appm concentration, we observe the opposite: a slight *decrease* (from 4.5 to 3.9nm at final dose) in average size from mono- to dual-beam. *Brimbal et al* argued that the size increase was related to the reduced loop mobility, allowing loops to reside in the thin foil longer and grow via absorption of interstitials from cascades. The argument on mobility affecting size can however be reversed: loops can grow not only via an Orowan

coarsening process, but also by loop-loop interactions. A decrease in mobility would lead to less loop-loop interactions, thereby giving a denser dislocation structure with smaller loops (as observed in Figure 4.5). The absolute size of dislocation loops may play a role in which mechanism is favoured: dislocation loop diameters in *Brimbal et al* [200] were an order of magnitude larger (∼40nm) than in the experiments here (∼3nm) in tungsten. Coarsening of loops due to He is only observed in this thesis for much higher He doses compared to [200] (peak 45000 appm concentration) suggesting the discrepancy might be related to specific material and irradiation conditions (or uncertainty in measurement error for nano-sized loops). These conditions are reviewed in Section 4.3.3.

3. The W^{2+} irradiation dose at which dislocation loop saturation is reached is *lower* when He is also present (0.086 instead of 0.166 $\cdot 10^{14}$ $W^{2+}cm^{-2}$), shown in Figure 4.4 (a)-(b).

This observation is in agreement with claims by *Arakawa et al* [199] that helium favours the nucleation of dislocation loops[1]. In [199] it was found that for equivalent dpa levels, defect density using He^+ was orders of magnitude greater, given that the total quantity of Frenkel pairs from cascades upon creation is constant between the two experiments (since the additional $10keV$ He^+ creates negligible levels of Frenkel pairs compared to 2MeV W^{2+} ions as verified by SRIM calculations).

Loop concentrations for the mono-beam *in situ* irradiation are only slightly lower than in the bulk irradiation results in Chapter 3, meaning that the presence of two surfaces acting as defect sinks in the *in situ* irradiation has a limited effect on defect density within a ∼100nm thick tungsten sample at 500°C.

Unfortunately it was difficult to extract the loop nature of the observed defect population post-irradiation due to the high dose and energies involved. *Arakawa et al* [199] find that for α-Fe the dislocation loops are preferentially of interstitial type. If a future study were repeated, a lower dose below the damage saturation level

[1]Such experiments were conducted on α-iron, using high energy electron or He^+ irradiations.

($8.33{\cdot}10^{12}W^{2+}cm^{-2}$) would be preferable for the purpose of loop nature identification.

4.3.2 Temperature variation

Comparing experiments 2 and 3 in Table 2.5 (irradiation at 500°C and 800°C with dual irradiation), one observes three main things:

1. To reach observable defect saturation, a much higher dose (1.0 instead of 0.086 $\cdot 10^{14}$ $W^{2+}cm^{-2}$) is required in the higher temperature 800°C case, as shown in Figure 4.4 (b)-(c).

Also, the defect saturation plateau is slightly lower at the higher temperature (1.3% instead of 1.6% of observable area), although it may arguably be within the measurement uncertainty levels.
The impact of increasing temperature on increasing the critical dose for damage saturation to occur is very clear, quantitatively from the processed data and qualitatively from micrographs in Figure 4.2. This is perhaps unsurprising, since a higher temperature causes a higher defect mobility, which in turn implies an increased likelihood of Frenkel pair annihilation and defect clusters diffusing to sinks (like the free surfaces). However, on increasing the sample temperature by 300°C (modest in comparison to the melting point of tungsten and by fusion reactor standards), the saturation dose increases by almost 12×.

2. The average diameter for dislocation loops is approximately the same at both temperatures (3.6-3.8nm), although there appears to be a small variation through the irradiation stages for the 800°C case, shown in Figure 4.4 (b)-(c).

The fact that the average diameter of dislocation loops at $1.0 \cdot 10^{14}$ $W^{2+}cm^{-2}$ is approximately equivalent for both 500°C and 800°C is reasonable, as bulk annealing to 800°C for ∼1hour (approximately the time to reach the required dose) yielded

only a slight increase in average loop diameter starting from a dislocation structure irradiated at 500°C (without the additional helium). Taking into account measurement uncertainties, one can say that the average dislocation size does not appreciably change with dose (Figure 4.5(c)). Small variations in the $\boldsymbol{g}$-vector excitation can change the observed size of a loop. During an *in situ* experiment involving high-energy irradiation and elevated temperatures, such small variations in imaging conditions (and foil deformations) are thus likely.

3. At 800°C (Figure 4.3(c)), dislocation loop density increases gradually with dose for all loop sizes, with $> 5nm$ loop densities increasing appreciably only at the highest dose level.

4.3.3 appm variation

The final experimental variation involved increasing the He dose (practically, this was achieved by increasing the helium dose rate, see Table 2.5) to as high levels as possible using the JANNuS equipment, from *peak* levels of 1800 appm (1200 appm/dpa) to 45 000 appm (25 000 appm/dpa), The motivation behind this was to see if voids could be observed, and whether high helium doses would change the damage morphology.

Figure 4.7 shows the damage microstructure at progressively higher W^{2+} doses, whilst being also irradiated by 20keV He^+ at $2.2 \cdot 10^{12}$ He·cm^{-2}s^{-1}. For low doses, shown in Figure 4.7(a), the dislocation structure appears similar to previous lower He fluence experiments, shown in Figure 4.2(b), with relatively homogenous distribution of isolated dislocation loops within a defined size distribution. In later stages of the irradiation, Figure 4.7(e-h), the dislocation loops coarsen and gradually turn into a complicated and highly dense dislocation network, which is difficult to quantitatively assess and characterise. A similar coarsening effect was observed experimentally by *Yi et al* [205], where pure tungsten irradiated to 1.5dpa by 2MeV W^+ ions at 500°C was subsequently exposed to high doses of 10keV He^+ ions at high temperatures. These experiments, conducted at Shimane University with Prof.

Arakawa were chosen as a baseline for conditions chosen here, conducted at JAN-NuS, where possible.

In addition to the interaction between dislocation loops and helium, increasing helium concentration causes the appearance of void-like features (presumably filled with helium) that are within the resolution of the TEM (> 1nm); these are characterised in Section 4.2.4.

Relation to fusion relevant conditions

Hydrogen and helium accumulation from neutron transmutation in tungsten, based on a fusion 14MeV neutron spectrum, is projected to be minimal in a reactor, at 76 H appm/5yrs and 33 He appm/5yrs production [19], or approximately ∼2 He appm/dpa and ∼1 He appm/dpa [21]. In ITER, fluxes of H+He from the plasma of $1.0 \cdot 10^{20}$ ions $cm^{-2}s^{-1}$ are projected, with approximately 95%H, and 5%He. Helium fluxes on divertor materials would therefore be in the order of $5.0 \cdot 10^{18}$ He $cm^{-2}s^{-1}$, impinging at low energies (∼50eV) [206, 102]. Even assuming a fractional pickup of the plasma ions [105, 207], the plasma-facing tungsten would be exposed to and be injected with orders of magnitude higher quantities of He than tested in these experiments. Helium is strongly bound to itself if in solid solution in tungsten and thus has the tendency to form helium clusters (and bubbles) diffusing less readily than hydrogen in tungsten [208, 209]. As a consequence, diffusion depths of hydrogen into tungsten are in the order of milimeters, and ∼1μm for helium [208] for operating timescales.

The high He fluxes and fluences present in a fusion reactor are impossible to probe in *in situ* transmission electron microscopy. However, plasma exposure experiments more close to operating conditions on UC-PISCES and other linear plasma devices show the formation of complex surface defects such as bubbles, blisters and *fuzz* [206], as shown in Figure 4.8. It is therefore very likely that high-dose He effects strongly dominate over radiation damage effects for the first few microns of plasma facing components (such as tungsten divertor tiles). For a bulk component, radiation

damage effects, in the form of dislocation damage production and embrittlement, transmutation and radiation-enhanced segregation, are likely to dominate.

4.3.4 Molecular statics: quantifying binding energy of He to dislocation loops in tungsten

To assess the attraction of helium to dislocations specifically in tungsten, molecular statics was employed. Using the molecular dynamics software LAMMPS [197], W-W and He-W potentials developed by *Juslin et al* [210], ∼3nm radius dislocation loops of either $\frac{1}{2}\langle 111\rangle$ or $\langle 100\rangle$ were set-up and relaxed at 0K. For the $\frac{1}{2}\langle 111\rangle$, the grain orientation was x=[111], y=[$1\bar{1}0$], z=[$11\bar{2}$]; size: 22×40×24 lattice units). For the $\langle 100\rangle$, the grain orientation was x=[100], y=[010], z=[001]; size: 30×30×30 lattice units) A helium atom was introduced in the habit plane of the dislocations in octahedral sites, in a similar procedure as in [198], the system using a steepest-gradient algorithm, and moved along the x and y-direction, such that an energy landscape through the loop could be plotted (the system was re-minimised after each move). The final potential energy of the system and the position of the He interstitial were subsequently saved, and the procedure repeated for different initial helium atom positions, to produce Figure 4.9. This yields a binding energy between a $\frac{1}{2}\langle 111\rangle$ loop and helium of $\sim$ 2.0eV (given by the potential well in Figure 4.9), and $\sim$ 2.61eV for a $\langle 100\rangle$ loop.

The potential well for the $\frac{1}{2}\langle 111\rangle$ is less than the $\langle 100\rangle$ loop. This is consistent with the notion that a $\langle 100\rangle$ dislocation loop causes a larger lattice misfit in the material than a $\frac{1}{2}\langle 111\rangle$.

4.3.5 Molecular dynamics: helium clustering around dislocation loop in tungsten

Molecular dynamics simulations were conducted to simulate a tungsten thin film containing a dislocation loop being irradiated with low energy He atoms. The dislocation loop structure chose had a ∼3nm diameter, equivalent to the mode of the

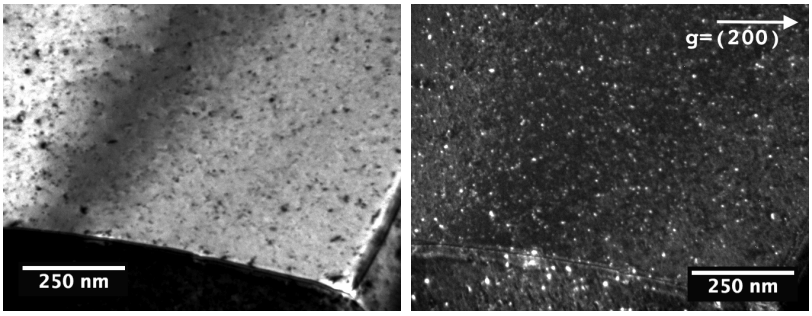

(a) $0.166{\cdot}10^{14}W^{2+}cm^{-2}$, $63.3{\cdot}10^{14}He^{+}cm^{-2}$, kmbf **(b)** $0.166{\cdot}10^{14}W^{2+}cm^{-2}$, $63.3{\cdot}10^{14}He^{+}cm^{-2}$, wbdf

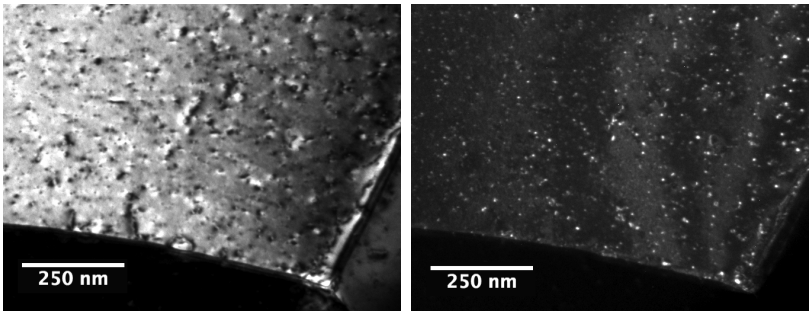

(c) $0.33{\cdot}10^{14}W^{2+}cm^{-2}$, $126.6{\cdot}10^{14}He^{+}cm^{-2}$, kmbf **(d)** $0.33\ {\cdot}10^{14}\ W^{2+}cm^{-2}$, $126.6{\cdot}10^{14}He^{+}cm^{-2}$, wbdf

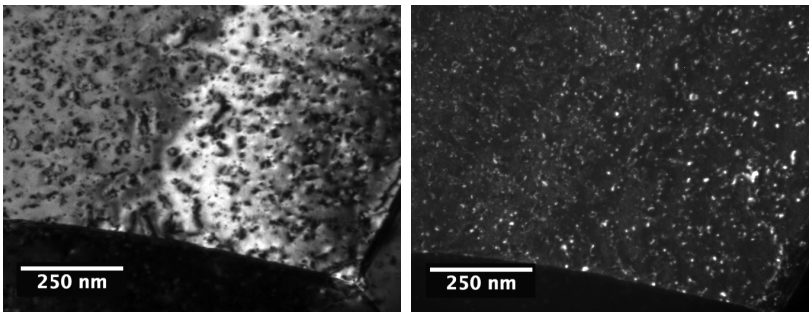

(e) $0.66{\cdot}10^{14}W^{2+}cm^{-2}$, $253.3{\cdot}10^{14}He^{+}cm^{-2}$, kmbf **(f)** $0.66{\cdot}10^{14}W^{2+}cm^{-2}$, $253.3{\cdot}10^{14}He^{+}cm^{-2}$, wbdf

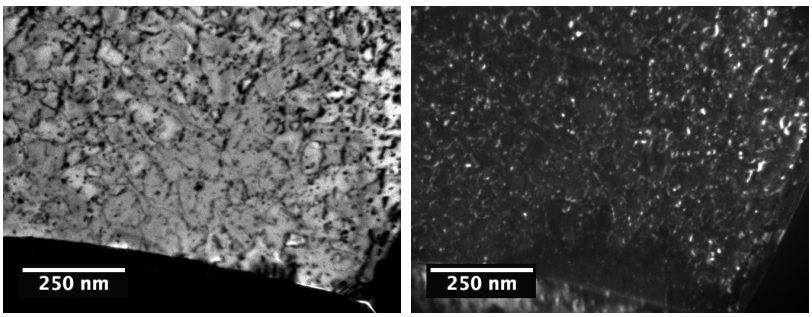

(g) $1.0{\cdot}10^{14}W^{2+}cm^{-2}$, $380{\cdot}10^{14}He^{+}cm^{-2}$, kmbf **(h)** $1.0{\cdot}10^{14}W^{2+}cm^{-2}$, $380{\cdot}10^{14}He^{+}cm^{-2}$, wbdf

Figure 4.7: Example kinematic bright field and weak beam dark field micrographs for *in situ* irradiation of UHP tungsten with 2MeV W^{+} and 20keV He^{2+} at different doses for peak 45000appm He. Sample temperature was 800°C. Diffraction condition used throughout was g=(200).

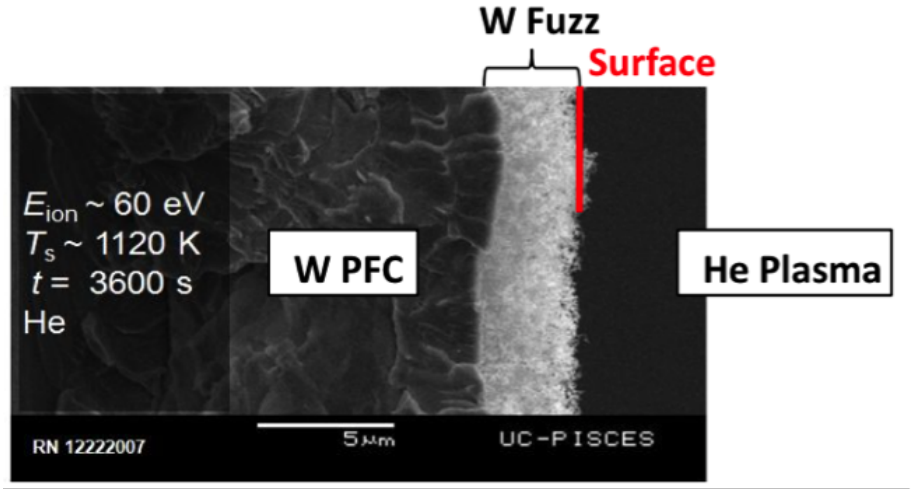

Figure 4.8: Formation of microns thick tungsten fuzz on plasma facing component after 1hr He plasma exposure. Image taken from Ref [206].

size distribution in experiments in Figure 4.3. Briefly, the simulation procedure was:

i Set up of the un-irradiated thin film section.

For a thin film containing a $\frac{1}{2}[111]$ loop, the rectangular simulation box chosen had an orientation of $\bar{x} = [111]$, $\bar{y} = [1\bar{1}0]$, and $\bar{z} = [11\bar{2}]$, and a size of 30×36×98 lattice units, giving a ∼16.5×16.2nm surface area with ∼70nm thickness (broadly similar to a tungsten TEM foil). The x- and y-directions were fully periodic, whereas the z-direction had free surface boundary conditions. The total number of W-atoms simulated was ∼1.2 million, requiring substantial computational resources.

ii Introduction of $\frac{1}{2}[111]$ loop, energy minimisation and thermalisation to 900K.

This procedure is similar to that explained later in Section 6.3.1. The orientation chosen was such that the loop's Burgers vector would not intersect with the free surfaces, preventing the possibility of the loop being absorbed by the surfaces through glide, instead moving diffusively solely in the x-direction. The atoms at the surface opposite the irradiation were kept immobile, to prevent drift of the sample and improve the results of the defect identification algorithm, which works from a reference perfect lattice.

iii Implantation of He atoms with a flux of $\sim 3.6 \cdot 10^{26}$ He·m^{-2}s^{-1}.

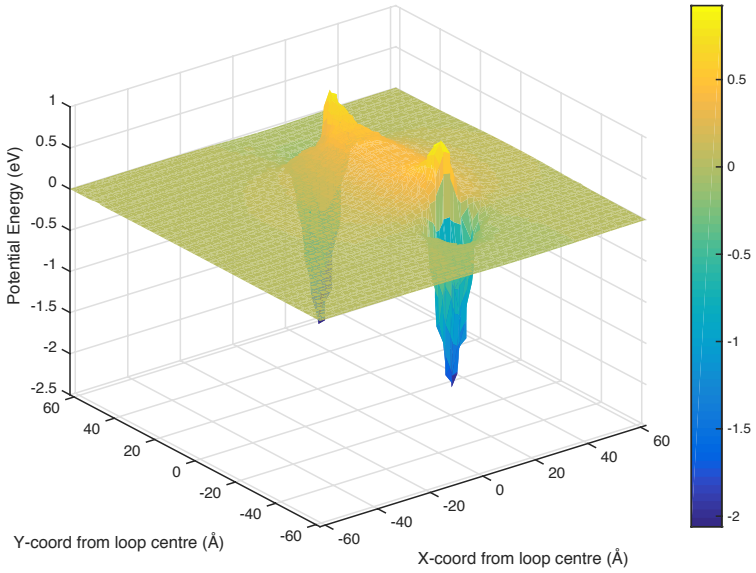

(a) $\frac{1}{2}\langle 111 \rangle$

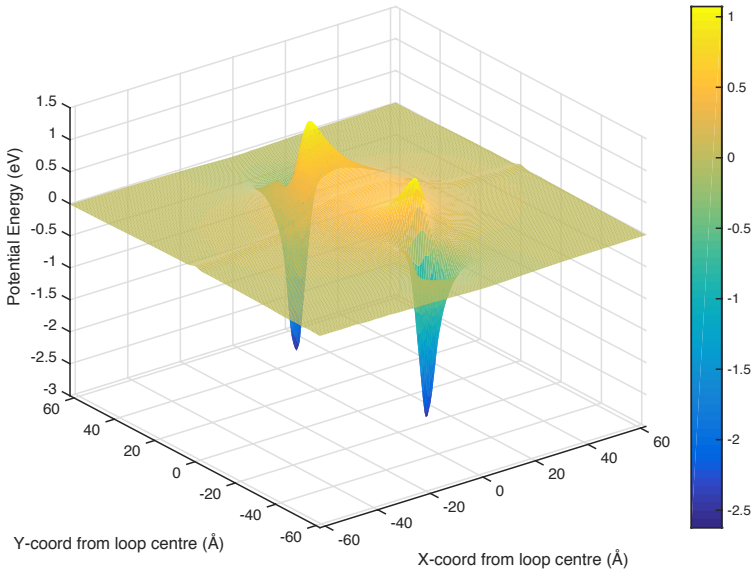

(b) $\langle 100 \rangle$

Figure 4.9: Variation of interaction energy between ∼6nm diameter dislocation loop (of either $\frac{1}{2}\langle 111 \rangle$ or $\langle 100 \rangle$ Burgers vector loop) and helium interstitial with respect to distance of the latter to the dislocation centre. A minimum can be seen at the edge of the loop (where there is a tensile stress), where an interstitial impurity (producing a compressive stress field) will be most stable. The inner part of the loop has a positive potential energy, meaning it is energetically unfavourable for the He to be here.

Each implantation was initiated at a random location over the surface. Following an implantation, the simulation was progressed for 10ps and temperature re-calibrated to 900K. Initially, the implantation was achieved by assigning an He^+ atom above the surface with a 500eV kinetic energy (similar to He energies in plasmas), moving perpendicularly towards the free surface. Although this worked flawlessly, it required substantially reduced time-steps (hence increased computational expense) in the deceleration stage of He into the thin film. To increase the simulation efficiency and achieve larger appm concentrations, the He atoms were randomly inserted into the domain with *thermal* energies, sampling a predetermined depth probability distribution. This implantation depth distribution can be estimated from SRIM, or more accurately from molecular dynamics (which accounts for crystallography).

Although such molecular dynamics simulation does not perfectly replicate the experimental conditions in Table 2.5 for the dual-irradiation experiments presented here (MD is constrained to higher fluxes, lower irradiation energies, and lower appm doses), observations were consistent with conclusions based on experimental observations here and elsewhere [206, 200, 107, 100, 102]:

1. Helium is strongly bound to itself when in solid solution in tungsten, and will thus form clusters (the density of these clusters increases closer to the surface), as shown in Figure 4.10. These clustering sites are observed as being seeds seeds for larger macro-scale defects such as bubbles (and potentially blisters and fuzz) with increasing helium doses.

Clusters grew in size during the implantations, as in other studies [208, 211, 212, 106]. The initiating mechanism for helium cluster formation was generally an interstitial cluster spontaneously forming in the bulk tungsten, when migrating He atoms came close enough to one another. This is essentially a probabilistic process. This interstitial seed would then turn into a substitutional cluster via the ejection of a tungsten atom near the cluster, when the helium cluster contained a large enough number of He atoms. The observed growth mechanism of substitutional clusters was by direct

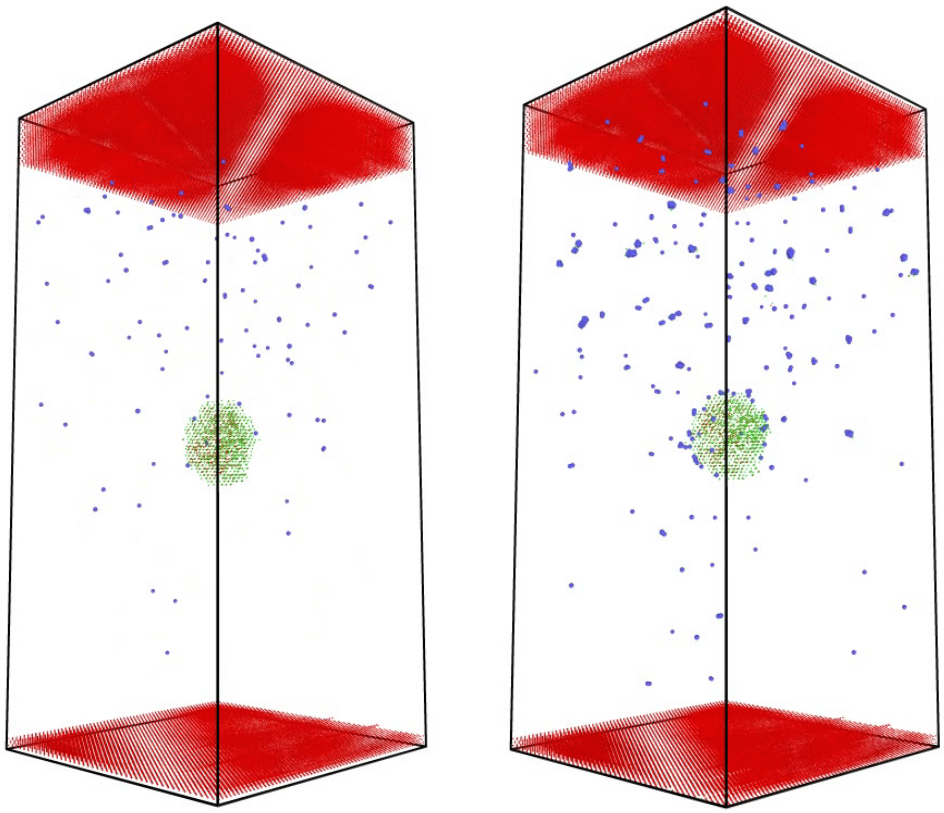

(a) ∼200 He appm **(b)** ∼500 He appm

Figure 4.10: Snapshots of molecular dynamics simulation at 900K of He injection (from top surface) in thin film containing $\frac{1}{2}\langle 111\rangle$ dislocation loop of ∼6nm diameter. He can be observed clustering preferentially at dislocation edge and also forming clusters. Top and bottom red areas are empty (free surfaces), blue atoms are helium, and green atoms are interstitials of dislocation loop.

absorption of He ions. Presumably, this increases the pressure of the bubble inside the cluster allowing it to displace further bulk tungsten atoms and grow in size.

2. The simulations confirmed the tendency of helium to cluster around dislocation loops (as suggested by the calculated binding energies), acting as pinning sites, as shown in Figure 4.11.

   Experimental observations in α-iron [200] showed He bubbles forming *inside* interstitial-type dislocation loops. This was not observed in tungsten in the experiments of Section 4.1, where void-like features were observed exclusively outside the loop regions, nor in the molecular dynamics simulations presented here. According to molecular statics simulations in Figure 4.9 it is not energetically favourable for He atoms to do so (at least for <6nm loops). Intuitively, the inner region of a I-type loop experiences a compressive stress in relation to the bulk (or the edge of a I-loop), making it unlikely for a He atom from the bulk to diffuse into the loop. Secondly, since the growth of helium clusters depends on the ability of the cluster to eventually displace tungsten atoms via a substitutional mechanism, a compressive stress would make this process more difficult. It is possible the differing experimental observations in [200] are due to multiple reasons: higher helium irradiation energies, allowing high-velocity He ions to be injected inside the interstitial loops; very large loop sizes ($\sim$40nm) which likely reduces aforementioned compressive stresses to nearer bulk values; and higher diffusivity of He in iron. From experiments in Figure 4.3, the characteristic sizes of dislocations in tungsten at 500-800°C are indeed significantly smaller, and the irradiation temperature $\sim 0.2\mathrm{T}_m$ rather than $0.4T_m$ in α-iron. The fact that in [200] the bubbles form *preferentially* inside the α-iron interstitial loops is nonetheless puzzling, as this should be rather expected for vacancy-type.

   Due to the required timescales and associated computational costs, it was not possible to subsequently calculate diffusion coefficients of the pinned dislocation and quantify the expected decrease in loop mobility (for $\frac{1}{2}\langle 111\rangle$ case).

However, diffusion of smaller-scale dislocation loops in pure tungsten is treated in more depth later, in Chapter 6.

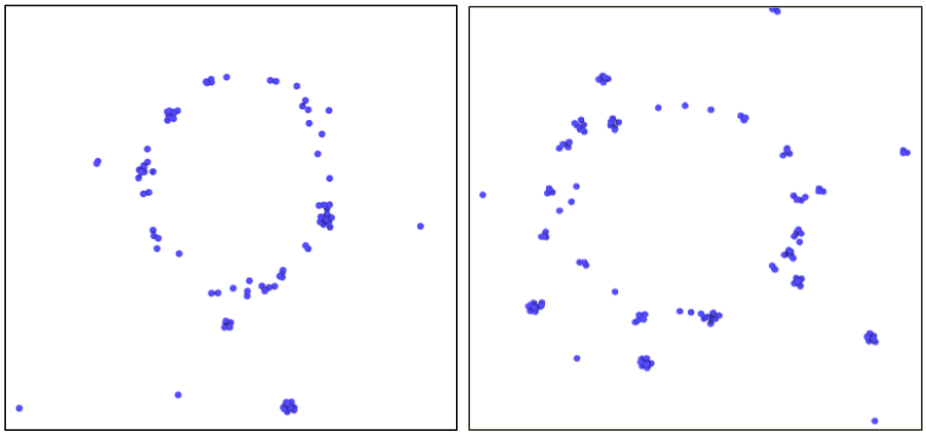

(a) $\frac{1}{2}\langle 111\rangle$ **(b)** $\langle 100\rangle$

Figure 4.11: Molecular dynamics simulation snapshot for (a) $\frac{1}{2}\langle 111\rangle$ and (b) $\langle 100\rangle$ ∼6nm diameter loop region, for ∼1000 He appm at 900K. Close-up of dislocation region, with only He atoms shown (evidently decorating the loop edges). CoM, in the y-axis label, stands for helium cluster centre of mass.

3. The effect of dose and dose rate was also probed by decreasing the amount of time between implantations from 10ps to 2.5ps, increasing flux from $\sim 3.6 \cdot 10^{26}$ He·m^{-2}s^{-1} to $\sim 1.5 \cdot 10^{27}$ He·m^{-2}s^{-1}, showing an increase in cluster size and reduction in average depth at higher flux (Figure 4.12).

From Figure 4.12, for the same final appm concentrations (300 appm), the higher flux condition yielded a more shallow cluster distribution with larger bubbles. Higher flux causes the He particles to have less time to diffuse inside the host material. This increases the likelihood of He atoms interacting as they are concentrated in a narrower region closer to the surface. Because He is strongly bound to itself inside the crystal, clusters readily form, become fixed, and can grow with increasing dose. Due to the computational expense of such simulations, no further simulations were carried out to explore the simulation parameter space. However, this effect is likely to be strongly dependent on surface orientation and temperature, as He can preferentially diffuse in certain directions.

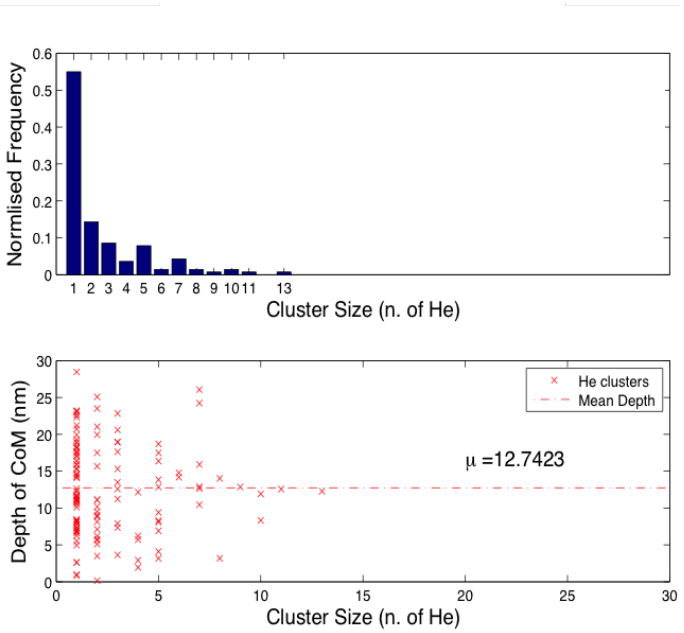

(a) Low flux

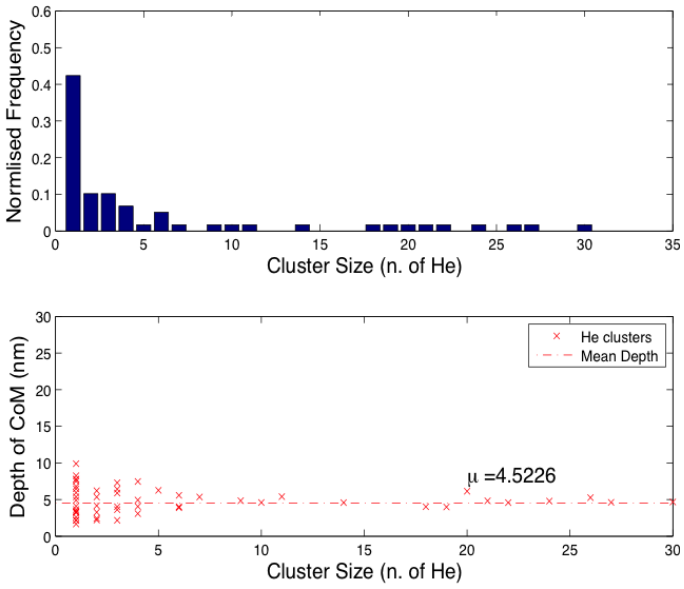

(b) High flux

Figure 4.12: Effect of helium flux on average depth and size of He clusters for (a) $\sim 3.6 \cdot 10^{26}$ He·m^{-2}s^{-1} and (b) $\sim 1.5 \cdot 10^{27}$He·m^{-2}s^{-1}

4.4 Summary

- The presence of He during irradiation favours the nucleation of dislocation loops, allowing higher defect densities and saturation at lower doses.

- Experimental observations such as no loop coarsening (for >5nm diameter) during dual-beam irradiation at 500°C (1800 appm cases) compared to single-beam irradiation suggests that He on dislocation cores impedes dislocation motion (and consequently loop-loop interactions).

- The binding energy between a dislocation loop and He is calculated as 2.0eV for $\frac{1}{2}\langle 111\rangle$ and 2.6eV for $\langle 100\rangle$. Helium is also observed clustering preferentially around pre-existing dislocation loops in separate molecular dynamics simulations. The calculated binding energies are inferior to He-vacancy binding energies, which corresponds to the experimental observations of *Armstrong et al* [108] of increased hardening effect of He on unirradiated tungsten compared to self-ion pre-irradiated tungsten.

- *In situ* mono beam defect concentrations ($6 \pm 2 \cdot 10^{21}$ loops·m^{-3} for $\sim$1.0·10^{14} W·m^{-2} dose at 500°C) are similar to bulk irradiation concentrations detailed in Chapter 3, specifically in Figure 3.2 ($3 \pm 1 \cdot 10^{21}$ loops·m^{-3} for $\sim$1.0·10^{14} W·m^{-2} dose at 500°C), suggesting a limited effect of the thin films (of thickness 100-160nm) on defect densities at 500°C. It is unexpected that the in situ concentrations are higher than the bulk, although this is likely attributable to the experimental uncertainties and inherent differences between the two irradiation setups.

- Injecting high doses of He (45000 peak He appm, at 25000 appm/dpa) causes morphological changes of the radiation damage structure, from a homogeneous defect concentration of dislocations in a narrow size range, into a complex dislocation network with voids.

- Loop nature is difficult to extract due to high defect concentrations when He

is present. For future experiments, a total W flux of $<8.33 \cdot 10^{12} W^{+} cm^{-2}$ is suggested, with unchanged He flux levels.

- Nanosized voids were *not* observed in the TEM in the 1800appm case at 500°C. However, they were observed both in the 1800 and 45000appm cases at 800°C, suggesting void formation depends strongly on temperature for these dose levels.

Chapter 5

Modelling of radiation damage recovery: continuum mechanics and classical discrete dislocation dynamics

5.1 Introduction

As discussed in the literature review, the modelling of radiation damage is multi-scale, which is problematic. Currently, there is no single technique that adequately allows for a complete physical treatment of radiation damage, at all time-scales, and its effect on important properties, like mechanical performance. Therefore, to model these effects, both continuum and atomistic tools will be used (and created) to probe different aspects of the problem. The continuum methods are detailed in this chapter; the next chapter will delve into atomistic and stochastic methods.
Broadly, the effects observed experimentally were:

- Rearranging of dislocation structures via glide, driven by elastic interactions.
- Absorption of defects by free surfaces.
- Stochastic, thermally activated processes like loop hopping.
- Dislocation climb.

The first two effects can be effectively treated by elastic interactions, making dislocation dynamics (coupled to continuum mechanics, in the form of finite element

method or spectral methods) a reasonable way to approach the problem. These will be covered in this chapter. The final two effects are more difficult to implement, but equally important when dealing with thermally driven effects in radiation recovery. A more detailed discussion how these effects have been treated will follow in the next chapter.

5.2 State of the art: simulating elastically driven dislocation behaviour via discrete dislocation dynamics

The radiation damage observed by transmission electron microscopy was in the form of prismatic dislocation loops. To capture the elastic interactions between such defects, discrete dislocation dynamics is a useful technique. As a starting point, DDLab was used, the development version of the parallel dislocation simulator ParaDis, developed by Lawrence Livermore National Laboratory in the US [213]. Other modern discrete dislocation dynamics packages exist, developed by a number of groups around the world, with similar functionalities and algorithms [214, 215, 216, 217, 218, 219, 220] The current state of the art is reviewed below.

5.2.1 Stress and force calculations in discrete dislocation dynamics

In an elastically isotropic material, such as tungsten, the stress field at $\boldsymbol{x}$ generated by a curved dislocation network C is given by the line integral [221]:

$$\begin{aligned}\sigma_{\alpha\beta}(\boldsymbol{x}) = &-\frac{\mu}{8\pi}\oint_C b_m\epsilon_{im\alpha}\frac{\partial}{\partial x_i'}\bigtriangledown'^2\, R\mathrm{d}x_\beta' - \frac{\mu}{8\pi}\oint_C b_m\epsilon_{im\beta}\frac{\partial}{\partial x_i'}\bigtriangledown'^2\, R\mathrm{d}x_\alpha' \\ &- \frac{\mu}{4\pi(1-\nu)}\oint_C b_m\epsilon_{imk}\left(\frac{\partial^3 R}{\partial x_i'\partial x_\alpha'\partial x_\beta'} - \delta_{\alpha\beta}\frac{\partial}{\partial x_i'}\bigtriangledown'^2\, R\right)\mathrm{d}x_k'\end{aligned} \tag{5.1}$$

where $R = |\boldsymbol{x}-\boldsymbol{x}'|$, $\boldsymbol{b}$ is the Burgers vector at location $\boldsymbol{x}'$, and ϵ_{ijk} is the permutation tensor.

In DDLab/ParaDis, the dislocation line is discretized into a series of interconnected straight dislocation segments[1], as shown in Figure 5.1. The degrees of freedom in the model are the coordinates of all nodes and the Burgers vectors of all segments connecting the nodes: $\{\boldsymbol{r}_i\ ,\ \boldsymbol{b}_{ij}\}$.

[1]N.B. Alternative representations are obviously possible. Other codes represent dislocations with a zig-zag edge-screw formulation [149] and cubic splines [217] etc. A linear representation is

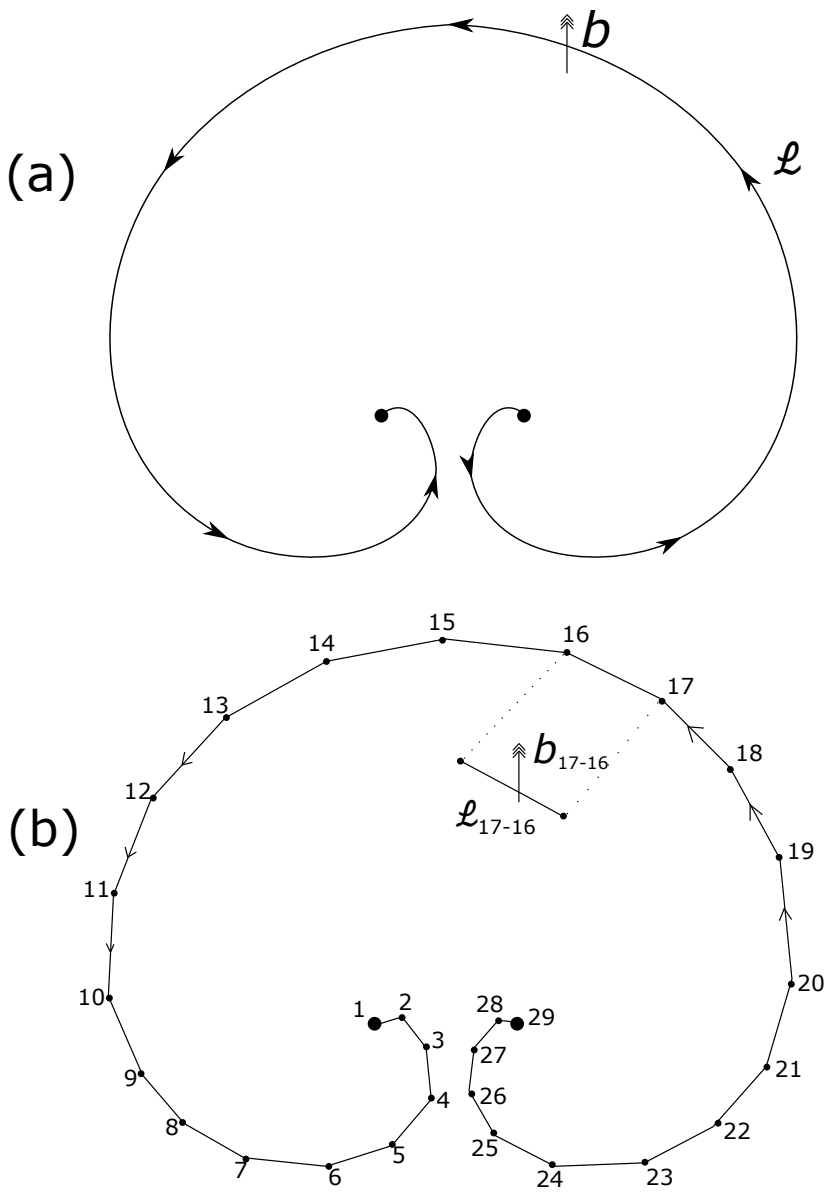

Figure 5.1: (a) Frank-Read source as a continuous dislocation line with Burgers vector b. (b) Discretized Frank-Read source represented by a set of nodes (circles) connected by straight segments. b_{ij} is the Burgers vector of the directed segment connecting node i to node j.

Dislocations experience a force per unit length that is proportional to the local stress through the Peach-Koehler formula.

$$f_i = \epsilon_{ijk}\sigma_{jl}b_l\hat{\xi}_k \tag{5.2}$$

where σ_{ij} is the local stress at point $\boldsymbol{x}$ on the dislocation line, b_l is the Burgers vector, and $\hat{\xi}_k$ is the local unit tangent vector of the dislocation line. Within the non-singular continuum theory of dislocations, by replacing R with $R_a = \sqrt{R^2 + a^2}$, where a is a chosen core radius length, Eq 5.1 becomes Eq 5.3.

$$\begin{aligned}\sigma_{\alpha\beta}(\boldsymbol{x}) = \frac{\mu}{8\pi}\oint_C \partial_i\partial_p\partial_p R_a \left(b_m\epsilon_{im\alpha}dx'_\beta + b_m\epsilon_{im\beta}dx'_\alpha\right) \\ + \frac{\mu}{4\pi(1-\nu)}\oint_C b_m\epsilon_{imk}(\partial_i\partial_\alpha\partial_\beta R_a - \delta_{\alpha\beta}\partial_i\partial_p\partial_p R_a)dx'_k\end{aligned} \tag{5.3}$$

There are several advantages to this non-singular form. Firstly, it removes the unphysical stress singularity at the dislocation line because the derivatives $\partial_i\partial_j R_a$ become finite and smooth everywhere. Secondly, the derivatives of R_a can be integrated analytically over straight segments leading to closed form expressions that are similar to the original singular theory.

The stress from a dislocation network at a given point is the sum of the stress contributions of individual dislocation segments, which can be evaluated analytically without needing numerical integration [138, 213]. Efficient computation of such quantity is desirable, particularly when zero-traction boundary conditions are required in the simulation (see Section 5.3). There are two ways to calculate stress from a discretised dislocation segment belonging to a network: either by direct differentiation of the elastic energy of the dislocation line by a displacement $\delta\boldsymbol{r}$ as shown in Eq 5.4, or by the integration of the Peach-Koehler force calculated in 5.2 over the swept space the dislocation covers by a displacement $\delta\boldsymbol{r}$, as shown in Eq 5.5.

however relatively accurate, computationally efficient, and easy enough for analytical optimizations.

$$\boldsymbol{f}_i^{el} = -\frac{\partial E_{el}}{\partial \boldsymbol{r}_i} \tag{5.4}$$

$$\boldsymbol{f}_i^{el} = \oint_C \boldsymbol{f}^{PK}(\boldsymbol{x}) \cdot \frac{\delta \boldsymbol{x}}{\delta \boldsymbol{r}_i} dL(\boldsymbol{x}) \tag{5.5}$$

ParaDis/DDLab use the second method, since using the Peach-Koehler formula relies on the local stress $\sigma_{\alpha\beta}(\boldsymbol{x})$ regardless of the origin of this stress. The Peach-Koehler force on a given node i is found by calculating the weighted sum using a linear shape function of the global stress field at a number of Gauss points along the segments to which the node is connected to. A shape function $N_i(\boldsymbol{x})$ for every node i is defined such that it is non-zero only when $\boldsymbol{x}$ lies on a segment connected to node i. On a given segment $i-j$, $N_i(\boldsymbol{x})$ decreases linearly from 1 at node i to 0 at node j, like Eq 5.6. A simple diagram is given in Figure 5.2.

$$N_i(\boldsymbol{x}) = \frac{||\boldsymbol{x} - \boldsymbol{r}_j||}{||\boldsymbol{r}_i - \boldsymbol{r}_j||} \tag{5.6}$$

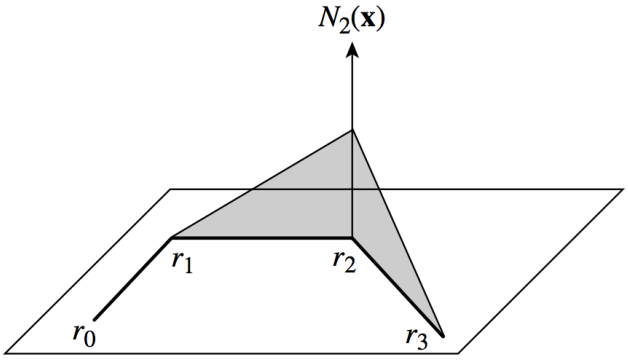

Figure 5.2: The shape function $N_2(\boldsymbol{x})$ is equal to one at node 2 and decreases linearly to zero at two neighbouring nodes 1 and 3. The work performed by the stress is obtained by integrating the Peach-Koehler force over the swept area (shaded). Taken from *Bulatov et al* [138].

Therefore, for a displacement of node i by $\delta \boldsymbol{r}_i$ causing the line to change its shape by $N_i(\boldsymbol{x})\delta \boldsymbol{r}_i$, Eq 5.5 becomes Eq 5.7,

$$\boldsymbol{f}_i^{el} = \oint_C \boldsymbol{f}^{PK}(\boldsymbol{x}) N_i(\boldsymbol{x}) dL(\boldsymbol{x}) = \oint_C \left(\boldsymbol{\sigma}_{\alpha\beta}(\boldsymbol{x} \cdot \boldsymbol{b}) \times \boldsymbol{\xi}(\boldsymbol{x})\right) N_i(\boldsymbol{x}) dL(\boldsymbol{x}) \tag{5.7}$$

Since the internal stress field is an integral over the entire dislocation network, it can be written as the sum of the line integrals of the straight segments making up the network as in Eq 5.8.

$$\sigma_{\alpha\beta}(\boldsymbol{x}) = \sum_{k-l} \sigma_{\alpha\beta}(\boldsymbol{x}; k-l) \tag{5.8}$$

Finally, to calculate the force on node i, the line integral in Eq 5.7 needs to be taken only over the segments node i is directly connected to (i.e. adjoining segments), due to the definition of the shape function $N_i(\boldsymbol{x})$ as zero everywhere else. This leads to Eq 5.9.

$$\boldsymbol{f}_i^{el} = \sum_j \sum_{k-l} \boldsymbol{f}_i^{el}(i-j; k-l) \tag{5.9}$$

where $\boldsymbol{f}_i^{el}(i-j; k-l)$ represents the force on node i due to the elastic interaction between segments $i-j$ and $k-l$. The first sum is over all nodes j connected to node i, and the second sum is over all line segments of the network. Analytic expressions are given in Appendix A. Owing to the long-range interactions of dislocations, the stress at $\boldsymbol{x}$ depends on all dislocation segments in the simulation, making the calculation computationally expensive, with $\mathcal{O}(N^2)$ increase in computation time where N is the number of dislocation segments [213]. It is possible to improve this by using fast multiple expansions [222, 223] which decrease the computational dependence to $\mathcal{O}(N\log(N))$ or $\mathcal{O}(N)$, but requires significant added algorithmic complexity. One can also take advantage of parallel computing architectures, such as GPUs, to parallelize the calculation process, as detailed in the Appendix B.

5.2.2 Self forces

In addition to interactions with other dislocation segments, a dislocation experiences a force from itself, due to the orientation-dependence of its elastic energy, called self-force. The elastic contribution of the self force for a straight dislocation can be derived using a non-singular theory, by evaluating a dislocation's stress field

along its own line and by applying the Peach-Koehler formula for the force. This is implemented in Paradis/DDLab (details can be found in [224]).

A further contribution to the self-force arises from the dislocation core energy, which is beyond the scope of continuum elasticity theory and can be calculated from molecular dynamics. However, estimates using elasticity have been implemented in ParaDis/DDLab, with simple expressions for core torsional and longitudinal force available (details can be found in [225]).

5.2.3 Nodal Mobility Functions

For each time step, the forces calculated previously are fed into a nodal mobility function which in turn give nodal velocities, evolving the dislocation structure. Provided specific mobility laws are available (e.g. from separate material-specific molecular dynamic simulations), simple mobility laws can be implemented on the DD level [224, 218]. ParaDis/DDLab uses a linear mobility function shown in Eq 5.10, which depends on the orientation of the dislocation segments, Burgers vector, and type of material.

$$\boldsymbol{v}_i = \boldsymbol{M}(\{\boldsymbol{f}_j\}) \tag{5.10}$$

The effects of inertia on dislocation motion can become important under conditions of very high strain rates, such as during shock propagation [226]. In the cases being simulated here, inertia can be safely ignored and to a good approximation the regime is over-damped leading to a first-order differential equation of motion, where the forces determine the instantaneous velocity and acceleration/mass of dislocations can be excluded. A simple viscous drag motion model is implemented in ParaDis/DDLab where the dislocation experiences a drag force per unit length of the line which is proportional to the local velocity, as in Eq 5.11.

$$\boldsymbol{f}^{drag}(\boldsymbol{x}) = -\mathfrak{B}(\boldsymbol{\xi}(\boldsymbol{x})) \cdot \boldsymbol{v}(\boldsymbol{x}) \tag{5.11}$$

where the drag coefficient tensor $\mathfrak{B}$ depends on the local tangent vector $\boldsymbol{\xi}$ at point $\boldsymbol{x}$ of the dislocation line. In an over-damped regime, the drag force should exactly balance the driving force at every point on the network. Due to the discretization of the dislocation network, this condition is satisfied in a weaker sense, i.e.

$$\oint_C N_i(\boldsymbol{x}) \left[\boldsymbol{f}^{drag}(\boldsymbol{x}) + \boldsymbol{f}^{local}(\boldsymbol{x})\right] dL(\boldsymbol{x}) = 0, \text{ for all } i \tag{5.12}$$

For a given node i, knowing that $\boldsymbol{v}(\boldsymbol{x}) = \sum_i \boldsymbol{v}_i N_i(\boldsymbol{x})$,

$$\begin{aligned} \boldsymbol{f}_i &= \oint_C N_i(\boldsymbol{x}) \mathfrak{B}(\boldsymbol{\xi}(\boldsymbol{x})) \cdot \boldsymbol{v}(\boldsymbol{x}) dL(\boldsymbol{x}) \\ &= \oint_C N_i(\boldsymbol{x}) \mathfrak{B}(\boldsymbol{\xi}(\boldsymbol{x})) \cdot \sum_i \boldsymbol{v}_j N_j(\boldsymbol{x}) dL(\boldsymbol{x})] \\ &= \sum_j \boldsymbol{B}_{ij} \cdot \boldsymbol{v}_j, \text{for all } i \end{aligned} \tag{5.13}$$

where,

$$\boldsymbol{B}_{ij} = \oint_C N_i(\boldsymbol{x}) \mathfrak{B}(\boldsymbol{\xi}(\boldsymbol{x})) N_j(\boldsymbol{x}) dL(\boldsymbol{x}) \tag{5.14}$$

In ParaDis/DDLab, nodal velocities are obtained by solving the linear set of equations in Eq 5.13 with respect to $\boldsymbol{B}_{ij}$, which is defined by the orientation-dependent drag coefficient tensor $\mathfrak{B}(\boldsymbol{\xi})$, which is related to the crystallography of the material in question.

Tungsten is a body-centred cubic material (BCC). The drag coefficient tensor is created such that a number of characteristics are captured.

- Screw dislocations have the same mobility in all directions perpendicular to the line. This isotropic mobility for screws mimics pencil-glide behaviour of dislocations in BCC metals at elevated temperatures.

$$\mathfrak{B}(\boldsymbol{\xi}) = B_{\text{screw}}(\boldsymbol{I} - \boldsymbol{\xi} \otimes \boldsymbol{\xi}), \text{ when } \boldsymbol{\xi} || \boldsymbol{b} \tag{5.15}$$

- Non-screw segments have anisotropic mobilities with respect to glide and climb, with the drag coefficient in the climb direction $B_{\text{edge}}^{\text{climb}}$ much larger ($> \mathcal{O}(10^4)$) than glide $B_{\text{edge}}^{\text{glide}}$.

$$\mathfrak{B}(\boldsymbol{\xi}) = B_{\text{edge}}^{\text{glide}}(\boldsymbol{m} \otimes \boldsymbol{m}) + B_{\text{edge}}^{\text{climb}}(\boldsymbol{n} \otimes \boldsymbol{n}), \text{ when } \boldsymbol{\xi} \perp \boldsymbol{b} \tag{5.16}$$

  where unit vectors are defined as $\boldsymbol{n} = \boldsymbol{b} \times \boldsymbol{\xi}/||\boldsymbol{b} \times \boldsymbol{\xi}||$ and $\boldsymbol{m} = \boldsymbol{n} \times \boldsymbol{\xi}$.

- Dislocations do not dissociate into partial dislocations.

To completely specify the drag coefficient tensor for all segment orientations, ParaDis/DDLab smoothly interpolates between the pure edge and pure screw limits, as shown in Eq 5.17, [227].

$$\begin{aligned} \mathfrak{B}(\boldsymbol{\xi}) &= B^{\text{glide}}(\boldsymbol{m} \otimes \boldsymbol{m}) + B^{\text{climb}}(\boldsymbol{n} \otimes \boldsymbol{n}), \text{ when } \boldsymbol{\xi} \times \boldsymbol{b} \neq 0 \\ B^{\text{glide}} &= \left[B_{\text{edge}}^{\text{glide}}||\boldsymbol{b} \times \boldsymbol{\xi}||^2 + B_{screw}^{-2}(\boldsymbol{b} \cdot \boldsymbol{\xi})^2\right]^{-1/2} \\ B^{\text{climb}} &= \left[B_{\text{edge}}^{\text{climb}}||\boldsymbol{b} \times \boldsymbol{\xi}||^2 + B_{screw}^{2}(\boldsymbol{b} \cdot \boldsymbol{\xi})^2\right]^{1/2} \end{aligned} \tag{5.17}$$

5.2.4 Time Integration

By taking the nodal forces ($\boldsymbol{f}_i^{el}$) calculated in Eq 5.9 and the mobility model ($\boldsymbol{B}_{ij}$) for BCC metals shown in Eq 5.17 and Eq 5.14, one can successfully solve for v_j in Eq 5.13. Because the motion is assumed to be over-damped, Eq 5.11 is a first order differential equation, which can be solved with a number of standard numerical integrators, depending on the desired order of accuracy and computational speed. For all the simulations, a simple predictor-corrector method was used, (*Heun's method* [228]) constructed from the *Euler method* (explicit) and the *trapezoidal method* (implicit):

$$\begin{aligned} &\text{Predictor: } \boldsymbol{r}_i^P(t+\delta t) = \boldsymbol{r}_i(t) + \boldsymbol{g}_i(\{\boldsymbol{r}_j(t)\})\delta t \\ &\text{Corrector: } \boldsymbol{r}_i(t+\delta t) = \boldsymbol{r}_i(t) + \frac{\boldsymbol{g}_i(\{\boldsymbol{r}_j(t)\} + \boldsymbol{g}_i(\{\boldsymbol{r}_j^P(t+\delta t)\})}{2}\delta t \end{aligned} \tag{5.18}$$

The difference between the $(t+\delta t)$ position as calculated by the predictor and corrector steps is used as a measure of integration error. If this is above a given amount ϵ, the time-step δt is reduced. Vice-versa, if the error is below ϵ, ParaDis/DDLab will try to increase the time-step up to a δt_{max}. By allowing a dynamic time-step, computational efficiency is increased. Nonetheless, particularly for scenarios where different variables of the system require very different time steps, the ordinary differential equation system is *stiff*[2].

5.2.5 Topological changes

Discrete dislocation dynamics does not just require a precise calculation of nodal forces, phenomenologically correct mobility laws, and accurate numerical integrators, but also a faithful topological treatment of dislocation line reactions. ParaDis/DDLab and other DDD codes account for:

- Re-meshing of segments, to refine or coarsen line representation, an example given in Figure 5.3.
- Splitting or merging of nodes and segments, an example given in Figure 5.4.

The details regarding topological treatment of dislocation networks in ParaDis/DDLab are covered elsewhere [227, 213]. Although important, they are not covered into as much detail as previous sections since they are not modified or expanded upon in this thesis (with the exception of rewriting the original to be more computationally efficient, given in Appendix B).

[2]Definition: *If a numerical method with a finite region of absolute stability, applied to a system with any initial conditions, is forced to use in a certain interval of integration a step length which is excessively small in relation to the smoothness of the exact solution in that interval, then the system is said to be stiff in that interval, so other numerical methods such as ode*15*s can be used [228]*

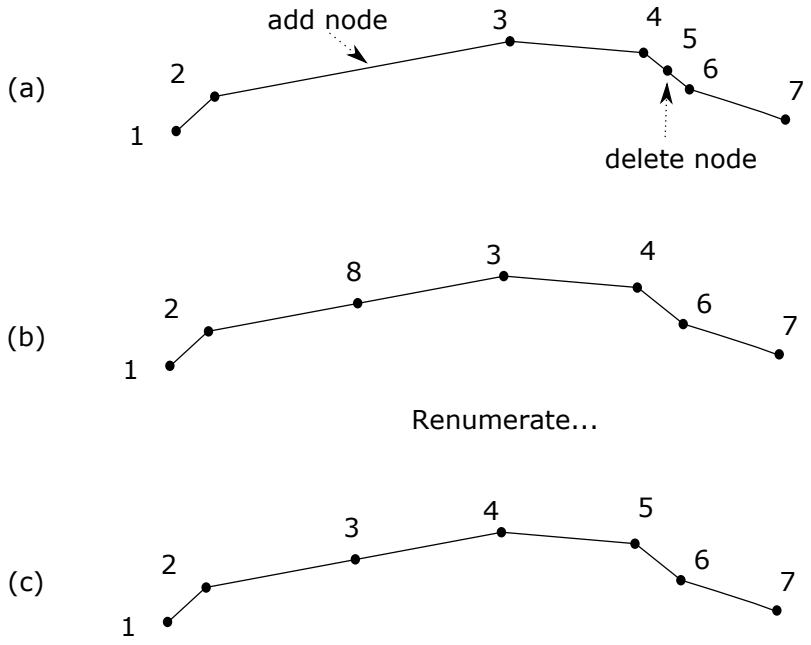

Figure 5.3: (a) Dislocation network with potential remeshing instances. Nodes are added in the middle of segments (i.e. 2-3) that exceed an input parameter specifying the maximum segment length (l_{max}); vice versa, nodes are removed between segments (i.e. 4-5 and 5-6) that may exceed an input parameter specifying the minimum segment length (l_{min}), transforming into (b). This dislocation network is then relabelled into (c) and checked for errors (i.e. non-conservation of Burgers vector). For areas of high local curvature, segments may be discretised further to prevent the orientation of sequential segments connected to a given node from differing excessively. This is done by monitoring the area of the triangle formed by the node in question and its two neighbours.

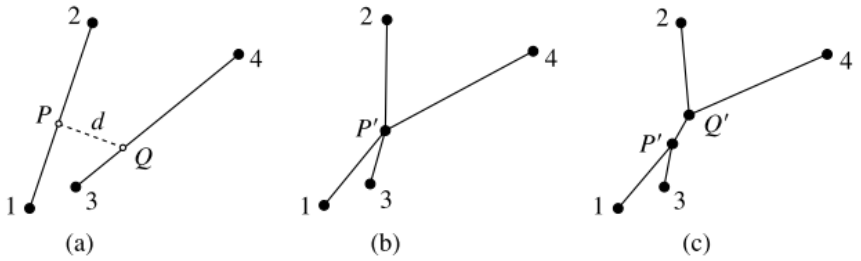

Figure 5.4: Dislocation segments merging. Every time iteration, ParaDis/DDLab calculates the minimum distance d between unconnected segments, given in (a). If this falls below a minimum r_a, the segments are considered to be in contact and merged at P' (b), and then creating a junction segment $P'Q'$ with potentially different topology. Diagram taken from *Bulatov et al* [138].

5.2.6 Summary

- An arbitrary dislocation network can be discretised into nodes connected by straight segments.
- The force on every node due to elastic interactions between segments can be calculated analytically in an efficient manner, but in its simplest formulation scales with $\mathcal{O}(N^2)$, where N is the number of dislocation segments.
- Self force (the force on a segment due to the orientation-dependence of its elastic energy) can also be calculated using a non-singular elastic theory, and core force terms estimated. These are added linearly onto other force contributions (see [225] more details).
- Excluding shock-loading, a first-order equation of over-damped motion (mobility function) is valid to describe relation between nodal velocity and nodal force, and employed in conjunction with a shape function.
- The mobility function is material-specific. BCC metals like tungsten are characterised by anisotropic drag in climb and glide directions for edge segments, and isotropic drag for screw segments.
- The numerical integrator used for nodal equation of motion is a predictor-corrector method, with automatic time-step adjustment to maintain error below given threshold.
- Using constitutive rules, interactions such as junction formation and other topological changes can be dealt with.

5.3 Introducing boundary conditions

DDLab does not have the capability to model free surfaces, relying instead on infinite medium or periodic boundary assumptions. Although this is sufficient for predicting mechanical behaviour of a *bulk* material [163], it will not capture size-effects, or the presence of free surfaces in TEM foils for example. This is an important limitation, and Sections 5.4 and 5.5 will detail my efforts to develop a more comprehensive simulation package that can handle such boundary conditions.

- Section 5.4 describes the specific case of free-standing thin films, of interest due to the relative similarity to TEM foils.

- Section 5.5 describes a general method based on the finite element method, able to deal with mixed boundary conditions (force, stress, displacement) for any convex shapes.

5.3.1 General boundary value problem (BVP)

The fundamental equations governing any linear elastic boundary value problem are based on three tensor partial differential equations for the balance of linear momentum and six infinitesimal strain-displacement relations, with the system closed by a set of linear algebraic constitutive relations. The governing equations in this case are

- Equation of motion:

$$\hat{\sigma}_{ij,j} + \rho f_i^b - \rho \ddot{u}_i = 0 \text{ in domain } \Omega$$

  which (assuming equilibrium, $\ddot{u}_i = 0$ and taking body forces as zero, $f_i^b = 0$) becomes,

$$\hat{\sigma}_{ij,j} = 0 \text{ in domain } \Omega \tag{5.19}$$

- Strain-displacement equation:

$$\hat{\epsilon}_{ij} = \frac{1}{2}(\hat{u}_{i,j} + \hat{u}_{j,i}) \tag{5.20}$$

- Constitutive equation (Hooke's Law):

$$\hat{\sigma}_{ij} = C_{ijkl}\hat{\epsilon}_{kl} \tag{5.21}$$

where C_{ijkl} is the linear elastic stiffness tensor, $\hat{\sigma}$, $\hat{u}$ and $\hat{\epsilon}$ are stress, displacement and strain fields, defined for a domain Ω. This domain has boundaries which are defined by either a displacement (Dirichlet) or traction (von Neumann) boundary condition. In other words, one can define a traction boundary condition T^{ext} on boundary Γ_t, or a displacement boundary condition u^{ext} on boundary Γ_u. As an example, a free surface bounded by Γ_t, will have a zero traction boundary condition $T^{\text{ext}} = 0$. Similarly, the base of a micro-pillar bounded by Γ_u could be defined as fixed, so $u^{\text{ext}} = 0$ at that position. Traction is the stress vector perpendicular to the surface (Eq 5.22), which is necessarily zero on a stationary free surface.

$$T_j = \sigma_{ij} n_i \tag{5.22}$$

From the perspective of dislocation motion, one is interested in the stress acting on the dislocations in a finite domain Ω, from which the Peach-Koehler force can be calculated. Since the stress equations given in the previous Section 5.2 are derived by assuming an infinite medium, one must correct for the presence of boundaries in a finite domain. The most common method to do this is by employing the traction-compensation method of van der Giessen and Needleman [229]. At the boundary Γ_t, the presence of dislocations would produce a traction $\tilde{T}$. To ensure that at Γ_t a given traction boundary condition T^{ext} is fulfilled, one can introduce an "image" traction $\hat{T}$ to compensate for the dislocation contribution. The same applies for displacement and stress. These are shown mathematically in Eq 5.23, and diagrammatically in

Figure 5.5.

$$
\begin{aligned}
T_i^{\text{ext}} &= \hat{T}_i + \tilde{T}_i, \text{ on } \Gamma_t \\
u_i^{\text{ext}} &= \hat{u}_i + \tilde{u}_i, \text{ on } \Gamma_u \\
\sigma_{ij} &= \hat{\sigma}_{ij} + \tilde{\sigma}_{ij}, \text{ in } \Omega
\end{aligned}
\tag{5.23}
$$

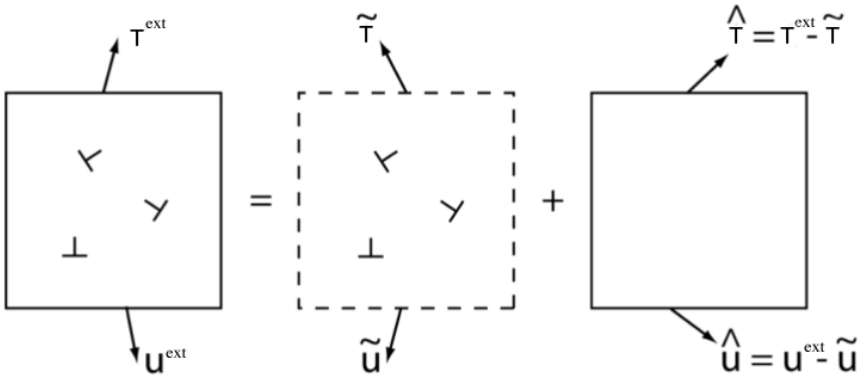

Figure 5.5: Diagram showing the traction-compensation method, where where T^{ext} and u^{ext} are externally applied traction on Γ_t and displacement on Γ_u boundary conditions, $\tilde{T}$ and $\tilde{u}$ are the traction and displacements on the boundary of the finite domain Ω due to all the dislocation segments.

$\tilde{T}$, $\tilde{u}$ and $\tilde{\sigma}$ depend on semi-analytical functions. For the case of traction, this is given previously in Eq 5.3 and 5.8. The calculation of $\tilde{u}$ is reviewed in Section 5.5.2.

5.3.2 Free surfaces

In general, *a free surface has zero traction* (Eq 5.24).

$$
T_j^{\text{ext}} = 0, \text{ on free surface } \Gamma_t \tag{5.24}
$$

Therefore, the sum of the image traction and the "infinite medium" traction arising from the dislocations should equal zero at the free surface. This is shown schematically in Figure 5.6.

These image stresses are superposed on the total stress field, affecting dislocation motion and introducing experimental features like dislocation denuded zones near

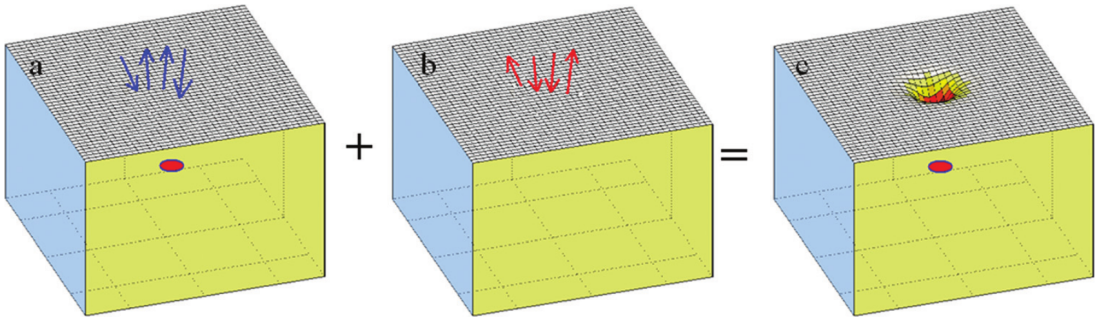

Figure 5.6: Schematics of the procedure to calculate the image stress of a defect in a crystal (red disk in the centre) due to the presence of a free surface. (a) Traction $\tilde{\sigma}_{ij}$ at the free surface position in the infinite crystal. (b) Image stress $\hat{\sigma}_{ij}$ introduced to cancel the traction stress. (c) The total stress field in the semi-infinite crystal is $\sigma_{ij} = \hat{\sigma_{ij}} + \tilde{\sigma}_{ij}$, with zero traction at the surface, with the resulting displacement visible as a dimple in the surface [230].

surfaces [231, 232] and size-effects in material plasticity. The following sections explain how to calculate this image stress.

5.4 Simulating free surfaces (thin films)

This section will illustrate what code additions were necessary to simulate free surfaces *in a thin film*. The benefit of constraining the geometry for the case of a thin film is computational efficiency, since image stress can be calculated using a semi-analytical method [233]. This calculation method was implemented, with additional formulae derived for stress, and integrated into DDLab. It is important to note that this method does not allow for an external applied stress, force, or displacement boundary condition. In other words, the thin film is *free standing*. This is satisfactory for a TEM foil, but not for *in situ* straining TEM samples, or micro mechanical tests such as pillars and cantilevers. These limitations are overcome by implementing a more general approach in Section 5.5.

5.4.1 Analytic solutions for image stress

To enforce the zero-traction boundary condition at the free surface, a suitable image stress field $\hat{\sigma}$ must be superposed on the standard infinite-medium dislocation stress fields $\tilde{\sigma}$. Due to the simple geometry of the thin film, analytic solutions can be obtained in Fourier space. Using fast discrete Fourier transforms leads to an efficient way to solve for the image stress, an important advantage since it must be done for every simulation time increment. Equations have been derived in Ref. [233] for this, and have been somewhat simplified for the non-singular stress formulation developed in Ref. [227]. This is briefly reviewed below.

In the absence of body forces, the stress equilibrium of an isotropic linear medium can be written in terms of the displacement as:

$$\mu u_{i,jj} + (\lambda + \mu) u_{j,ji} = 0 \tag{5.25}$$

where $\lambda = 2\mu\nu/(1-2\nu)$, μ is the shear modulus and ν is Poisson's ratio. In the thin film geometry, the solution in Fourier space is exponential in the direction of the surface normal (taken to be z) and periodic in the other two orthogonal directions

x and y. This means that only the top and bottom surfaces of the thin film are considered, with the lateral surfaces neglected. This is a reasonable assumption for TEM foils, where the lateral dimensions range from several hundreds of microns to millimetres, whereas the vertical thickness can be as as little as 40 nm[3].

The image displacement field $\hat{u}$ can be written as the sum of Fourier modes $\hat{\mathcal{U}}$, as shown in 5.26.

$$\hat{\mathcal{U}}(x,y,z) = \sum_{k_x}\sum_{k_y}\hat{\mathcal{U}}(k_x,k_y,z)e^{ik_x x + ik_y y} \tag{5.26}$$

where $k_z = \sqrt{k_x^2 + k_y^2}$, $k_x = 2\pi n_x/L_x$ and $k_y = 2\pi n_y/L_y$ are wave numbers for n_x,n_y = 0, $\pm 1, \pm 2 ... \pm n$.

The equations for the individual Fourier modes $\hat{\mathcal{U}}$ of image displacement $\hat{u}$ are given in Eq 5.27 in terms of hyperbolic functions, where $-t \leq z \leq t$ in a thin film domain, t being the half-thickness (see Fig.5.7). A, B, C, E, F, G are constants.

$$\begin{aligned}
\hat{\mathcal{U}}_1 &= (Ak_x z - Fk_y + iGk_x)\sinh k_z z + (Ek_x z + Bk_y + iCk_x)\cosh k_z z \\
\hat{\mathcal{U}}_2 &= (Ak_y z + Fk_x + iGk_y)\sinh k_z z + (Ek_y z - Bk_x + iCk_y)\cosh -k_z z \\
\hat{\mathcal{U}}_3 &= (-iAk_z z - iE\frac{\lambda+3\mu}{\lambda+\mu} + Gk_z)\cosh k_z z + (-iEk_z z + iA\frac{\lambda+3\mu}{\lambda+\mu} - Ck_z)\sinh k_z z
\end{aligned} \tag{5.27}$$

This method of defining an arbitrary field in Fourier space is very useful because, if the constants A to G are known, the field is fully defined *analytically* within the domain. Since one is primarily interested in calculating Peach-Koehler forces, it is more convenient to know the image stress fields $\hat{\sigma}$ in the thin film. Similarly to displacement, this stress field can be expressed as a sum over its Fourier modes, as in Eq 5.28.

[3]To avoid confusion between notations, one defines the 2-dimensional discrete Fourier transform in x and y of a function $f(x,y,z)$ as $\mathcal{F}(k_x,k_y,z)$, where $f : \mathbb{R} \to \mathbb{C}$. Similarly, $\sigma(x,y,z)$ becomes $\Sigma(k_x,k_y,z)$, and $u(x,y,z)$ becomes $\mathcal{U}(k_x,k_y,z)$ in Fourier space.

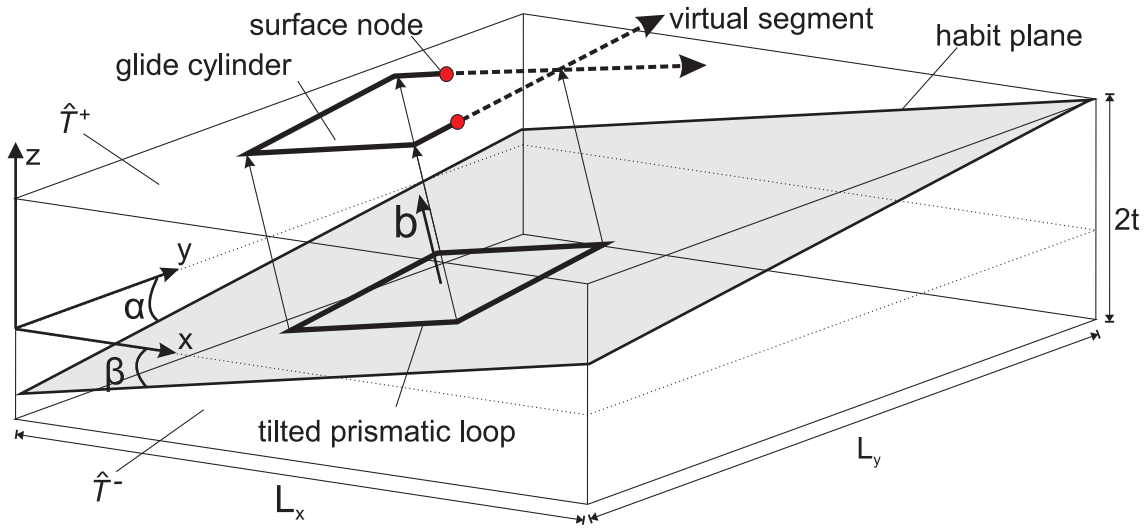

Figure 5.7: Model geometry illustrating a tilted loop which will glide along the direction of $\boldsymbol{b}$. Virtual segments are required for a partially exited loop.

$$\hat{\sigma}(x,y,z) = \sum_{k_x}\sum_{k_y} \hat{\Sigma}(k_x,k_y,z)e^{ik_x x + ik_y y} \tag{5.28}$$

By inserting $\hat{u}$ into Hooke's Law, $\hat{\sigma}_{ij} = \lambda \hat{u}_{k,k}\delta_{ij} + \mu(\hat{u}_{i,j} + \hat{u}_{j,i})$, one can derive the image stress field $\hat{\sigma}$ and extract the Fourier modes $\hat{\Sigma}$. The first term of this Cauchy stress tensor (in Fourier space) is shown in Eq 5.29. For the complete set, please refer to Eq A.1 in Section A.1.1 of the Appendix A.

$$\begin{aligned}\hat{\Sigma}_{11} = 2\mu \Bigg[&\left(\frac{iA\lambda k_z}{\lambda+\mu} + (iEk_x^2 z + iBk_x k_y - Ck_x^2) \right) \cosh(k_z z) \\ &+ \left(\frac{iE\lambda k_z}{\lambda+\mu} + (iAk_x^2 z - iFk_x k_y - Gk_x^2) \right) \sinh(k_z z) \Bigg]\end{aligned} \tag{5.29}$$

One question remains: how to calculate the constants A, B, C and E, F, G which define the stress fields. The Fourier solution of the equilibrium equation in a free-standing thin film $-t \leq z \leq t$ must contain six traction components (dependent on the dislocation structure) which relate to the six unknown Fourier coefficients through a 6×6 matrix. Due to the symmetry of hyperbolic functions, this problem can be split into two independent 3×3 problems, by using symmetric and anti-symmetric tractions.

Given appropriate linear combinations, the part of the traction field that is symmetric under reflection $\tilde{\mathcal{T}}^S$ is decoupled from the anti-symmetric part $\tilde{\mathcal{T}}^A$, as in Eq 5.30. The tractions on the top and bottom surface depend on the dislocation structure in the thin film domain, and are calculated by Eq 5.22 and 5.8.

$$\begin{aligned}
\tilde{\mathcal{T}}^S &= \frac{1}{2}\begin{pmatrix} \tilde{\mathcal{T}}_x^+ + \tilde{\mathcal{T}}_x^- \\ \tilde{\mathcal{T}}_y^+ + \tilde{\mathcal{T}}_y^- \\ \tilde{\mathcal{T}}_z^+ - \tilde{\mathcal{T}}_z^- \end{pmatrix} = [M^S]\begin{pmatrix} A \\ B \\ C \end{pmatrix} \\
\tilde{\mathcal{T}}^A &= \frac{1}{2}\begin{pmatrix} \tilde{\mathcal{T}}_x^+ - \tilde{\mathcal{T}}_x^- \\ \tilde{\mathcal{T}}_y^+ - \tilde{\mathcal{T}}_y^- \\ \tilde{\mathcal{T}}_z^+ + \tilde{\mathcal{T}}_z^- \end{pmatrix} = [M^A]\begin{pmatrix} E \\ F \\ G \end{pmatrix}
\end{aligned} \tag{5.30}$$

where superscripts $^+$ and $^-$ distinguish top and bottom surface tractions.

Therefore, the unknowns A, B, C, E, F, G can be found from the inverse of the 3×3 matrices M^S and M^A. These matrices can be derived in the form given in Eq 5.31 and 5.32, and are unique for each Fourier mode.

$$M^S = \begin{bmatrix} 2\mu k_x(k_z t\cosh(k_z t) - \frac{\mu}{\lambda+\mu}\sinh(k_z t)) & \mu k_z k_y \sinh(k_z t) & 2i\mu k_z k_x \sinh(k_z t) \\ 2\mu k_y(k_z t\cosh(k_z t) - \frac{\mu}{\lambda+\mu}\sinh(k_z t)) & -\mu k_z k_x \sinh(k_z t) & 2i\mu k_z k_y \sinh(k_z t) \\ 2i\mu(\frac{2\mu+\lambda}{\lambda+\mu}k_z\cosh(k_z t) - k_z^2 t\sinh(k_z t)) & 0 & 2\mu k_z^2\cosh(k_z t) \end{bmatrix} \tag{5.31}$$

$$M^A = \begin{bmatrix} 2\mu k_x(k_z t\sinh(k_z t) - \frac{\mu}{\lambda+\mu}\cosh(k_z t)) & -\mu k_z k_y \cosh(k_z t) & 2i\mu k_z k_x \cosh(k_z t) \\ 2\mu k_y(k_z t\sinh(k_z t) - \frac{\mu}{\lambda+\mu}\cosh(k_z t)) & \mu k_z k_x \cosh(k_z t) & 2i\mu k_z k_y \cosh(k_z t) \\ 2i\mu(\frac{2\mu+\lambda}{\lambda+\mu}k_z\sinh(k_z t) - k_z^2 t\cosh(k_z t)) & 0 & 2\mu k_z^2\sinh(k_z t) \end{bmatrix} \tag{5.32}$$

Eq 5.31 and 5.32 can be used to calculate the inverse numerically, or directly through the analytical solutions given in Eq A.2 and A.3 in the Appendix A. Fortunately, because the number of Fourier modes is generally chosen *a priori*, matrices M^S and M^A (or rather their inverses) can be calculated at the beginning of the DD

simulation for each mode and stored. For each subsequent time-step, these can be accessed on the fly from memory.

5.4.2 Description of algorithm

Figure 5.8 shows a flowchart of the algorithm, and how it incorporates within the general DD code. In words, the procedure used for calculating the image stress at a point (x, y, z) in the thin film domain is as follows:

0. Precompute $[M^S]^{-1}$ (Eq A.2) and $[M^A]^{-1}$ (Eq A.3), for all k_x and k_y, and store in memory.

For each subsequent time-step of the DD simulation:

1. Calculate stress $\tilde{\sigma}_{ij}$ due to the dislocation network (Eq 5.8) at the top and bottom surface, at regularly spaced locations defined by all the combinations of k_x and k_y, creating a $n_x \times n_y$ array for each stress component (i.e. $\tilde{\sigma}_{xx}$, $\tilde{\sigma}_{yy}$, $\tilde{\sigma}_{zz}$, $\tilde{\sigma}_{xy}$, $\tilde{\sigma}_{xz}$, $\tilde{\sigma}_{yz}$).

2. Calculate traction (Eq 5.22), yielding a $n_x \times n_y$ array for each surface, for each traction component (i.e. $\tilde{T}_x^+$, $\tilde{T}_y^+$, $\tilde{T}_z^+$, $\tilde{T}_x^-$, $\tilde{T}_y^-$, $\tilde{T}_z^-$).

3. Calculate symmetric and anti-symmetric traction arrays (Eq 5.30) and pass them through a DFFT (Discrete Fast Fourier Transform) function, to get the equivalent $n_x \times n_y$ arrays ($\tilde{\mathcal{T}}^S$ and $\tilde{\mathcal{T}}^A$) in Fourier space.

Once these steps are performed, to calculate image stress $\hat{\sigma}$ at a specific point (x,y,z) within the thin film domain, for each Fourier mode (i.e. for each k_x and k_y combination):

4. Solve for A, B, C, E, F, G (Eq 5.30).

5. Calculate image Cauchy stress tensor components $\tilde{\Sigma}$ (Eq 5.29) for given mode, and sum into total image Cauchy stress tensor (Eq 5.28).

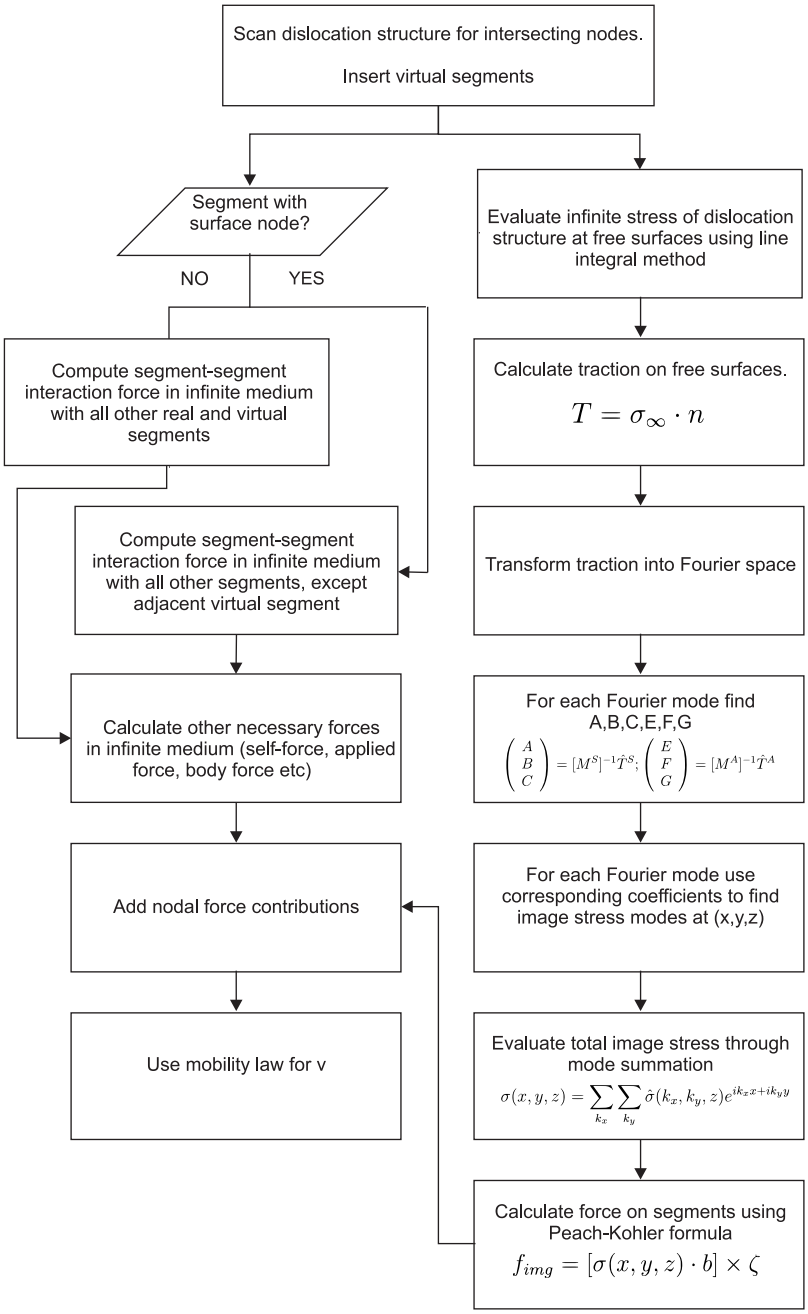

Figure 5.8: Algorithm flowchart for implementing free surfaces using spectral-methods. The geometry of the domain is constrained to be a thin film.

The dislocation segments within the thin film medium will be affected by this image stress. To account for this contribution, the image stress is evaluated at the mid-point of each dislocation segment, and the Peach-Koehler force is then multiplied by the segment length, and added to the other contributions (self-force, dislocation-dislocation interaction forces, body forces etc.), as shown in Figure 5.8. One can also integrate along segments for more precision.

5.4.3 Dislocations intersecting a free surface

When dislocation segments intersect the free surface, care must be taken in how the image stress is calculated. At every node i, the sum of Burgers vectors of all connecting segments must be conserved such that:

$$\sum_j b_{ij} = 0 \tag{5.33}$$

where b_{ij} is the Burgers vector of the segment ij starting at node i and ending at node j, and $b_{ij} = -b_{ji}$. As a result, all dislocations must form closed loops, for which unique analytical stress field expressions are valid. Since the DD algorithm uses the line integral method, whereby the infinite medium stress field computed for a given dislocation structure is correct only if the dislocation line is closed (i.e. a loop) or infinite, a terminating segment at the free surface would break this condition and lead to an erroneous stress calculation. For this reason, when calculating the infinite medium stress, one must extend terminating dislocation segments to infinity using *virtual segments*. In this implementation, the extensions follow the same direction as the terminating segments, as it has been shown to yield the lowest error [233], as shown in Fig. 5.7.

These virtual segments do not physically exist but are necessary to calculate the infinite (medium) stress correctly. Therefore, they will not be affected themselves by stresses or dislocation interactions. However, because they contribute to the stress field, they will affect all other *real* dislocations in the thin film and thus must

be included when calculating interaction forces on real segments. The exception is for surface nodes that are shared between a real segment and a virtual segment. In this case, the virtual segment must be excluded from the force on the surface node. Previous work by Refs. [233, 234] used standard singular continuum theory for the stress solutions. This required introducing additional semi-infinite straight dislocations with analytical expressions developed by Yoffe [235], such that, when superimposed on the original dislocation structure, the singularities in the calculated tractions near segments intersecting the free surfaces would cancel out. This was necessary because the singularities caused convergence difficulties in the image stress algorithms. However, by employing the non-singular continuum theory of dislocations [227], this approach is not necessary since the calculated tractions are already free from singularities due to a smoothing parameter in the stress equations. Fig. 5.8 shows how intersecting segments are treated within the broader image force calculation procedure.

5.4.4 Validation

Zero traction

An initial fundamental validation procedure is to evaluate the residual traction resulting from the superposition of the infinite body stress and image stress at a free surface. Any residual traction equates to the error. Unsurprisingly, this error decays rapidly with increasing Fourier modes (directly related to the number of discretisation points on the thin film used for infinite stress traction evaluation), as shown in Figure 5.9.

Fig. 5.10 shows that artefacts in the image stress disappear after $n_x = n_y > 50$. For fewer Fourier modes, there is an under-estimation of the peak stress as well as gradually bigger spurious oscillations caused by the premature truncation of terms in the Fourier series describing the image stress. Based on this, subsequent force calculations were performed at $n_x = n_y > 200$ to account for potentially larger

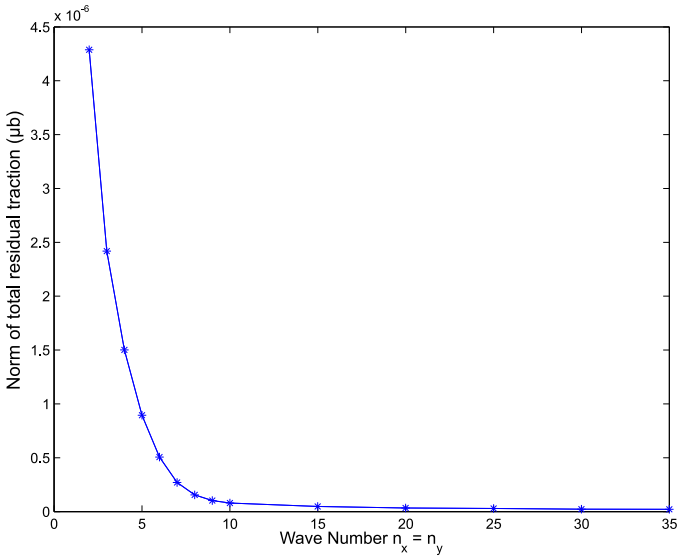

Figure 5.9: Norm of total residual x, y, z traction at free surface. Dislocation structure: $\langle 001 \rangle$ square loop, $125b$ side-length, in a thin film with $L_x = L_y = 5000b$, thickness $= 3000b$, contained in x-y plane at depth $1500b$.

stresses resulting from loops very close to the surface.

Edge Dislocation in Homogeneous Media

It was demonstrated that the code can impose a zero-traction condition on the free surfaces, with an error related to the number of discretisation points on the surface and thus the modes available in the Fourier transformation. However, this does not demonstrate whether the stress *inside* the thin film domain is calculated correctly. Therefore, I made a comparison with the analytical solutions for edge dislocations in a semi-infinite solid with a free surface developed in [236]. This article contains several misprints, and the correct analytical solutions are given in [237]. The calculated stress field matches very well, with a comparative plot given in Fig. 5.11.

There will be slight differences owing to the fact that the analytical solution is a half-space (and singular), and the computational one is a thin film (non-singular and dependent on a smoothing factor). However, to minimise this discrepancy, the ratio between dislocation line depth and the total thin film thickness was maximised.

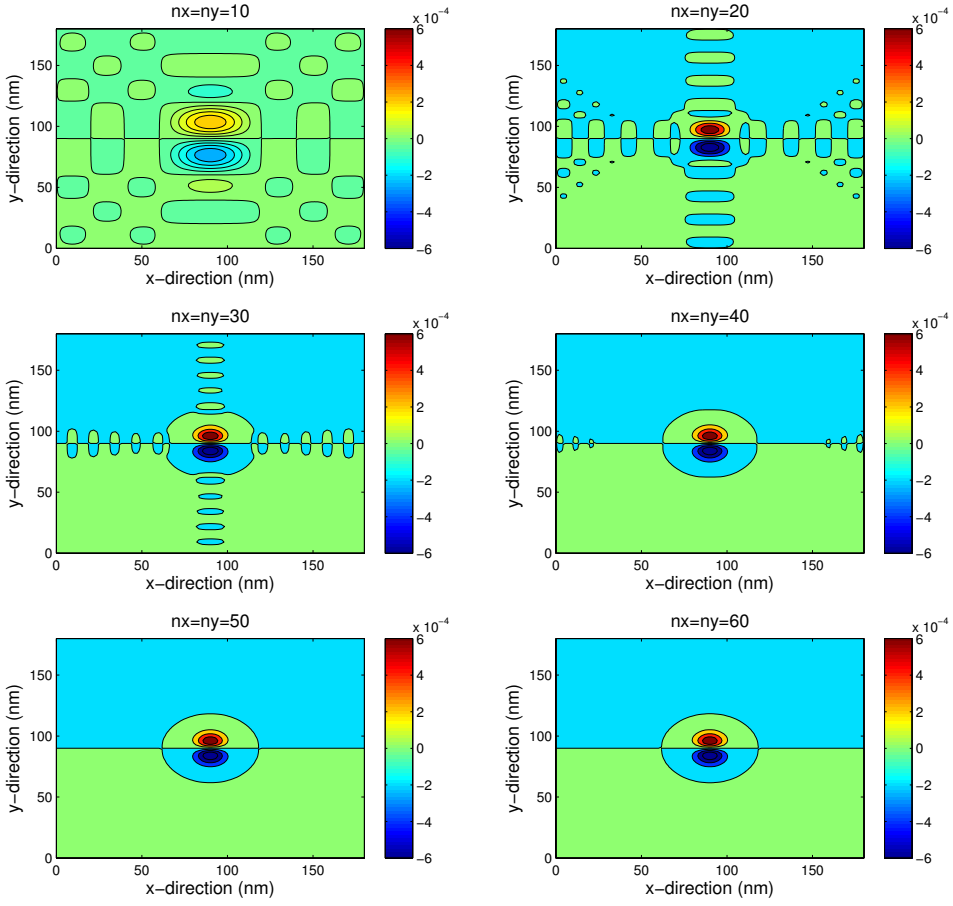

Figure 5.10: Image stress (σ_{xy} component) on thin film surface with increasing wave numbers (dislocation structure: circular [001] loop with 3nm radius at 14nm depth in a 28nm thick film, 180×180 nm surface grid, $\mu = 1$, $\nu = 0.305$)

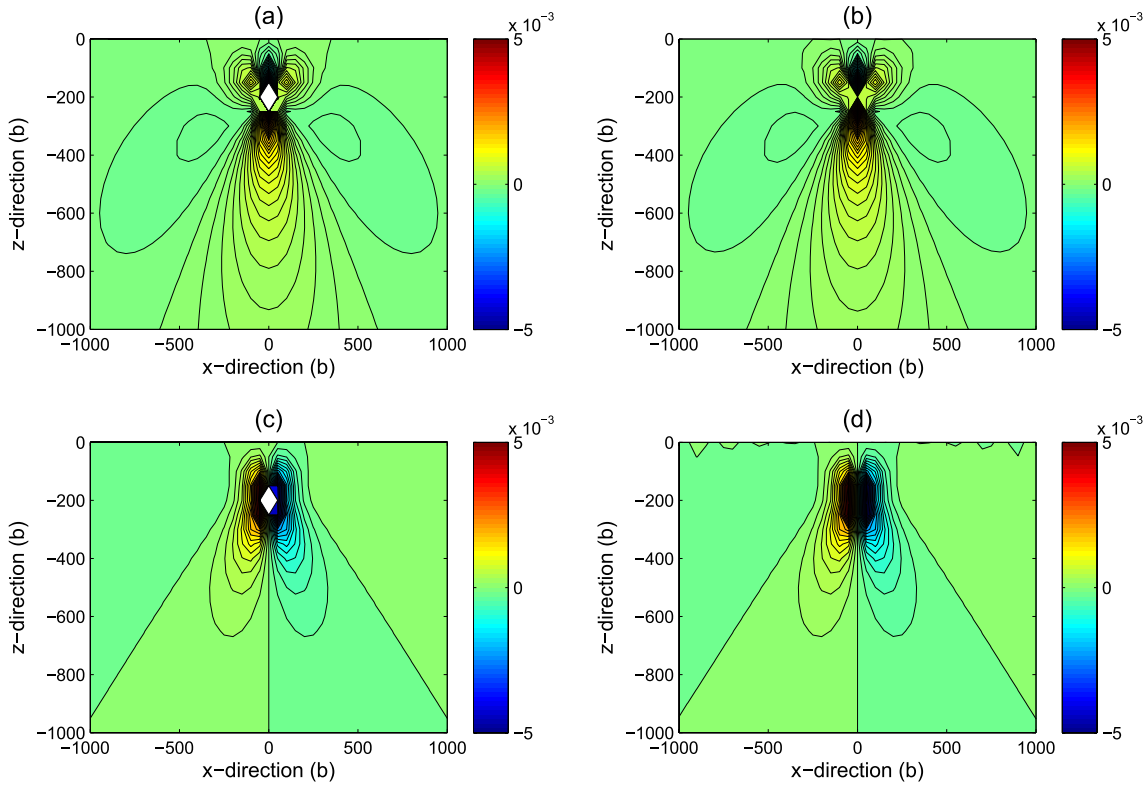

Figure 5.11: Comparison between analytical solution of [236] for the σ_{zz} component of the total stress (image+infinite body) resulting from a straight edge dislocation in a half-space for (a) Burgers vector parallel to the free surface and (c) Burgers vector perpendicular to the free surface. (b) and (d): corresponding numerical solution obtained with the spectral method implemented in a non-singular dislocation dynamics code. Dislocation structure: $10^4 b$ long edge dislocation, $200b$ depth in $20 \cdot 10^3 b$ thick film, $n_x = n_y = 150$, $\mu = 1$, $\nu = 0.305$.

Force calculations

A final validation was to compare the force calculated by the code with available analytical solutions. For the simplest, idealized cases Groves and Bacon [232] give an analytical formula for the variation with depth of the total force per unit segment length F^T of a square prismatic loop with a Burgers vector perpendicular to the surface as,

$$F^T = \frac{\mu b^2 y}{4\pi(1-\nu)h}\left(\frac{y^2+40y+768}{(y+16)^{5/2}} + \frac{16(105y^3+460y^2-544y-3072)}{(y+4)^3(5+16)^{5/2}}\right) \quad (5.34)$$

where a is the depth, h is the segment length and $y = h^2/a^2$. The code correctly matches this force profile as shown in Figure 5.12. The thin film simulation agrees well with the analytical half-space solution, since the film thickness was appreciably larger than the segment length (20×). According to Groves and Bacon, surfaces have short-range effects and only exert significant influence if $a \leq 3h$. For a given frictional force opposing dislocation motion, one is thus likely to see a characteristic depth denuded of dislocations close to the surface. Due to the nature of the non-singular stress formulation, depending on the magnitude of the smoothing factor, one will observe a peak in the force profile close to the free surface rather than a singularity. Therefore, in order to effectively compare the non-singular numerical solution to the singular analytical solution, it is necessary to keep the value of the smoothing factor of the same order of magnitude as the minimum distance the dislocation segments are allowed to travel near the free surface before being absorbed.

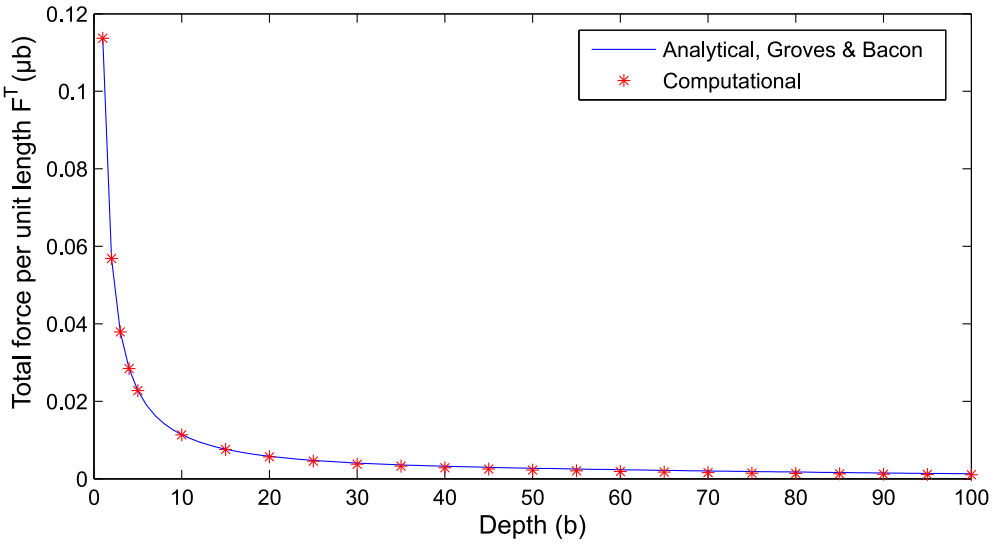

Figure 5.12: Variation with depth of total force per unit length of segment in square prismatic loop. (h=200b, μ = 1, ν = 0.305, b=1; Simulation parameters: L_x = L_y = 5000b, n_x = n_y = 200, thickness=4000b, smoothing factor for non-singular dislocation stress formula: 10^{-4}b)

5.4.5 Summary

- Analytical equations for image stress in a thin film were re-derived from [233] and implemented into computer code.
- A widely used dislocation dynamics code was modified to incorporate these equations and handle free-surfaces, for the case of a thin film.
- An optimised algorithm was tested and successfully validated against a number of parameters.

5.5 Simulating DD with mixed boundaries for any convex shape

Section 5.4 explained how to model free surfaces for a free-standing thin film within the context of a DD simulation, describing the theory, implementation and validation. The approach taken for a free-standing thin film is conceptually similar to the generalised procedure, except with added layers of complexity due to the generality of the problem. Section 5.5 will describe a procedure to handle arbitrary convex shapes, and any type of elastic boundary value problem (BVP). The additional considerations required for concave shapes will also be discussed.

5.5.1 Finite element method

To calculate $\hat{\sigma}$ for an arbitrarily complicated geometry, one option is to use the finite element method (FEM). The finite element method uses a displacement-based method in that it involves the determination of the unknown displacement field $\boldsymbol{u}(\boldsymbol{x})$.

Recalling Section 5.3, consider a body V, with boundary $\Gamma = \Gamma_u + \Gamma_t$, where displacements are specified on the displacement boundary Γ_u and tractions T on the traction boundary Γ_t. The equation of conservation of linear momentum, Eq 5.19, is given in its strong form. It is convenient to express this in its weak form, shown in Eq 5.35.

$$\sigma_{ij,j} = 0 \rightarrow \int_V \sigma_{ij} \delta u_{i,j} dV - \int_{\Gamma_t} \delta u_i T_i d\Gamma = 0 \tag{5.35}$$

where ∂u_i are the virtual displacements[4]. To solve Eq 5.35, one discretises domain V into small, discrete, finite-sized quadrilaterals. Along the sides of each element, one designates nodes which define the shape of the element. Here, quadrilaterals were used. The full collection of nodes and elements which represent the body V is known as the FEM mesh. The number of nodes in the mesh is N_n, and the

[4]A virtual displacement field can take any value, provided it is continuous and bounded (not infinite) over V and $\delta_i = 0$ on Γ_u

number of elements N_e. To obtain the unknown displacement field $u_i(x)$ within V, one defines the displacements using shape functions:

$$u_i(x) = \sum_{a=1}^{N_n} N_a(x) U_i^a \tag{5.36}$$

where U_i^a are the discrete unknown nodal displacements and $N_a(x)$ the known shape functions. With some mathematical rearrangements, one can write Eq 5.35 as 5.37.

$$\int_V \sigma_{ij} N_{a,j} dV = \int_{\Gamma_t} N_a T_i d\Gamma \tag{5.37}$$

where i ranges from 1 to 3 in a general three-dimensional case, and a ranges from 1 to N_n. In words, this is simply,

$$\text{Internal node forces} = \text{External node forces} \tag{5.38}$$

Now, recalling the constitutive equation 5.21 for linear elasticity $\sigma_{ij} = C_{ijkl}\epsilon_{kl}$, by substituting the small strain-displacement relationship 5.20 into ϵ_{kl}, and using the stiffness tensor's symmetry, one gets,

$$\sigma_{ij} = \sum_{b=1}^{N_n} C_{ijkl} N_{b,l} U_k^b \tag{5.39}$$

Substituting Eq 5.39 into the weak-form of the conservation of momentum equation 5.35, and re-writing it into a matrix equation yields,

$$\begin{aligned} K_{iakb} U_k^b &= f_i^a \\ \boldsymbol{KU} &= \boldsymbol{f} \end{aligned} \tag{5.40}$$

where $\boldsymbol{U}$ is the vector of unknown nodal displacements, $\boldsymbol{f}$ is the nodal force vector and $\boldsymbol{K}$ is the *global* stiffness matrix.

The global stiffness matrix can also be defined (through a similar derivation) as Eq 5.41,

$$\boldsymbol{K} = \int_V \boldsymbol{B}^T \boldsymbol{D} \boldsymbol{B} dV \tag{5.41}$$

where $\boldsymbol{D}$ is the elasticity matrix containing all the material properties, and $\boldsymbol{B}$ is the matrix containing all the derivatives of the shape functions.

5.5.2 Displacement calculations

To account for displacement boundary conditions on a surface Γ_u, one needs to be able to calculate the displacement $\tilde{u}$ due to the dislocation structure. For example, when a dislocation leaves a free surface, it may leave a displacement step. A visible example of this behaviour is slip bands on micro-cantilevers. *Hirth and Lothe* [186] give the equation for displacement $\boldsymbol{u}(\boldsymbol{r})$ at $\boldsymbol{r}$, for a closed dislocation loop C of Burgers vector $\boldsymbol{b}$ and area A as,

$$\tilde{\boldsymbol{u}}(\boldsymbol{r}) = -\frac{\boldsymbol{b}}{4\pi}\Omega - \frac{1}{4\pi}\oint_C \frac{\boldsymbol{b} \times d\boldsymbol{l'}}{R} + \frac{1}{8\pi(1-\nu)} \nabla \oint_C \frac{(\boldsymbol{b} \times \boldsymbol{R}) \cdot d\boldsymbol{l'}}{R} \tag{5.42}$$

where $R = |\boldsymbol{r'} - \boldsymbol{r}|$, and $\boldsymbol{R} = \boldsymbol{r'} - \boldsymbol{r}$, and $\Omega = -\int_A \frac{\boldsymbol{R} \cdot d\boldsymbol{A}}{R}$ is the solid angle through which the positive side of dislocation area A is seen from point $\boldsymbol{r}$.

It also includes a procedure to calculate the displacement field for a triangular dislocation loop, composed of straight dislocation segments, in an infinite isotropic solid. This is a more convenient formulation for the purposes of computer simulations, which deal with discretised straight dislocation segments. However, the prescription is problematic due to numerical issues associated with the inverse trigonometric functions appearing in the formulas for the solid angle, partly due to the fact that the loop field is constructed from individual segment fields and the solid angle is not uniquely defined for a line segment.

Barnett [238, 239] gives a more numerically-friendly formula.

$$\tilde{\boldsymbol{u}} = -\frac{\boldsymbol{b}\Omega}{4\pi} - \frac{(1-2\nu)}{8\pi(1-\nu)} \left[\boldsymbol{f}_{AB} + \boldsymbol{f}_{BC} + \boldsymbol{f}_{CA}\right] + \frac{1}{8\pi(1-\nu)} \left[\boldsymbol{g}_{AB} + \boldsymbol{g}_{BC} + \boldsymbol{g}_{CA}\right] \tag{5.43}$$

For a triangular dislocation loop ABC and a field point P, $\boldsymbol{R}_A$, $\boldsymbol{R}_B$ and $\boldsymbol{R}_C$ denote the vectors from P to the vertices A, B and C respectively, and the unit normal N to the plane ABC is chosen such that one traverses the triangular boundary from A to B to C counterclockwise, as seen by an observer looking in direction $\rightarrow \boldsymbol{N}$, as shown in Figure 5.13. Terms λ_A, $\boldsymbol{f}_{AB}$ and $\boldsymbol{g}_{AB}$ are given in Eq 5.44, with the remaining $\boldsymbol{f}$s and $\boldsymbol{g}$s obtained by cyclic interchange.

$$\begin{aligned}
\lambda_A &= \frac{\boldsymbol{R}_A}{R_A} \\
\boldsymbol{f}_{AB} &= (\boldsymbol{b} \times \boldsymbol{t}_{AB}) \ln \left(\frac{R_B}{R_A} \cdot \frac{1 + \lambda_B \cdot \boldsymbol{t}_{AB}}{1 + \lambda_A \cdot \boldsymbol{t}_{AB}} \right) \\
\boldsymbol{g}_{AB} &= \frac{[\boldsymbol{b} \cdot (\lambda_A \times \lambda_B]\,(\lambda_A + \lambda_B)}{1 + \lambda_A \cdot \lambda_B}
\end{aligned} \tag{5.44}$$

The remaining solid angle term Ω can be unequivocally calculated employing L'Huillier's Theorem, taking the form of Eq 5.45.

$$\Omega = -\mathrm{sgn}(\lambda \cdot \boldsymbol{N}) \tan^{-1} \sqrt{4 \tan\left(\frac{s}{2}\right) \tan\left(\frac{s-a}{2}\right) \tan\left(\frac{s-b}{2}\right) \tan\left(\frac{s-c}{2}\right)} \tag{5.45}$$

where $a = \cos^{-1}(\boldsymbol{\lambda}_B \cdot \boldsymbol{\lambda}_C)$, $b = \cos^{-1}(\boldsymbol{\lambda}_A \cdot \boldsymbol{\lambda}_C)$, $c = \cos^{-1}(\boldsymbol{\lambda}_A \cdot \boldsymbol{\lambda}_B)$, $s = (a+b+c)/2$, and λ can be either λ_A, λ_B, λ_C.

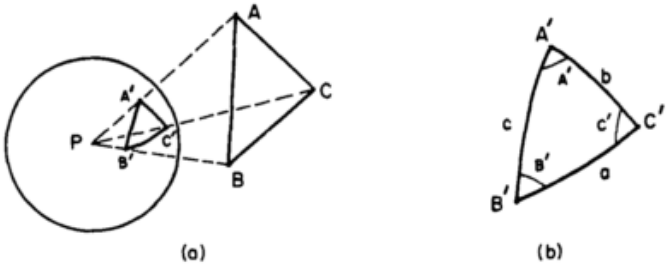

Figure 5.13: (a) The plane triangle ABC and its projection, the spherical triangle A'B'C', on the unit sphere; (b) the geometry associated with the spherical triangle A'B'C' [238].

Therefore, Eq 5.43 gives a displacement field due to a triangular loop, in a purely vectorial form dependent only on the Burgers vector, the tangent vectors of the

segments and the position of the field point. To employ this method in a discrete dislocation dynamics simulation, one would have to decompose a dislocation network structure into groups of triangular loops, as shown in Figure 5.14. Generally, one defines a closure point C_p in the middle of the loop, and then builds the triangles as having vertices at two ends of a dislocation segment and the centroid C_p. Each internal side of the triangle should be defined twice with two opposite directions such that their contribution to the displacement field will cancel each other leading to the calculation of the displacement of the closed loop structure.

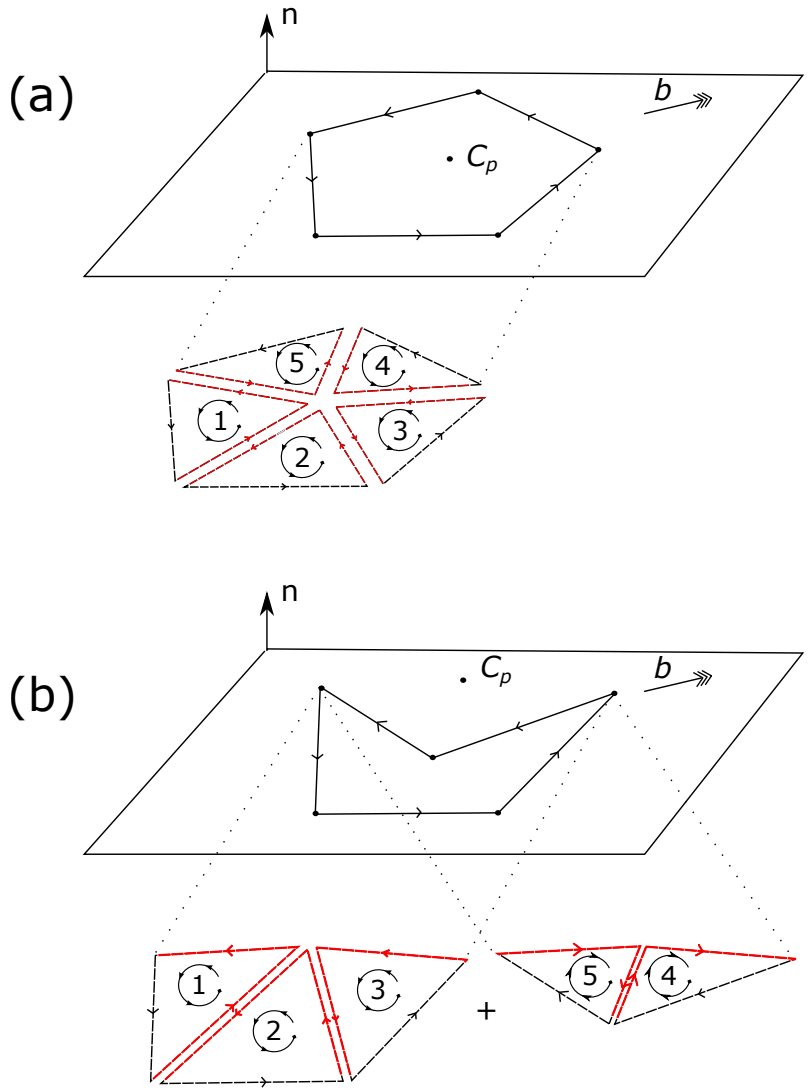

Figure 5.14: Decomposition of a dislocation loop into triangular elements for centroid inside (a) and outside (b) loop.

Although possible, this procedure is not ideal, since it requires a substantial amount of book-keeping to track evolving *closed-loop* dislocation structures, and a verbose

decomposition algorithm. Furthermore, it would strictly only be possible for loops that are *planar*. A more elegant method is proposed by Fivel [240], which does not require the aforementioned calculations of segment connectivity. This involves creating two triangles for each dislocation segment. In this way, each triangle would be closed by the orthogonal projection of the closure point on the line collinear to the Burgers vector and passing through the extremity of the segment. Taking a dislocation segment $\vec{\boldsymbol{AB}}$, with a Burgers vector $\boldsymbol{b}$, and denoting $\boldsymbol{A}_p$ as the projection of the closure point $\boldsymbol{C}_p$ on the line with direction $\boldsymbol{b}$ passing through $\boldsymbol{A}$, and $\boldsymbol{B}_p$ as the projection of the closure point $\boldsymbol{C}_p$ on the line with direction $\boldsymbol{b}$ passing through $\boldsymbol{B}$, the displacement field associated with segment $\vec{\boldsymbol{AB}}$ is given as the contribution of triangle $\boldsymbol{B_pAB}$ and triangle $\boldsymbol{A_pAB_p}$. Note that in the case of a pure screw dislocation, where the dislocation segment $\vec{\boldsymbol{AB}}$ is parallel to $\boldsymbol{b}$, the two triangle areas vanish and the segment contribution to the displacement field is zero.

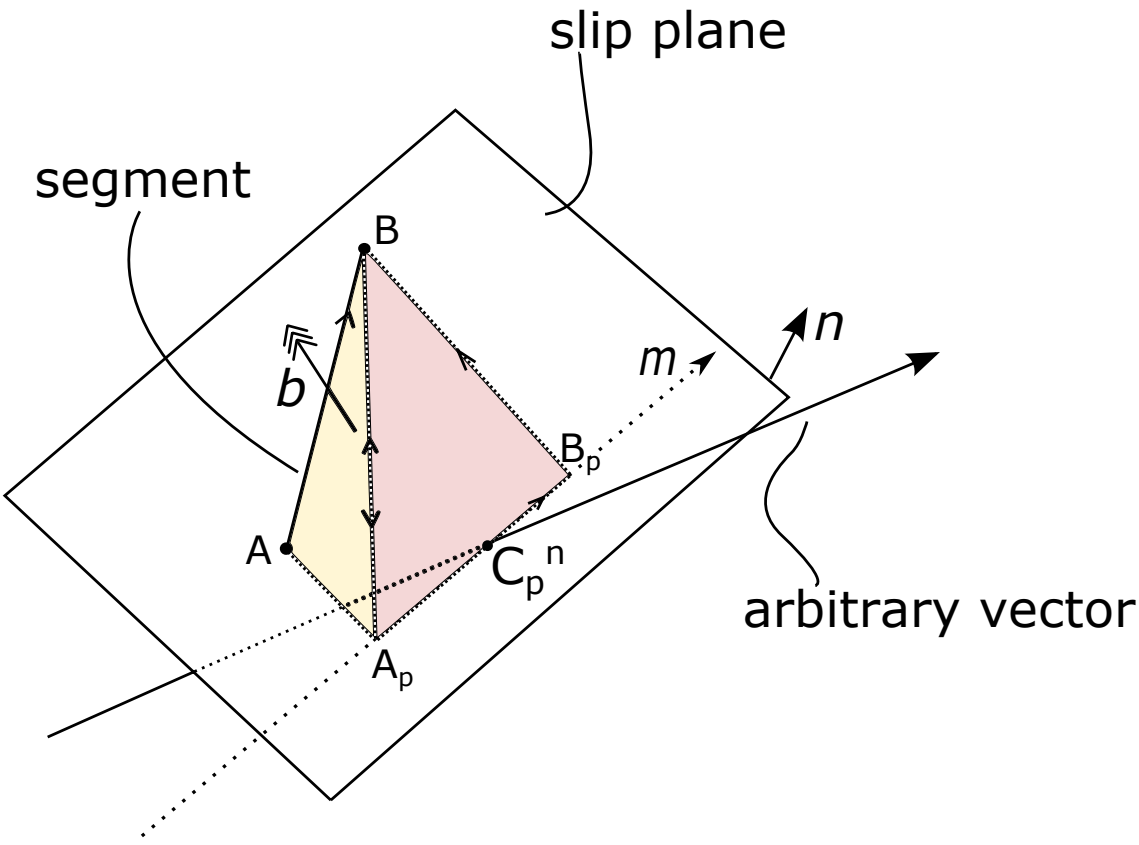

Figure 5.15: General Barnett triangle meshing algorithm to calculate displacement $\tilde{u}$ in DDD code for single segment with slip plane n and Burgers vector b. The arbitrary vector will result in a specific C_p for each slip plane. All segments on the same slip plane n must use the given C_p^n to construct the triangle pairs.

The general algorithm, for the displacement calculation at field point $\boldsymbol{r}$, for each dislocation segment $\vec{\boldsymbol{AB}}$, is given as (shown schematically in 5.16):

1. Calculate slip plane normal, $\boldsymbol{n} = \boldsymbol{l} \times \boldsymbol{b}$.

2. Calculate intersection point C_p between slip plane $\boldsymbol{n}$ and arbitrary vector (constant for each slip plane).

3. Calculate orthogonal projection of closure point $\boldsymbol{C}_p$ on the line collinear with $\boldsymbol{b}$ which passes through a node A, defined as $\boldsymbol{A}_p$, and node B, defined as $\boldsymbol{B}_p$. $\boldsymbol{AA_p}$ and $\boldsymbol{BB_p}$ are thus perpendicular to m.

4. Calculate displacement due to the contributions of the two triangles ($\boldsymbol{ABA_p}$ and $\boldsymbol{A_pB_pB}$; *or* $\boldsymbol{B_pAB}$ and $\boldsymbol{A_pAB_p}$, either works if kept consistent) associated with segment $\vec{\boldsymbol{AB}}$.

5. Add this contribution to total $\tilde{\boldsymbol{u}}(\boldsymbol{r})$, and proceed to next segment.

5.5.3 Description of Peach-Koehler force calculation algorithm for mixed BVPs

Previously, it was shown how to calculate image displacement $\hat{u}$ and image stress $\hat{\sigma}$ using the finite element method, using equations 5.43. The procedure to calculate displacements $\tilde{u}$ and stress $\tilde{\sigma}$ arising from dislocations in an isotropic infinite medium was also described. With all these separate solvers developed, one can successfully couple discrete dislocation dynamics and the finite element method, thereby allowing treatment of mixed boundary valued problems, on arbitrary meshed geometries. The coupling algorithm will now be reviewed.

For each time iteration,

1. **Create global stiffness matrices K_g and K_r.**

   K_g is the global matrix which includes boundary value elements. K_r is the *reduced global matrix* which excludes the boundary value elements. For a

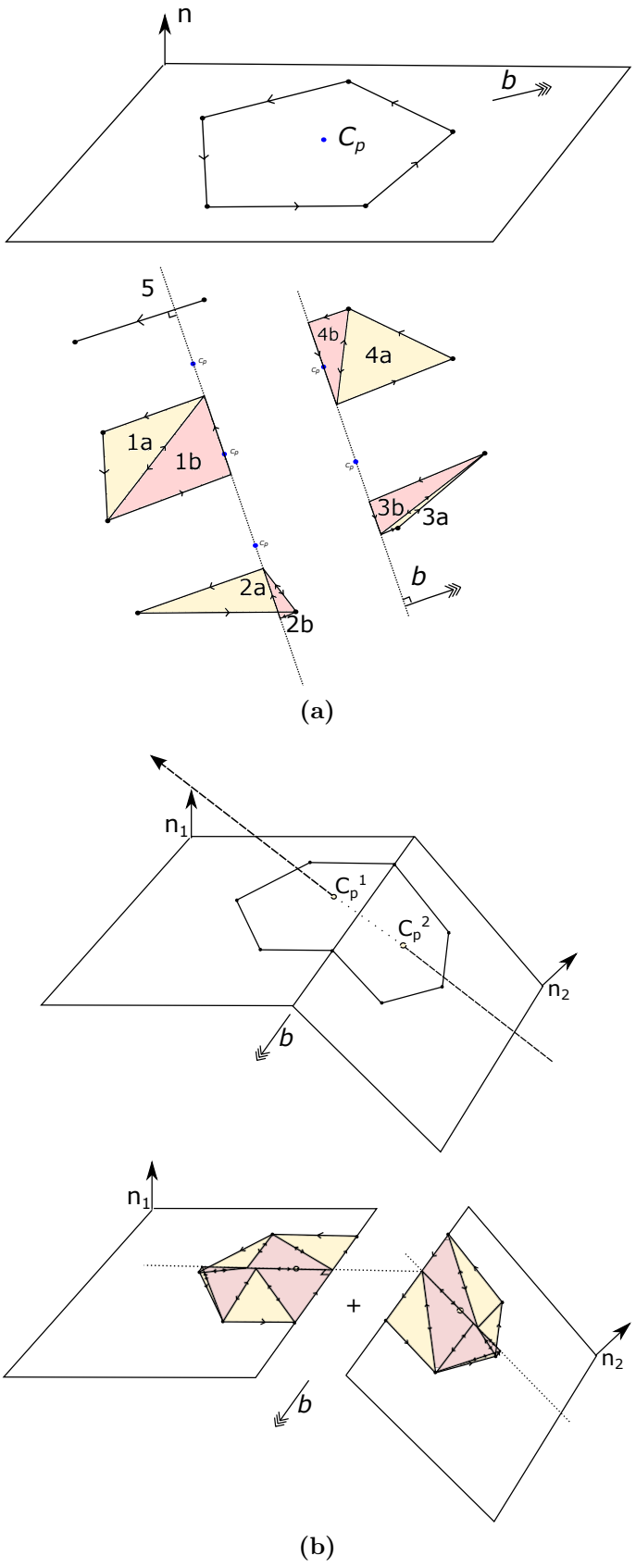

Figure 5.16: General Barnett triangle meshing algorithm applied to (a) a planar loop, and (b) a non-planar loop. By maintaining the C_p constant for each slip plane, adding segment displacement contributions will yield the correct global displacement field. Screw segments (parallel to Burgers vector) cause zero displacement.

general stiffness matrix K, recall Eq 5.41,

$$K = B^T D B$$

where B is the shape function derivative matrix, and D the elastic tensor. At small strains, $K_r^{t=0} \approx K_r^{t=end}$, so K can be decomposed using L-U decomposition for computational efficiency:

$$[L, U] = \mathrm{lu}(K_r) \sim \mathcal{O}(n^3)$$

2. **Calculate $\tilde{f}$ on Γ_t**

   Γ_t is the traction boundary, Γ_u is the displacement boundary. $\tilde{f}$ and $\tilde{u}$ depend on the dislocation network through analytical functions detailed previously in Eq 5.8.

3. **Calculate $\tilde{u}$ on Γ_u.**

   Γ_u is the displacement boundary. $\tilde{u}$ depends on the dislocation network through analytical functions detailed previously in Eq 5.43.

4. **Calculate image force $\hat{f}$.**

$$\hat{f} = f^{\mathrm{ext}} - \tilde{f}$$

   f^{ext} is the applied force, which depends on the boundary conditions input. If there are displacement boundary conditions one needs to correct for this in the image force, $\hat{f^{\mathrm{corr}}}$.

$$\hat{u} = u^{\mathrm{ext}} - \tilde{u}, \text{ on } \Gamma_u$$
$$\hat{f^{\mathrm{corr}}} = \hat{f} - K_g \hat{u}, \text{ on } \Gamma_t$$

5. **Calculate image displacement $\hat{u}$**

   Image displacement field $\hat{u}$ is calculated throughout the mesh by the FEM

code. N.B. This uses the corrected $\hat{f}$.

$$\hat{u} = K_r \backslash \hat{f}$$

If the L-U decomposition was carried out in Step 1., it is preferable to use the following to solve for image displacement, since the operations it requires to compute scales with $\sim 2\mathcal{O}(n^2)$ as opposed to $\mathcal{O}(n^3)$ for a standard matrix inversion.

$$\hat{u} = U \backslash (L \backslash \hat{f})$$

6. **Calculate image stress $\hat{\sigma}$.**

$$\hat{\sigma} = DB\hat{u}$$

where D is the elastic tensor, and B the shape function derivative matrix.

7. **Calculate Peach-Koehler force f_{PK}** The image stress $\hat{\sigma}$ at a segment midpoint can be used to calculate the Peach-Koehler force.

$$f_{PK}(\hat{\sigma}) = (\hat{\sigma} b) \times l$$

This force is added linearly to the other nodal forces.

$$f_{seg} = f_{PK}(\hat{\sigma}(\boldsymbol{x})) + f_{\text{seg-seg}} + f_{\text{self}}$$

The segments of the discretised dislocations now feel the presence of the mixed boundary conditions in a finite medium.

For a purely free-standing finite medium with free surfaces, the displacement boundary conditions are non-existent, so Step 3. can be ignored, and the correction of $\hat{f}$ need not be carried out. Therefore this finite element method approach can also be used to simulate a thin film geometry given in Section 5.4.

5.5.4 Handling dislocations exiting arbitrary convex domain

General considerations

Handling exiting dislocations in the case of the finite element method approach for mixed boundary values is more complicated than in the thin film case. This is because an exiting dislocation cannot simply be deleted, and replaced by a single semi-infinite segment if the displacement field is to be evaluated correctly. Rather, the exiting segments must be stored in the simulation after being moved far away from the surface - this way, the displacement steps on the surface of the domain are correctly represented in the displacement calculations. In general, there are a few things to remember:

- Exiting segments are moved to infinity (practically, a large distance from the free surface).

- Connectivity of the exited segments to the dislocation structure in the domain should remain the same.

- The exited segments should be *fixed* at "infinity" and not allowed to move, although surface nodes must remain mobile.

- The exited segments should *not* be considered in the calculation of image stress $\hat{\sigma}$, since they are not real and therefore not interact with dislocations within the domain.

- The exited segments *should* be considered in the calculation of image displacement, since although they are not real, their exit has affected the surface topology by leaving a step.

- To prevent the simulation from becoming too slow due to excessive storage of exited elements, the exited dislocation structures should be re-meshed periodically to reduce unnecessary segment discretisations.

Algorithms exist to consider 2D *concave* domains [151], but become cumbersome in 3D.

5.5.5 Description of re-meshing algorithm

In addition to the normal re-meshing routines to handle topological changes of the dislocation network due to interactions, junction formation, and annihilation, further routines to appropriately handle the exiting of dislocations have been added, for a convex general surface. For the sake of clarity, one should emphasise the difference between *surface meshing* and *dislocation meshing*. The first relates to how the surface finite elements are meshed, whereas dislocation meshing refers to the procedures to account for topological changes of the dislocations.

Step 1: Delaunay triangulation of surface mesh nodes

The surface enclosing the domain Ω can be defined by the surface nodes of the finite elements making up the structure. Due to the popularity of the finite element and boundary element method, automatic surface meshing algorithms are highly developed and efficient. The Delaunay triangulation method was employed to create a set of triangles to use as surface polygons, as shown in Figure 5.17. Each surface triangle is fully defined by its surface normal $\boldsymbol{n}$, the element midpoint and vertices locations. Because of the small strains applied to these coupled FEM/DDD simulations, it is reasonable to assume that the surface mesh does not change appreciably throughout the simulation. As such, the surface triangulation was pre-computed at the beginning of the simulation, and accessed from memory. Nonetheless, it is relatively simple to change the algorithm to update the mesh periodically if the magnitudes of strain are more substantial, at the expense of performance as shown in Table 5.1.

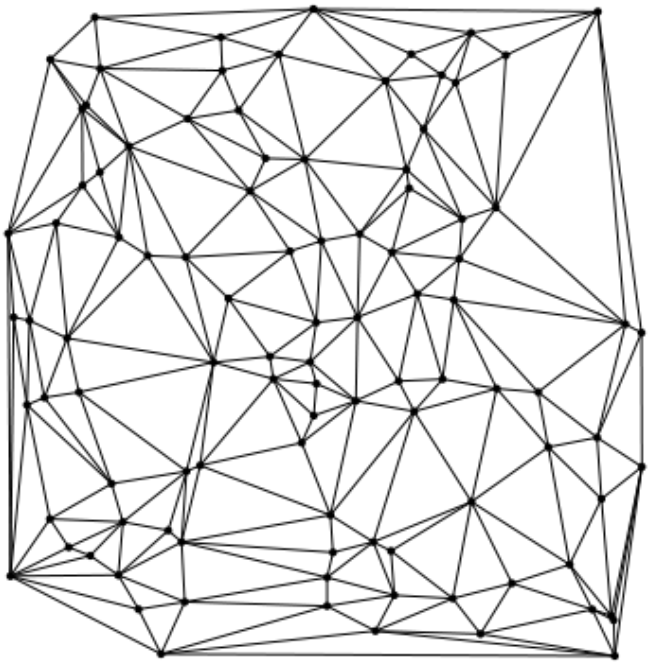

Figure 5.17: A Delaunay triangulation of 100 random points on a 2D surface.

Number of surface mesh nodes	10^1	10^2	10^3	10^4	10^5	10^6
Time for triangulation (s)	0.0169	0.0017	0.0156	0.2312	4.0780	83.2425

Table 5.1: Time (s) taken for a Delaunay triangulation of a given number of random nodes, using built-in Matlab functions (Version 2014b) and a 2.3GHz Intel Core i7 processor.

Step 2: Check whether dislocation line nodes are *outside* the finite element domain

At every iteration, one has to check whether dislocation segments in the finite domain have moved outside, either entirely or at one end. This is achieved by a function called *inhull.m*, which checks the positions of the segment nodal list versus the domain surface defined by the Delaunay triangle list, and gives a logical array where points are outside or inside the convex domain. This is done very efficiently by converting all the facets of the convex surface into linear inequalities, such that the calculation essentially reduces to a large, sparse matrix multiplication. This approach is possible only if the object is convex. To carry out this test in a concave domain, the surface tessellations would have to be converted into a list of simplexes that fill the region. A point would be inside the surface if it is inside any of the component simplexes. Alternatively, a ray-tracing method could be utilised. Both would be less computationally efficient than the current implementation.
The dislocation segments which have one or both nodes outside of the domain Ω are flagged with a logical array associated to the nodal list, and subsequently handled by the re-meshing algorithm for exiting dislocations. An example is given in Figure C.5.

Step 3: Remesh the dislocation segments which are outside the domain or intersecting the surface

In Step 2, the list of segments intersecting the surface or outside the domain is extracted from the global segment list. For each segment in this reduced list, the re-meshing algorithm calculates whether one or both nodes of the segment is outside the domain. If only one node is outside, it calculates the point where the segment intersects the surface, and adds a node at this point, thereby *splits* the segment into two connected segments, updating the connectivity list. If both segments are outside the domain, it calculates the intersection points to the surface of the segments connected to it and similarly inserts extra nodes at the surface intersection points.
The surface to calculate the intersection with a segment is chosen by checking which

triangular tessellation the segment intersects with. The information on the particular tessellation, particularly the surface normal $\boldsymbol{S}$, is subsequently used to define the surface. This calculation can be done either geometrically, or numerically by finding the minima of the distances between the exited node and the triangle centroids. The latter approach is substantially faster, but its accuracy depends on the degree of the surface discretisation.

Step 4: Extend the virtual nodes to pseudo-infinity

Once the segment connectivity lists are updated to account for the added nodes, the nodes which were flagged in Step 2 as exited are extended to pseudo-infinity (i.e. by a fixed length, generally a multiple (5-10×) of the largest dimension of the domain). The extension is done in the direction (p_i) of the projection of the segment slip plane normal (n_i) on the surface plane normal (S_i). This ensures that the segment is not extended in a direction where it would potentially re-enter the domain, and still effectively move in its preferred slip direction. Mathematically, the simple calculation in Eq 5.46 is performed:

$$\begin{aligned} P_{ij} &= n_i n_j \\ p_i &= S_i(\delta_{ij} - P_{ij}) \end{aligned} \tag{5.46}$$

Step 5: Pin virtual nodes, mark surface nodes, and coarsen virtual segments if possible

Once the exited nodes of the dislocations have been extended to pseudo-infinity, the algorithm "pins" these nodes, by assigning them a numerical flag which defines them as immobile *and* outside the domain. These are referred to as virtual nodes, and are excluded from any velocity calculations. Similarly, the surface nodes that were added in Step 3 are assigned a numerical flag which defines them as surface nodes. This is necessary when calculating the forces on the node, as explained in

Section 5.4.3.

Once this is done, the virtual segment network (i.e. all the segments that are flagged as virtual nodes) is coarsened, if possible. This is attempted by looking at the minimum length of segments, to see if they are below a certain length threshold, and the curvature between segments. The checks are essentially similar as for the re-meshing of the dislocation network *inside* the domain.

5.5.6 Validation

In this section, the code's applicability is demonstrated via a case study example. The case study will be a 3D single crystal tungsten micro-cantilever with mixed boundaries: free surfaces, applied end load, and fixed base. Due to thesis length constraints, detailed validations for the 3D FEM-coupled mixed-boundary dislocation dynamics software are confined to the Appendix C.

Example simulation

Figure 5.18 simulates a cantilever being loaded at the free end. This is an extension of 2D work [151], and demonstrates added functionality (displacement boundaries) to existing state of the art 3D codes like [150].

Figure 5.18 shows a number of effects:

- A transition on the force-displacement curve, from purely elastic to elasto-plastic. During the elastoplastic regime, the response gradient is shallower (compared to the elastic region which is determined by the Young's modulus of the material). Also, fluctuations in the force response caused by exiting dislocations and shearing of material can be observed.

- The code correctly simulates the activation of dislocation sources. At zero load, there are no active dislocation sources. By increasing load, the sources in the highest stress regions are progressively activated, from the fixed end moving towards the free end. This occurs because the highest stresses are

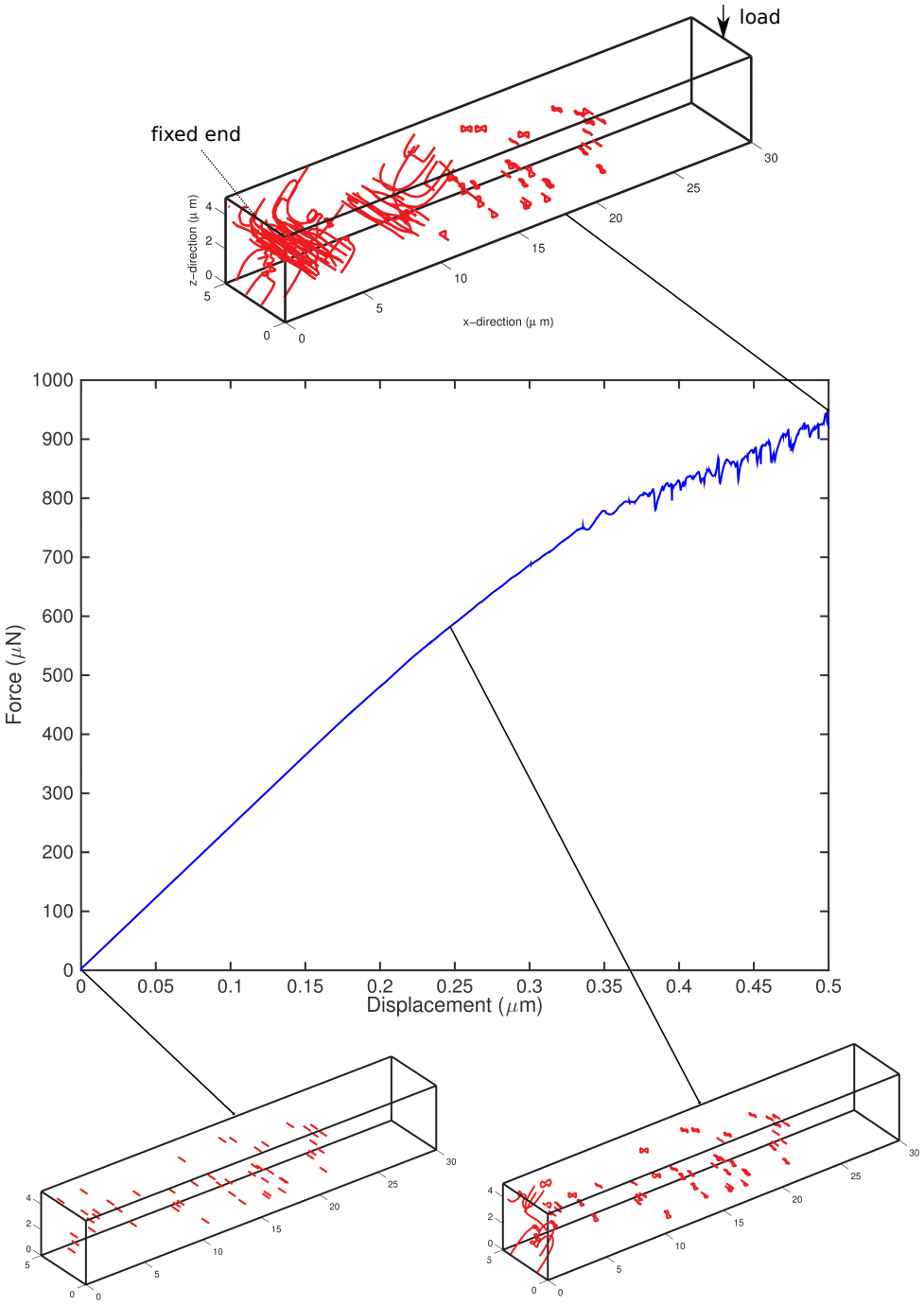

Figure 5.18: Load displacement curve of a 30x5x5μm rectangular cantilever of single-crystal tungsten (160GPa, ν=0.305, τ_{nuc}=110MPa), with the dislocation structure shown at various intervals. The starting condition was 50 randomly distributed sources (prismatic loops) with $\boldsymbol{b} = \frac{1}{2}[101]$ and slip plane $\boldsymbol{n} = [\bar{1}01]$. *Virtual* loops of each were also added outside the boundary, with the same habit plane and glide cylinder, but an opposite line direction (not pictured). The loading was on the right face (x=30μm), with a fixed *displacement* boundary condition on the left face (x=0μm), with all other surfaces free. The crystallographic directions of the beam were x = [100], y = [010], z = [001].

near the fixed-end of the cantilever and close to the top and bottom surfaces, as shown in Figure 5.19.

- As dislocation lines multiply, they can be seen forming pile-ups (known as soft pile-ups), for example along the neutral axis of the cantilever beam (where the stress due to bending is zero).
- The exiting dislocations cause a shearing of the material along the slip planes. This can be calculated and fully quantified, as shown in Figure 5.20.

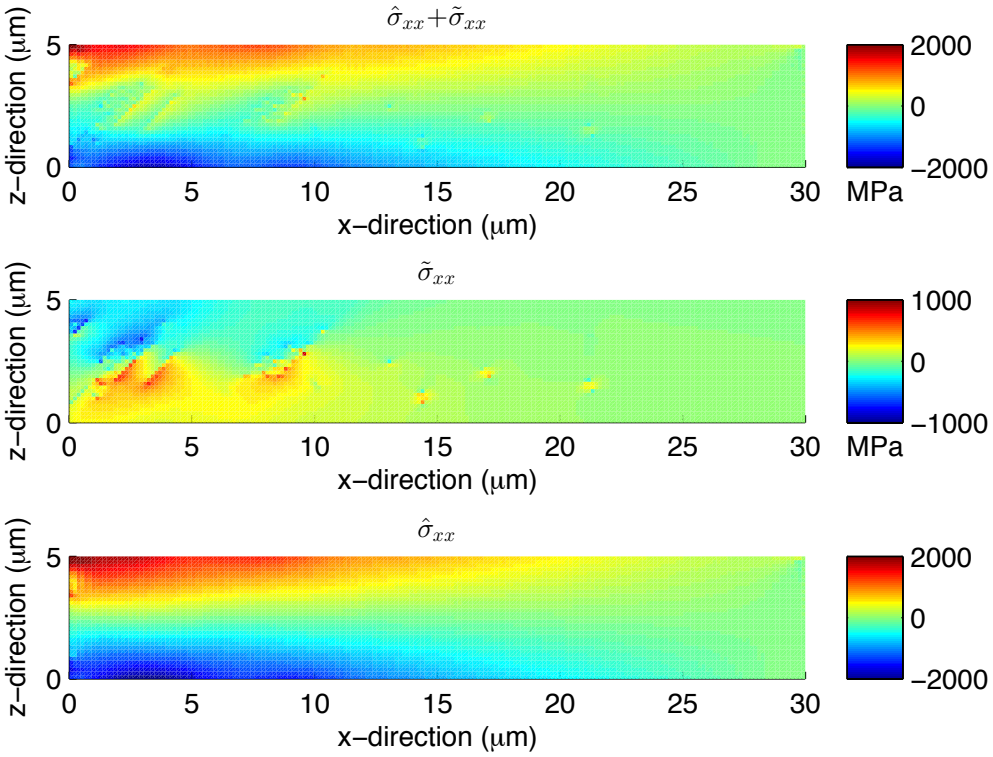

Figure 5.19: Stress component σ_{xx} for cantilever in x- and z- directions, taking a half-section in the y-direction. (a) is total stress, (b) is $\tilde{\sigma}_{xx}$, and (c) is $\hat{\sigma}_{xx}$. The predicted stresses are similar to 2D work such as [151]

.

The simulation technique is not without caveats. To accurately predict the load-displacement curve of a material, one needs to first fit two important parameters: dislocation source nucleation stress τ_{nuc} and dislocation source density ρ_{source}. The first affects the yield point of the material: a higher nucleation stress will result in a higher yield point. This directly affects the dislocation source length, given by

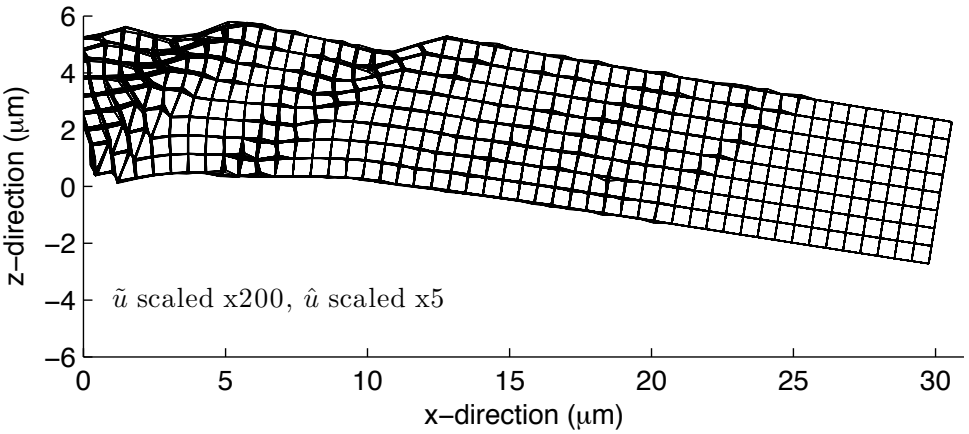

Figure 5.20: Deformation u of cantilever mesh, which is composed of $\tilde{u}$ magnified by 200× and $\hat{u}$ magnified by 5× for clarify. One can observe the appearance of slip bands (due to $\tilde{u}$) where sources where activated and dislocation lines exited, as well as beam bending (due to $\hat{u}$).

$$L_{\text{nuc}} = \frac{\mu b}{2\pi(1-\nu)\tau_{\text{nuc}}} \tag{5.47}$$

The second parameter, the dislocation source density, will instead affect the slope (in σ vs ϵ) of the plastic deformation region: a higher density will cause more plastic slip, flattening the curve. A cantilever with no dislocation sources will behave perfectly elastically. Therefore, both parameters need to be fitted to pre-existing experiments on the material in question. This has been done for 2D cases [151] where experimental σ-ϵ curves where fitted using first τ_{nuc}, then dislocation density. Each dislocation source was assigned a random τ_{nuc} nucleation stress from a normal distribution with given average and standard deviation. In the 3D case, this can be repeated by simply varying the dislocation source *length* L_{nuc}.

5.5.7 Summary

In this section, the development of a mixed boundary condition FEM-DD coupling, that is capable of handling arbitrary convex geometries is detailed. Briefly,

- The forces on dislocation nodes due to surface boundaries are calculated via a finite element method, by constructing an appropriate stiffness matrix (K), shape function derivative matrix (B), elastic tensor (D) and solving $\hat{\boldsymbol{f}} = \boldsymbol{K}\hat{\boldsymbol{u}}$ and $\hat{\boldsymbol{\sigma}} = \boldsymbol{DB}\hat{\boldsymbol{u}}$, taking into account appropriate corrections for traction and displacement boundaries.

- The displacements due to dislocations are calculated using analytical equations developed by Barnett [238, 239], and an algorithm developed by Fivel [240].

- The surface is accounted for by Delaunay triangulation of the nodes of the surface elements of the finite element mesh, and an appropriate algorithm designed for convex shapes is used to re-mesh the dislocation network accordingly.

- It can model stress-driven dislocation motion in a confined domain. Dislocation behaviour observed matches that found in literature on cantilevers, replicating features such as slip bands, soft pile-ups and stress-strain curves characteristic of plastic deformation effects [241, 242, 243, 151, 150].

Chapter 6

Modelling of radiation damage recovery: stochastic dislocation dynamics and molecular dynamics simulations

The previous chapter extended a dislocation dynamics software package to include mixed displacement and traction boundary conditions, necessary to model thin films, via an optimized spectral methods algorithm or a more general finite element based technique. This chapter will instead focus on improving the treatment of dislocation *mobility*, particularly regarding temperature. It will firstly look at developing a stochastic implementation of the discrete dislocation dynamics model, to accommodate thermal effects in a more explicit way. Secondly, it will look at molecular dynamics simulations of loop mobility, and how such information can be used to help parametrize a stochastic DDD code.

6.1 State of the art: simulating thermally driven dislocation behaviour in discrete dislocation dynamics

As covered in the literature review in Chapter 1, there are a number of techniques to model dislocation behaviour, mainly atomistic and continuum-based. Several *atomistic* studies have looked at thermally driven diffusion of radiation defects in various metals and specifically in tungsten (crowdions and vacancies [160, 244, 162], kink diffusion [156]), and more generally the effect of temperature on dislocation mobility [245]. Kinetic Monte Carlo simulations have been employed to study defect recovery stages in annealing (though in bcc-iron, not tungsten [135]), and also thermally-activated screw dislocation motion [158]. Recently, inroads have been made to develop atomistically-informed continuum-based stochastic models of dislocations using Langevin dynamics [157, 159].

Discrete dislocation dynamics, described extensively in Chapter 5, is deterministic in its classical form, with temperature indirectly being accounted for (or not at all) as a variation in the global dislocation mobility parameters[1]. These global dislocation mobility parameters are ideally informed by experiments [246, 247], or molecular dynamics simulations [248, 148, 249, 155]. This approach may be suitable for simulations where *stress-driven* dislocation motion is dominant, but for other scenarios, like annealing of free standing thin films, it falls short of replicating observed behaviour. Elastically driven motion due to dislocation-dislocation interactions, or free surfaces are important, but they act in conjunction with thermally-driven effects. Continuum models based on bulk diffusion of vacancies [188, 191] have been developed to model thermally-activated dislocation climb in a DDD context, and show some success modelling coarsening, but only when coupled with a dual time-step to account for short scale glide effects and long term climb effects. This has been incorporated into the DDD model used[2].

[1] In some codes, the likelihood of dislocation cross-slipping is treated as a temperature-dependent probability sampled by a random number generator [138]

[2] This involved introducing an osmotic force which depends on temperature and vacancy under or super-saturation. Due to the fact that in in-situ annealing experiments no Ostwald ripening

However, since thermal effects are inherently *stochastic*, other observed behaviours like loop hopping, loop drift and accelerated coalescence due to thermal fluctuations (which cause Brownian-like motion and thus effect the defect evolution), are lost. No published literature on discrete dislocation dynamics describes this functionality. By adding it, one should observe diffusive thermal motion of dislocation structures within a DDD context and, perhaps more importantly, create a stochastic framework for dislocation mobility, allowing the addition of other thermal effects if necessary.

mechanism was observed, this force appears to be negligible for such physical conditions

6.2 Stochastic Dislocation Dynamics

6.2.1 Brownian motion

In order to better account for thermally-driven processes described above, a stochastic term is added to the partial differential equation describing dislocation motion, making it into a *stochastic differential equation* (SDEs). SDEs are used to model diverse phenomena from changing stock market prices to physical systems involving thermal fluctuations. Because stochastic descriptions of dislocations have been successfully used to model kink diffusion [156], nanoscale defects [139], and thermally activated screw dislocation motion [158], this approach seems reasonable.

6.2.2 Langevin equation example

The time evolution of the position of a dislocation segment is best described using the Langevin equation, an equation which involves a random force representing the effect of thermal fluctuations. For clarity, consider the simple case of a Brownian particle moving in 1D, which is not acted upon by any other force apart from those arising from thermal collisions. Recall Newton's second law of motion as Eq 6.1,

$$m\frac{dv}{dt} = F \tag{6.1}$$

where m, v and F are the mass, velocity and force acting upon the particle. In a Langevin equation, the force F can be split into two parts. The first is frictional force F_d (viscous drag) which represents the friction experienced by the particle, proportional to the velocity of the particle as in Eq. 6.2 (recall the force-velocity relationship of dislocation motion).

$$F_d = -Bv \tag{6.2}$$

where B is the drag/friction coefficient. The second part is a random force $F_s(t)$ which does not depend on the motion of the particle. This is generated from Gaus-

sian white noise (or from other distributions), fulfilling stochastic conditions such as time-average of zero, and δ-correlated force[3] such that:

$$\langle F_s(t)\rangle = 0\langle F_s(t)F_s(t')\rangle = 2BT\delta(t-t') \tag{6.3}$$

where $\delta(t)$ denotes the Dirac delta function, t and t' are different times, $\langle\rangle$ denotes the expectation value, and T is absolute temperature.

Therefore, Newton's second law of motion can be written in the Langevin form in Eq 6.5

$$m\frac{dv}{dt} = -Bv + F_s(t) \tag{6.4}$$

When the particle is also acted upon by an external force F, one can simply say,

$$m\frac{dv}{dt} = F - Bv + F_s(t) \tag{6.5}$$

The Langevin equation is thus an applicable prototype description for coarse-grained molecular systems, reducing to conservative particle motion when $B \to 0$, and also describes dissipative dynamics of particles in the limit $T \to 0$, i.e. no Brownian motion.

6.2.3 Generalised Langevin formulation and numerical integration via Suzuki-Trotter decomposition

The previous section explained the Langevin equation through a simple 1D equation of Newton's 2nd law of motion. However, this approach can be generalized to any differential equation with a deterministic and stochastic term. Consider a first-order differential equation of the form

$$\frac{d\boldsymbol{\phi}}{dt} = \hat{A}\boldsymbol{\phi} + \hat{B}\boldsymbol{\phi} = (\hat{A}+\hat{B})\boldsymbol{\phi} \tag{6.6}$$

where $\boldsymbol{\phi}$ is a vector variable, and $\hat{A}$ and $\hat{B}$ are operators acting on $\boldsymbol{\phi}$. $\hat{A}$ is the

[3] i.e. F_s(t) is correlated only at one single moment of time

deterministic operator, and $\hat{B}$ is the *stochastic* operator. The formal solution to the above equation is

$$\boldsymbol{\phi}(t) = \exp[(\hat{A} + \hat{B})t]\boldsymbol{\phi}(0) \tag{6.7}$$

The following is *not* true, due to the nature of operator products.

$$\exp[(\hat{A} + \hat{B})t]\boldsymbol{\phi}(0) \neq \exp[\hat{A}t]\exp[\hat{B}t]\boldsymbol{\phi}(0) \tag{6.8}$$

In other words, $[\hat{A}, \hat{B}] \neq 0$. Instead, using Suzuki-Trotter decomposition (STD) [250], one can transform the evolution operator into

$$\exp[(\hat{A} + \hat{B})t]\boldsymbol{\phi}(0) \approx \exp(\hat{B}t/2)\exp(\hat{A}t)\exp(\hat{B}t/2)\boldsymbol{\phi}(0) \tag{6.9}$$

where the numerical error associated with the transformation is of the order $\mathcal{O}(t^3)$. This efficient and accurate method allows for a separation in the evaluation of deterministic and stochastic terms in the integral. Furthermore, integration algorithms involving the Suzuki-Trotter decomposition are known to accumulate small numerical error over long time intervals due to their symplectic nature [250, 251]. Practically, this is implemented in the following way [250]:

1. Add half of the contribution from the stochastic operator term $\hat{B}$, sampled from a standard normal distribution, updating positions.

2. Add the entire contribution from the deterministic operator term $\hat{A}$, evaluated at updated positions. This updates the motion based on elastic interactions.

3. Add the remaining half of the contribution from the stochastic operator term $\hat{B}$, using the same sample of Step 1, further updating the positions. For the subsequent iteration, a new sampling is used.

The evaluation of the stochastic operator relevant to the newly developed stochastic dislocation dynamics shown here is explained in more detail in Section 6.2.4. The

evaluation of the deterministic operator, the velocity due to classical dislocation dynamics force interactions, is explained in previous Chapter 5, Section 5.2.

6.2.4 Incorporating Langevin formulation into DD algorithm

To evaluate stochastic contributions within a dislocation dynamics context requires some consideration, due to problems stemming from the nature of discrete dislocations:

- Dislocations are idealised as segments with a given connectivity, not as individual particles with a characteristic mass, as in a standard Langevin equation.
- Dislocations move preferentially in certain directions, as defined by the crystallographic structure of the matrix and the characteristics of the dislocation segment (anisotropic mobility).

To tackle these, for every iteration in the dislocation dynamics code, a 3D random force term is generated *for each node* i in the dislocation structure. In other words, a $L \times 3$ matrix is sampled from a normal distribution $\mathfrak{N}(0,1)$, where L is the number of nodes, for x, y and z directions. This is then scaled by a prefactor $\sqrt{2k_BT}$ to give a Gaussian distribution $X \sim \mathfrak{N}(0, 2k_BT)$, where k_B is Boltzmann's constant and T is temperature in Kelvin. The expression for the stochastic force is thus [252],

$$F_s^i = \sqrt{2k_BT}\mathfrak{N}(0,1) \tag{6.10}$$

The dislocation dynamics algorithm numerically integrates velocity, so the random force term for each dislocation node i needs to be converted into a velocity. This is done in a similar same way to the deterministic part by using the drag coefficient tensor $\mathfrak{B}$ described in Chapter 5. In a simple 1D case where $\mathfrak{B}$ is scalar B,

$$v_s^i = \sqrt{2k_BT/B}\mathfrak{N}(0,1) \tag{6.11}$$

For a 3D case, $\mathfrak{B}$ is a 3×3 matrix depending on crystallography (BCC or FCC

lattice), segment orientation and type (edge, screw, mixed). For the stochastic velocity, one is interested in the square root of the drag coefficient tensor $\mathfrak{B}$ (see Eq. 6.11). This can be computed by diagonaliation of $\mathfrak{B}$. A matrix $\mathfrak{B}$ is diagonalizable if there is a matrix $\boldsymbol{V}$ and a diagonal matrix $\boldsymbol{D}$ such that $\mathfrak{B} = \boldsymbol{V}\boldsymbol{D}\boldsymbol{V}^{-1}$. If $\mathfrak{B}$ has n eigenvectors which constitute a basis for $\boldsymbol{C}^n$, then $\boldsymbol{V}$ is chosen to be the matrix with the n eigenvectors as columns (three in this case), and $\boldsymbol{D}$ a diagonal matrix containing the eigenvalues λ_1, λ_2, λ_3.

$$D = \begin{pmatrix} \lambda_1 & 0 & 0 \\ 0 & \lambda_2 & 0 \\ 0 & 0 & \lambda_3 \end{pmatrix} \tag{6.12}$$

Furthermore, because $\mathfrak{B}$ is symmetric, matrix $\boldsymbol{V}$ is an orthogonal matrix, so the inverse of $\boldsymbol{V}$ is simply its transpose, $\mathfrak{B} = \boldsymbol{V}\boldsymbol{D}\boldsymbol{V}^T$. The square root of $\mathfrak{B}$ is thus,

$$\sqrt{\mathfrak{B}} = \boldsymbol{V}\sqrt{\boldsymbol{D}}\boldsymbol{V}^T = \boldsymbol{V} \begin{pmatrix} \sqrt{\lambda_1} & 0 & 0 \\ 0 & \sqrt{\lambda_2} & 0 \\ 0 & 0 & \sqrt{\lambda_3} \end{pmatrix} \boldsymbol{V}^T \tag{6.13}$$

To solve for v_s, rather than calculating $\sqrt{\mathfrak{B}}$ and then inverting it, it is best to directly invert the diagonal matrix $\boldsymbol{D}$. Therefore, the final equation for the stochastic velocity is,

$$v_s^i = \boldsymbol{V} \begin{pmatrix} \frac{1}{\sqrt{\lambda_1}} & 0 & 0 \\ 0 & \frac{1}{\sqrt{\lambda_2}} & 0 \\ 0 & 0 & \frac{1}{\sqrt{\lambda_3}} \end{pmatrix} \boldsymbol{V}^T F_s^i \tag{6.14}$$

It is a computationally efficient approach, as the $\mathfrak{B}$ drag coefficient tensors can be computed only once per time-step and re-used for both the deterministic and stochastic parts.

Nodal Geometry

In the form in Eq 6.14, the net global stochastic velocity of a dislocation structure is *correlated* to the discretisation level. Instead, it is desirable for drift velocity to be independent of discretisation, since the dislocation structure will be remeshed, refined and coarsened automatically. The velocity should however still depend on the total line length.

The erroneous correlation can be tested in a thought-experiment or in a simulation by creating a simple discretised line dislocation, and varying its discretisation from 2 to L nodes and tracking the speed of drift of the line along its preferred direction. In Figure 6.1(a) and (c) one can observe that increasing the discretisation causes the drift velocity (and the diffusion coefficient) to decrease, even though the total line length is unchanged. This is because of the nature of the underlying Gaussian distribution where mean is zero ($\mu = 0$, where $\sigma_{\text{global}} = \sigma_{\text{sample}}/\sqrt{N}$, where N is the number of samples). By increasing the number of nodes (samples) on the dislocation line, the segments become shorter and the fluctuations along the segment are more frequent, having the effect of averaging out fluctuations along the line, bringing the net global drift closer to zero.

This is solved by *weighting* the velocity fluctuation of each node by the square root of the length of dislocation segments connected to it, as shown in Eq 6.15.

$$v^i_{s,\text{weighted}} = \frac{1}{\sqrt{\sum_n \frac{1}{2}|l_n|}} v^i_s \tag{6.15}$$

where n is the number of segments connected to node i, and l is the length vector of the segment. The global drift is now independent of discretisation, and only depends on the *total* dislocation length, as shown in Figure 6.1(b). This is confirmed by calculating the diffusion coefficient, as shown in Figure 6.1(c). In this Figure, normalisation simply refers to the fact that values are scaled based on the first data point (2-node segment), since the relationship between the level of discretisation and calculated diffusion coefficient is of interest, rather than the absolute values (which

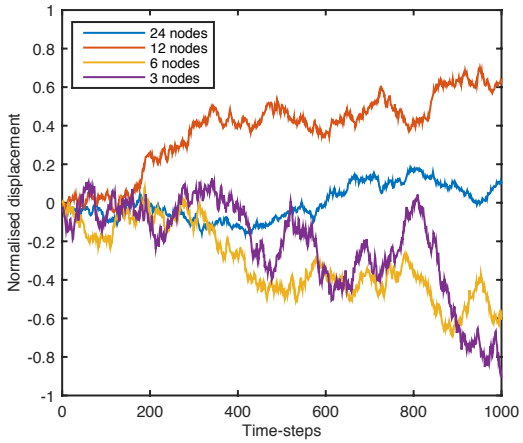

(a)

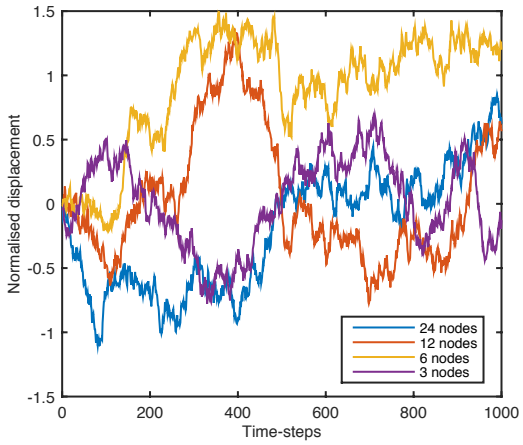

(b)

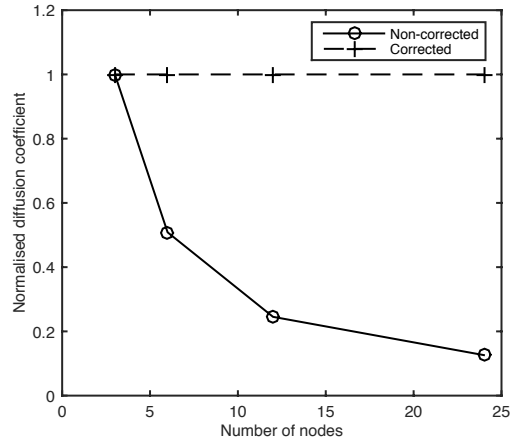

(c)

Figure 6.1: (a) Plot showing drift of line dislocation (of constant length) for different discretisation levels. Stochastic term is *not* corrected. (b) Plot showing drift of dislocation line dislocation (of constant length) for different discretisation levels. Stochastic term *is* corrected. (c) Normalised diffusion coefficient is uncorrelated for corrected stochastic term, and correlated (inversely proportional) for non-corrected term.

are dependent on units and material specific constants).

Variable Timestep

A further issue that must be corrected for is time-step variability. The velocity integrator algorithm in the classical dislocation dynamics formulation presented in Section 5.2, has a variable time step δt. Similarly to the previous dependence to segment discretisation, the global drift velocity is dependent to time-step in the form given in Eq 6.14. Assume a line dislocation comprising of two end nodes, is integrated from time $t = 0$ to $t = 1$ in 1 step with $\delta t = 1$, as opposed to 100 steps with $\delta t = 0.01$. Although the dislocation structure, discretisation and total simulation time is identical, the net drift in the first case, where δt is larger, will be more pronounced due to the effective variance being larger. To uncorrelate time step to drift velocity magnitude, velocity is weighted as in Eq 6.16. By means of simulation, this can be confirmed from calculation of diffusion coefficients, as shown in Figure 6.2. In this Figure, normalisation simply refers to the fact that values are scaled based on the first data point (smallest time step), since of interest is the relationship between time step and calculated diffusion coefficient, rather than the absolute values (which are dependent on units and material specific constants).

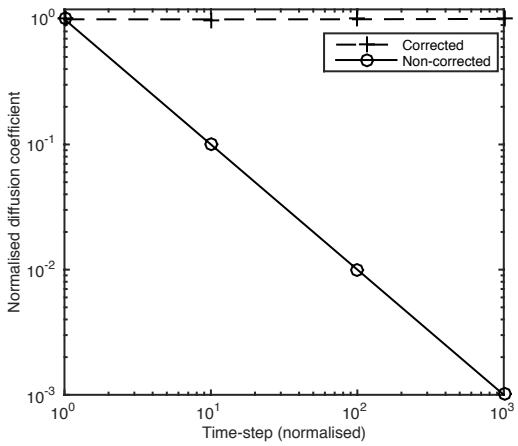

Figure 6.2: Normalised diffusion coefficient is uncorrelated to time-step for corrected stochastic term, and correlated (inversely proportional) for non-corrected term.

$$v_{s,\text{weighted}} = \frac{1}{\sqrt{\delta t}} v_s \tag{6.16}$$

Final form

Accounting for crystallographic constraints, dislocation characteristics, mobility, and correcting for timestep and discretisation variability, the final form of the stochastic 3D velocity term to be added to the deterministic contribution given by classical dislocation dynamics calculations, is found in Eq 6.17.

$$v^i_{s,\text{weighted}} = \frac{1}{\sqrt{\delta t}} \frac{1}{\sqrt{\sum_n \frac{1}{2}|\boldsymbol{l}_n|}} \boldsymbol{V} \begin{pmatrix} \frac{1}{\sqrt{\lambda_1}} & 0 & 0 \\ 0 & \frac{1}{\sqrt{\lambda_2}} & 0 \\ 0 & 0 & \frac{1}{\sqrt{\lambda_3}} \end{pmatrix} \boldsymbol{V}^T F^i_s \sqrt{2k_B T} \mathfrak{N}(0,1) \tag{6.17}$$

Using the Suzuki-Trotter decomposition, the numerical integration algorithm is as follows

1. $\boldsymbol{r}_i = \boldsymbol{r}_{i,\text{initial}} + \frac{1}{2} v^i_{s,\text{weighted}}(0)\delta t$
2. $\boldsymbol{r}_i = \boldsymbol{r}_i + v_d \delta t$
3. $\boldsymbol{r}_{i,\text{final}} = \boldsymbol{r}_i + \frac{1}{2} v^i_{s,\text{weighted}}(0)\delta t$

where v_d is determined from the deterministic classical dislocation dynamics Eq 5.13. This is inserted within the broader corrector-predictor algorithm used in DDLab.

6.3 Molecular Dynamics of Loop Mobility

To introduce thermal effects within a dislocation dynamics simulation, one can resort to molecular dynamics (MD) to gather information on the dependence on temperature of the mobility of dislocation loops in tungsten. This section will illustrate the set-up of such molecular dynamics simulations, and the extraction of important tungsten-specific parameters such as dislocation loop diffusion coefficients. For all the simulations, the software LAMMPS [197] was used. The interatomic potentials used were the Ackland-Thetford modification of the Finnis-Sinclair N-body potential for tungsten [143, 253], as modified at small interatomic separations for radiation defect simulations by *Juslin et al.* [210]. Computational resources from the University of Oxford Advanced Research Computing (ARC) facility, and the University of Tennessee Newton computing facility are acknowledged.

6.3.1 Implementation

From dislocation damage characterisation in previous chapters, the predominant dislocation loop was found to be $\frac{1}{2}\langle 111\rangle$ of interstitial-type, with a mean diameter of $\sim$3nm for a 500°C self-ion irradiation.

For computational reasons, it was unfeasible to create and track the diffusion of a 3nm dislocation loop, due to the size of the simulation box and number of atoms needed. Significantly smaller prismatic loops consisting of 7 to 91 tungsten atoms were run and parameters for larger dislocations extrapolated by fitting these smaller simulation conditions. Example core structures can be found in Figure 6.3. For each condition, four different trials were run, each with a different thermalisation *seed*. A different *seed* meant that each trial had a different starting thermal distribution, although the overall domain temperature was constant. The length of time for each trial was $\sim$0.5ns (total of $\sim$2.0ns) to allow for sufficiently long time series for a statistically valid analysis.

The following conditions were considered:

- Molecular dynamics simulations of a 7-atom and a 61-atom prismatic interstitial $\frac{1}{2}\langle 111\rangle$ dislocation loop in tungsten, at a constant temperature of 50 to 1500K.

- Molecular dynamics simulations of a 7, 19, 61, 91-atom prismatic interstitial $\frac{1}{2}\langle 111\rangle$ dislocation loop in tungsten, at a constant 900K temperature.

Setting up a simulation

For all the loop-diffusion molecular dynamics studies, the simulation boundaries were fully periodic. The rectangular simulation box had an orientation of $\bar{x} = [111]$, $\bar{y} = [1\bar{1}0]$, and $\bar{z} = [11\bar{2}]$ with dimensions of $48 \times 24 \times 16$ lattice units, or $264.45 \times 107.96 \times 124.67$nm, yielding a $\sim$220,000 atom ensemble. A size convergence study was carried out using the largest loop (91-atom), since it is important that the dislocation loop does not "feel" the presence of its periodic boundary reflections. Domain sizes above the chosen dimensions were found to yield no appreciable change in diffusion behaviour, and as such this simulation box size was kept constant for all conditions. The dislocation loop Burgers vector was $\frac{1}{2}[111]$, meaning that thermal diffusion in the glide direction would happen along the x-axis, making it straightforward to visualise, track and extract. The loop plane normal was also [111], making it of prismatic type. A single simulation consisted of several steps:

1. Creation and minimisation.

   The global simulation domain dimensions and periodic boundary conditions were defined, together with the particular interatomic potential (*Juslin et al* [210]), lattice constant, atomic mass (183.841 au), and size of the dislocation loop. The domain of the dislocation loop was defined at approximately the middle of the simulation box, and its constitutive atoms positioned accordingly (following a b.c.c crystal structure), as in Figure 6.3, remembering a $\frac{1}{2}\langle 111\rangle$ loop has three layers of interstitials (in an ABC arrangement), and favours a hexagonal shape [254]. This domain was subsequently *shifted by half a Burgers*

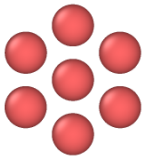

(a) 7 SIAs, front

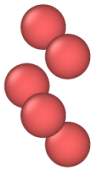

(b) 7 SIAs, side

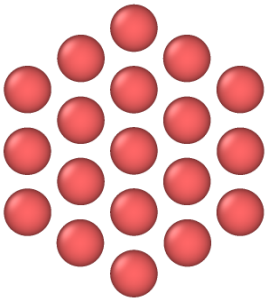

(c) 19 SIAs, front

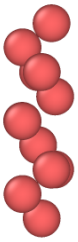

(d) 19 SIAs, side

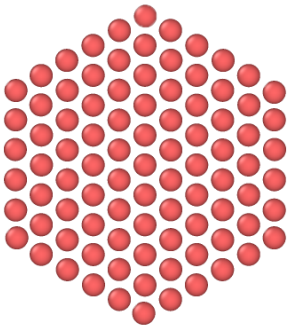

(e) 91 SIAs, front

(f) 91 SIAs, side

Figure 6.3: Dislocation cores of different sizes for $\frac{1}{2}\langle 111\rangle$ prismatic interstitial loops

vector. The global domain was then populated by a b.c.c. atomic lattice and the entire simulation box relaxed via an energy minimisation routine which iteratively adjusts atom coordinates, using a backtracking algorithm. This procedure yielded a tungsten b.c.c. lattice with an interstitial prismatic dislocation loop in the middle, with the correct Burgers vector and atomic positions. This minimised condition was saved and re-used for simulations at different temperatures and/or thermalisation seeds.

2. Thermalisation.

   Once a satisfactory defected crystallographic structure was created, the simulation domain was thermalised to the required temperature. This was done by first generating an ensemble of velocities using a random number generator with a specified seed at the specified temperature. The domain was subsequently relaxed by performing a time integration on Nose-Hoover style non-Hamiltonian equations of motion (*Shinoda et al* [255]) designed to generate positions and velocities sampled from a canonical ensemble. This updated the position and velocity for atoms in the domain each timestep, and was easily achieved within a LAMMPS syntax in relatively few, concise commands.

3. Progression and tracking.

   Following thermalisation, the thermostat condition was removed and the simulation run for an appropriate amount of time-steps to reach the desired real time (2.5 ns). The maximum time step was 0.0005ps, and automatically decreased if any atom in the simulation would move more than 10% of one lattice unit at each iteration. This was done to prevent integration errors and preserve total energy in the system. At regular intervals (generally 0.05ps), the dislocation loop's centre of mass was calculated and stored. The tracking of the interstitials was done via Frenkel defect analysis [256, 257], as shown in Figure 6.4.

   This routine essentially consists in calculating distances between each atom

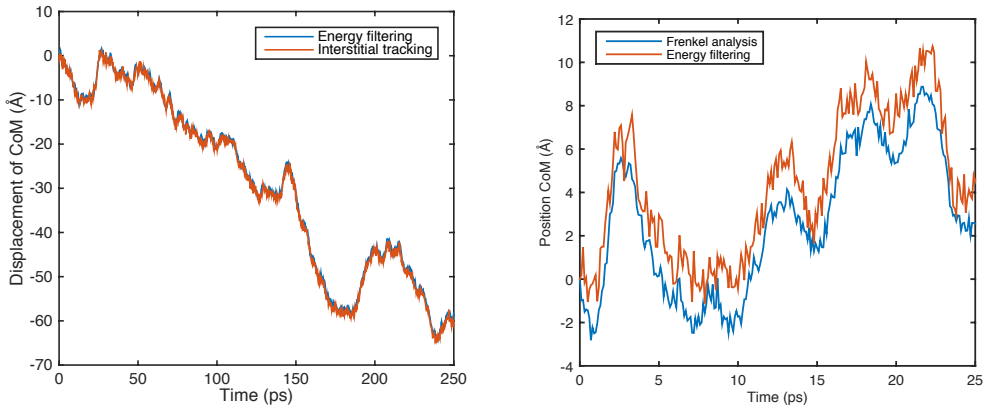

(a) Long time scale **(b)** Short time scale

Figure 6.4: Tracking of 7-SIA centre of mass via Frenkel pair analysis or energy filtering.

and a reference perfect lattice, and filtering those which are below a certain *distance* threshold. Using this technique, all the added interstitials composing the loop should be identified, as shown in 6.5. The mean position of all filtered interstitals was taken as the centre of mass of the loop.

An alternative approach to calculate the centre of mass is via filtering of atoms above a certain *energy* threshold compared to the average thermal energy. This approach does not identify the self-interstitials of the loop, but rather the $\frac{1}{2}\langle 111\rangle$ crowdions along the dislocation line, as shown in Figure 6.6.

Both are sensible techniques, and when averaging for the centre of mass and extracting diffusion quantities, give largely equivalent results, as shown in Figure 6.4. It is important to note that for both tracking methods it was necessary to use energies or distances averaged over a short interval rather than instantaneous quantities, to remove false positives due to thermal fluctuations and calculate values closer to the real thermodynamic values. Higher temperature simulations generally require a longer averaging interval since thermal fluctuations are more extreme, as demonstrated in Figure 6.7 using energy filtering. For example, for 1500K, the interval had to be extended to 0.25ps to completely remove false positives in the bulk, as shown in Figure 6.8. In general, the Frenkel analysis algorithm was observed to be less sensitive to fluctuations,

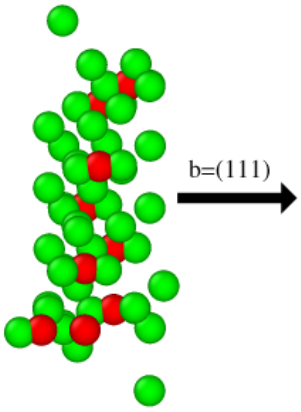

(a) 91 SIAs, side

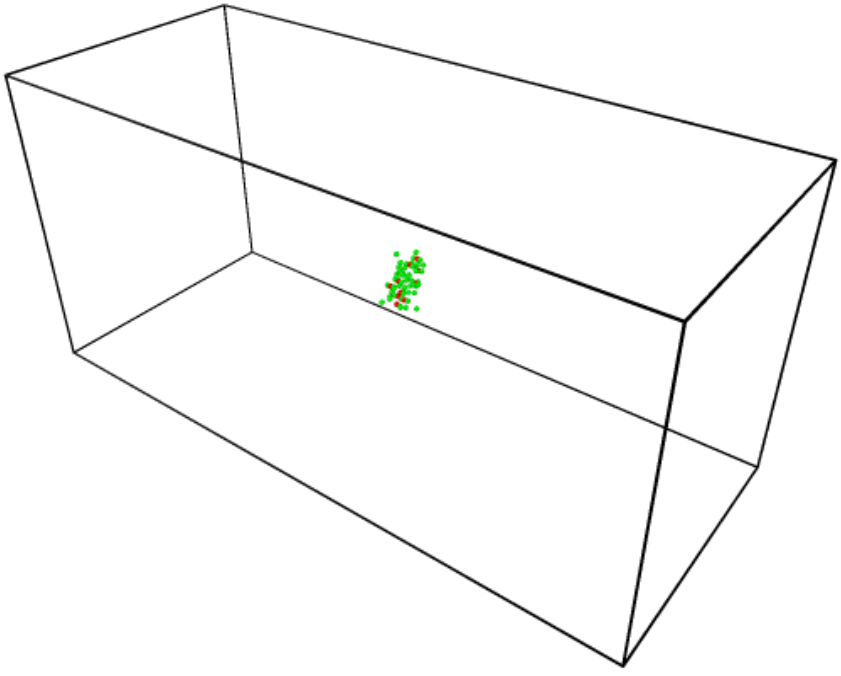

(b) 91 SIAs in domain, orthogonal

Figure 6.5: Instantaneous simulation snapshot of thermalised dislocation core (600K) of 91 SIA interstitial $\frac{1}{2}\langle 111\rangle$ prismatic loop identified by Frenkel-pair analysis. Red are vacancies, green are interstitials.

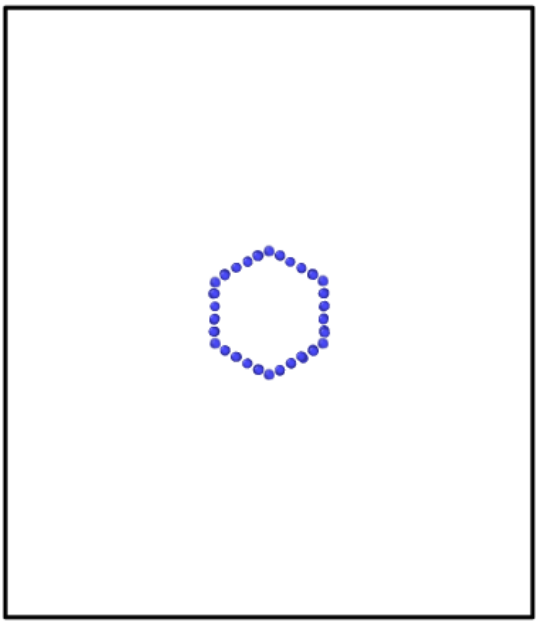

(a) 91 SIAs in domain, front

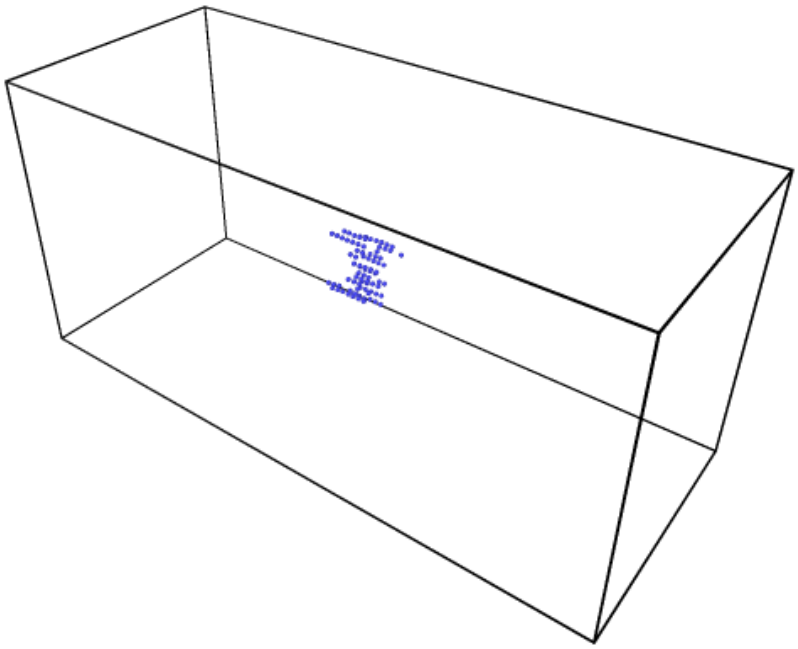

(b) 91 SIAs in domain, orthogonal

Figure 6.6: Simulation snapshot of thermalised dislocation core (600K) of 91 SIA interstitial $\frac{1}{2}\langle 111\rangle$ prismatic loop identified by energy filtering analysis (0.1ps averaging interval).

allowing a finer-grained tracking of the centre of mass, making it the preferred method. As well as from the centre of mass, the positions of the individual filtered atoms was also stored to identify any potential issues and diffusion mechanisms.

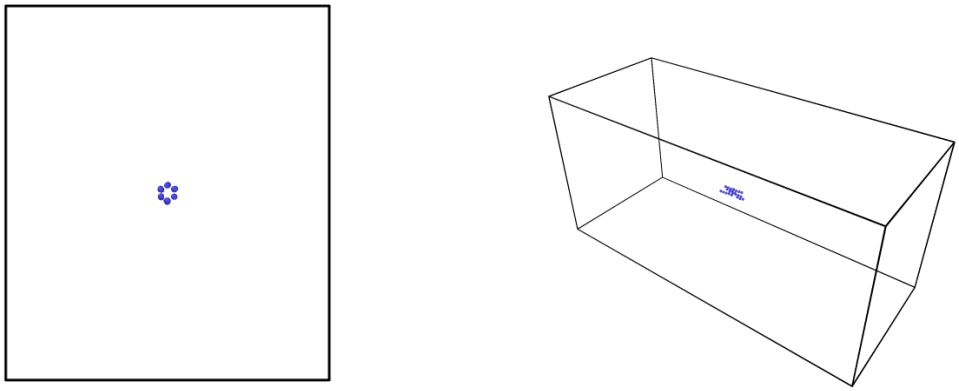

(a) 600K, 0.025ps averaging interval

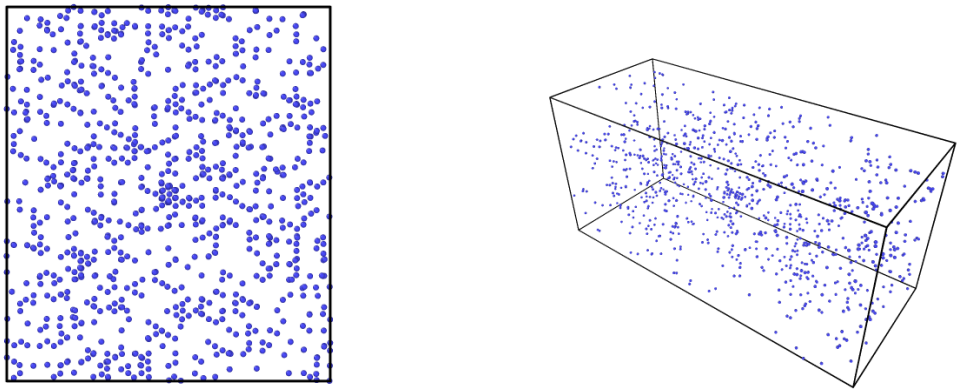

(b) 1500K, 0.025ps averaging interval

Figure 6.7: Energy filtering of 7-SIA interstitial loop at 600K and 1500K using same 0.025ps averaging interval. For the higher temperature case, averaging over 0.025ps intervals is clearly insufficient, yielding a very noisy result.

4. Post-processing.

   To reach the desired real time of several nanoseconds for each condition (temperature and loop size) and thermalisation seed (approximately 60 separate simulations) required 6 months of simulations using hundreds of cores on a high-performance computing cluster. The resultant 3-dimensional diffusion pathways of the dislocation loops were analysed to yield a diffusion coefficient. The exact method of calculation is described in Section 6.3.2. Predictably,

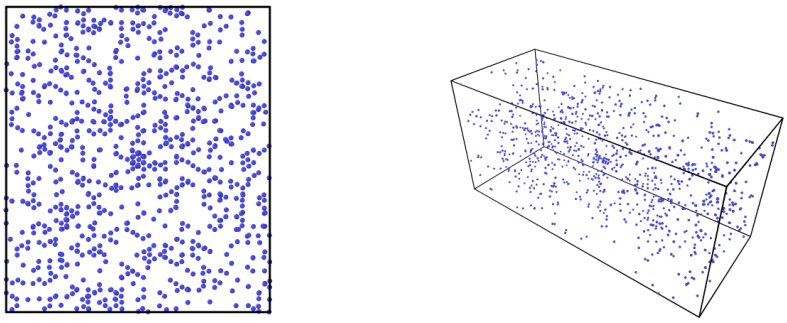

(a) 0.025ps averaging interval, 1500K

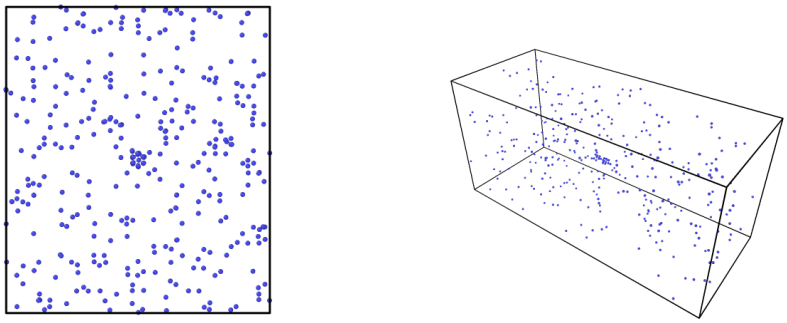

(b) 0.05ps averaging interval, 1500K

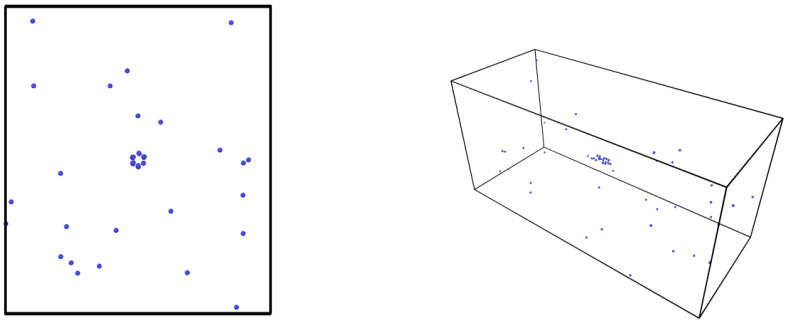

(c) 0.1ps averaging interval, 1500K

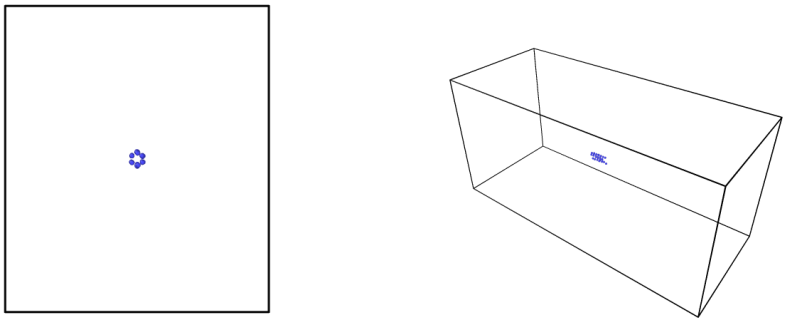

(d) 0.25ps averaging interval, 1500K

Figure 6.8: Energy filtering of 7-SIA interstitial loop at 1500K using different averaging intervals. 7-SIA loop correctly identified only at 0.25ps averaging interval.

appreciable thermal diffusion occurred exclusively in the glide-direction of the dislocation loop (any climb processes take far longer than the timescales scoped by the molecular dynamics simulations described). Interestingly, at the temperatures probed (500-1500K) the variation of diffusion coefficient with T was found to be *linear* as opposed to an Arrhenius-type relationship, consistent with [156]. This is discussed later in Section 6.3.3.

6.3.2 Calculation of Mean Square Displacement and Diffusion Coefficient

The mean square displacement (msd) is a measure of the average distance squared an object travels. In this case, the object is the centre of mass of a dislocation loop which on the molecular scale is a closed chain of crowdions, exibiting stochastic motion, and preferentially moving in the loop glide direction. Mathematically, the mean square displacement is defined as

$$msd(t) = \langle x_i(t)^2 \rangle = \langle (x_i(t) - x_i(0))^2 \rangle \tag{6.18}$$

where $x_i(t) - x_i(0)$ is the distance the loop's midpoint i, traveling over some time interval t. $\langle\rangle$ is the ensemble average, the statistical average of the quantity over all systems of the ensemble.

The diffusion coefficient D can be then calculated via the Einstein relation

$$D = \langle x^2(t_0) \rangle / 2t_0 \tag{6.19}$$

This relation becomes exact in the limit of large t_0 and large number of realisations implicit in $\langle ... \rangle$. Due to the computational cost of molecular dynamic simulations, simulations of loop trajectories are of *finite* temporal length. Furthermore, a single trajectory is split into many separate shorter trajectories from which an average of the mean displacement is calculated, on the assumption that such subtrajectories are statistically independent [156]. As such, these subtrajectories do not have a

mean displacement of zero, and literature suggests taking a *drift corrected* diffusion coefficient [161], defined as

$$D = \frac{1}{2t_0}\left\langle \left(x(t_0) - \frac{2}{t_0}\int_0^{t_0} d\tau x(\tau) \right)^2 \right\rangle \tag{6.20}$$

where the second additional term is the drift-correction.

For diffusive motion with a diffusive constant $D_{\text{loop}}/2$,

$$\langle \triangle \bar{x}^2 \rangle(\tau) = D_{\text{loop}}\tau \tag{6.21}$$

However, if one plots the mean squared displacement of the dislocation loop versus time step, one will see two distinct regions. For very small time steps (i.e. δ =0.1ps), the gradient changes non-linearly (quadratically) because the loop is in the *ballistic* region, acting like a Newtonian body which is travelling at constant speed (if $x \sim v \cdot t$ then $x \cdot x \sim t^2$). For longer time steps, thermal collisions make the movement of the loop diffusive, and the gradient will be linear (as in Eq. 6.21). This is shown graphically in Figure 6.9.

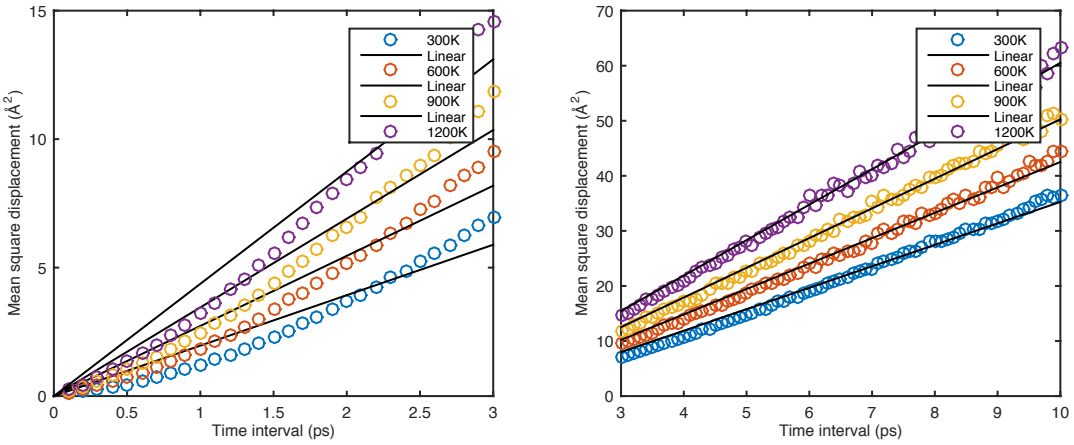

Figure 6.9: Linear fit of mean squared displacement vs time interval (ps) for diffusion of 61 SIA interstitial $\frac{1}{2}\langle 111 \rangle$ loop at different temperatures, *for different time intervals* (a) 0.1 to 3ps, (b) 3 to 10ps intervals.

To accurately extrapolate a diffusion coefficient, one should add an extra term to Eq 6.21 which decays exponentially in time. This is captured by the Ornstein-Uhlenbeck

process, a stochastic process describing the velocity of a Brownian particle under the influence of friction.

$$\langle x^2(t)\rangle = \frac{2k_BT}{\gamma}t(1-e^{-\frac{\gamma t}{m}}) \tag{6.22}$$

For long timescales, with $t >> m/\gamma$, the exponential term disappears giving,

$$\langle x^2(t)\rangle \approx \frac{2k_BT}{\gamma}t \tag{6.23}$$

For short time-scales, where $t << m/\gamma$, the loop acts as a freely moving particle. Taylor expanding the exponential term, one can see the squared distance grows quadratically.

$$\langle x^2(t)\rangle \approx \frac{2k_BT}{m}t^2 \tag{6.24}$$

Therefore, it is best to fit

$$\langle x^2(t)\rangle = Dt(1-e^{-\frac{\gamma t}{m}}) \tag{6.25}$$

to the data set. One can extrapolate a more accurate diffusion constant D and γ/m, which reflects the drag force that opposes the loop's motion through the crystal, using a two-parameter fit. This can be seen in Figure 6.10 for different temperatures. Furthermore, the extrapolated diffusion coefficient can be plotted with respect to temperature as shown in Figure 6.11(b).

6.3.3 Variation with Temperature

Time series of 61 and 7 self-interstitial atom (SIA) dislocation loops diffusing along the x-direction (glide direction), with the calculated 1D diffusion coefficient D at different temperatures, are shown in Figure 6.11 and 6.12 respectively. Temperatures ranged from 50K to 1500K. Although it is not immediately obvious from the raw time series (a), the calculated diffusion coefficient (b) rises linearly with

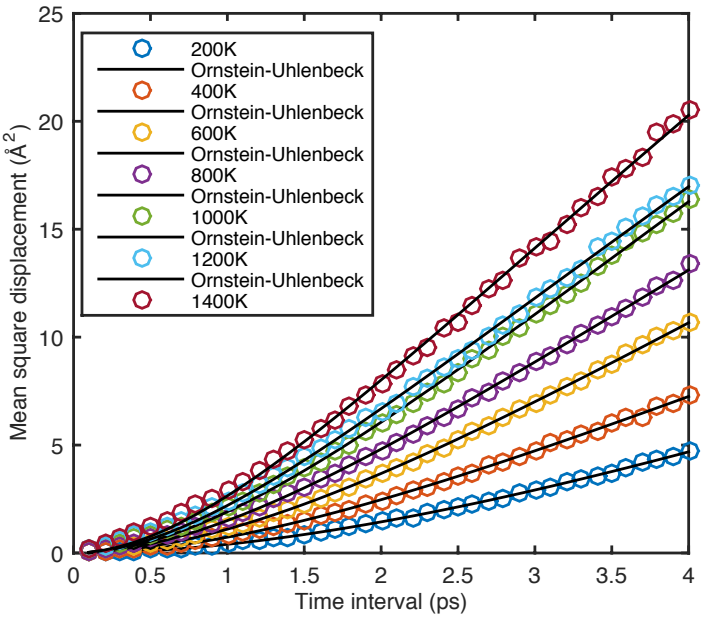

Figure 6.10: Two parameter fit (D and γ/m) of mean squared displacement vs time interval (ps) for diffusion of 61 SIA interstitial $\frac{1}{2}\langle 111\rangle$ loop at different temperatures.

temperature above the Debye temperature (310K), implying a vanishingly small migration barrier. One can fit this to a one dimensional exact solution given by the Lifson-Jackson formula given in Eq 6.26, as opposed to a traditional Arrhenius form $D_0 \exp(-E_{mig}/k_B T)$.

$$D_{\text{loop}} = \frac{k_B T a^2}{\gamma_{\text{loop}}} \left(\int_0^a e^{-V(x)/k_B T} dx \int_0^a e^{V(x)/k_B T} dx \right)^{-1} \tag{6.26}$$

where k_B is Boltzmann's constant and γ_{loop} is the friction or dissipation parameter [159], which measures the rate of momentum transfer from the diffusing object to the heat bath.

This form is useful as it can capture both Arrhenius-type and freely diffusing particle motion. If the amplitude of the migration potential $E_{mig} = V_{max} - V_{min}$ is much greater than the thermal energy $k_B T$, Eq 6.26 can be evaluated analytically and reduces to

$$D_{\text{loop}} \approx a^2 \frac{\sqrt{V''_{min} V''_{max}}}{2\pi\gamma_{\text{loop}}} e^{-(V''_{max} - V''_{min})/k_B T} \tag{6.27}$$

where V'' is the second derivative. This is an Arrhenius form for thermally activated motion, as given by Kramers [258], where "rare event" escapes are captured with an attempt frequency pre-factor. In the other limit, where the migration potential E_{mig} is much smaller than the thermal energy k_BT and there are no longer any rare events, Eq 6.26 reduces to a linear relationship given by

$$D_{\text{loop}} \approx \frac{k_BT}{\gamma_{\text{loop}}} \tag{6.28}$$

first described by Einstein [259] for a freely diffusing particle. In the case of 1D loop diffusion along the glide direction for temperatures between 400 and 1500K, which are well above the Debye temperature of tungsten [260], one observes this type of *linear* diffusive behaviour, due to a negligible migration barrier compared to the thermal energy of the system. A "back-of-the-envelope" calculation confirms this: taking the migration energy E_{mig} of a highly mobile $\frac{1}{2}\langle 111\rangle$ crowdion configuration as 0.018eV [244], and a temperature of 500°K, the thermal energy k_BT is 0.043eV, hence $k_BT > E_{mig}$.

These simulations were repeated for a smaller 7 SIA prismatic $\frac{1}{2}\langle 111\rangle$ loop, and the same behaviour is observed, as shown in Figure 6.12. Simulations using 7 interstitials are useful for two reasons. Firstly, due to the smaller cluster size, the loop remains coplanar to a higher degree than a 61 SIA loop, meaning the calculation of a centre of mass and the idealisation of the motion as a particle moving in 1D will be more accurate. Secondly, diffusion coefficient calculations in tungsten for small clusters have already been calculated for temperatures in the lower spectrum, making direct comparisons possible. A recent study by *Swinburne et al* [159], using a MD potential by *Marinica et al* [261] gives a D of between $3-6.5$ Å^2/ps for temperatures between $300-600$K, which is consistent with the values calculated in this thesis.

In the framework of a one-dimensional Langevin equation,

$$\frac{dx}{dt} = \sqrt{2D_{\text{loop}}}\zeta(t) = \sqrt{\frac{2k_BT}{\gamma_{\text{loop}}}}\zeta(t) \tag{6.29}$$

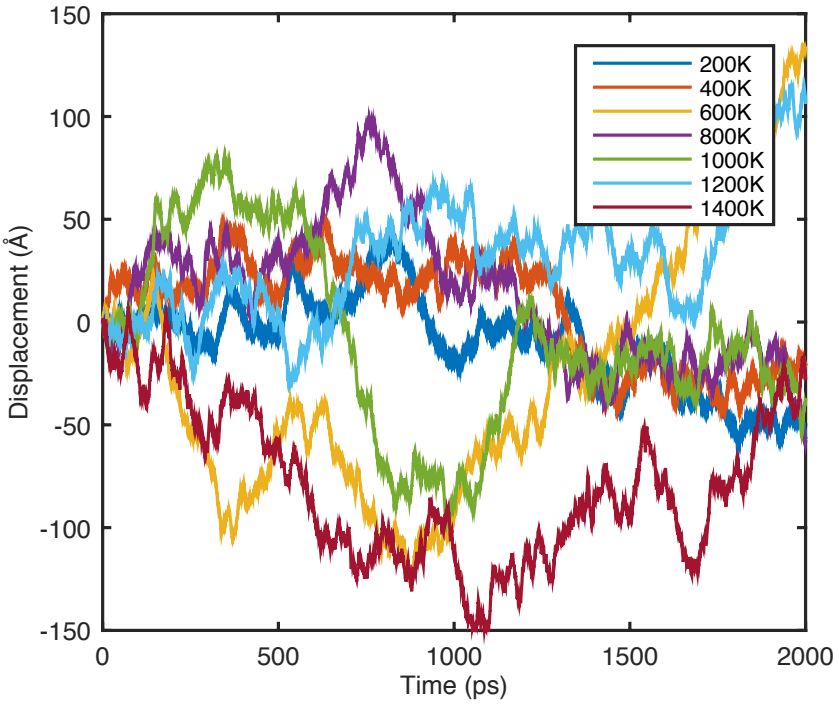

(a)

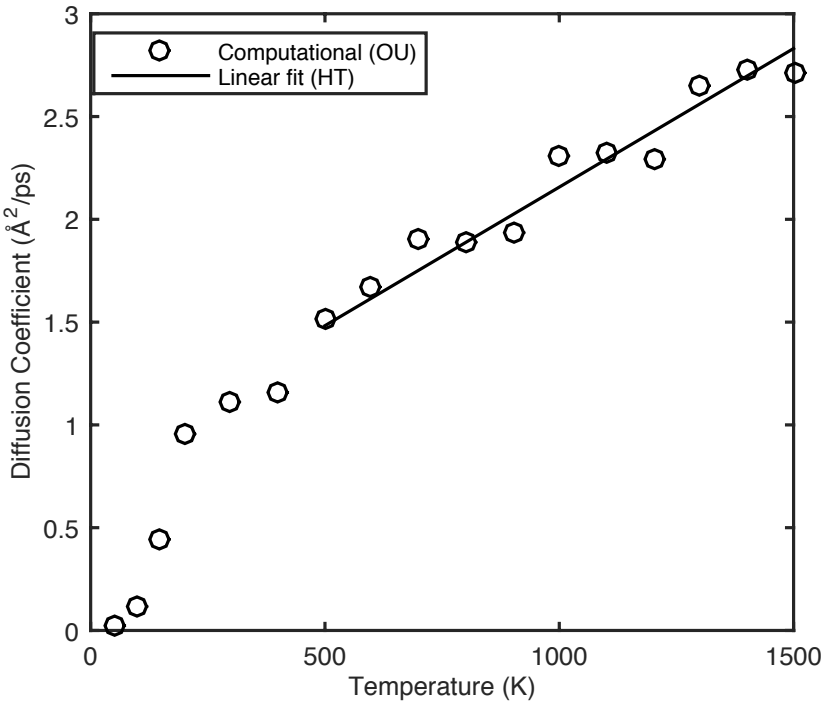

(b)

Figure 6.11: Molecular dynamics simulations of an interstitial 61-atom $\frac{1}{2}\langle 111\rangle$ prismatic loop in tungsten for varying temperatures. (a) Dislocation loop centre of mass diffusion over time (ps) for varying temperatures (b) Diffusion coefficient calculated from time series varying with respect to simulation temperature.

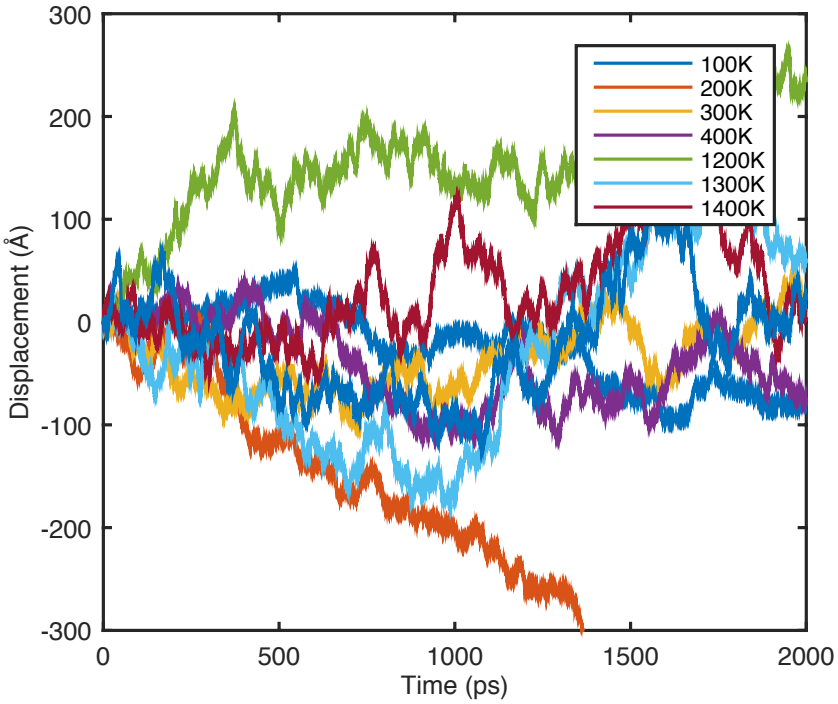

(a)

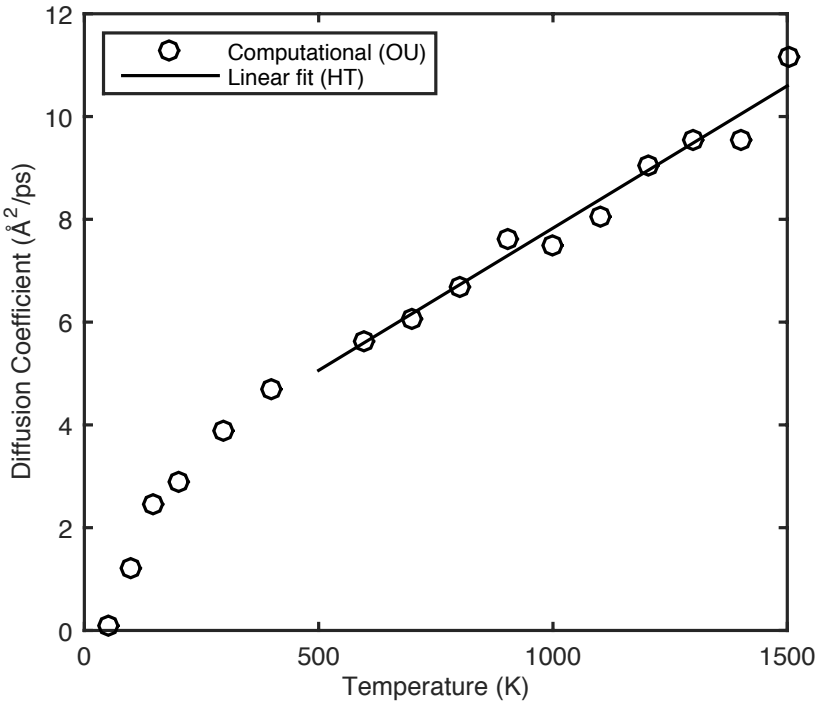

(b)

Figure 6.12: Molecular dynamics simulations of an interstitial 7-atom $\frac{1}{2}\langle 111\rangle$ prismatic loop in tungsten for varying temperatures. (a) Dislocation loop centre of mass diffusion over time (ps) for varying temperatures (b) Diffusion coefficient calculated from time series varying with respect to simulation temperature.

where $\langle \zeta(t)\zeta(t') \rangle = \delta(t - t')$.

6.3.4 Variation with Size

Example time series of different sized dislocation loops diffusing at 900K are given in Figure 6.13(a), comprising of 7, 19, 61 or 91 self-interstitial atoms. The variation in the calculated diffusion coefficient is shown in Figure 6.13(b)-(c). Qualitatively, the diffusion coefficient decreases with loop size. From (c), one can see a linear relationship between the inverse of the diffusion coefficient and dislocation loop perimeter length, with the exception of the smallest 7-SIA. Therefore, diffusion coefficient is *inversely proportional* to length.

This observation is important for several reasons. Firstly, it is consistent with the idea that as a cluster of crowdions grows in size, it converges to the behaviour of a prismatic $\frac{1}{2}\langle 111 \rangle$ dislocation loop which also displays an inverse proportionality of diffusion coefficient to length [156]. Secondly, it further justifies the formulation given in the stochastic dislocation dynamics model developed above, given in Equation 6.17. The model correctly captures this behaviour, with the observed diffusion coefficient of a discrete dislocation segment also being inversely proportional to its length.

As dislocation loop size decreases, its behaviour should converge to that of a single crowdion. If one describes this as the lowest possible bound of loop size ($\approx$ atomic diameter), it is reasonable that the inverse proportionality $D \propto \frac{1}{L}$ relation breaks down with small loop clusters (7-SIA), and instead converges to a non-zero discrete value of diffusion of an individual crowdion. For such small clusters, the dislocation core atoms on one side of the loop are highly correlated to the other sides, making their behaviour different from an idealised scenario of six edge dislocations.

For the purposes of simulating the dislocation loop ensembles observed in the experimental sections of the thesis, which have sizes of predominantly $\sim$3nm or larger in diameter, one can justifiably ignore the anomalous (not $D \propto \frac{1}{L}$) relationship observed in the 7-SIA case, since a 7-SIA loop is equivalent to a $\sim$ 0.8nm diameter

loop: smaller than a visible dislocation loop using transmission electron microscopy. Furthermore, since dislocation dynamics is a continuum model, elasticity theory would be inaccurate in any case at such length scales [198, 262].

For completeness, Figure 6.14 shows the diffusion coefficients of various sized loops (including the limiting case of a single crowdion). It can be observed that regardless of the size, the crowdion clusters display a transition to freely-diffusing particles at higher temperatures ($\geq 300°$K), characterised by a relatively linear (as opposed to Arrhenius) increase in diffusion coefficient with respect to temperature. At temperatures at 700K or above, the single crowdion was observed changing directions. Fluctuations at higher temperatures are due to noise and the necessity of running very long and computationally expensive simulations.

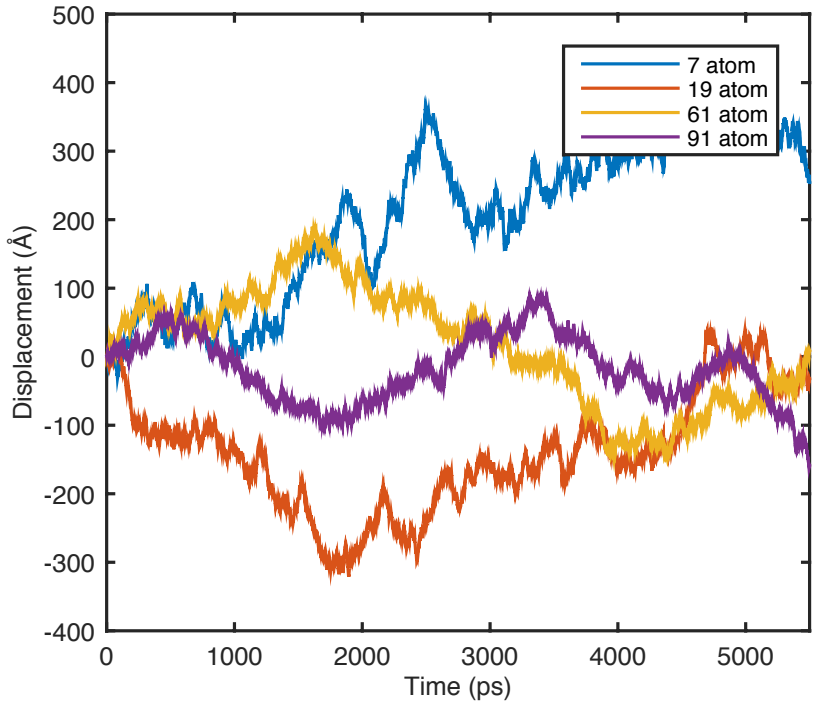

(a)

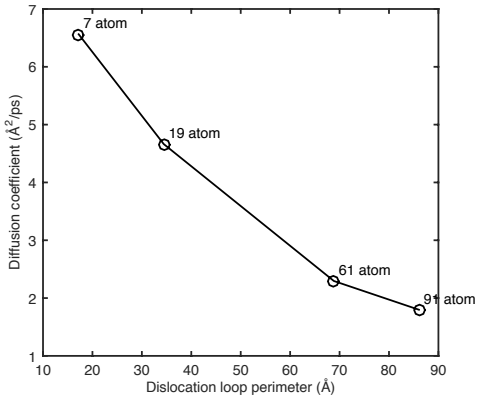

(b)

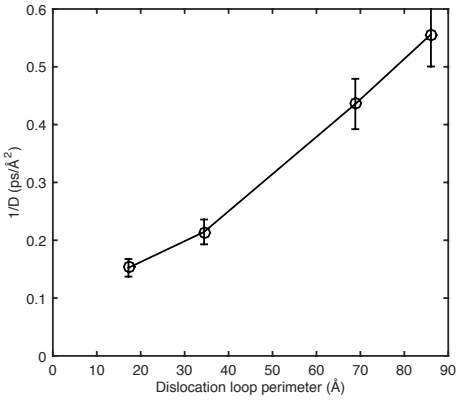

(c)

Figure 6.13: Molecular dynamics simulations of an interstitial $\frac{1}{2}\langle 111\rangle$ prismatic loops of varying size in tungsten at 900K. (a) Dislocation loop centre of mass diffusion over time (ps) for varying sizes, (b) Diffusion coefficient calculated from time series varying with respect to loop perimeter, (c) Inverse of diffusion coefficient with respect to loop perimeter.

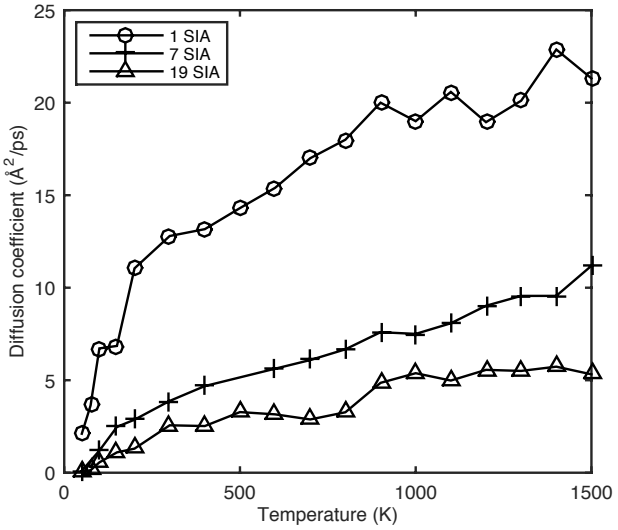

Figure 6.14: Molecular dynamics simulations of an interstitial $\frac{1}{2}\langle 111\rangle$ crowdion clusters loops of varying size in tungsten from 50 to 1500K.

6.4 Connecting MD to Stochastic DD

6.4.1 Fluctuation-Dissipation Theorem

The fluctuation-dissipation theorem, otherwise known as the Einstein-Smoluchowski relation for Brownian motion, provides a fundamental link between diffusion quantitites and drag, in Eq 6.17. It quantifies the relation between the fluctuations in a system at thermal equilibrium and the response of the system to applied perturbations, such as forces.

In the context of discrete dislocation dynamics formulations, the resultant velocity of a dislocation segment due to a force is determined by a drag matrix $\mathfrak{B}$, constructed using mobility parameters μ for screws, edges etc. For a particular component (such as glide),

$$v = \mu F \tag{6.30}$$

where μ is mobility (units of $\mathrm{s{\cdot}kg^{-1}}$), the inverse of γ_{loop}. One can therefore link the diffusion coefficient calculated experimentally [182] or via molecular dynamics, as done in this work, to calculate an effective mobility μ.

$$D = \mu k_B T. \tag{6.31}$$

The caveats are many. For example, diffusion coefficients calculated via molecular dynamics simulations are orders of magnitude greater than those observed experimentally. This is due to impurities or Cottrell atmospheres impeding motion [263]. Even extremely small quantities of impurities, which are always present in commercial grade metals (and even "pure" materials), can significantly alter the mobility of dislocations via solid solution hardening and pinning. Nonetheless, the general methodology and Eq 6.31 still holds, regardless of the absolute value of D.

6.4.2 Introducing appropriate temperature dependent mobilities in DDD code

For a more accurate dislocation dynamics simulation of radiation damage, one would need to incorporate the diffusion properties of the dislocation loops calculated in the previous molecular dynamics simulations, taking into account the variations in temperature and size. Using the fluctuation-dissipation theorem and the material-specific molecular dynamics data in Figure 6.13 or 6.12 one can calculate temperature dependent drag for a loop of a particular size. From Figure 6.11, loop diffusion is also inversely proportional to perimeter length (for >1nm diameter sizes). It is thus straightforward to incorporate a drag value per unit length in the DD code for the purposes of simulating prismatic dislocation loops such as those found in the experimental sections. Section 6.4.3 will demonstrate that this approach yields identical diffusive timescales and behaviour in the stochastic DD formulation as those found in MD, making it a computationally efficient alternative to simulative diffusion of large ensembles of dislocation loops.

Another option is, rather than use molecular dynamics data from crowdion cluster simulations, to simply input a temperature-dependent parametrisation for edge mobility in the DD model (such as Eq 6.32), since prismatic dislocation loop can be described as a combination of edge dislocations. The problem is that although

a loop can be described as a combination of edge dislocations for the purposes of stress and elastic interactions, the *mobility* of such structure is in reality different from that of a pure straight edge dislocation. The core region for an edge dislocation is at least 3 by 6 atomic planes [156], meaning the motion of crowdions in a small cluster or dislocation loop would be highly correlated.

Edge drag

Molecular dynamics simulations can be used to fit the drag with respect to temperature of an edge dislocation, in a similar way to how dislocation loops were modelled in Section 6.3.1. Using this simple fitting, a drag value can be evaluated when initialising the DDD simulation which will in turn define the characteristic time-scales of motion. From *Swinburne* [264], MD simulations for a $\frac{1}{2}\langle 111\rangle(10\bar{1})$ dislocation in tungsten give the relation,

$$\gamma_{\text{edge}} = L \cdot (101 + 1.69T) \text{ MPaÅps} \tag{6.32}$$

in the range of 300 to 900K. At these temperatures, one can also employ the Einstein relation to express the temperature dependence in terms of diffusion coefficient.

$$D_{\text{edge}} = \frac{k_B T}{L \cdot (101 + 1.69T)} \tag{6.33}$$

As explained in the previous chapter, in the DDD code used in the thesis (DDLab), the segment forces are converted into *nodal* forces, and the drag coefficient γ for an edge dislocation in the glide direction is used to construct a global drag matrix $\mathfrak{B}$, which is then inverted to calculate *nodal* velocities ($v_{\text{nodes}} = \mathfrak{B}^{-1} f_{\text{nodes}}$). This conversion from segment to nodes implicitly deals with the length dependence in Equation 6.32. Therefore, when calculating the input drag parameter, one can ignore the L term (as this will be dealt with during the simulation). This is very convenient since it allows, in conjunction to the stochastic model, to account for temperature dependent mobility of edge segments of any length by simply calculating the drag for

a normalised-length edge dislocation *a priori* for the appropriate temperature and material when initialising the simulation. The units of DDLab are non-standard, as opposed to the ParaDis program, so further appropriate unit conversions are necessary when inputting the parameter.

Screw drag

Incorporating temperature dependence of screw dislocations within a DDD code is not as straightforward as for edge dislocations. The difficulty arises from capturing the kink nucleation rate dependent on the *local* stress [158], when the stress applied is below the Peierls stress.

Trying to use this formulation within a discrete dislocation dynamics program would mean utilizing a *non-global* screw mobility value. One way to get around this programmatic limitation would involve an additional algorithm:

- Calculating kink-pair nucleation energies under stress for each discrete dislocation segment.
- Calculating segment velocities.
- Turning these segment velocities into nodal velocities.
- Adding the contributions to the nodal velocities to other regular drag-type velocities calculated in the mobility function

In this thesis, this kind of additional algorithm was *not* implemented, due to simulations occurring well-above the Peierls stress.

Climb drag

Climb is a non-conservative process which occurs through the absorption or emission of point defects on a dislocation line. Therefore, capturing the process exhaustively using a single mobility parameter is difficult. Nonetheless, from [188, 191], a climb

drag has been derived. Similarly to the edge drag case, it can be calculated *a priori* to the simulation. Recalling Eq. **??**.

$$M_{\mathrm{cl}}(\theta) = \frac{2\pi D_v \Omega c_0^v}{kTb^2 \sin^2(\theta) ln(r_\infty / r_c)}$$

where Ω the atomic volume, θ the dislocation character [4], k the Boltzmann constant, T the temperature and r_c the inner core radius of the dislocation line. $D_v = D_v^0 \exp\left(\frac{U_v^m}{kT}\right)$, with U_v^m being the vacancy migration energy, D_v^0 the constant prefactor characterising vacancy diffusion, and $c_0^v = \exp\left[-(U_v^f - P\Delta V_v / kT\right]$, where U_v^f is the vacancy formation energy, and ΔV_v the associated relaxation volume. The vacancy migration and formation energies of tungsten, U_v^m and U_v^f, are 1.78 and 3.56eV respectively [160], and the vacancy diffusion prefactor is $\sim 1.5 \cdot 10^{-5}$ $\mathrm{m}^2 \cdot \mathrm{s}^{-1}$ according to DFT studies [190]. With core radius $5b$, and $r_\infty \sim 10^4 b$, a tungsten-specific climb drag temperature parameterisation for a pure edge can be estimated,

$$\gamma_{\mathrm{climb}} = 3.8863 \cdot 10^{-9} T \cdot \exp(6.1968 \cdot 10^4 / T) \tag{6.34}$$

In the case of tungsten, due to the very high migration and formation energies, conventional non-conservative climb does not significantly affect the outcome of discrete dislocation dynamics simulations for practical temperatures. For very high temperature regimes (>1150K), an anomalous conservative climb mechanism has been observed in this thesis at experimental timescales (see Chapter 2), but this cannot be captured by neither bulk diffusion models, nor by the stochastic formulation. This could instead be a pipe diffusion mechanism [265] which the above model ignores. Similar coalescence events of dislocation loops attributed to such a self-climb pipe diffusion mechanism have been observed in UO_2 [180] and MgO [181].

[4] $\theta = \frac{\pi}{2}$ for pure edge, and 0 for pure screw (capped at a maximum mobility)

6.4.3 Validations

Case set-up

To test that the stochastic dislocation dynamics algorithm can correctly replicate the diffusive behaviour in dislocation loops, a $\boldsymbol{b} = \frac{1}{2}\langle 111 \rangle$ dislocation loop was set up, with a hexagonal shape consisting of edge dislocations of (110) and (121)-type direction, having segment nodes at the vertices of the hexagon.

Variation with loop size

Here we compare with the molecular dynamics simulations of dislocation loops of various sizes at 900K, as shown in Figure 6.15. In the stochastic DD formulation the shear modulus was 160GPa, with an edge drag per unit length γ of $7.9 \cdot 10^{-5}$. The latter parameter is calculated using the fluctuation dissipation theorem ($B_{\text{glide}} = kT/D$), taking the diffusion coefficient of the 19 SIA loop at 900K ($D \sim 4.5\dot{A}^2$/ps with a perimeter of ∼3.5nm). B_{climb} is estimated using the climb equation Eq 6.34, and is many orders (∼25) of magnitude higher than the climb. As can be seen from Figure 6.15, the two simulations yield distinctly similar diffusion coefficients and show an inverse relationship with dislocation loop perimeter. This demonstrates that a stochastic implementation of DD can quantitively reproduce the behaviour seen in molecular dynamics (or indeed experiments, if these yield drag parameters). The added benefit of stochastic DD is the gained ability to simulate much larger ensembles of dislocation loops at longer timescales, whilst retaining all elastic interactions.

Variation with temperature

The same comparison between molecular dynamics and stochastic dislocation dynamics can be done with respect to temperature, keeping size constant. Using the same edge segment drag per unit length γ of $7.9 \cdot 10^{-5}$Pa·s as found previously, one can extract diffusion constants to the various generated time-series. Figure 6.16

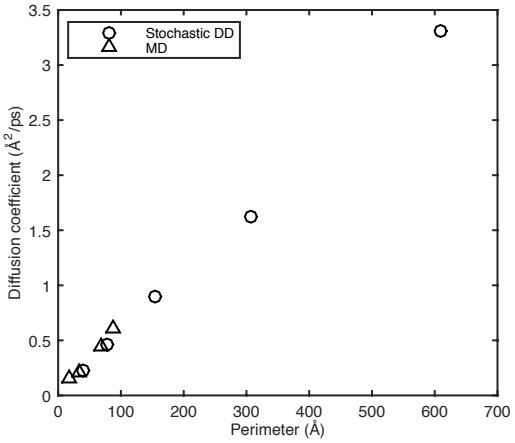

Figure 6.15: Comparison between diffusion coefficients of interstitial $\frac{1}{2}\langle 111\rangle$ prismatic loops of varying sizes in tungsten at 900K, calculated from molecular dynamics and stochastic dislocation dynamics.

shows good agreement at temperatures of interest between MD and stochastic DD, despite the latter being many orders of magnitude faster. It should be noted that the drag per unit length used was taken from a MD simulation at a *single* temperature (900K), yet the stochastic implementation still provides an relatively accurate prediction of diffusive behaviour. This is useful since a complete parameterization over many temperatures may not necessarily be available (and requires a large computational expense if simulated via molecular dynamics). However, if this information *is* available, it is equally straightforward to include it in the stochastic DD implementation, with an "optimal" drag value for the specific temperature chosen as an input parameter (in fact, if time units are scaled with drag and made dimensionless, this procedure can be done *post* simulation [5]).

Example simulation: three loops coalescing

A coarsening mechanism observed in the annealing experiments involved the formation of loop chains, which subsequently turned into single oblong loops. Here we set up a simple simulation of three hexagonal prismatic loops ($r = 3$nm) of $\boldsymbol{b} = \frac{1}{2}[111]$

[5]DDLab has dimensionless units, for example. Length is scaled with the lattice constant a, stress by shear modulus σ and time units with edge drag B_{edge} and shear modulus, $t^{\text{SI}} = t^{\text{DDLab}} B/\sigma$. Therefore, if the other drag parameters (such as climb, screw) are scaled with respect to edge in the simulation, the simulation need not have a physically/numerically accurate edge drag parameter (instead $B_{\text{edge}} = 1$) until post-processing, when real units of time are of interest.

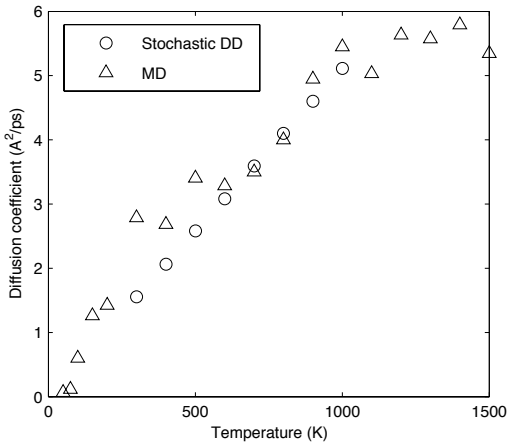

Figure 6.16: Comparison between diffusion coefficients calculated from molecular dynamics and stochastic dislocation dynamics of a ∼3.5nm perimeter (19SIA) interstitial $\frac{1}{2}\langle 111\rangle$ prismatic loop in tungsten at varying temperatures.

in a 100nm thick thin film, at 500°C, residing (111) habit planes ∼10nm apart. The loops' glide cylinders do not overlap, and touch externally. The three loops are offset in the z-direction ∼10nm from the thin film midplane. Snapshots in the simulation can be found in Figure 6.17.

The loops initially exist on three different habit planes. The equilibrium distance between the three habit planes depends on the elastic energy, which depends on the Burgers vector and the separation between the three loops. In this simulation, the Burgers vector are identical and the segments are of edge-type, making the energy minima occur when the separation between the glide cylinders is equal to the distance between the habit planes. Therefore, the farther apart the glide cylinders are, the larger the separation between habit planes, and the more difficult for the loops to coalesce. In the simulation, the glide cylinders almost intersect making the preferred habit plane distance small enough for the dislocation lines of separate loops to coalesce (Figure 6.17(b)). Once coalescence takes place, dislocation line tension is high enough to straighten the lateral edges to create an oblong shape which resides approximately on the same habit plane. Due to the presence of image forces, the loop moves tendentially in the +z direction towards the upper thin film surface.

The simulation can thus adequately simulate the formation of oblong structures

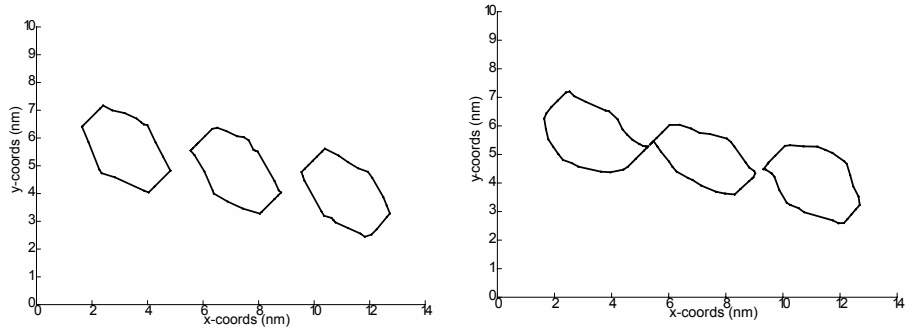

(a) t=0ps **(b)** t=1.5ps

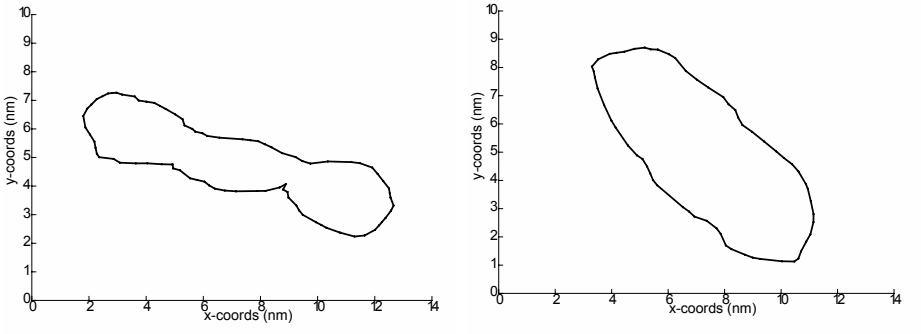

(c) t=5ps **(d)** t=200ps

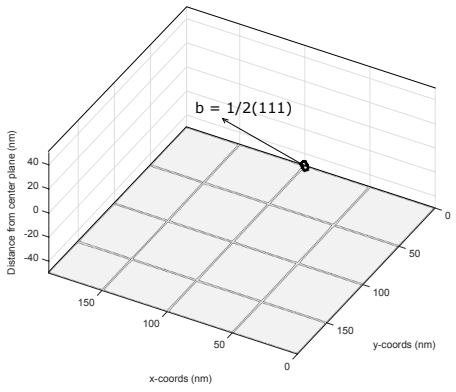

(e) t=200ps, 3D

Figure 6.17: (a)-(d) Stages in coalescence of three dislocation loops of identical $\boldsymbol{b} = \frac{1}{2}[111]$, shown from a [001] perspective: (a) Initial condition, (b) attraction between loop edges and glide dislocation motion, (c) coalescence between edges, (d) formation of oblong dislocation loop and straightening of sides due to line tension, and slight tilting of loop due to surface force attraction (strongest on top left corner due to orientation). In the final image (e), the coalesced loop is shown with respect to the free surfaces with the arrow pointing along the $\boldsymbol{b}$-vector. It will eventually exit the thin film via glide.

via glide-based mechanisms. However, if the loops' glide cylinders were sufficiently separated, such structures would not form, preferring to remain in a chain/raft-like formation. This is because, as mentioned in Section 3.5.3, the climb drag estimated by vacancy bulk-diffusion is much higher than such a process would allow. Using much longer time steps, the loops simply remain in a raft-formation, until they shrink and annihilate independently (or move in lock-step towards a free surface, if present, and get absorbed). It is possible therefore that a *non*-elastic based mechanism is being observed in experimental observations (Figure 3.16), such as pipe diffusion of vacancies along the dislocation loop [265].

Example simulation: spatial reordering of loops in a thin film

To demonstrate that elastic interactions play an important role in the formation of loop chains, a sample simulation is created whereby loops of $\frac{1}{2}\langle 111\rangle$ of $r_{\text{mean}} = 3\text{nm}$ and variance of 0.5nm are distributed homogeneously (with small perturbations) in the x-y plane in a thin-film of 100nm, around the mid plane. The simulation is run at 1000K.

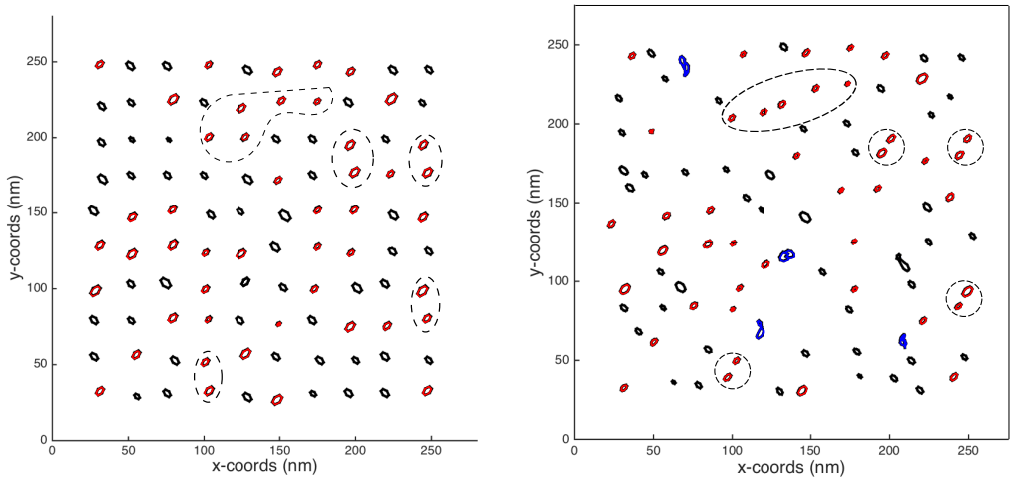

(a) Before **(b)** After

Figure 6.18: Spatial reordering of $\frac{1}{2}\langle 111\rangle$ loops in a 100nm thin film from (a) homogeneous distribution to (b) displaying loop chains and local reordering. Red loops are of one orientation, black another orientation, and blue are collided loops. The loops circled by dotted lines are examples of loop chains, which can become correlated in their glide motion (see 6.19).

In Figure 6.18, it can be observed that loops with collinear Burgers vectors which are close to each other form bound configurations, whereas loops with non-collinear Burgers vectors do not exhibit such tendency towards self-confinement, although they may interact with other defects should their glide cylinders intersect. The evolution of the system is continuous, not reaching a steady-state in the timescale of the simulation, due to the diffusive nature of the defects. However, the formations of locally ordered many-body loop structures, involving loops with collinear Burgers vectors, remain stable over long intervals of time. These configurations form spontaneously in the simulations, similarly to how they form in *in situ* observations in Chapter 3, despite a homogeneous irradiation. This can be further demonstrated in Figure 6.19, which shows the simulated Brownian trajectories of three nanoscale interstitial loops. Loops A and B are close to each other (∼2nm), and share the same $\frac{1}{2}(111)$ Burgers vector. Due to the high degree of elastic interaction between the two defects, their trajectories are highly correlated, and they behave as a "chain". Loop C on the other hand, also with $\frac{1}{2}(111)$ Burgers vector, but much farther to Loop A and B (∼20nm), does *not* display this diffusive correlation. This behaviour has also been observed experimentally elsewhere [162].

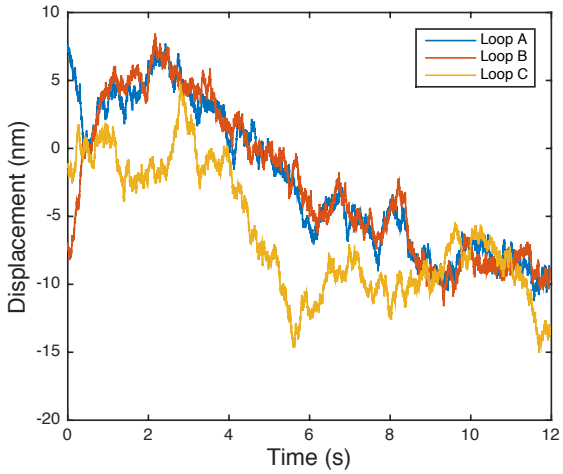

Figure 6.19: Simulated trajectories of motion for three interacting dislocation loops at 950K. All loops are prismatic interstitial type, with Burgers vector $\frac{1}{2}(111)$, and radius of 1nm. Loops A and B are separated by ∼2nm in coplanar direction, loop C is separated by ∼20nm in coplanar direction from A and B. One can see the high degree of correlation of motion between A and B, but not C.

Defect density needs to be sufficiently high for elastic interactions between nanoscale loops play a significant role. Furthermore, results in Figure 6.18 and 6.19 show that elastic interactions and reactions between radiation defects drive microstructural evolution. Similar conclusions are reached by *Dudarev et al* [187] in recent publications employing a Langevin dynamics method.

With regards to the timescales of this reordering, it depends on the drag parameters in the model. Using dislocation loop diffusion coefficients calculated in Section 6.3.3 via molecular dynamics, the process is predicted to occur in timescales of pico to nanoseconds. This does *not* match the timescales observed in experiments, which occur in the order of seconds to hours, depending on the temperature. This discrepancy is attributed to pinning by material impurities, as the values from molecular dynamics assume an obstacle-free matrix. In α-iron, the migration activation barrier for an interstitial $\frac{1}{2}\langle 111\rangle$ extracted from experiments is $\sim$1.3eV, from *Arakawa et al* [182]. This is in contrast to a migration activation barrier of $\sim$0.024eV from molecular dynamics [266].

One can try to estimate the difference in timescales in tungsten by the following procedure. The simulation in Figure 6.18 was run at 1000K, or $0.27T_m$, where one would expect to see loop re-ordering in timescales of seconds. Assuming the diffusivity of dislocation defects at $0.27T_m$ in tungsten (1000K) is approximately the same as that in α-iron at $0.27T_m$ (489K)[6], then using the latter temperature and the experimental activation barrier 1.3eV in Eq 6.35 from Ref [187, 161],

$$D(T) = (\bar{D}/2\rho)\exp(-E_a/k_BT) \tag{6.35}$$

where $\bar{D} = 5.7\cdot 10^{13}\text{nm}^3/\text{s}$ and ρ is the loop radius ($\approx$ 3nm), we get a diffusion coefficient of $D_{\text{exp}} = 3.79\cdot 10^{-11}\dot{A}^2/\text{ps}$, much smaller than those calculated via molecular dynamics in Section 6.3.3 (Figures 6.13 and 6.14), and a $\mathfrak{B}_{\text{exp}} \approx 1\cdot 10^6\text{Pa}\cdot\text{s}$[7]. Using the drag coefficient calculated from the empirical migration activation energy in the

[6]Empirically from [68], this is qualitatively correct

[7]$\mathfrak{B} \approx k_BT/(D2\rho\pi)$, and $t_{\text{SI}} = \mathfrak{B}/\sigma$ where σ is the shear modulus of the material.

stochastic dislocation dynamics code, yields a process timescale of seconds, as opposed to nanoseconds. The re-ordering of loops in Figure 6.18 would be predicted to take ~ 22 seconds instead of $\sim$1.8 *nano*seconds (from a $\mathfrak{B}_{\mathrm{MD}} \approx 8 \cdot 10^{-5}$Pa·s from Section 6.3.3).

In conclusion, the stochastic DD formulation works standalone and in conjunction with free surfaces and other boundary conditions, correctly predicting the formation of experimentally observed dislocation structures and behaviours. However, it will only predict the timescales of such processes correctly with correct drag parameters. If one wants to model *experiments*, the drag parameters from molecular dynamics simulations *cannot* be used, unless these somehow account for impurities and other effects which cause the large discrepancies in predicted diffusivity.

6.5 Comparisons with experiments

This section will briefly look at benchmarking the DDLab code incorporating free surfaces (Chapter 5) and stochastic mobility (Chapter 6) to experimental data gathered in Chapter 3, mainly the predicted loop density and loop size distributions based on different heat treatments.

6.5.1 Set-up

A randomised dislocation structure was generated with similar characteristics as "as-irradiated" TEM foils analysed in Section 3.2, with $\sim 3 \cdot 10^{22}$ loops·m^{-3} density and size distribution found in Figure 3.3. Practically, this was achieved by generating 300 loops with mean diameter of ∼4nm in a 316×316nm^2 area in a thin-film of 100nm thickness. The interstitial-type loops had Burgers vector $\frac{1}{2}\langle 111 \rangle$. Subsequently, the dislocation structure was progressed temporally, at a specified temperature (which also affected the magnitude of stochastic fluctuations). Total dislocation line length, loop density, and average loop size were tracked. Results shown here took ∼1 month to calculate on a single GPU.

6.5.2 Defect density

Figures 6.20 and 6.21 show the results of the simulation compared to experimental isochronal annealing data at 800°C, taken from Figure 3.10, Chapter 3. The inlaid plots magnify the initial 10 minutes. It can be seen that the computational method has good predictive capabilities with respect to defect number density.
The experimental data is fitted with either a power (a) or logarithmic (b) fit, given in Eq 6.36. The same fit type is used for the simulation data.

$$\begin{aligned} N(t) &= N(0) \cdot (1 - At)^B \text{ , power fit} \\ N(t) &= A + log(B)t \text{ , logarithmic fit} \end{aligned} \tag{6.36}$$

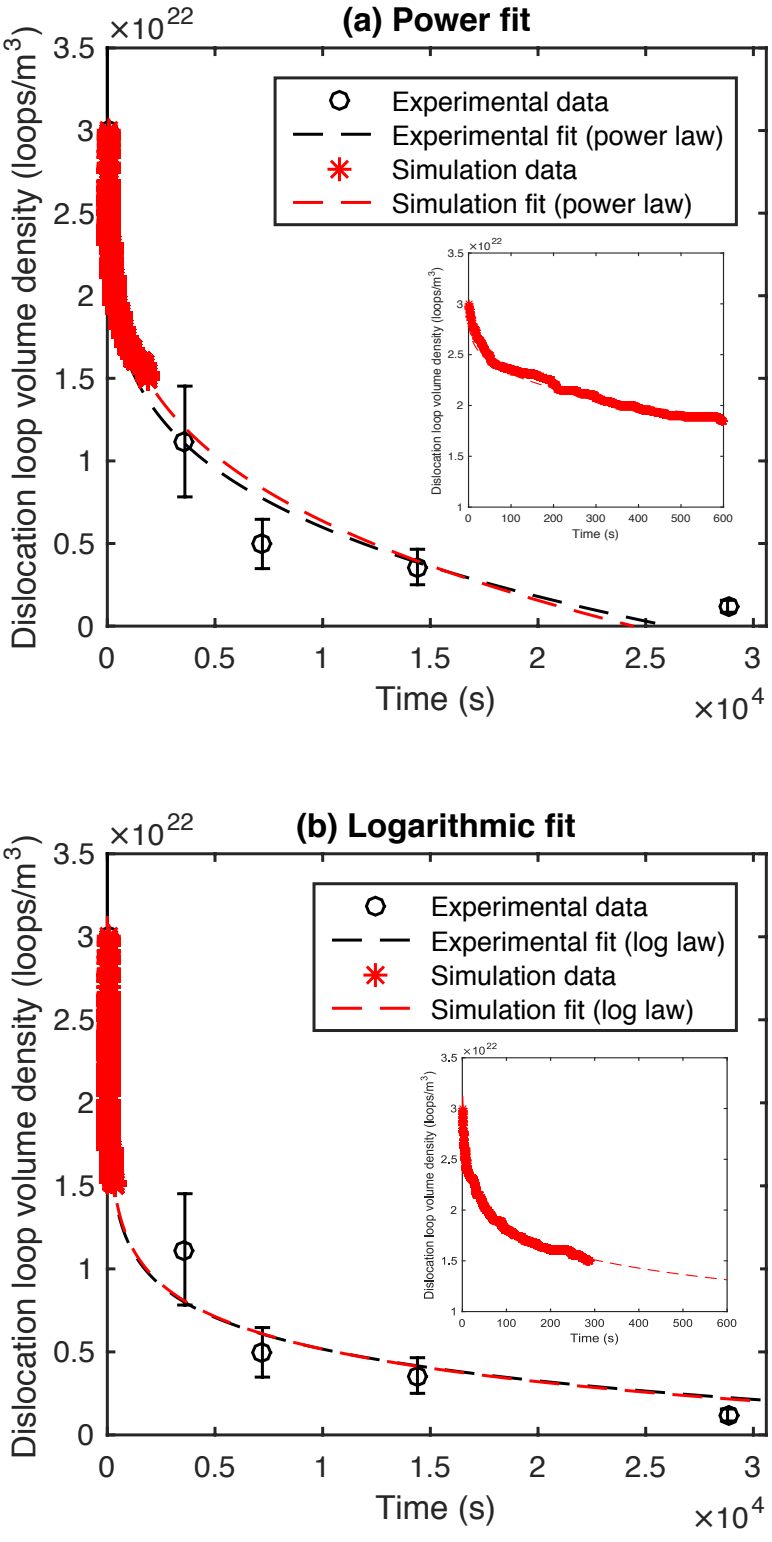

Figure 6.20: Comparison of simulation and experimental data of isothermal annealing at 800°C. The dashed lines are fits using two different models, a power law and a logarithmic law. The inlaid graphs magnify the first 10 minutes of annealing.

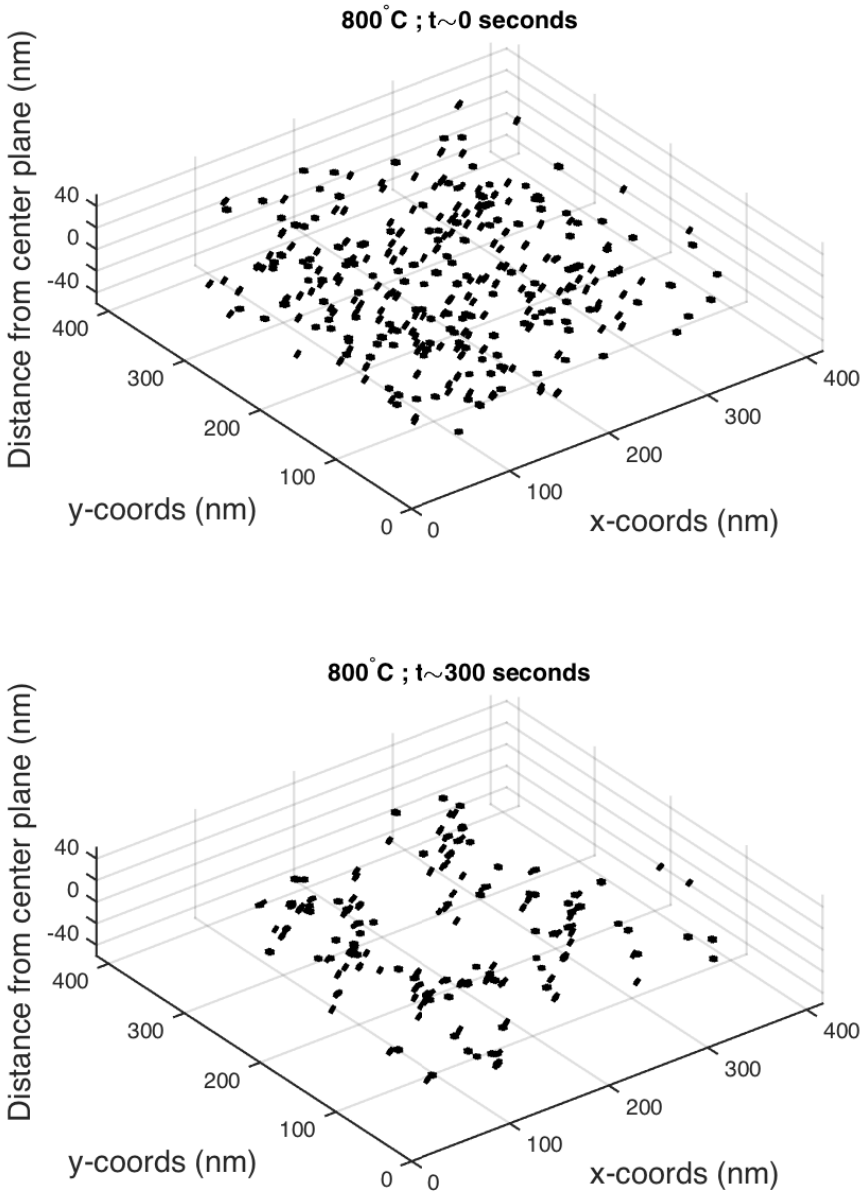

Figure 6.21: Example dislocation structure in simulated thin film at t=0 and 300 seconds, for 800°C isothermal annealing.

In the simulated data, real time linearly depends on a glide mobility parameter which is unknown experimentally in tungsten, and cannot be estimated reliably via molecular dynamics (as discussed in Section 6.4.3). Therefore, this is kept as a free parameter, with a particular value chosen for Figure 6.20(a) or (b) as the one giving the lowest error when compared to the experimental data. Figure 6.22 shows the variation of this error with glide mobility parameter. It is evident that the logarithmic fit is better than the power law at fitting the experimental data, particularly at longer timescales. This is because at a given temperature some defects (or defect complexes) may be extremely difficult to anneal away due to elastic interactions creating unsurmountable energy barriers (as captured in the computational model). The glide mobility at 800°C extracted from Figure 6.22 is $\sim 6 \cdot 10^5$ Pa·s for the logarithmic fit, and $\sim 4 \cdot 10^6$ Pa·s for the power fit. This is a reasonable answer, considering that glide mobility estimated semi-analytically from [187, 161] in Section 6.4.3 gave $\sim 1 \cdot 10^6$ Pa·s.

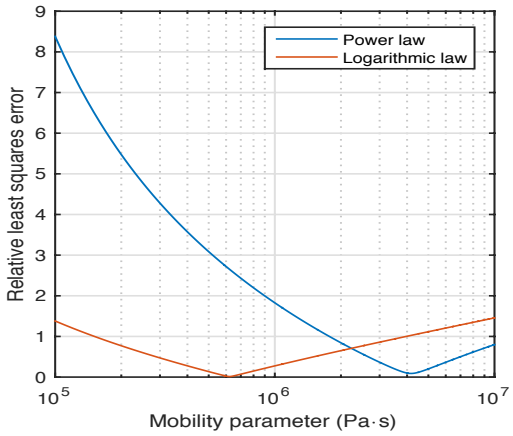

Figure 6.22: Relative least square error between simulation fit and experimental fit, both using either a power law or a logarithmic decay law. The simulation data in Figure 6.20 is scaled using the mobility parameter corresponding to the error minima shown here.

Importance of stochasticity

To get a quantitatively correct behaviour during annealing, stochasticity of dislocation mobility as implemented in Chapter 6 is important. In a completely deter-

	Experimental	Simulation
Power fit coefficients	A = 0.0957 B = 0.2307	A = 0.0682 B = 0.2658
Logarithmic fit coefficients	A = $3.0547 \cdot 10^{22}$ B = $-2.7556 \cdot 10^{21}$	A = $3.05468 \cdot 10^{22}$ B = $-2.7556 \cdot 10^{21}$

Table 6.1: Comparison of experimental and simulation fit coefficients (from Eq. 6.36). Units are loops$\cdot m^{-3}$ for defect density and seconds for time.

ministic, traditional DDD framework, some defect complexes within the thin film maybe be in a meta-stable equilibrium (due to elastic interactions with other defects) which, on the other hand, could be potentially "escaped" from if stochastic fluctuations were present. Such situation may eventually lead to higher defect densities in the deterministic case. This is shown in Figure 6.23, where the simulation is annealed at 800°C (in terms of timescale-determinant mobility parameter) with and without a stochastic mobility implementation. The blue line represents annealing using a stochastic mobility law. At around ∼200 seconds the dislocation structure was saved and progressed in parallel also without stochasticity. One can see that the density plateau at $\sim 1.6 \cdot 10^{22}$ loops$\cdot m^{-3}$ lasts longer for the purely deterministic case due to self-trapped loop configurations unable to escape when there are no fluctuations.[8]

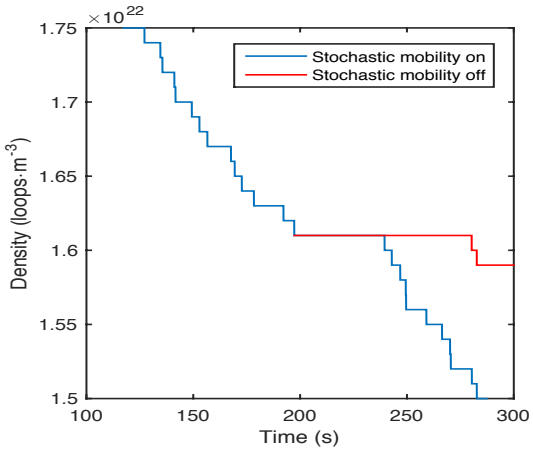

Figure 6.23: Variation of dislocation loop density during 800°C isothermal annealing with (blue line) and without (red line) stochastic mobility.

[8]The drop at ∼280 seconds when stochastic mobility is switched off is due to some loops escaping in another location in the thin film, which are presumably not self-trapped.

6.5.3 Defect size

Figure 6.24 shows the change in size distribution of dislocation loops with annealing time in the 800°C isothermal annealing simulation. This is characterised by a decrease in number frequency of smaller (2-5nm) diameter loops (absorbed by free surfaces) and an increase in number frequency of larger (5-8nm) diameter loops created from loop-loop glide cylinder interactions similar to those shown in Figure 6.17. Experimentally, from Figure 3.2 in Chapter 3, dislocation loop coarsening at 800°C even after several hours of annealing is modest (<10% increase in loop diameter); therefore, the simulation seemingly agrees with experimental observations. However, there is disagreement for temperatures of 950°C and above, where coarsening is very significant experimentally, but not so in simulations. At these temperatures, in-situ annealing in Section 3.4.1 revealed additional *non-glide* coarsening mechanisms being activated, mainly loop conservative self-climb resulting in coalescence of loop chains with non-intersecting glide cylinders.

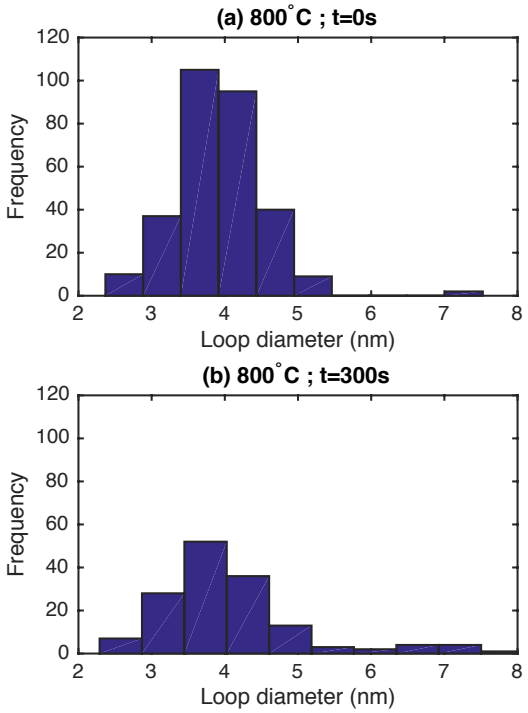

Figure 6.24: Change of size distribution of dislocation loops with annealing time in isothermal simulation at 800°C. 5 minutes yields a ∼5% increase in mean size.

Missing phenomena

The marked coarsening of dislocation loops at temperatures above 950°C, attributed to self-climb of loops, cannot be replicated in the current modelling simulation framework, as it relies on climb mobilities being dependent on local stress. As future work, this should be tackled to better simulate radiation damage annealing. To the author's knowledge, no publicly available dislocation dynamics code has this capability, which has been shown to have an important effect on defect topology at high temperatures, here and also in other materials [181, 180].

6.6 Chapter Summary

This chapter describes the theoretical basis, implementation, testing and validation, and experimental comparison of a stochastic approach to modelling temperature dependence of dislocations in the context of discrete dislocation dynamics, to extend the functionality of DDD and complement bulk diffusion models and parameterized fittings of dislocation mobility already developed. The method consists in adding a stochastic velocity term which depends on temperature, edge and screw mobilities, dislocation segment characteristics (Burgers vector, line direction, slip plane), and has been shown to match molecular dynamics simulations without the need of complex parameterizations or empirical models. It has also been shown to broadly match the timescales of annealing experiments, but only if *experimentally* derived drag parameters are used. The key behaviours it can successfully replicate, additionally to all the non-thermal stress-driven dislocation mechanisms described in previous chapters, are:

- Physically representative, material specific thermally-driven diffusive motion of dislocations segments and loops, whether individually or in ensembles, acting in conjunction to elastically-driven motion.
- Physically representative, material-specific diffusive timescales in the glide direction, when used with realistic drag parameters.
- Inverse proportionality of diffusion coefficient to dislocation segment length.
- Quantitatively accurate dislocation loop density changes with isothermal annealing in thin films compared to experiments, although failing at capturing significant loop coarsening at temperatures of 950°C and above.

This formulation does not require additional parameters to those used in a standard dislocation dynamics simulation. However, to get *quantitatively* accurate diffusive timescales, the drag parameters (B_{edge}, B_{screw}, B_{climb}), which also depend on temperature, need to be picked accordingly to the temperature and material used in

the simulation. B_{edge} is the most important parameter and can be estimated via molecular dynamics or empirically, depending on the need. It has been shown that there is a large discrepancy in the drag parameter whether the estimation is done via MD or experiment, possibly due to the role of impurities as obstacles in real-life scenarios.

This mobility will *not* accurately predict the conservative self-*climb* observed in Chapter 2. associated with the drastic coarsening of loops from >900°C, with further modifications necessary. The time scales associated with this latter effect cannot be described neither via bulk diffusion models nor using this new stochastic formulation.

Chapter 7

Conclusions

Looking back at the aims of the project, these involved gathering quantitative information on damage morphology in tungsten for (as close as possible) fusion relevant conditions, identifying any recovery stages, pathways, and quantifying rates and activation energies. Furthermore, the challenge was set to use theory and computational tools to attempt simulations of thermal effects on dislocation structures in tungsten, and ultimately relate such dislocations to overall mechanical performance.

Chapters 3 and 4 achieved the first part of the task, looking at the effect of annealing (temperature and time), and the presence of helium, on radiation damage. Several key points were found. For annealing of self-ion irradiation damage at fusion-relevant temperatures, no $\mathbf{b}=\langle 100\rangle$-type loops were found, only $\frac{1}{2}\langle 111\rangle$-type, of predominantly interstitial nature. The exact behaviour of dislocations changed with temperature: small dislocation loops were observed hopping from 300°C (in glide directions), increasing in frequency from 500°C. By 800°C, loops had rearranged into loop "chains" or clusters. Increasing the temperature resulted in formation of larger irregular or oblong finger loops from coalescence of smaller loops in such chains. Above 1000°C, dislocation lines moved relatively freely, interacting with smaller dislocation networks and "sweeping" out damage. In some instances, *conservative climb* of dislocation loops was observed in *in situ* annealing at high temperature ($\geq$900°C). However, the rates at which this process occured was found to be inconsistent with current models, suggesting a different kind of pathway. It is hypothesized this process might also be partly responsible for the accelerated coars-

ening of observed dislocation loops at high temperature. With regards to helium, its presence favours the nucleation of dislocation loops, allowing higher defect densities and saturation at lower doses, as well as impeding dislocation motion (and consequently loop-loop interactions). This experimental analysis was supplemented by molecular statics and dynamics simulations. Furthermore, injecting high doses of He (45,000 appm) causes morphological changes of the radiation damage structure, from a homogeneous defect concentration of dislocations in a narrow size range, into a complex dislocation network with voids. Nanosized voids were *not* observed in the TEM in the 1,800appm case at 500°C. However, they were observed both in the 1,800 and 45,000appm cases at 800°C, suggesting void formation depends strongly on temperature for these dose levels.

Chapters 5 and 6 achieved the second part of the task, but not without caveats. In summary, the functionality of a commonly available open source dislocation dynamics program (DDLab) was greatly extended to: 1) deal with thin films, relevant to transmission electron microscopy, 2) deal with mixed displacement and traction boundary conditions, to allow a fundamental connection between dislocation structures and mechanical response of an arbitrary convex meshed shape, and 3) the addition of a stochastic mobility law allowing the incorporation of more realistic temperature fluctuations (previously inexistant) on dislocations, fitted specifically for tungsten via molecular dynamics. These functional extensions were possible also due to a complete re-writing of large sections of the original program, utilising novel analytical solutions where possible, or computational improvements (such as parallelisation), given in Appendix B.

From such developments, it was found that important physical effects observed in the experimental work presented in this study and/or literature could also be observed in the models. In the case of dislocations in thin films, it was shown that the presence of free surfaces may enhance the absorption of loops considerably, producing denuded zones near such surfaces (see Figure B.8 in Appendix B). The magnitude of the effect depends on multiple factors, such as mobility in the glide direction, loop sizes

and sample thickness. By incorporating a stochastic formulation of mobility, effects such as loop diffusion and loop hopping was replicated, as seen in experiments, as well as formation of loop chains/rafts. The stochastic formulation relies on mobility parameters, and when these were taken from molecular dynamics, quantitatively correct diffusive coefficients were extrapolated. There is thus no practical reason why the model formulation cannot accept experimentally-derived mobilities if available (these are preferable for practical reasons, since MD and experimental dislocation drag differ by many orders of magnitude due to unavoidable presence of impurities and other defects in the latter). Finally, incorporating a fully 3-dimensional coupling to a finite element method solver allowed the prediction of important mechanical processes such as yield, elastoplastic deformation, slip bands and dislocation pile-ups. These predictions can be fitted to a specific material, in this case tungsten, with only two variables: dislocation source density, and dislocation source nucleation stress.

For future work, an accelerated recovery of defects was observed at $\geq$900°C, whereby loop chains coalesced via climb to form oblong ellipsoids, which were more prone to becoming absorbed or turning into dislocation lines. This process should occur at timescales far longer than observed based on standard interpretations of climb, pointing rather to a self-climb mechanism. This should be implemented. Furthermore, experiments to estimate diffusion coefficients of nanoscale defects should be undertaken in tungsten, similar to excellent experiments done in α-iron [182]. Furthermore, the fundamental force-velocity dependency of dislocations segments in conventional discrete dislocation dynamics is dependent on largely arbitrary drag parameters for screw, edge and climb which have a great effect on predicted *timescales* of processes, and which are known to vary according to temperature. Here we presented an improvement using a stochastic mobility formulation which describes important physical effects such as loop diffusion and hopping previously unreproducible using standard models. However, a more coherent, less ad-hoc formulation would be desirable. This is in fact an active area of research [264].

Appendix A

Appendix A: Formulae

A.1 Image stress in thin film

A.1.1 Analytical solutions for stress tensor components of image stress Fourier mode

$$
\begin{aligned}
\hat{\sigma}_{xx} &= 2\mu \left[\left(\frac{iA\lambda k_z}{\lambda+\mu} + (iEk_x^2 z + iBk_x k_y - Ck_x^2) \right) \cosh(k_z z) \right. \\
&\quad \left. + \left(\frac{iE\lambda k_z}{\lambda+\mu} + (iAk_x^2 z - iFk_x k_y - Gk_x^2) \right) \sinh(k_z z) \right] \\
\hat{\sigma}_{yy} &= 2\mu \left[\left(\frac{iA\lambda k_z}{\lambda+\mu} + (iEk_y^2 z - iBk_x k_y - Ck_y^2) \right) \cosh(k_z z) \right. \\
&\quad \left. + \left(\frac{iE\lambda k_z}{\lambda+\mu} + (iAk_y^2 z + iFk_x k_y - Gk_y^2) \right) \sinh(k_z z) \right] \\
\hat{\sigma}_{zz} &= -2\mu \left[\left((iEz(k_x^2+k_y^2) - C(k_x^2+k_y^2)) - \frac{(\lambda+2\mu)iAk_z}{\lambda+\mu} \right) \cosh(k_z z) \right. \\
&\quad \left. + \left((iAz(k_x^2+k_y^2) - G(k_x^2+k_y^2)) - \frac{(\lambda+2\mu)iEk_z}{\lambda+\mu} \right) \sinh(k_z z) \right] \\
\hat{\sigma}_{xy} &= i\mu \left[\left(2Ek_x k_y z - (k_x^2 - k_y^2)B + 2ik_x k_y C \right) \cosh(k_z z) \right. \\
&\quad \left. + (2Ak_x k_y z + (k_x^2 - k_y^2)F + 2ik_x k_y G) \sinh(k_z z) \right] \\
\hat{\sigma}_{yz} &= \mu \left[\left((2Ak_y z + Fk_x + 2ik_y G)k_z - \frac{2Ek_y \mu}{\lambda+\mu} \right) \cosh(k_z z) \right. \\
&\quad \left. + \left((2Ek_y z - Bk_x + 2ik_y C)k_z - \frac{2Ak_y \mu}{\lambda+\mu} \right) \sinh(k_z z) \right] \\
\hat{\sigma}_{xz} &= \mu \left[\left((2Ak_x z - Fk_y + 2ik_x G)k_z - \frac{2Ek_x \mu}{\lambda+\mu} \right) \cosh(k_z z) \right. \\
&\quad \left. + \left((2Ek_x z + Bk_y + 2ik_x C)k_z - \frac{2Ak_x \mu}{\lambda+\mu} \right) \sinh(k_z z) \right]
\end{aligned}
\tag{A.1}
$$

A.1.2 Inverse of M^S and M^A matrices

The inverse of M^S and M^A matrices used in the calculation of image stress for thin films can be computed numerically from Eq 5.31 and 5.32 in Section 5.4. However, for better performance and accuracy, M^S and M^A can be inverted analytically, as given here in Eq A.2 and A.3.

$$(M^S)^{-1} = \frac{1}{\mu(k_z^4 t + k_z^3 \sinh(k_z t)\cosh(k_z t))}\cdot$$

$$\begin{bmatrix} \frac{1}{2}k_x k_z \cosh(k_z t) & \frac{1}{2}k_y k_z \cosh(k_z t) & -\frac{1}{2}ik_z^2 \sinh(k_z t) \\ k_y(\frac{k_z t}{\sinh(k_z t)} + \cosh(k_z t)) & -k_x(\frac{k_z t}{\sinh(k_z t)} + \cosh(k_z t)) & 0 \\ \frac{1}{2}ik_x(\sinh(k_z t)k_z t - \frac{\lambda+2\mu}{\lambda+\mu}\cosh(k_z t)) & \frac{1}{2}ik_y(\sinh(k_z t)k_z t - \frac{\lambda+2\mu}{\lambda+\mu}\cosh(k_z t)) & \frac{1}{2}(-\frac{\mu k_z}{\lambda+\mu}\sinh(k_z t) + k_z^2\cosh(k_z t)t) \end{bmatrix} \tag{A.2}$$

$$(M^A)^{-1} = \frac{1}{\mu(k_z^4 t - k_z^3 \sinh(k_z t)\cosh(k_z t))}\cdot$$

$$\begin{bmatrix} -\frac{1}{2}k_x k_z \sinh(k_z t) & -\frac{1}{2}k_y k_z \sinh(k_z t) & \frac{1}{2}ik_z^2 \cosh(k_z t) \\ -k_y(\frac{k_z t}{\cosh(k_z t)} - \sinh(k_z t)) & k_x(\frac{k_z t}{\cosh(k_z t)} - \sinh(k_z t)) & 0 \\ -\frac{1}{2}ik_x(\cosh(k_z t)k_z t - \frac{\lambda+2\mu}{\lambda+\mu}\sinh(k_z t)) & -\frac{1}{2}ik_y(\cosh(k_z t)k_z t - \frac{\lambda+2\mu}{\lambda+\mu}\sinh(k_z t)) & -\frac{1}{2}(\frac{-\mu k_z}{\lambda+\mu}\cosh(k_z t) + k_z^2\cosh(k_z t)t) \end{bmatrix} \tag{A.3}$$

Appendix B

Appendix B: Computational optimizations

B.1 Necessity for computational efficiency in dislocation dynamics

Several computationally intensive tasks are present in dislocation dynamics simulations, which have the potential of being parallelized. Whereas particular codes have been engineered to run on CPU clusters [213], this work presents acceleration techniques leveraging the computing power of Graphical Processing Unit (GPU) hardware. Order-of-magnitude speed-ups have been observed, at a fraction of the hardware cost, with little added algorithmic complexity.

In this Appendix, the main computational bottlenecks will be reviewed; secondly, the parallelization strategies will be discussed along with the motivations of such approaches; thirdly, benchmarking results will be presented; finally, an example large simulation is demonstrated.

The benchmarking was done on a NVIDIA Kepler-architecture GeForce GTX670, with 2048MB of device memory and 1344 cores at 915MHz clock speed, *or* a NVIDIA Tesla K20, with 5120MB of device memory and 2496 cores at 745MHz clock speed. The CPU used was an Intel i7-3930K with 6 cores at 3.2GHz clock speed.

B.2 DD Algorithms

Three main computational bottlenecks are present in dislocation dynamics, which have potential for parallelization. These are segment-segment interactions, surface traction calculations, and image-stress calculations. The latter two are relevant for DD simulations in which free surfaces are important.

B.2.1 Segment-Segment Interactions

For straight dislocation segment, the stress tensor expressions are non-trivial so to calculate the PK force between one pair of segments requires ≈ 1200 flops. Given the $1/R$ dependence of dislocation stress fields, in principle all segments of the network interact with each other, making it an N-body problem, thus:

$$t_{\text{seg}-\text{seg}} = \mathcal{O}(N^2) \tag{B.1}$$

where N is the number of segments. In straining experiments for example, the number of segments increases dramatically with strain. This algorithm is typically the most time consuming part of a line DD simulation.

B.2.2 Surface Traction

This is a grid-based problem, where the calculation of traction at a given point in a grid is independent of the calculation at another grid location. Equally, the calculation of the contribution of the stress from a segment on a point is independent of the contribution of stress from another segment on the same point. The computational time thus depends on the number of segments in the simulation N and the total number of surface grid points k.

$$t_{\text{traction}} = \mathcal{O}(kN) \tag{B.2}$$

B.2.3 Image Stresses

Using a spectral-based method, an arbitrary displacement field u can be written as the superposition of Fourier components $\hat{u}$. The stress field in Fourier space is then obtained via Hooke's Law, $\hat{\sigma}_{ij} = \lambda \hat{u}_{k,k}\delta_{ij} + \mu(\hat{u}_{i,j} + \hat{u}_{j,i})$. Arbitrary stress and traction fields can thus be written as a superposition of Fourier modes. This calculation must be repeated *at least* once for each segment (N) with midpoint position x,y,z. Therefore, the computational time of such an algorithm depends linearly on the number of segments in the simulation N, and the number of grid points $k = n^2$, which defines the size of the input traction grids (3D for FEM and 2D for BEM).

$$t_{\text{image}} = \mathcal{O}(kN) \tag{B.3}$$

B.3 Parallelization Techniques on GPUs

B.3.1 Segment-Segment Interactions

The all-pairs approach to an N-body simulation is a brute-force technique that evaluates all pair-wise interactions among the N segments. For very large networks, the all-pairs approach is typically combined with a faster method based on a far-field approximation of longer-range forces. General fast N-body algorithms include the Barnes-Hut method [267], the fast multipole method (FMM) [268], and the particle-mesh method [269], and have been shown to benefit from GPU treatment [270]. ParaDiS, a CPU-cluster DD code [213], uses the FMM algorithm, reducing global computation to $\mathcal{O}(N\log(N))$, as opposed to $\mathcal{O}(N^2)$. Regardless, the near-field (all-pairs) component of the algorithms mentioned above still depend on $\mathcal{O}(N^2)$ and require substantial time to compute; therefore, they are the target for GPU acceleration. Improving the performance of the all-pairs algorithm will have synergistic effects on the far-field performance. An accelerated all-pairs component means the balance between far-field and an accelerated near-field (all-pairs) can be

shifted to assign more work to the latter [271].

From Figure B.1, one can imagine the all-pairs algorithm as calculating each entry f_{ij} in an $N \times N$ grid of all segment pair-wise forces. The total force f_i on segment i is obtained from the sum of all entries in row i.

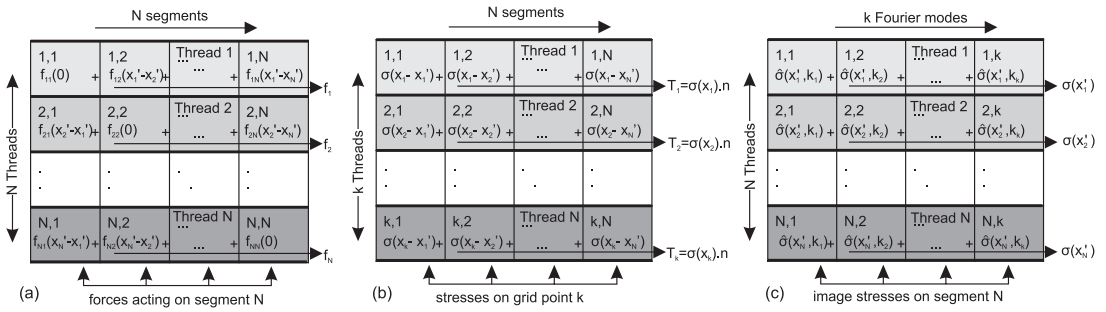

Figure B.1: Parallelism of the N^2 segment interactions (a), surface traction at k grid points (b) and image stress on N segments (c).

$\mathcal{O}(N^2)$ parallelism is available, thus each entry can be computed independently, and then globally reduced. However, this approach also requires $\mathcal{O}(N^2)$ memory and is limited by memory bandwidth.

Consequently, N-order parallelism is utilized, with N-order serialization. In other words, a number of threads equal to the number of segments in the simulation is invoked. Each thread is assigned a unique segment, and each thread serially computes the forces between that segment and all the other segments and adds (serially) the force contributions, see figure B.1 (a). Therefore, each thread gives the nodal force on a single segment as a result of the entire dislocation structure. This approach also has the advantage that there is no read/write competition of memory addresses between threads. The order in which single threads sequentially compute segment-segment interactions is kept identical. This thread synchronization allows for optimal data reuse, since the data defining the particular segment (nodal positions, burgers vector) used for a particular sequential calculation is the same for all threads.

In earlier GPU architectures, such as NVIDIA Fermi, the way to achieve this data reuse necessitated employing shared memory, and was limited to each thread block.

One must remember that a large allocation of shared memory means a smaller amount of register space per thread.

Owing to an addition of a global L2 cache in Kepler (and future) architecture GPUs, use of shared memory was not found to be strictly necessary for good performance. Shared GPU memory supports concurrent reads from multiple threads to a single memory address, so there are no shared-memory-bank conflicts of the interactions. However, the use of shared memory requires a greater algorithmic complexity and more indexing operations, and its allocation comes at the expense of total register space. For DD segment-segment force calculations, the simple approach without shared memory was found to be most suitable, with memory re-usage occurring on the L2 cache level if necessary. Owing to the complexity of calculations per thread and many intermediate variables that required temporary storage, register pressure and overspill were more detrimental to performance.

B.3.2 Surface Traction

Given that there are analytical solutions for the stress at a point due to a discrete dislocation segment, the parallelization potential for the surface traction algorithm is $\mathcal{O}(kN)$ where k is the number of grid points, and N is the number of threads. Since the stress of the entire dislocation structure on a given grid point (for many points) is the variable of interest, if this maximum parallelization strategy was taken, a subsequent global reduction of the stresses of individual dislocation segments on the point into a total stress would have to be executed.

This strategy was not chosen due to memory requirements. Instead, a parallelization of $\mathcal{O}(k)$ was chosen, with sequential calculation of stress from each dislocation segment and sequential addition onto the total stress. Individual threads were assigned to each grid point, and told to sequentially scan through the dislocation segment list in synchrony, see figure B.1 (b) In doing so, the amount of intermediate variables stored per thread is kept at a minimum, and can be stored in lower memory levels such as directly in registers or L1 cache, which have significantly lower memory

latency than global device memory.

B.3.3 Image Stresses

The details of the parallelization strategy depend on the method used, either semi-analytical spectral methods or FEM. Regardless of the inner workings of the particular algorithm, the most obvious parallelization strategy is to invoke the image stress algorithm in parallel for each dislocation segment in the simulation. In the case of the spectral method, the image stress at a given point in the simulation space is given by the addition of wave modes, the number of which is equal to size of the input traction mesh. Thus, by assigning parallel threads based on dislocation segments, all wave mode stress contributions are added sequentially, see figure B.1 (c), and potential competition of memory overwriting by concurrent threads is avoided.

B.4 Benchmarking

The code to be accelerated was DDLab[138], a freely downloadable DD code written in Matlab. The three bottlenecks described above were implemented in CUDA and benchmarked, and the Matlab GPU-kernel (parallel.gpu.CUDA.Kernel()) function from the Parallel Computing Toolbox was used to subsequently link such GPU routines to the main Matlab program, in a conceptually similar fashion to how C/C++ or FORTRAN routines can be invoked, except the latter are sequential codes and run on the CPU.

All benchmarking gives both the Matlab equivalent (as found in DDLab), as well as standalone C/C++ equivalent for comparison.

B.4.1 Segment-Segment Interactions

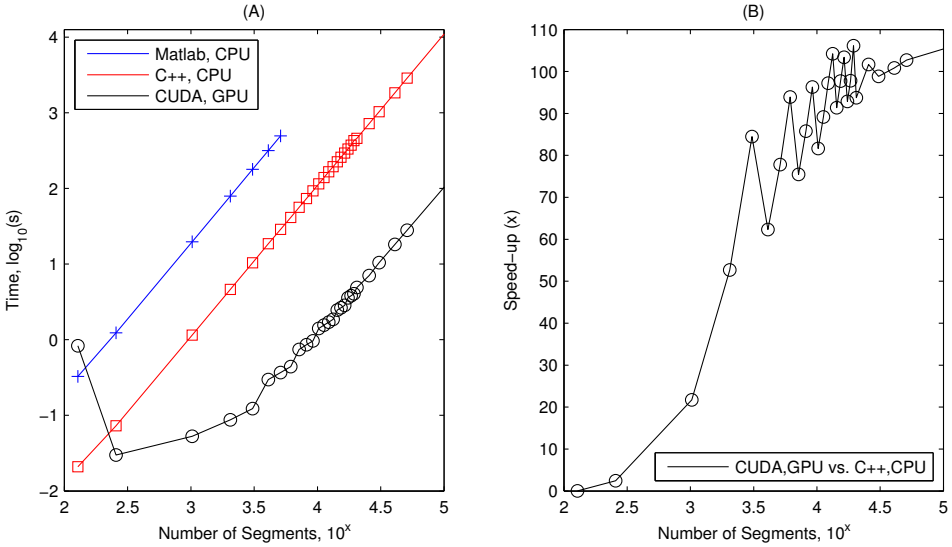

Figure B.2: (A) Time taken for segment-segment force calculations using original DDLab code, a serial standalone C/C++ code, and the GPU CUDA code, for increasing number of segments, up to $\sim 1 \cdot 10^5$. (B) Speed-up of the GPU CUDA code compared to the CPU C++ code. Benchmarked on a NVIDIA K20.

B.4.2 Surface Traction

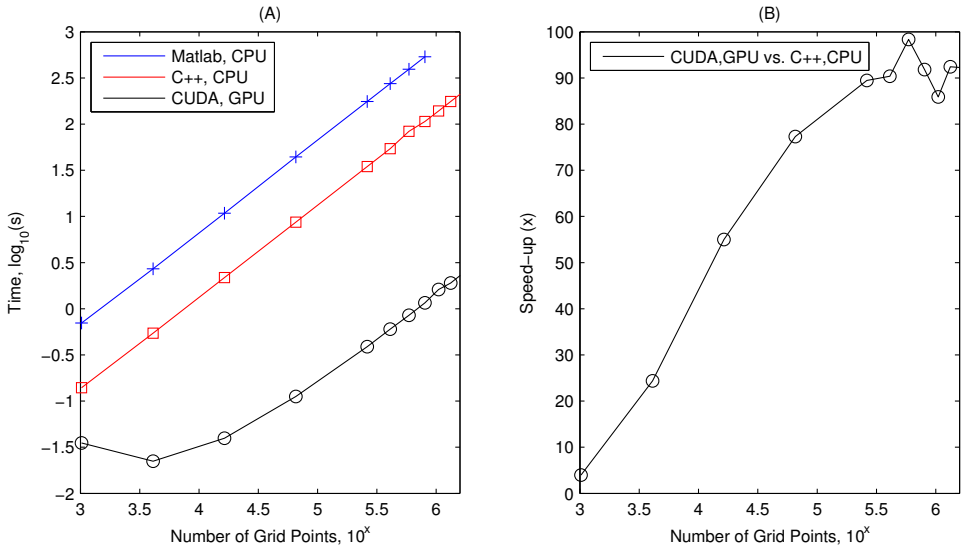

Figure B.3: (A) Time taken for surface traction calculations using original DDLab code, a serial standalone C/C++ code, and the GPU CUDA code, for increasing number of *grid points*, up to $\sim 1 \cdot 10^6$. 512 dislocation segments in domain. (B) Speed-up of the GPU CUDA code compared to the CPU C++ code. Benchmarked on a NVIDIA K20.

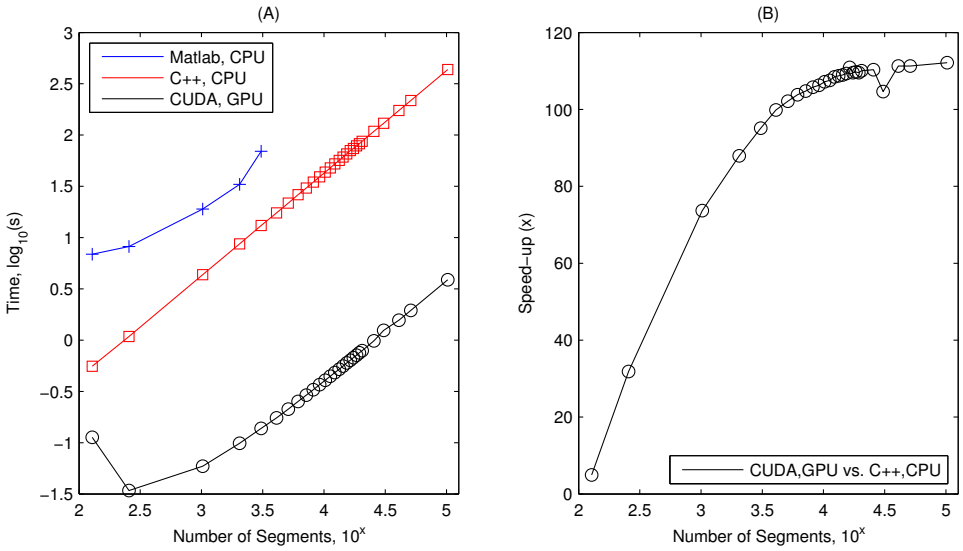

Figure B.4: (A) Time taken for surface traction calculations using original DDLab code, a serial standalone C/C++ code, and the GPU CUDA code, for increasing number of *segments*, up to $\sim 1 \cdot 10^5$. 128×128 point grid. (B) Speed-up of the GPU CUDA code compared to the CPU C++ code. Benchmarked on a NVIDIA K20.

B.4.3 Image Stresses

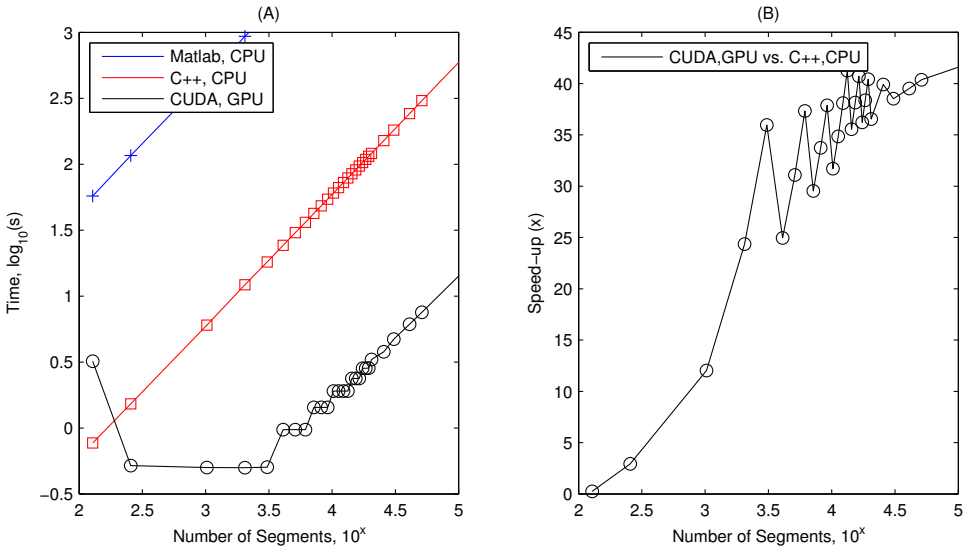

Figure B.5: (A) Time taken for surface traction calculations using original DDLab code, a serial standalone C/C++ code, and the GPU CUDA code, for increasing number of *segments*, up to $\sim 1 \cdot 10^5$. 128×128 point grid. (B) Speed-up of the GPU CUDA code compared to the CPU C++ code. Benchmarked on a NVIDIA K20.

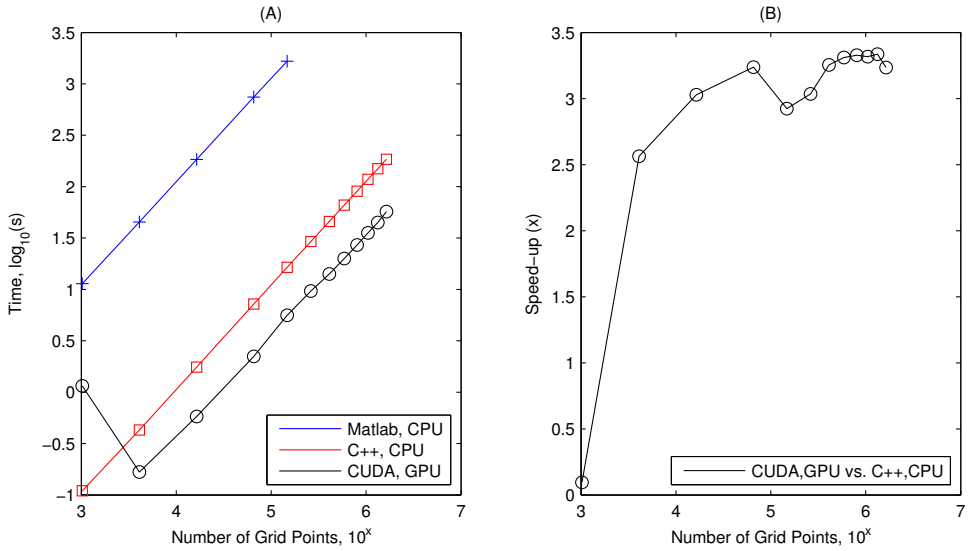

Figure B.6: (A) Time taken for surface traction calculations using original DDLab code, a serial standalone C/C++ code, and the GPU CUDA code, for increasing number of *grid points*, up to $\sim 1 \cdot 10^6$. 512 dislocation segments in domain. (B) Speed-up of the GPU CUDA code compared to the CPU C++ code. Benchmarked on a NVIDIA K20.

It can be seen in log-log plot Figure B.2 that the slope for execution time vs. segment count is equal to 2, consistent with Equation (3). GPU computation becomes beneficial at ≥300 segments, with $\mathcal{O}(10^2)$ speedup compared to a serial C++ code for $\geq 10^4$ segments. The slopes in Figure B.3 to B.6 are equal to 1, also consistent with Equations (5) and (7). For the image stress computations, because parallelisation occurs in the segment dimension, for the benchmarked 512 segments in Figure B.6, the speed-up is not dramatic. This is because GPU computation of image stresses (for 128^2 Fourier modes) becomes particularly beneficial for $\geq \mathcal{O}(10^3)$ segments, as seen in Figure B.5.

B.5 Further Optimization Remarks

Further computational optimizations can increase the performance by another ∼25% depending on the simulation parameters.

B.5.1 Input Data Structure

One key implementation decision is how to store the datasets containing several data elements for each set element (i.e. 3D nodal locations of a dislocation segment and their Burger's vector). Two main options are Array-of-Structures (AoS) or Structure-of-Arrays (SoA). The first views the segment variables as a contiguous item, and holds an array of these. The latter has a separate array for each type of data element, as shown in Figure B.7.

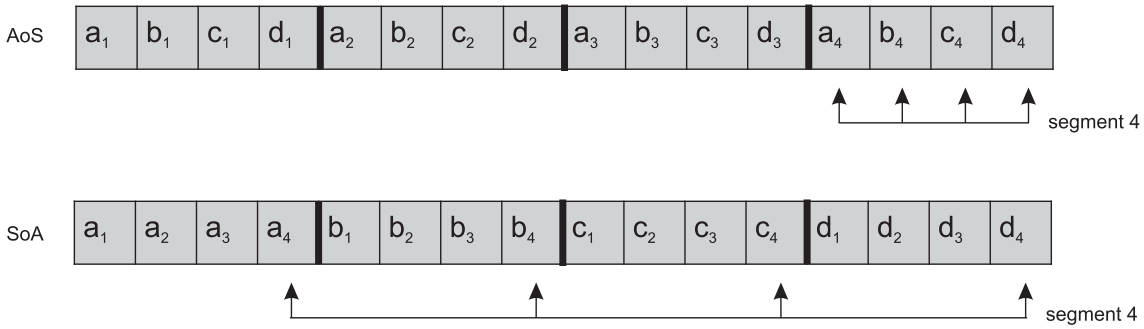

Figure B.7: Memory locations of variables for each segment, for AoS (top) and SoA (bottom) options.

The SoA approach is a natural choice for parallel streaming. The AoS approach is natural for conventional CPUs as it requires few active virtual pages at a time and, provided all the local elements are used, cache utilization is efficient. Despite being highly parallel, for the kernels described above the AoS approach is suggested. Taking the segment-segment algorithm as an example, this is perhaps counter-intuitive. An N-order number of threads must access information in parallel regarding their assigned dislocation segment, and a SoA data structure would be beneficial for this. However, since every thread must subsequently scan through all other segments sequentially, an AoS data structure becomes more favorable since cache line utilization is more efficient.

Given that the DD algorithms are compute-limited rather then memory-limited, memory latency is relatively unimportant due to the long compute times. However, a simple optimization of input data structures as described above still gives an average performance benefit of $\sim$20% and was implemented in the DD code reported here.

B.5.2 Constant Memory

For constant physical parameters, such as shear modulus, Poisson ratio and dislocation core radius, it is suggested to allocate such variables to constant memory. This produces an average performance benefit of $\sim$5%.

Since such physical parameters do not change during the entire simulations, one could also hard-code them into the CUDA files, and pre-compile the required executables before initiating a simulation. The physical constants would be computed at compile time and would not require to be fetched in memory during runtime. An automatic parsing script was developed to automatically modify the CUDA files depending on the input Matlab physical parameters, and compiled automatically. Although this approach can have significant performance benefits in other applications, it was found to have negligible performance improvements for the added complexity in the DD code so was not implemented here.

B.5.3 Block Size

It is difficult to decide on an optimal block-size because of the potentially large variation of total thread count depending on the simulation. A brute-force optimization was conducted where several block sizes were tested for given simulation sizes, with a fluctuation of up to +/-30% in performance. It is difficult to decide *a-priori* this parameter and thus it is suggested to perform such an optimization for each particular GPU architecture used, as well as average simulation size. A good middle ground between large and small simulations was found to be 256 threads per block.

B.6 Large Simulation Demonstration

B.6.1 Thin Film Simulation

An example of all three described algorithms working simultaneously is the simulation of dislocation loops in a thin film. A simulation on a 1×1 micron surface (100

nm thickness) was performed, see Figure B.8, using a NVIDIA Kepler-architecture GeForce GTX670. The CPU used was an Intel i7-3930K.

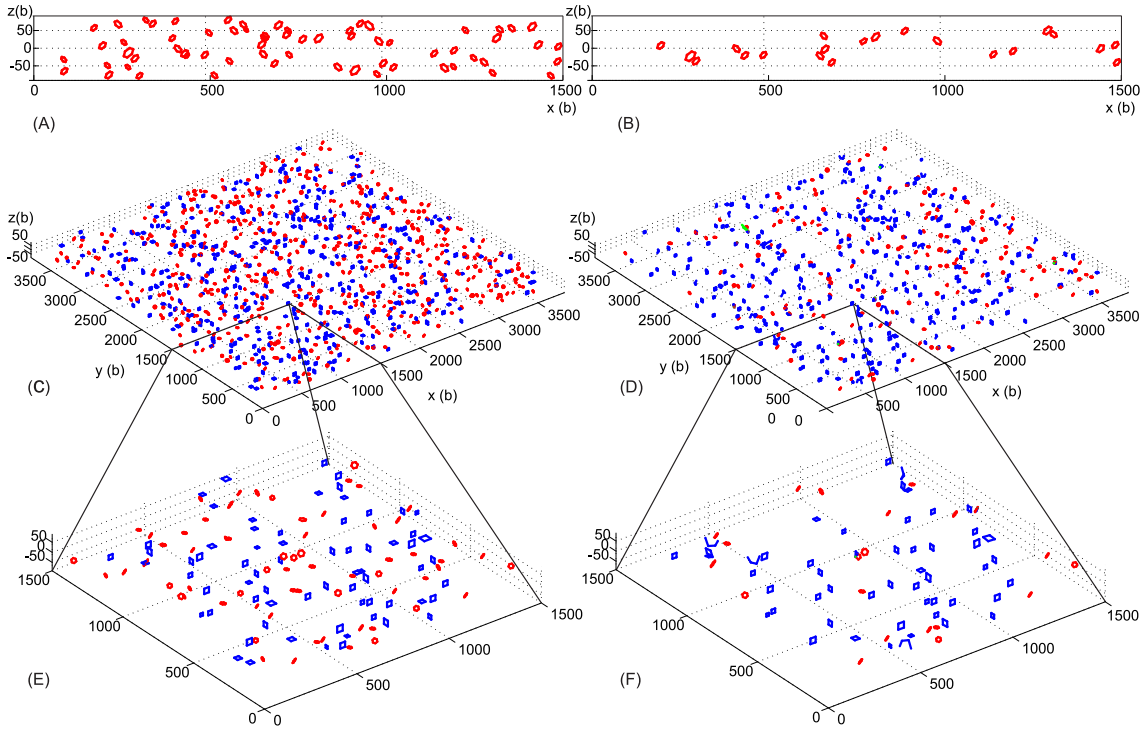

Figure B.8: Side view of the thin-film, showing ⟨111⟩ type loops in red at start (A) and finish (B) and the formation of a denuded zone near the surface in the latter. 3D view of thin film, showing all loop types, ⟨111⟩ in red, ⟨100⟩ in blue, ⟨110⟩ in green, at start (C) and finish (D). 3D view of magnified area of thin film, showing all loop types at start (E) and finish (F). Benchmarked on NVIDIA GTX670.

Such a simulation would have been be unfeasible for the original DDLab, as well as a sequential C/C++ code. For 1000 dislocation loops and 5000 iteration time-steps, the GPU simulation was complete in 57.2hours, including free surface calculations and a brute-force $\mathcal{O}(N^2)$ algorithm for segment-segment interactions. For a CPU simulation, this would have equated roughly to 6-7 months of compute time (or an equivalent real-time on a 84-cpu cluster, *assuming perfect scalability*). Given that the retail price of the CPU and the GPU used at the time of writing was roughly equivalent, the GPU offers a better performance/price ratio.

It is important to note that the GPU card used, a GeForce GTX670, can only reach *1/24th* of its maximum capable GFLOPs when performing operations on double precision numbers (as was done in this case). Had a card with double-precision hardware optimisation been used (i.e. K-series), the completion time would have

been a further $\sim 5\times$ faster. A single-precision implementation of the above algorithms was also tested and found to be even faster; however, its accuracy was unsatisfactory for general purpose simulations and therefore is not considered.

Appendix C

Appendix C: Validation of 3D FEM-coupled DDD software

C.1 Calculation of $\tilde{\sigma}$, the stress due to dislocations in an infinite domain

The value of $\tilde{\sigma}$ depends on the dislocation structure. There are non-singular equations to analytically calculate $\tilde{\sigma}$, as shown previously in Formula 5.3. However, it is also possible to calculate this stress via the finite element method, by deriving it numerically from the displacement $\tilde{u}$, using $\sigma = DBu$. In Figure C.2, using a sample dislocation structure, the $\tilde{\sigma}$ stress as calculated via analytical equations is compared to FEM, on the entire left-hand surface of the cantilever, showing all unique stress tensor components. The stress matches, and the difference between the two methods becomes increasingly small with the refinement of the finite-element mesh.

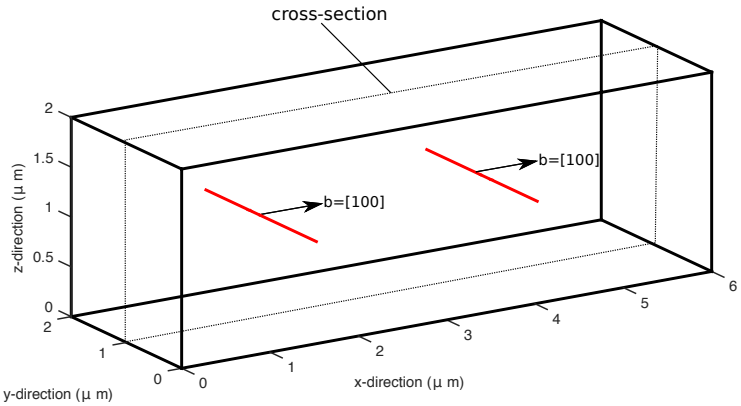

Figure C.1: Simple dislocation structure used as example for the traction and force comparisons in Figures C.2 and C.4

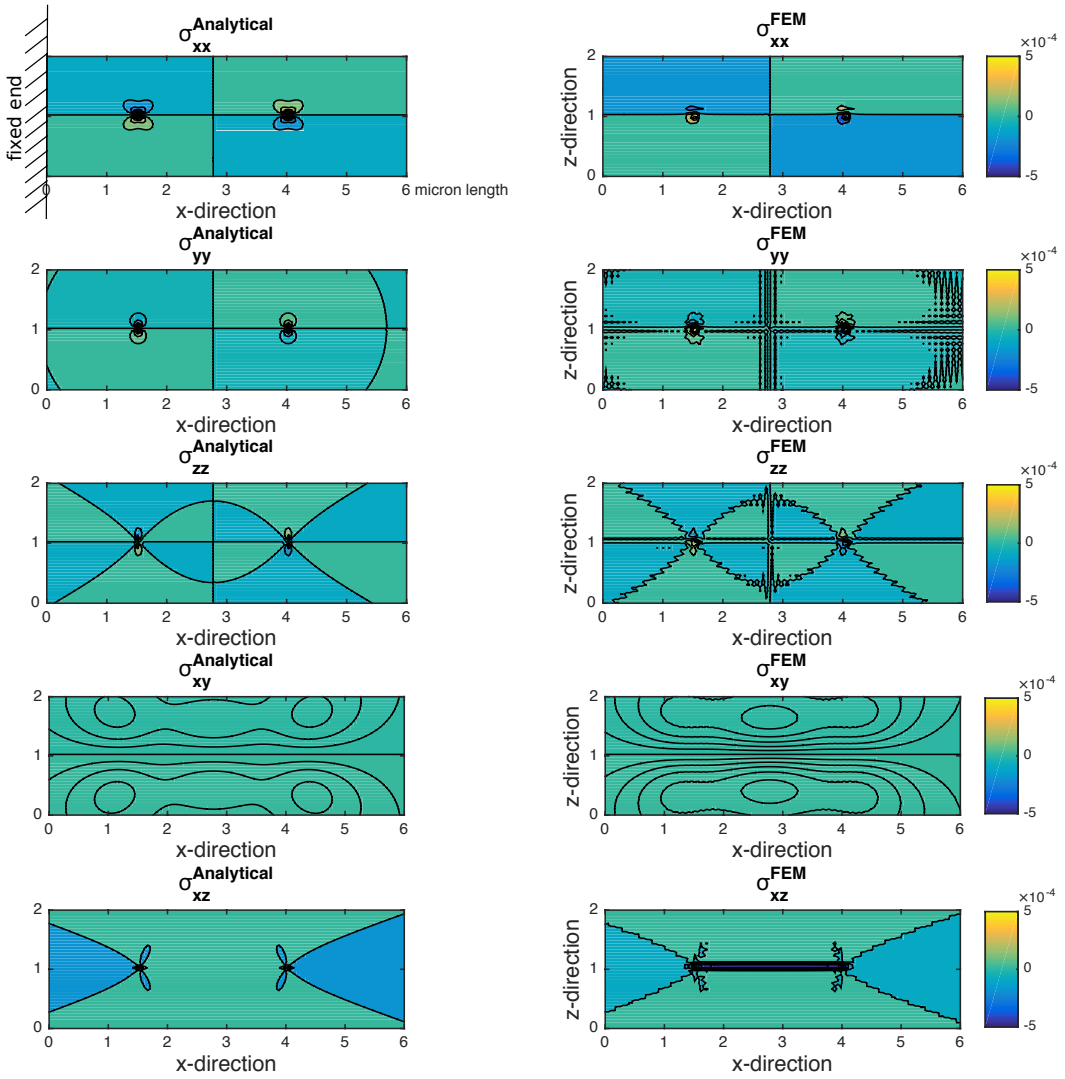

Figure C.2: Consistency check between $\tilde{\sigma}$ calculated using analytical formulas (left side) and from displacement fields via FEM (right side). The dislocation structure and plotted cross-section are shown in Figure C.1. 50 FEM elements were used in the x-direction.

The equivalence between the two methods (accounting for numerical errors in the finite element case), implies that: 1) the semi-analytical equations for $\tilde{u}$ are correctly implemented, and that 2) the finite element method correctly converts an element displacement into its associated stress tensor.

C.2 Calculation of $\tilde{f}$, the force due to dislocations on a mesh element

Equations for $\tilde{f}$ derived by *Queyreau et al* [272] have been implemented. These allow the analytical calculation of the force on mesh element nodes due to a given dislocation structure, $\tilde{f}$. The alternative approach would be based on the finite element method: the stress due to the dislocations ($\tilde{\sigma}$) is calculated at the mesh element midpoint, the traction calculated by the dotting this stress with the element plane normal, and the force calculated by multiplying the traction by the element's surface area. This accuracy of the second approach is dependent on the level of discretization of the finite element mesh.

The equations by Queyreau are very useful as they allow to decouple this important calculation from a numerical FEM approach. This is critical particularly when dealing with dislocations close to a free surface, as the force gradients are high and only resolvable to a good degree of accuracy with extremely high levels of discretisation, implying a high computational cost. The comparison between the numerical and analytical approach is shown in Figure C.3. It can be seen that the two match, taking into account the numerical error associated with the FEM approach, and that by refining the mesh, the error in $\tilde{f}$ decreases, as shown in Figure C.4. The error here is defined as $|(f^{\text{analytical}} - f^{\text{FEM}})|/f^{\text{analytical}}$, averaged over the elements.

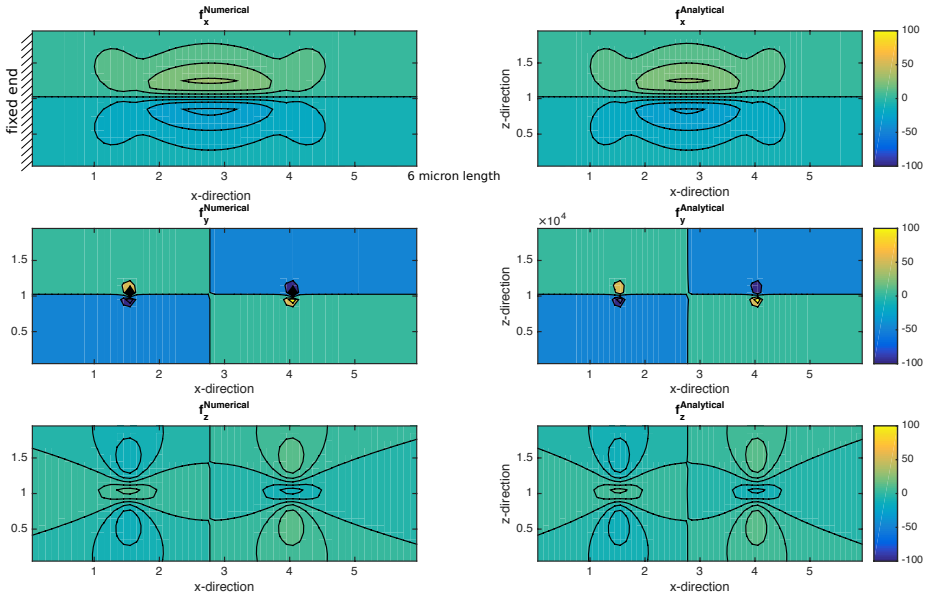

Figure C.3: Calculation of $\tilde{f}$ due to presence of a dislocation structure. Right side shows analytical procedure using equations by Queyreau et al. [272]. Left side shows numerical procedure using the finite element method. The dislocation structure and plotted cross-section are shown in Figure C.1. 50 FEM elements were used in the x-direction.

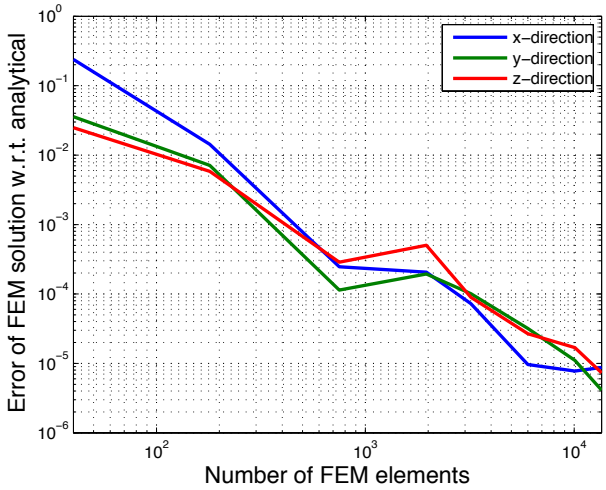

Figure C.4: Relative error of x, y, z components of $\tilde{f}$ as calculated analytically and numerically (via FEM) in case study cantilever scenario.

C.3 Identification of external and internal dislocation segment nodes for arbitrary tessellated domain geometry

The tessellation procedure for an arbitrary surface, and the correct implementation of the algorithm identifying dislocation segment nodes inside or outside an arbitrary convex domain defined by a tessellated surface will be demonstrated. In Figure C.5, one can see the identification of nodes inside and outside the domain in two dimensions (N.B the algorithm works readily in three dimensions, but has been shown in two dimensions for clarity).

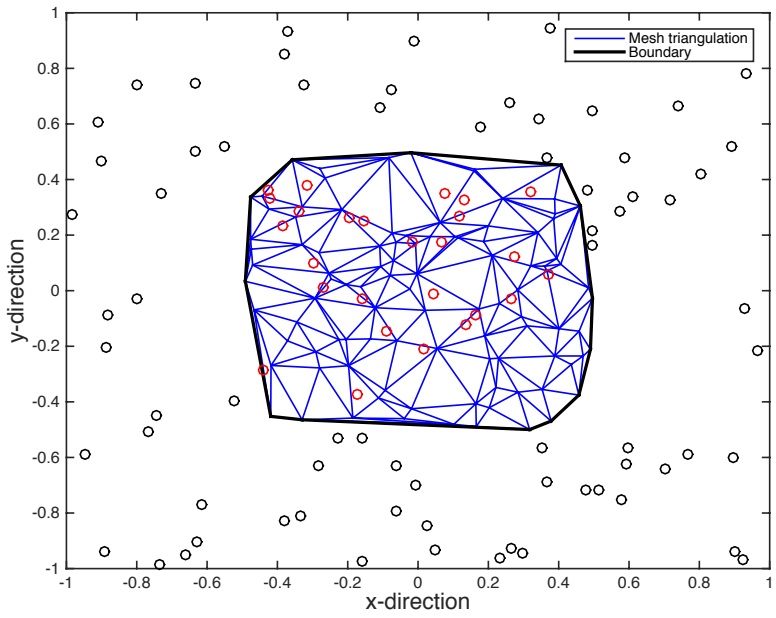

Figure C.5: 2D example to demonstrate the identification of nodes outside or inside a domain. The blue lines are the triangulation created from the list of nodes, where the thick black line delineates the surface boundary. Black circles are nodes which have a logical value of 0 (i.e. outside the domain). Red circles are points which have a logical value of 1 (i.e. inside the domain).

C.4 Remeshing exiting dislocations

The general algorithm for handling dislocations exiting an arbitrary tessellated surface was explained in Section 5.5.5. Here one can demonstrate it in action with the

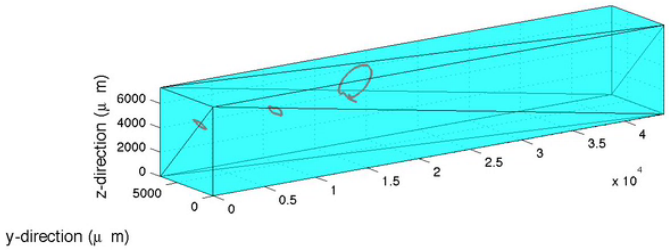

(a)

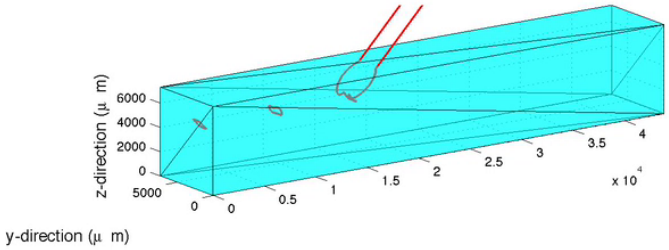

(b)

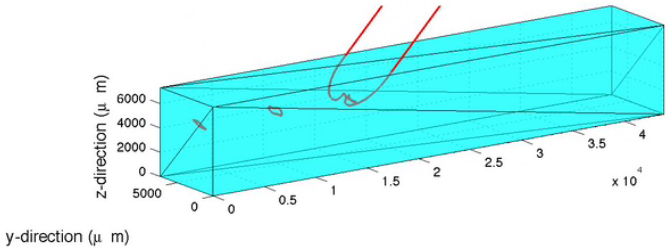

(c)

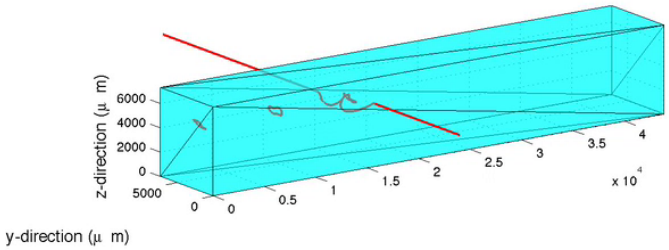

(d)

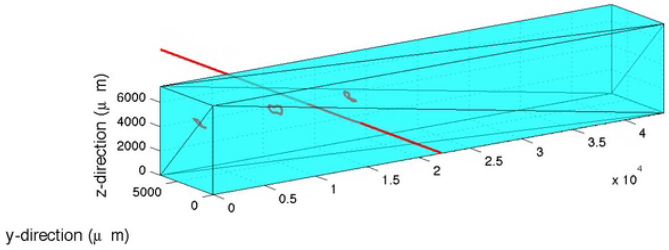

(e)

Figure C.6: Demonstration of the re-meshing of an exiting dislocation segment, for multiple surfaces of varying orientation.

case study of a micro cantilever. The left side is fixed, with the right side being loaded at a constant rate of displacement. In C.6(a) one can see the bowing out of a dislocation source, due to the applied stress from the loading. In this instance, the dislocation is contained within the finite element domain. In C.6(b) part of this line exits the top surface of the cantilever. The remeshing algorithm extends this edge section a long distance away, in the direction found by taking the projection of the segment's Burgers vector on the slip plane. In C.6(c) the dislocation bows out further. The virtual dislocation line far away remains unchanged (not shown), but the dislocation surface nodes are kept mobile to allow further surface slip. In C.6(d), the dislocation bows out sufficiently to intersect with another surface tessellation. This transition is handled correctly by the algorithm, which changes the virtual segment extension direction accordingly. Finally, in C.6(e), the dislocation line separates from the Frank-Read source, and stabilises at the cantilever's neutral axis, where the net force in the z-direction is zero.

Bibliography

[1] F. Ferroni, X. Yi, K. Arakawa, S.P. Fitzgerald, P.D. Edmondson, and S.G. Roberts. High temperature annealing of ion irradiated tungsten. *Acta Materialia*, 90:380–393, 2015.

[2] F. Ferroni, E. Tarleton, and S.P. Fitzgerald. Dislocation dynamics modelling of radiation damage in thin films. *Modelling and Simulation in Materials Science and Engineering*, 22(4):045009, 2014.

[3] F. Ferroni, E. Tarleton, and S.P. Fitzgerald. GPU accelerated dislocation dynamics. *Journal of Computational Physics*, 272:619–628, 2014.

[4] F. Ferroni, K.D. Hammond, and B.D. Wirth. Sputtering yields of pure and helium-implanted tungsten under fusion-relevant conditions calculated using molecular dynamics. *Journal of Nuclear Materials*, 458:419–424, 2015.

[5] British Petroleum Plc. BP Statistical Review of World Energy. `http://www.bp.com/statisticalreview`, 2013.

[6] R.K. Pachuari and A. Reisinger. Climate Change 2007. Synthesis Report: Contribution of Working Groups I, II and III to the Fourth Assessment Report, 2008.

[7] United States. Congress. Office of Technology Assessment. *Starpower: the U.S. and the international quest for fusion energy.* Congress of the U.S., Office of Technology Assessment, 1987.

[8] K. Ehrlich. The development of structural materials for fusion reactors. *Philosophical Transactions of the Royal Society A: Mathematical, Physical and Engineering Sciences*, 357(1752):595–623, 1999.

[9] E. E. Bloom, S. J. Zinkle, and F. W. Wiffen. Materials to deliver the promise of fusion power - progress and challenges. *Journal of Nuclear Materials*, 329:12–19, 2004.

[10] EFDA. Jet's maximum achieved parameters. `http://www.jet.efda.org/wp-content/uploads/Focus_on.pdf`, 2015.

[11] ITER. The international ITER project for fusion: Why? `http://www.iter.org/proj/itermission`, 2015.

[12] K. Miyamoto. *Plasma Physics for Nuclear Fusion.* MIT Press, 1980.

[13] M. Kotschenreuther, P. M. Valanju, S. M. Mahajan, and J. C. Wiley. On heat loading, novel divertors, and fusion reactors. *Physics of Plasmas*, 14(7):072502, 2007.

[14] J. Wesson. *Tokamaks.* International Series of Monographs on Physics. OUP Oxford, 2011.

[15] M. Merola, D. Loesser, A. Martin, P. Chappuis, R. Mitteau, V. Komarov, R.A. Pitts, S. Gicquel, V. Barabash, L. Giancarli, J. Palmer, M. Nakahira, A. Loarte, D. Campbell, R. Eaton, A. Kukushkin, M. Sugihara, F. Zhang, C.S. Kim, R. Raffray, L. Ferrand, D. Yao, S. Sadakov, A. Furmanek, V. Rozov, T. Hirai, F. Escourbiac, T. Jokinen, B. Calcagno, and S. Mori. ITER plasma-facing components. *Fusion Engineering and Design*, 85(10-12):2312–2322, 2010.

[16] B. Riccardi, R. Giniatulin, N. Klimov, and A. Loarte. Preliminary results of the experimental study of PFC's exposure to ELMs-like transient loads followed by high heat flux thermal fatigue. *26th Symposium on Fusion Technology*, 2010.

[17] P. Norajitra, S. Antusch, R. Giniyatulin, and V. Kuznetsov. Current status of He-cooled divertor development for DEMO. *26th Symposium on Fusion Technology*, 84:1429–1433, 2009.

[18] H. Bolt, V.R. Barabash, G. Federici, J. Linke, A. Loarte, J. Roth, and K. Sato. Plasma facing and high heat flux materials - needs for ITER and beyond. *Journal of Nuclear Materials*, 307-311:43–52, 2002.

[19] M.R. Gilbert and J.-Ch. Sublet. Neutron-induced transmutation effects in W and W-alloys in a fusion environment. *Nuclear Fusion*, 51(4):043005, 2011.

[20] S.J. Zinkle and G.S. Was. Materials challenges in nuclear energy. *Acta Materialia*, 61:735–758, 2013.

[21] M.R. Gilbert, S.L. Dudarev, S. Zheng, L.W. Packer, and J.-Ch. Sublet. An integrated model for materials in a fusion power plant: transmutation, gas production, and helium embrittlement under neutron irradiation. *Nuclear Fusion*, 52(8):083019, 2012.

[22] S.J Zinkle and N.M. Ghoniem. Operating temperature windows for fusion reactor structural materials. *Fusion Engineering and Design*, 51–52:55–71, 2000.

[23] L Singheiser, T Hirai, J Linke, G Pintsuk, and M Rödig. Transactions of The Indian Institute of Metals Plasma-facing materials for thermo-nuclear fusion devices. *Transactions of The Indian Institute of Metals*, 62(2):123–128, 2009.

[24] T. Munsat. High-Temperature Carbon-Irradiation Issues for the Sombrero ICF Reactor. *Fusion Engineering and Design*, 54(2):249–261, 2001.

[25] S. Pestchanyi, V. Safronov, and I. Landman. Estimation of carbon fibre composites as ITER divertor armour. *Journal of Nuclear Materials*, 329-333:697–701, 2004.

[26] Y. Igitkhanov, B. Bazylev, and I. Landman. Modelling of PFC life-time in tokamak fusion reactor. *KIT Scientific Reports 7612*, 2012.

[27] E.T. Cheng. Assessment of low activation materials. *The 14th IEEE/NPSS Symposium Fusion Engineering*, pages 621–625, 1992.

[28] R. Lindau, A. Möslang, M. Rieth, M. Klimiankou, E. Materna-Morris, A. Alamo, A.A.F. Tavassoli, C. Cayron, A.M. Lancha, P. Fernandez, N. Baluc, R. Schäublin, E. Diegele, G. Filacchioni, J.W. Rensman, B.V.D. Schaaf, E. Lucon, and W. Dietz. Present development status of EUROFER and ODS-EUROFER for application in blanket concepts. *Fusion Engineering and Design*, 75-79:989–996, 2005.

[29] T. Loarer. Tritium inventory in iter: Laboratory data and extrapolation from tokamaks. *6th EU PWI TF Meeting Madrid*, 2007.

[30] J. Roth, E. Tsitrone, T. Loarer, V. Philipps, S. Brezinsek, A. Loarte, G.F. Counsell, R.P. Doerner, K. Schmid, O.V. Ogorodnikova, and R.A. Causey. Tritium inventory in ITER plasma-facing materials and tritium removal procedures. *Plasma Physics and Controlled Fusion*, 50(10):103001, 2008.

[31] M. Rieth, S.L. Dudarev, S.M. Gonzalez de Vicente, J. Aktaa, T. Ahlgren, S. Antusch, D.E.J. Armstrong, M. Balden, N. Baluc, M.-F. Barthe, W.W. Basuki, M. Battabyal, C.S. Becquart, D. Blagoeva, H. Boldyryeva, J. Brinkmann, M. Celino, L. Ciupinski, J.B. Correia, A. De Backer, C. Domain, E. Gaganidze, C. García-Rosales, J. Gibson, M.R. Gilbert, S. Giusepponi, B. Gludovatz, H. Greuner, K. Heinola, T. Höschen, A. Hoffmann, N. Holstein, F. Koch, W. Krauss, H. Li, S. Lindig, J. Linke, Ch. Linsmeier, P. López-Ruiz, H. Maier, J. Matejicek, T.P. Mishra, M. Muhammed, A. Muñoz, M. Muzyk, K. Nordlund, D. Nguyen-Manh, J. Opschoor, N. Ordás, T. Palacios, G. Pintsuk, R. Pippan, J. Reiser, J. Riesch, S.G. Roberts, L. Romaner, M. Rosiński, M. Sanchez, W. Schulmeyer, H. Traxler, A. Ureña, J.G. van der Laan, L. Veleva, S. Wahlberg, M. Walter, T. Weber, T. Weitkamp, S. Wurster, M.A. Yar, J.H. You, and A. Zivelonghi. Recent progress in research on tungsten materials for nuclear fusion applications in europe. *Journal of Nuclear Materials*, 432(1–3):482 – 500, 2013.

[32] J.N. Brooks, J.P. Allain, R.P. Doerner, a. Hassanein, R. Nygren, T.D. Rognlien, and D.G. Whyte. Plasma-surface interaction issues of an all-metal ITER. *Nuclear Fusion*, 49(3):035007, 2009.

[33] H. Bolt, V. Barabash, W. Krauss, J. Linke, R. Neu, S. Suzuki, and N. Yoshida. Materials for the plasma-facing components of fusion reactors. *Journal of Nuclear Materials*, 329-333:66–73, 2004.

[34] B. I. Khripunov, L. S. Danelyan, V. G. Vostrikov, V. V. Zatekin, V. S. Koidan, V. S. Kulikauskas, S. T. Latushkin, V. B. Petrov, E. a. Romanovsky, a. I. Ryazanov, and V. N. Unezhev. Accumulation of deuterium in radiation-damaged tungsten. *Journal of Surface Investigation. X-ray, Synchrotron and Neutron Techniques*, 5(2):272–275, 2011.

[35] P. Gumbsch. Brittle fracture and the brittle-to-ductile transition of tungsten. *Journal of Nuclear Materials*, 323(2-3):304–312, 2003.

[36] R.W. Margevicius, J. Riedle, and P. Gumbsch. Fracture toughness of polycrystalline tungsten under mode I and mixed mode I/II loading. *Materials Science and Engineering: A*, 270(2):197–209, 1999.

[37] T.H Loi, J P Morniroli, and M Gantois. Brittle fracture of polycrystalline tungsten. *Journal of Materials Science*, 20:199–206, 1985.

[38] V. Barabash, G Federici, M Rodig, L L Snead, and C H Wu. Neutron irradiation effects on plasma facing materials. *Journal of Nuclear Materials*, pages 138–146, 2000.

[39] I.V. Gorynin, V.A. Ignatov, V.V. Rybin, S.A. Fabritsiev, V.A. Kazakov, V.P. Chakin, V.A. Tsykanov, V.R. Barabash, and Y.G. Prokofyev. Effects of neutron irradiation on properties of refractory metals. *Journal of Nuclear Materials*, 191-194:421–425, 1992.

[40] G.H. Kinchin and R.J. Pease. The displacement of atoms in solids by radiation. *Reports on Progress in Physics*, 18(1):1, 1955.

[41] N. Bohr. *The Penetration of Atomic Particles Through Matter*. Kongelige Danske Videnskabernes Selskab-Mathematisk-Fysiske. I Kommission hos Ejnar Munksgaard, 1953.

[42] J.A. Brinkman. On the nature of radiation damage in metals. *Journal of Applied Physics*, 25(8):961–970, 1954.

[43] J. Silcox and P. B. Hirsch. Dislocation loops in neutron-irradiated copper. *Philosophical Magazine*, 4(48):1356–1374, 1959.

[44] M.L. Jenkins and M.A. Kirk. *Characterization of Radiation Damage by Transmission Electron Microscopy*. Series in Microscopy in Materials Science Series. Taylor & Francis Group, 2001.

[45] R.J.M. Konings, T.R. Allen, R.E. Stoller, and S. Yamanaka. *Comprehensive Nuclear Materials*. Elsevier Science Limited, 2012.

[46] M.J. Norgett, M.T. Robinson, and I.M. Torrens. A proposed method of calculating displacement dose rates. *Nuclear Engineering and Design*, 33(1):50 – 54, 1975.

[47] A.M. Ougouag. *Defect Production Efficiency in Neutron-Irradiated Iron*. ASTM STP 1125. Effects of Radiation on Materials: 15th International Symposium, 1992.

[48] M. Robinson. Basic physics of radiation damage production. *Journal of Nuclear Materials*, 216:1–28, 1994.

[49] S.J. Zinkle and B.N. Singh. Analysis of displacement damage and defect production under cascade damage conditions. *Journal of Nuclear Materials*, 199(3):173 – 191, 1993.

[50] F. Maury, M. Biget, P. Vajda, a. Lucasson, and P. Lucasson. Frenkel pair creation and stage I recovery in W crystals irradiated near threshold. *Radiation Effects*, 38(1-2):53–65, 1978.

[51] C.H.M. Broeders and A.Y. Konobeyev. Defect production efficiency in metals under neutron irradiation. *Journal of Nuclear Materials*, 328(2-3):197–214, 2004.

[52] R.N. Stuart, M.W. Guinan, and R.J. Borg. A computer simulation of the effect of temperature on the threshold atomic displacement energy in tungsten metal. *Radiation Effects: Incorporating Plasma Science and Plasma Technology*, 30(3):129–133, 1976.

[53] J.F. Ziegler, J.P. Biersack, and U. Littmark. *The Stopping and Range of Ions in Matter (SRIM)*. Pergamon, New York, 1985.

[54] L.W. Packer, M. Gilbert, S. Hughes, S. Lilley, R. Pampin, and J.-C. Sublet. UK fusion technology experimental activities at the ASP 14MeV neutron irradiation facility. *Fusion Engineering and Design*, 87(5–6):662 – 666, 2012.

[55] A. Moslang. IFMIF: the intense neutron source to qualify materials for fusion reactors. *Comptes Rendus Physique*, 9(3):457 – 468, 2008.

[56] N. Baluc, R. Schaublin, P. Spatig, N. Ilchuk, L. Veleva, Z. Oksiuta, J. Theile, and M.Q. Tran. From materials development to their test in IFMIF: an overview. *Nuclear Fusion*, 51(11):113006, 2011.

[57] G.M. Voss, S. Davis, A. Dnestrovskij, A. Kirk, P.J. Knight, M. Loughlin, M.H. O'Brien, D. Sychugov, A. Tabasso, and H.R. Wilson. Conceptual design of a component test facility based on the spherical tokamak. *Fusion Engineering and Design*, 83(10-12):1648–1653, 2008.

[58] R.S. Averback. Atomic displacement processes in irradiated metals. *Journal of Nuclear Materials*, 216(0):49–62, 1994.

[59] J. Koike, P. R. Okamoto, L. E. Rehn, and M. Meshii. The dose, temperature, and projectile-mass dependence for irradiation-induced amorphization of cuti. *Journal of Materials Research*, 4:1143–1150, 1989.

[60] S. J. Zinkle and L. L. Snead. Influence of irradiation spectrum and implanted ions on the amorphization of ceramics. *Nuclear Instruments and Methods in Physics Research B*, 116:92–101, 1996.

[61] H. Kinoshita, N. Akasaka, H. Takahashi, I. Shibahara, and S. Onose. Microstructural change on electron irradiated oxide dispersion strengthened ferritic steels. *Journal of Nuclear Materials*, 191–194, Part B:874 – 878, 1992.

[62] J. Saito, T. Suda, S. Yamashita, S. Ohnuki, H. Takahashi, N. Akasaka, M. Nishida, and S. Ukai. Void formation and microstructural development in oxide dispersion strengthened ferritic steels during electron-irradiation. *Journal of Nuclear Materials*, 258–263, Part 2:1264 – 1268, 1998.

[63] G. Monnet, B. Devincre, and L.P. Kubin. Dislocation study of prismatic slip systems and their interactions in hexagonal close packed metals: application to zirconium. *Acta Materialia*, 52(14):4317–4328, 2004.

[64] K. Arakawa, K. Ono, H. Mori, A.S. Avilov, S.L. Dudarev, and L.D. Marks. In-Situ Transmission Electron Microscopy of the Dynamics of Point-Defect Clusters in Metals. *AIP Conference Proceedings*, 999(2008):66–78, 2008.

[65] C.M. Parish, P.D. Edmondson, Y. Zhang, and M.K. Miller. Direct observation of ion-irradiation-induced chemical mixing. *Journal of Nuclear Materials*, 418(1–3):106 – 109, 2011.

[66] X. Yi, M.L. Jenkins, M. Briceno, S.G. Roberts, Z. Zhou, and M.A. Kirk. In situ study of self-ion irradiation damage in W and W-5Re at 500C. *Philosophical Magazine*, 93(14):1715–1738, 2012.

[67] X. Yi. *Electron microscopy study of radiation damage in tungsten and alloys*. PhD thesis, University of Oxford (Wolfson College), 2013.

[68] Z. Yao, M.L. Jenkins, M. Hernández-Mayoral, and M.A. Kirk. The temperature dependence of heavy-ion damage in iron: A microstructural transition at elevated temperatures. *Philosophical Magazine*, 90(35-36):4623–4634, 2010.

[69] D E J Armstrong, a J Wilkinson, and S G Roberts. Mechanical properties of ion-implanted tungsten-5wt% tantalum. *Physica Scripta*, T145(014076), 2011.

[70] D.E.J. Armstrong, A.J. Wilkinson, and S.G. Roberts. Measuring local mechanical properties using fib machined cantilevers. *MRS Proceedings*, 1185(Symposium II), 2009.

[71] E.M. Grieveson, D.E.J. Armstrong, S. Xu, and S.G. Roberts. Compression of self-ion implanted iron micropillars. *Journal of Nuclear Materials*, 430(1–3):119 – 124, 2012.

[72] J.C. He, A. Hasegawa, and K. Abe. Effects of transmutation elements on the defect structure development of W irradiated by protons and neutrons. *Journal of Nuclear Materials*, 377(2):348 – 351, 2008.

[73] G.A. Cottrell. Sigma phase formation in irradiated tungsten, tantalum and molybdenum in a fusion power plant. *Journal of Nuclear Materials*, 334(2-3):166 – 168, 2004.

[74] G.A. Cotrell, R. Pampin, and N.P. Taylor. Transmutation and phase stability of tungsten armor in fusion power plants. *Fusion Science and Technology*, 50:89–98, 2006.

[75] R. Pampin and EURATOM/UKAEA Fusion Association. *Tungsten Transmutation and Resonance Self-shielding in PPCS Models for the Study of Sigma-phase Formation*. EURATOM/UKAEA Fusion Association, 2005.

[76] T. Tanno, A. Hasegawa, J.C. He, M. Fujiwara, M. Satou, S. Nogami, K. Abe, and T. Shishido. Effects of transmutation elements on the microstructural evolution and electrical resistivity of neutron-irradiated tungsten. *Journal of Nuclear Materials*, 386-388(0):218 – 221, 2009.

[77] T. Tanno, M. Fukuda, S. Nogami, and A. Hasegawa. Microstructure Development in Neutron Irradiated Tungsten Alloys. *Materials Transactions*, 52(7):1447–1451, 2011.

[78] R. Herschitz and D.N. Seidman. Radiation-induced precipitation in fast-neutron irradiated tungsten-rhenium alloys: An atom-probe field-ion microscope study. *Nuclear Inst. and Methods in Physics Research, B*, 7-8(PART 1):137–142, 1985.

[79] P. Krautwasser. Influence of Fast Neutron Fluence on the BDTT of Tunsgten, W10Re and W3.4Ni1.6Fe. *12th International Plansee Seminar*, 1:673–681, 1989.

[80] T. Tanno, A. Hasegawa, J.-C. He, M. Fujiwara, S. Nogami, M. Satou, T. Shishido, and K. Abe. Effects of Transmutation Elements on Neutron Irradiation Hardening of Tungsten. *Materials Transactions*, 48(9):2399–2402, 2007.

[81] V. Barabash, G. Federici, J. Linke, and C.H. Wu. Material/plasma surface interaction issues following neutron damage. *Journal of Nuclear Materials*, 313 – 316:42 – 51, 2003.

[82] B. Gludovatz, S. Wurster, A. Hoffmann, and R. Pippan. A study into the crack propagation resistance of pure tungsten. *Engineering Fracture Mechanics*, 100(0):76 – 85, 2013.

[83] M Rodig, R Conrad, H Derz, R Duwe, J Linke, A Lodato, M Merola, G Pott, G Vieider, and B Wiechers. Neutron-irradiation effects on high heat flux components and examination of plasma-facing materials and their joints. *Journal of Nuclear Materials*, 282-287, Part 2(0):1161 – 1165, 2000.

[84] G. Pintsuk, J. Compan, T. Hirai, J. Linke, and M. Rödig. Effect of transient heat loads on neutron irradiated tungsten and carbon based materials. In *22nd Symposium on 'Fusion Engineering'*, 2007. Record converted from VDB: 12.11.2012.

[85] V.F. Haussermann. A study of the radiation damage produced by energetic gold ions in molybdenum and tungsten. *Philosophical Magazine*, 25:583–598, 1972.

[86] F. Haussermann, M. Rohle, and M. Wilkens. Analysis of Dislocation Loops in Tungsten Produced by 60keV Ion Irradiation. *Philosophical Magazine*, 25(3):561–581, 1972.

[87] M.-C. Marinica and F. Willaime. Orientation of interstitials in clusters in α-Fe: A comparison between empirical potentials. *Diffusion and Defect Data Pt. B: Solid State Phenomena*, 129:67–74, 2007.

[88] E.A. Marquis and J.M. Hyde. Applications of atom-probe tomography to the characterisation of solute behaviours. *Materials Science and Engineering R: Reports*, 69(4-5):37 – 62, 2010.

[89] M. Muzyk, D. Nguyen-Manh, K.J. Kurzydcowski, N.L. Baluc, and S.L. Dudarev. Phase stability, point defects, and elastic properties of W-V and W-Ta alloys. *Physical Review B - Condensed Matter and Materials Physics*, 84(10), 2011.

[90] D.E.J. Armstrong, X. Yi, E.A. Marquis, and S.G. Roberts. Hardening of self ion implanted tungsten and tungsten 5-wt% rhenium. *Journal of Nuclear Materials*, 432(1-3):428–436, 2013.

[91] K.L. Wilson, M.I. Baskes, and D.N. Seidman. An in situ field-ion microscope study of the recovery behavior of ion-irradiated tungsten and tungsten alloys. *Acta Metallurgica*, 28(1):89–102, 1980.

[92] A.F. Bobkov, V.T. Zabolotnyi, L.I. Ivanov, G.M. Kukavadze, N.A. Makhlin, and A.L. Suvorov. Field ion microscopy of radiation defects in tungsten irradiated with 50 keV W+ ions - I. Method and results. *Soviet Atomic Energy*, 48(5):331–333, 1980.

[93] V.T. Zabolotnyi, L.I. Ivanov, N.A. Makhlin, and A.L. Suvorov. Field ion microscopy of radiation defects in tungsten irradiated with 50-keV W+ ions - II. Discussion of experimental results. *Soviet Atomic Energy*, 48(5):333–334, 1980.

[94] Yasuhisa Oya, Masashi Shimada, Makoto Kobayashi, Takuji Oda, Masanori Hara, Hideo Watanabe, Yuji Hatano, Pattrick Calderoni, and Kenji Okuno. Comparison of deuterium retention for ion-irradiated and neutron-irradiated tungsten. *Physica Scripta*, T145:014050, 2011.

[95] M. Shimada, Y. Hatano, Y. Oya, T. Oda, M. Hara, G. Cao, M. Kobayashi, M. Sokolov, H. Watanabe, B. Tyburska-Püschel, Y. Ueda, P. Calderoni, and K. Okuno. Overview of the US-Japan collaborative investigation on hydrogen isotope retention in neutron-irradiated and ion-damaged tungsten. *Fusion Engineering and Design*, 87(7-8):1166–1170, 2012.

[96] C.D. Hardie, C.A. Williams, S. Xu, and S.G. Roberts. Effects of irradiation temperature and dose rate on the mechanical properties of self-ion implanted Fe and Fe-Cr alloys. *Journal of Nuclear Materials*, 439(1-3):33–40, 2013.

[97] S. Wang, L. Wang, and R. Ewing. Irradiation-induced amorphization: Effects of temperature, ion mass, cascade size, and dose rate. *Physical Review B*, 63(2):024105, 2000.

[98] I.I. Arkhipov, S.L. Kanashenko, V.M. Sharapov, R.K. Zalavutdinov, and A.E. Gorodetsky. Deuterium trapping in ion-damaged tungsten single crystal. *Journal of Nuclear Materials*, 363-365(PSI-17):1168–1172, 2007.

[99] O. V. Ogorodnikova, T. Schwarz-Selinger, K. Sugiyama, and V. Kh. Alimov. Deuterium retention in tungsten exposed to low-energy pure and helium-seeded deuterium plasmas. *Journal of Applied Physics*, 109(1):013309, 2011.

[100] N. Hashimoto, J.D. Hunn, N. Parikh, S. Gilliam, S. Gidcumb, B. Patnaik, and L.L. Snead. Microstructural analysis on helium retention of ion-irradiated and annealed tungsten foils. *Journal of Nuclear Materials*, 347(3):307–313, 2005.

[101] T. Matsui, S. Muto, and T. Tanabe. TEM study on deuterium-irradiation-induced defects in tungsten and molybdenum. *Journal of Nuclear Materials*, 283-287:1139–1143, 2000.

[102] N. Yoshida, H. Iwakiri, K. Tokunaga, and T. Baba. Impact of low energy helium irradiation on plasma facing metals. *Journal of Nuclear Materials*, 337-339:946–950, 2005.

[103] H. Iwakiri, K. Yasunaga, K. Morishita, and N. Yoshida. Microstructure evolution in tungsten during low-energy helium ion irradiation. *Journal of Nuclear Materials*, 283-287:1134–1138, 2000.

[104] K. Tokunaga, O. Yoshikawa, K. Makise, and N. Yoshida. Effects of helium irradiation on high heat load properties of tungsten. *Journal of Nuclear Materials*, 307-311(1 SUPPL.):130–134, 2002.

[105] Q. Xu, N. Yoshida, and T. Yoshiie. Accumulation of helium in tungsten irradiated by helium and neutrons. *Journal of Nuclear Materials*, 367-370(A):806–811, 2007.

[106] Y.G. Li, W.H. Zhou, L.F. Huang, Z. Zeng, and X. Ju. Cluster dynamics modeling of accumulation and diffusion of helium in neutron irradiated tungsten. *Journal of Nuclear Materials*, 431(1-3):26–32, 2012.

[107] S.B. Gilliam, S.M. Gidcumb, N.R. Parikh, D.G. Forsythe, B.K. Patnaik, J.D. Hunn, L.L. Snead, and G.P. Lamaze. Retention and surface blistering of helium irradiated tungsten as a first wall material. *Journal of Nuclear Materials*, 347(3):289–297, 2005.

[108] D.E.J. Armstrong, P.D. Edmondson, and S.G. Roberts. Effects of sequential tungsten and helium ion implantation on nano-indentation hardness of tungsten. *Applied Physics Letters*, 102(251901):1–5, 2013.

[109] H. Iwakiri, K. Morishita, and N. Yoshida. Effects of helium bombardment on the deuterium behavior in tungsten. *Journal of Nuclear Materials*, 307-311:135–138, 2002.

[110] D.F. Johnson and E.A. Carter. Hydrogen in tungsten: Absorption, diffusion, vacancy trapping, and decohesion. *Journal of Materials Research*, 25(02):315–327, 2011.

[111] H. Schultz. Die erholung des elektrischen widerstandes kaltverformtem wolfram. *Acta Metallurgica*, 12(May):649–664, 1964.

[112] L.K. Keys, J. Smith, and J. Moteff. Stage iii recovery in neutron irradiated tungsten. *Scripta Metallurgica*, 1:71–72, 1967.

[113] L.K. Keys, J. Smith, and J. Moteff. High-temperature recovery of tungsten after neutron irradiation. *Physical Review*, 176(3):851–856, 1968.

[114] L.K. Keys. Comparison of the recovery of damage in w and mo after neutron irradiation. *Journal of Applied Physics*, 40(9):3866, 1969.

[115] L.K. Keys and J. Moteff. Neutron irradiation and defect recovery of tungsten. *Journal of Nuclear Materials*, 34(3):260 – 280, 1970.

[116] V.N. Bykov, G.A. Birzhevoi, M.I. Zakharova, and V.A. Solov'ev. Nature and stability of radiation defects in single-crystal tungsten. *Atomnaya Energiya*, 33(4):809–813, 1972.

[117] Y. Kim and J.M. Galligan. Radiation damage and stage III defect annealing in thermal neutron irradiated tungsten. *Acta Metallurgica*, 26:379–390, 1978.

[118] M.S. Anand, B.M. Pande, and R.P. Agarwala. Recovery in neutron irradiated tungsten. *Radiation Effects*, 39(3-4):149–155, 1978.

[119] D. Jeannotte. Energy of motion of vacancies in tungsten. *Physical Review Letters*, 19(5):232–233, 1967.

[120] D. Jeannotte and J. M. Galligan. A study of radiation damage in tungsten - i. *Acta Metallurgica*, 18:71–79, 1970.

[121] L. Lacefield, J. Moteff, and J.P. Smith. Neutron radiation damage in tungsten single crystals. *Philosophical Magazine*, 13(125):1079–1081, 1966.

[122] B. L. Eyre and D. M. Maher. Neutron irradiation damage in molybdenum. *Philosophical Magazine*, 24(190):767–797, 1971.

[123] C.J. Meechan and J.A. Brinkman. Electrical resistivity study of lattice defects introduced in copper by 1.25MeV electron irradiation at 80K. *Physical Review*, 103(5):1193–1202, 1956.

[124] B.L. Eyre. Transmission electron microscope studies of point defect clusters in fcc and bcc metals. *Journal of Physics F: Metal Physics*, 3:422–470, 1973.

[125] M.W. Thompson. The damage and recovery of neutron irradiated tungsten. *Philosophical Magazine*, 5(51):278–296, 1960.

[126] P. Ehrhart, P. Jung, H. Schultz, and H. Ullmaier. *Landolt-Bornstein: Atomic Defects in Metals*, volume 25 (Group III). Springer-Verlag, Berlin, 1991.

[127] D.R. Mason, X. Yi, M.A. Kirk, and S.L. Dudarev. Elastic trapping of dislocation loops in cascades in ion-irradiated tungsten foils. *Journal of Condensed Matter*, 26(37):375701, 2014.

[128] K-D. Rasch, R.W. Siegel, and H Schultz. Quenching and recovery investigations of vacancies in tungsten. *Philosophical Magazine A*, 41(1):91–117, 1980.

[129] J. N. Mundy, S. T. Ockers, and L. C. Smedskjaer. Vacancy migration enthalpy in tungsten at high temperatures. *Philosophical Magazine A*, 56(6):851–860, 1987.

[130] A. Debelle, M.F. Barthe, and T. Sauvage. First temperature stage evolution of irradiation-induced defects in tungsten studied by positron annihilation spectroscopy. *Journal of Nuclear Materials*, 376:216–221, 2008.

[131] D. Nguyen-Manh, A. Horsfield, and S. Dudarev. Self-interstitial atom defects in bcc transition metals: group-specific trends. *Physical Review B*, 73(2):020101, 2006.

[132] M.I. Zakharova, V.A. Solov'ev, and V.N. Bykov. High-temperature stages of the annealing of radiation defects in refractory bcc metals. *Atomnaya Energiya*, 38(2):78–81, 1975.

[133] L. Ventelon, F. Willaime, C.-C. Fu, M. Heran, and I. Ginoux. Ab initio investigation of radiation defects in tungsten: Structure of self-interstitials and specificity of di-vacancies compared to other bcc transition metals. *Journal of Nuclear Materials*, 425:16–21, 2012.

[134] Y.L. Liu, Z.H. Dai, and W.T. Wang. Influence of carbon-vacancy interaction on carbon and vacancy diffusivity in tungsten. *Computational Materials Science*, 83:1–4, 2014.

[135] T. Jourdan, C.C. Fu, L. Joly, J.L. Bocquet, M.J. Caturla, and F. Willaime. Direct simulation of resistivity recovery experiments in carbon-doped α-iron. *Physica Scripta*, T145:014049, 2011.

[136] D. Terentyev, G. Bonny, A. Bakaev, and D. Van Neck. On the thermal stability of vacancy-carbon complexes in alpha iron. *Journal of Physics: Condensed Matter*, 24(38):385401, 2012.

[137] S.L. Dudarev. Density functional theory models for radiation damage. *Annual Review of Materials Research*, 43(1):35–61, 2013.

[138] V.V. Bulatov and W. Cai. *Computer Simulations of Dislocations*. Oxford University Press, 2006.

[139] S.L. Dudarev, J.-L. Boutard, R. Lässer, M.J. Caturla, P.M. Derlet, M. Fivel, C.-C. Fu, M.Y. Lavrentiev, L. Malerba, M. Mrovec, D. Nguyen-Manh, K. Nordlund, M. Perlado, R. Schäublin, H.V. Swygenhoven, D. Terentyev, J. Wallenius, and F. Willaime D. Weygand. The EU programme for modelling radiation effects in fusion reactor materials: An overview of recent advances and future goals. *Journal of Nuclear Materials*, 386–388:1–7, 2009.

[140] Marius Stan. Discovery and design of nuclear fuels. *Materials Today*, 12(11):20 – 28, 2009.

[141] A.P. Sutton. *Electronic Structure of Materials*. Clarendon Press, 1993.

[142] J.E. Jones. On the determination of molecular fields. ii. from the equation of state of a gas. *Proceedings of the Royal Society of London. Series A*, 106(738):463–477, 1924.

[143] M. W. Finnis and J. E. Sinclair. A simple empirical n-body potential for transition metals. *Philosophical Magazine A*, 50(1):45–55, 1984.

[144] T. Diaz De La Rubia, R. S. Averback, R. Benedek, and W. E. King. Role of thermal spikes in energetic displacement cascades. *Physical Review Letters*, 60:76–76, 1988.

[145] A.F. Calder, D.J. Bacon, A.V. Barashev, and Y.N. Osetsky. On the origin of large interstitial clusters in displacement cascades. *Philosophical Magazine*, 90:863–884, 2010.

[146] H Trinkaus, B.N Singh, and S.I Golubov. Progress in modelling the microstructural evolution in metals under cascade damage conditions. *Journal of Nuclear Materials*, 283–287, Part 1:89–98, 2000.

[147] W.J. Phythian, R.E. Stoller, A.J.E. Foreman, A.F. Calder, and D.J. Bacon. A comparison of displacement cascades in copper and iron by molecular dynamics and its application to microstructural evolution. *Journal of Nuclear Materials*, 223(3):245 – 261, 1995.

[148] J. Chang, W. Cai, V.V. Bulatov, and S. Yip. Dislocation motion in BCC metals by molecular dynamics. *Materials Science and Engineering: A*, 309-310:160–163, 2001.

[149] M.C. Fivel and A.A. El-Azab. Linking continuum mechanics and 3D discrete dislocation dynamics. *J. Phys. IV France*, 09:261–270, 1999.

[150] J.C. Crone, P.W. Chung, K.W. Leiter, J. Knap, S. Aubry, G. Hommes, and A. Arsenlis. A multiply parallel implementation of finite-element discrete dislocation dynamics for arbitrary geometries. *Journal of Modelling and Simulation of Materials Science and Engineering*, 22(035014):27, 2014.

[151] E. Tarleton, D.S. Balint, J. Gong, and A.J. Wilkinson. A discrete dislocation plasticity study of the micro-cantilever size effect. *Acta Materialia*, 88:271–282, 2015.

[152] A. Vattré, B. Devincre, F. Feyel, R. Gatti, S. Groh, O. Jamond, and A. Roos. Modelling crystal plasticity by 3D dislocation dynamics and the finite element method: the discrete-continuous model revisited. *Journal of the Mechanics and Physics of Solids*, 63:491–505, 2014.

[153] A. Arsenlis, M. Rhee, G. Hommes, R. Cook, and J. Marian. A dislocation dynamics study of the transition from homogeneous to heterogeneous deformation in irradiated body-centered cubic iron. *Acta Materialia*, 60(9):3748–3757, 2012.

[154] N.R. Barton, A. Arsenlis, and J. Marian. A polycrystal plasticity model of strain localization in irradiated iron. *Journal of the Mechanics and Physics of Solids*, 61(2):341–351, 2013.

[155] E. Martínez, J. Marian, A. Arsenlis, M. Victoria, and J.M. Perlado. Atomistically informed dislocation dynamics in fcc crystals. *Journal of the Mechanics and Physics of Solids*, 56(3):869–895, 2008.

[156] T.D. Swinburne, S.L. Dudarev, S.P. Fitzgerald, M.R. Gilbert, and A.P. Sutton. Theory and simulation of the diffusion of kinks on dislocations in bcc metals. *Physical Review B*, 87:064108, 2013.

[157] T.D. Swinburne. Collective transport in the discrete Frenkel-Kontorova model. *Physical Review E*, 88:012135, 2013.

[158] A. Stukowski, D. Cereceda, T.D. Swinburne, and J. Marian. Thermally-activated non-Schmid glide of screw dislocations in W using atomistically-informed kinetic Monte Carlo simulations. *International Journal of Plasticity*, 65:108–130, 2015.

[159] T.D. Swinburne, S.L. Dudarev, and A.P. Sutton. The classical mobility of highly mobile crystal defects. *Physical Review Letters*, 113(21):215501, 2014.

[160] P.M. Derlet, D. Nguyen-Manh, and S.L. Dudarev. Multiscale modeling of crowdion and vacancy defects in body-centered-cubic transition metals. *Physical Review B*, 76:054107, 2007.

[161] P.M. Derlet, M.R. Gilbert, and S.L. Dudarev. Simulating dislocation loop internal dynamics and collective diffusion using stochastic differential equations. *Physical Review B*, 84:134109, 2011.

[162] S. Dudarev, M. Gilbert, K. Arakawa, H. Mori, Z. Yao, M. Jenkins, and P. Derlet. Langevin model for real-time Brownian dynamics of interacting nanodefects in irradiated metals. *Physical Review B*, 81(22):224107, 2010.

[163] J. Marian, E. Martínez, H.J. Lee, and B.D. Wirth. Micro/meso-scale computational study of dislocation-stacking-fault tetrahedron interactions in copper. *Journal of Materials Research*, 24:3628–3635, 2009.

[164] Oxford Instruments. Electrolytic polishing and etching: sample preparation for EBSD. `http://www.ebsd.com/images/articles/29/fig8.jpg`.

[165] O. Piotrowski, C. Madore, and D. Landolt. Electropolishing of tantalum in sulfuric acid-methanol electrolytes. *Electrochimica Acta*, 44(19):3389–3899, 1999.

[166] Centre de Sciences Nucléaires et de Sciences de la Matière. Accélérateurs. `http://www.csnsm.in2p3.fr/Accelerateurs`, 2015.

[167] D.E.J. Armstrong and S.G. Roberts. Radiation resistance of nano-structured tungsten-rhenium sheet. *MRS Proceedings*, 1513(1), 2013.

[168] J.A. Hinks and S.E. Donnelly. Copper indium diselenide : crystallography and radiation-induced dislocation loops. *Philosophical Magazine*, 91(4):517–536, 2011.

[169] B.L. Eyre and R. Bullough. On the formation of interstitial loops in bcc metals. *Philosophical Magazine*, 12(115):31–39, 1965.

[170] University of Cambridge. DoITPoMS. `http://www.doitpoms.ac.uk/tlplib/stereographic/wulff_plot_poles.php`, 2015.

[171] G.W. Groves and A. Kelley. Interstitial dislocation loops in magnesium oxide. *Philosophical Magazine*, 6(72):1527, 1961.

[172] D. M. Maher and B.L. Eyre. Neutron irradiation damage in molybdenum, Part I: Characterization of small perfect dislocation loops by transmission electron microscopy. *Philosophical Magazine*, 23:409–437, 1971.

[173] P.B. Hirsch and A. Howie. *Electron microscopy of thin crystals*. Butterworths, 1971.

[174] C.A. Schneider, W.S. Rasband, and K.W. Eliceiri. NIH Image to ImageJ: 25 years of image analysis. *Nature Methods*, 9:671–675, 2012.

[175] X Yi, A E Sand, D R Mason, M A Kirk, S G Roberts, K Nordlund, and S L Dudarev. Direction observation of size scaling and elastic interaction between nanoscale defects in collision cascades. *EPL*, 110:36001, 2015.

[176] T W Ridler and S Calvard. Picture thresholding using an iterative section method. *IEEE Transactions on Systems, Man, and Cybernetics*, SMC-8(8):630, 1978.

[177] W.K. Brown and K.H. Wohletz. Derivation of the Weibull distribution based on physical principles and its connection to the Rossin-Rammler and lognormal distributions. *Journal of Applied Physics*, 78(4):2758–2763, 1995.

[178] A.E. Sand, S. Dudarev, and K. Nordlund. High energy collision cascades in tungsten: dislocation loops structure and clustering scaling laws. *EPL*, 103:46003, 2013.

[179] K. Arakawa, T. Amino, and H. Mori. Direct observation of the coalescence process between nanoscale dislocation loops with different Burgers vectors. *Acta Materialia*, 59(1):141–145, 2011.

[180] J. A. Turnbull. The coalescence of dislocation loops by self climb. *Philosophical Magazine*, 21(21:169):83–94, 1970.

[181] J. Narayan and J. Washburn. Self-climb of dislocation loops in magnesium oxide. *Philosophical Magazine*, 26(5):1179–1190, 1972.

[182] K. Arakawa, K. Ono, M. Isshiki, K. Mimura, M. Uchikoshi, and H. Mori. Observation of the one-dimensional diffusion of nanometer-sized dislocation loops. *Science*, 318(5852):956–9, 2007.

[183] Z.S. Basinski, J.S. Dugdale, and A. Howie. The electrical resistivity of dislocations. *Philosophical Magazine*, 8(96):1989–1997, 1963.

[184] R.A. Brown. Electrical resistivity of dislocations in metals. *Journal of Applied Physics: Metal Physics*, 7(7):1283–1295, 1977.

[185] D. Mason. Private communication. CCFE, 2014.

[186] J.B. Hirth and J. Lothe. *Theory of Dislocations*. Krieger Publishing Company, 1982.

[187] S.L. Dudarev, K. Arakawa, X. Yi, Z. Yao, M. L. Jenkins, M.R. Gilbert, and P.M. Derlet. Spatial ordering of nano-dislocation loops in ion-irradiated materials. *Journal of Nuclear Materials*, 455:16–20, 2014.

[188] D. Mordehai, E. Clouet, M. Fivel, and M. Verdier. Introducing dislocation climb by bulk diffusion in discrete dislocation dynamics. *Philosophical Magazine*, 88(6):899–925, 2008.

[189] B. Bakó, E. Clouet, L.M. Dupuy, and M. Blétry. Dislocation dynamics simulations with climb: kinetics of dislocation loop coarsening controlled by bulk diffusion. *Philosophical Magazine*, 91(23):3173–3191, 2011.

[190] L. Bukonte, T. Ahlgren, and K. Heinola. Modelling of monovacancy diffusion in w over a wide temperature range. *Journal of Applied Physics*, 115(123504):1–5, 2014.

[191] B. Bakó, E. Clouet, L.M. Dupuy, and M. Blétry. Dislocation dynamics simulations with climb: Kinetics of dislocation loop coarsening controlled by bulk diffusion. *Philosophical Magazine*, 91(23):3173–3191, 2011.

[192] H. Merher. Dislocation pipe diffusion. In *Diffusion in Solids*, volume 155 of *Springer Series in Solid-State Sciences*, pages 583–591. Springer Berlin Heidelberg, 2007.

[193] P. Chen and K. Nordlund. Modified embedded-atom method used to derive interatomic potentials for defects and phase formation in the w-c system. *Physical Review B*, 88(214101):1–9, 2013.

[194] N. Juslin, P. Erhart, P. Traskelin, J. Nord, K. Henriksson, E. Salonen, K. Nordlund, and K. Albe. Analytical interatomic potential for modeling nonequilibrium processes in the W-C-H system. *Journal of Applied Physics*, 98(123520):1–12, 2005.

[195] B-J. Lee, M.I. Baskes, H. Kim, and Y.K. Cho. Second nearest-neighbor modified embedded atom method potentials for bcc transition metals. *Physical Review B*, 64(184102):1–11, 2001.

[196] B-J. Lee and J.W. Lee. A modified embedded atom method interatomic potential for carbon. *Computer Coupling of Phase Diagrams and Thermochemistry*, 29:7–16, 2005.

[197] S. Plimpton. Fast parallel algorithms for short-range molecular dynamics. *Journal of Computational Physics*, 117(1):1–19, 1995.

[198] E. Clouet, S. Garruchet, H. Nguyen, M. Perez, and C. Becquart. Dislocation interaction with C in alpha-Fe: a comparison between atomic simulations and elasticity theory. *Acta Materialia*, 56:3450–3460, 2008.

[199] K. Arakawa, R. Imamura, K. Ohota, and K. Ono. Evolution of point defect clusters in pure iron under low-energy He^+ irradiation. *Journal of Applied Physics*, 89:4752, 2001.

[200] D Brimbal, B Decamps, J Henry, E Meslin, and A Barbu. Single- and dual-beam in situ irradiations of high-purity iron in a transmission electron microscope: effects of heavy ion irradiation and helium injection. *Acta Materialia*, 64:391–401, 2014.

[201] A.H. Cottrell and B.A. Bilby. Dislocation theory of yielding and strain ageing of iron. *Proceedings of the Royal Society. Section A*, 62(1):49–62, 1949.

[202] A Prokhodtseva, B Decamps, A Ramar, and R Schäublin. Impact of He and Cr on defect accumulation in ion-irradiated ultrahigh-purity Fe(Cr) alloys. *Acta Materialia*, 61(18):6958–6971, 2013.

[203] G Lucas and R Schäublin. Helium effects on displacement cascades in α-iron. *Journal of Physics: Condensed Matter*, 20(41):1–12, 2008.

[204] L Ventelon, B D Wirth, and C Domain. Helium-self interstitial atom interaction in α-iron. *Journal of Nuclear Materials*, 351(1–3):119–132, 2006.

[205] X. Yi. Unpublished work. University of Oxford, 2014.

[206] M.J. Baldwin and R.P. Doerner. Formation of helium induced nanostructure fuzz on various tungsten grades. *Journal of Nuclear Materials*, 404:165–173, 2010.

[207] P.E. Lhuillier, T. Belhabib, P. Desgardin, B. Courtois, T. Sauvage, M.F. Barthe, A.L. Thomann, P. Brault, and Y. Tessier. Trapping and release of helium in tungsten. *Journal of Nuclear Materials*, 416(1–2):13–17, 2011.

[208] K.O.E. Henriksson, K. Nordlund, A. Krasheninnikov, and J. Keinonen. The depths of hydrogen and helium bubbles in tungsten: a comparison. *Fusion Science and Technology*, 50:43–57, 2006.

[209] K.O.E. Henriksson, K. Nordlund, and J. Keinonen. Molecular dynamics simulations of helium cluster formation in tungsten. *Nuclear Inst. and Methods in Physics Research, B*, 244:377–391, 2006.

[210] Niklas Juslin and Brian D. Wirth. Interatomic potentials for simulation of He bubble formation in W. *Journal of Nuclear Materials*, 432(1–3):61–66, 2013.

[211] F. Sefta, N. Juslin, K.D. Hammond, and B. D. Wirth. Molecular dynamics simulations on the effect on sub-surface helium bubbles on the sputtering yield of tungsten. *Journal of Nuclear Materials*, 438:S493–S496, 2013.

[212] K.D. Hammond and D.B. Wirth. Crystal orientation effects on helium ion depth distributions and adatom formation processes in plasma-facing tungsten. *Journal of Applied Physics*, 116:143301, 2014.

[213] A. Arsenlis, W. Cai, M. Tang, M. Rhee, T. Oppelstrup, G. Hommes, T.G. Pierce, and Bulatov V.V. Enabling strain hardening simulations with dislocation dynamics. *Modelling and Simulation in Materials Science and Engineering*, 15(6):553–595, 2007.

[214] M. Fivel and M. Verdier. TRIDIS. `http://www.numodis.fr/tridis/`, 2015.

[215] H.M. Zbib, M. Rhee, and J.P. Hirth. On plastic deformation and the dynamics of 3D dislocations. *International Journal of Mechanical Sciences*, 40(2–3):113–127, 1998.

[216] G. Po, M. Lazar, D. Seif, and N. Ghoniem. Singularity-free dislocation dynamics with strain gradient elasticity. *Journal of the Mechanics and Physics of Solids*, 68:161–178, 2014.

[217] N. Ghoniem, S.-H. Tong, and L. Sun. Parametric dislocation dynamics: A thermodynamics-based approach to investigations of mesoscopic plastic deformation. *Physical Review B*, 61(2):913–927, 2000.

[218] L.P. Kubin, B. Devincre, and M. Tang. Mesoscopic modelling and simulation of plasticity in fcc and bcc crystals : Dislocation intersections and mobility. *Journal of Computer-Aided Materials Design*, 5:31–54, 1998.

[219] D. Weygand, L.H. Friedman, E. Van Der Giessen, and A. Needleman. Discrete dislocation modeling in three-dimensional confined volumes. *Materials Science and Engineering A*, 309-310:420–424, 2001.

[220] B. Devincre, R. Madec, G. Monnet, S. Queyreau, R. Gatti, and L. Kubin. Modeling crystal plasticity with dislocation dynamics simulations: the microMegas code. *Mechanics of nano-objects: Presses de l'Ecole des Mines de Paris*, pages 81–100, 2011.

[221] J.P. Hirth and J. Lothe. *Theory of dislocations*. McGraw-Hill, 1967.

[222] Z. Wang, N. Ghoniem, and R. LeSar. Multipole representation of the elastic field of dislocation ensembles. *Physical Review B*, 69(17):174102, 2004.

[223] J. Yin, D.M. Barnett, S.P. Fitzgerald, and W. Cai. Computing dislocation stress fields in anisotropic elastic media using fast multipole expansions. *Modelling and Simulation in Materials Science and Engineering*, 20(4):045015, 2012.

[224] W. Cai and V.V. Bulatov. Mobility laws in dislocation dynamics simulations. *Materials Science and Engineering: A*, 387-389(0):277 – 281, 2004.

[225] S.P. Fitzgerald and S. Aubry. Self-force on dislocation segments in anisotropic crystals. *Journal of Physics: Condensed Matter*, 22(29):5403, 2010.

[226] B. Gurrutxaga-Lerma, D. Balint, D. Dini, D.E. Eakins, and A.P. Sutton. Attenuation of the dynamic yield point of shocked aluminum using elastodynamic simulations of dislocation dynamics. *Phys. Rev. Lett.*, 114:174301, 2015.

[227] W. Cai, A. Arsenlis, C.R. Weinberger, and V.V. Bulaton. A non-singular continuum theory of dislocations. *Journal of the Mechanics and Physics of Solids*, 54(3):561–587, 2006.

[228] J.M. Cushing. *Differential Equations: an applied approach.* Pearson Prentice Hall, 2004.

[229] A. Hartmaier, M.C. Fivel, G.R. Canova, and P. Gumbsch. Image stresses in a free-standing thin film. *Modelling and Simulation in Materials Science and Engineering*, 7:781–793, 1999.

[230] J. Chen. General dislocation image stress of anisotropic cubic thin film. *Journal of Applied Physics*, 093522(112):1–18, 2012.

[231] J. Bastecka. Interaction of dislocation loop with free surface. *Czech. J. Phys.*, 14B:430–441, 1964.

[232] P.P. Groves and D.J. Bacon. The dislocation loop near a free surface. *Philosophical Magazine*, 22(175):83–91, 1970.

[233] C.R. Weinberger, S. Aubry, S.-W. Lee, W.D. Nix, and W. Cai. Modelling dislocations in a free-standing thin film. *Modelling and Simulation in Materials Science and Engineering*, 17(7):075007, 2009.

[234] M. Tang, W. Cai, G. Xu, and V.V. Bulatov. A hybrid method for computing forces on curved dislocations intersecting free surfaces in three-dimensional dislocation dynamics. *Modelling and Simulation in Materials Science and Engineering*, 14(7):1139–1151, 2006.

[235] E.H. Yoffe. A dislocation at a free surface. *Philosophical Magazine*, 6(69):1147–1155, 1961.

[236] A. K. Head. Edge dislocations in inhomogeneous media. *Proceedings of the Physical Society. Section B*, 66(9):793–801, 1953.

[237] Y. Du, P. Segall, and H. Gao. Dislocations in inhomogeneous media via a moduli perturbation approach: General formulation and two dimensional solutions. *Journal of Geophysical Research*, 99(7):13767–13779, 1994.

[238] D.M. Barnett. The displacement field of a triangular dislocation loop. *Philosophical Magazine A*, 51(3):383–387, 1985.

[239] D.M. Barnett and R.W. Balluffi. The displacement field of a triangular dislocation loop - a correction with commentary. *Philosophical Magazine Letters*, 87(12):943–944, 2007.

[240] M. Fivel and C. Depres. An easy implementation of displacement calculations in 3D discrete dislocation dynamics codes. *Philosophical Magazine*, 94(28):3206–3214, 2014.

[241] C. Motz, D. Weygand, J. Senger, and P. Gumbsch. Micro-bending tests: a comparison between three-dimensional discrete dislocation dynamics simulations and experiments. *Acta Materialia*, 56(9):1942–1955, 2008.

[242] C. Motz, D. Weygand, J. Senger, and P. Gumbsch. Initial dislocation structures in 3-d discrete dislocation dynamics and their influence on microscale plasticity. *Acta Materialia*, 57(6):1744–1754, 2009.

[243] J.A. El-Awady, S.B. Bulent, and N.M. Ghoniem. A self-consistent boundary element, parametric dislocation dynamics formulation of plastic flow in finite volumes. *Journal of Mechanics and Physics of Solids*, 56(5):2019–2035, 2008.

[244] P.M. Derlet, D. Nguyen-Manh, and S.L. Dudarev. Multiscale modelling of crowdion and vacancy defects in body-centred cubic transition metals. Technical report, EURATOM/UKAEA Fusion, 2007.

[245] M. R. Gilbert, S. Queyreau, and J. Marian. Stress and temperature dependence of screw dislocation mobility in α-Fe by molecular dynamics. *Phys. Rev. B*, 84:174103, 2011.

[246] HL Prekel and H Conrad. Dislocation velocity measurements in high purity molybdenum. *Acta Metallurgica*, 16:337–346, 1967.

[247] D. Caillard. Kinematics of dislocations in pure Fe. Part I. In-situ straining experiments at room temperature. *Acta Materialia*, 58:3493–3503, 2010.

[248] Jinpeng Chang, Vasily V Bulatov, and Sidney Yip. Molecular dynamics study of edge dislocation motion in a bcc metal. *Journal of Computer-Aided Materials Design*, 6:165–173, 1999.

[249] J. Chang, W. Cai, V.V. Bulatov, and S. Yip. Molecular dynamics simulations of motion of edge and screw dislocations in a metal. *Computational Materials Science*, 23:111–115, 2002.

[250] P.-W. Ma and S.L. Dudarev. Langevin spin dynamics. *Physical Review B*, 83:134418, 2011.

[251] Pui-Wai Ma and S. Dudarev. Longitudinal magnetic fluctuations in Langevin spin dynamics. *Physical Review B*, 86(5):054416, 2012.

[252] S.P. Fitzgerald. Private communication. University of Oxford, 2015.

[253] G. J. Ackland and R. Thetford. An improved N-body semi-empirical model for b.c.c transition metals. *Philosophical Magazine A*, 56(1):15–30, 1987.

[254] W.H. Zhou, C.G. Zhang, Y.G. Li, and Z. Zeng. Transport, dissociation and rotation of small self-interstitial atom clusters in tungsten. *Journal of Nuclear Materials*, 453:202–209, 2014.

[255] W. Shinoda, M. Shiga, and M. Mikami. Rapid estimation of elastic constants by molecular dynamics simulation under constant stress. *Physical Review B*, 64:134103, 2004.

[256] A.F. Calder and D.J. Bacon. A molecular dynamics study of displacement cascades in α-iron. *Journal of Nuclear Materials*, 207:25–45, 1993.

[257] K. Nordlund, M. Ghaly, R.S. Averback, M. Caturla, T. Diaz de la Rubia, and J. Tarus. Defect production in collision cascades in elemental semiconductors and fcc metals. *Physical Review B*, 57(13):7556–7570, 1998.

[258] H.A. Kramers. Brownian motion in a field of force and the diffusion model of chemical reactions. *Physica*, 7(4):284–304, 1940.

[259] A. Einstein. Über die von der molekularkinetischen Theorie der Wärme geforderte Bewegung von in ruhenden Flüssigkeiten suspendierten Teilchen. *Annalen der Physik*, 322(8):549–560, 1905.

[260] R.C.G. Killean and E.J. Lisher. The Debye temperatures of the cubic elements and their relationship to melting points. *Journal of Physics C: Solid State Physics*, 8(21):3510, 1975.

[261] M.-C. Marinica, L. Ventelon, M.R. Gilbert, L. Proville, S.L. Dudarev, J. Marian, G. Bencteux, and F. Willaime. Interatomic potentials for modelling radiation defects and dislocations in tungsten. *Journal of Physics: Condensed Matter*, 25(39):395502, 2013.

[262] M. Lazar and G.A. Maugin. Dislocations in gradient elasticity revisited. *Proceedings of the Physical Society. Section A*, 462(2075):3465–3480, 2006.

[263] G.A. Cottrell, S.L. Dudarev, and R.A. Forrest. Immobilization of interstitial loops by substitutional alloy and transmutation atoms in irradiated metals. *Journal of Nuclear Materials*, 325:195–201, 2004.

[264] T.D. Swinburne. *Stochastic Dynamics of Crystal Defects*. PhD thesis, Imperial College London, 2015.

[265] G.R. Love. Dislocation pipe diffusion. *Acta Metallurgica*, 12, 1964.

[266] Y.N. Osetsky, D.J. Bacon, A. Serra, B.N. Singh, and S.I. Golubov. One-dimensional atomic transport by clusters of self-interstitial atoms in iron and copper. *Philosophical Magazine*, 83(1):61–91, 2003.

[267] J. Barnes and P. Hut. A hierarchical $O(NlogN)$ force calculation algorithm. *Nature*, 324:446–449, 1986.

[268] V. Rokhlin. Rapid solution of integral equations of classical potential theory. *Journal of Computational Physics*, 60(2):187 – 207, 1985.

[269] T. Darden, D. York, and L. Pedersen. Particle mesh Ewald: An $Nlog(N)$ method for Ewald sums in large systems. *Journal of Chemical Physics*, 98(12):10089–10092, 1993.

[270] M. Burtscher and K. Pingali. An Efficient CUDA Implementation of the Tree-Based Barnes Hutt n-body Algorithm. In *GPU Computing Gems, NVIDIA Corporation*, chapter 6, pages 75–92. Elsevier Inc, 2011.

[271] L. Nyland, M. Harris, and J. Prins. Fast n-body simulation with CUDA. In *GPU Gems 3, NVIDIA Corporation*, chapter 31. Addison-Wesley Professional, 2007.

[272] S. Queyreau, J. Marian, B.D. Wirth, and A. Arsenlis. Analytical integration of the forces induced by dislocations on a surface element. *Modelling and Simulation in Materials Science and Engineering*, 22:035004, 2014.